Title

Terahertz metasurface laser design and study of optical feedback

Author

Kim, Anthony

Publication Date

2024

Peer reviewed|Thesis/dissertation

UNIVERSITY OF CALIFORNIA
Los Angeles

Terahertz metasurface laser design and study of optical feedback

A dissertation submitted in partial satisfaction
of the requirements for the degree
Doctor of Philosophy in Electrical and Computer Engineering

by

Anthony D. Kim

2024

ABSTRACT OF THE DISSERTATION

Terahertz metasurface laser design and study of optical feedback

by

Anthony D. Kim
Doctor of Philosophy in Electrical and Computer Engineering
University of California, Los Angeles, 2024
Professor Benjamin S. Williams, Chair

Terahertz (THz) external-cavity lasers based on quantum-cascade (QC) metasurfaces are emerging as widely-tunable, single-mode sources with the potential to cover the 1-6 THz range in discrete bands with watt-level output power. By operating on an ultra-short cavity with a length on the order of the wavelength, the QC vertical-external-cavity surface-emitting-laser (VECSEL) architecture enables continuous, broadband tuning while producing high quality beam patterns and scalable power output. These properties are favorable for spectroscopic applications that can benefit from large bandwidths and high output powers, such as serving as a local-oscillator (LO) for heterodyne receivers in astronomy. THz QC-lasers have garnered much attention in the past decade in the astrophysics community due to the lack of well-established THz LO sources above 3 THz. The QC-VECSEL has potential to fill this technological gap, and provide the power output levels necessary for next-generation heterodyne receiver arrays.

In this thesis, we discuss the methods and challenges for designing the metasurface at various frequencies across the 1–6 THz bandwidth, and establish fundamental rules for VECSEL scaling. We discuss the methods and challenges for designing the metasurface at various frequencies across the THz bandwidth, and demonstrate single-mode lasing up to 5.72 THz. The device is enabled by a reflectarray metasurface composed of sub-wavelength metallic antennas loaded with quantum-cascade gain material. In theory, wavelength-scaling the metasurface is a matter of scaling up or down the geometric parameters proportionally,

maintaining the electromagnetic properties of the structure. However, as the QC-VECSEL is scaled below 2 THz, the primary challenges are reduced gain from the QC active region, increased metasurface quality factor and its effect on tunable bandwidth, and larger power consumption due to a correspondingly scaled metasurface area. At frequencies above 4.5 THz, challenges arise from a reduced metasurface quality factor and the excess absorption that occurs from proximity to the *Reststrahlen* band. Additionally, the effect of different output couplers on device performance across the whole tuning bandwidth is studied, demonstrating a significant trade-off between the slope efficiency and tuning bandwidth.

The second half of this thesis details the first study of self-mixing and optical feedback in the QC-VECSEL. The self-mixing effect has been well explored in THz QCLs over the past couple decades, and has potential to be a highly sensitive, compact, and cost-effective metrological tool with applications in spectroscopy and imaging. In this study, a single-mode 2.80 THz QC-VECSEL operating in continuous-wave is subjected to various optical feedback conditions (i.e. feedback strength, round-trip time, and angular misalignment) while variations in its terminal voltage associated with self-mixing are monitored. Due to its large radiating aperture and near-Gaussian beam shape, we find that the QC-VECSEL is strongly susceptible to optical feedback, which is robust against misalignment of external optics. This, in addition to the use of a high-reflectance flat output coupler, results in high feedback levels associated with multiple round-trips within the external cavity — a phenomenon not typically observed for ridge-waveguide QC-lasers. Thus, a new theoretical model is established to describe self-mixing in the QC-VECSEL. The stability of the device under variable optical feedback conditions is also studied. Any mechanical instabilities of the external cavity (such as vibrations of the output coupler), are enhanced due to feedback and result in low-frequency oscillations of the terminal voltage. The work reveals how the self-mixing response differs for the QC-VECSEL architecture, informs other systems in which optical feedback is unavoidable, and paves the way for QC-VECSEL self-mixing applications.

The dissertation of Anthony D. Kim is approved.

Raymond M. Spearrin

Sergio Carbajo Garcia

Subramanian S. Iyer

Benjamin S. Williams, Committee Chair

University of California, Los Angeles

2024

TABLE OF CONTENTS

LIST OF FIGURES

LIST OF TABLES

ACKNOWLEDGMENTS

I express tremendous gratitude towards my advisor, Professor Ben Williams, for help guiding me in this tumultuous journey. As both a mentor and a role model, Ben has largely shaped both my intellectual growth, and my approach to difficult challenges. I met Ben in my very first quarter at UCLA in 2016 while taking his 101A Electromagnetics class, and was taken in as an undergraduate researcher several months later. I am incredibly thankful and privileged to have been given that initial opportunity, which ultimately led to one of the most impactful and rewarding chapters of my life.

I express love to my family, who, with their monumental financial and emotional support, have made it possible for me to pursue this doctorate degree in the United States and at UCLA. I am forever grateful to my brother, who has always wanted what's best for me, pushed me to be stronger, and showed no limits to his compassion. Most of all, I owe everything to my mother, who dedicated so much of her life in hopes of bettering ours. Thank you Sukhwa "Lucia" Kang for everything you've done for me.

I am extremely grateful for all my friends and labmates that have been with me throughout my academic career. Though we only overlapped for a couple years, Chris Curwen was integral to my early development in the lab. I am immensively appreciative of his mentorship and willingness to help whenever I was in need. I am thankful to all the great people who I've met in the lab over the years. To Chris Curwen, Luyao Xu, Sudeep Khanal, Jiawei Wang, Yue Shen, Parastou Mortazavian, Zhaowen He, Eilam Morag, Mohammad Shahili, Yu Wu, Jordane Bloomfield, and Daniel McGovern: thank you all for your cooperative energy and kindness. Furthermore, I'm deeply grateful to my friends beyond the lab whose presence has consistently brightened my days, even through the most stressful times. Your support has been invaluable throughout my graduate studies.

Next, I would like to express my sincerest appreciation for my dissertation committee: Prof. Mitchell Spearrin, Prof. Sergio Carbajo, and Prof. Subramanian Iyer. Their counsel and constructive recommendations have helped guide my research and helped me maintain a

broader perspective of my research and research field. Additionally, I am very grateful to the team at Jet Propulsion Laboratory including Chris Curwen, Jonathan Kawamura, and Boris Karasik, for their mentorship and enthusiastic collaboration. It has been an absolute privilege to work with the team and perform collaborative research at JPL laboratories. Lastly, special thanks to funding support from Jet Propulsion Laboratory, the National Science Foundation (2041165), and the National Aeronautics and Space Administration (80NSSC22K1894).

VITA

2016–2018 B.S. in Electrical and Computer Engineering, University of California, Los Angeles (UCLA).

2018–2020 M.S. in Electrical and Computer Engineering, University of California, Los Angeles (UCLA).

2020–present Ph.D. Candidate in Electrical and Computer Engineering, University of California, Los Angeles (UCLA).

PUBLICATIONS

A. D. Kim, D. McGovern, and B. S. Williams, "Multi-bounce self-mixing in terahertz metasurface external-cavity lasers." *Optics Express*, vol. 32, no. 11, pp. 18880–18895, May 2024.

Y. Wu, **A. D. Kim**, S. J. Addamane, and B. S. Williams, "Harmonic and Sub-harmonic RF Injection Locking of THz Metasurface Quantum-cascade VECSEL Comb." *ACS Photonics* (in review), 2024.

M. Shahili, S. J. Addamane, **A. D. Kim**, C. A. Curwen, J. H. Kawamura, and B. S. Williams, "Continuous-wave GaAs/AlGaAs quantum cascade laser at 5.7 THz." *Nanophotonics*, vol. 13, no. 10, pp. 1735–1743, Apr. 2024.

C. A. Curwen, **A. D. Kim**, B. S. Karasik, J. H. Kawamura, and B. S. Williams, "Optical injection locking of a THz quantum-cascade VECSEL with an electronic source." *Optics Letters*, vol. 48, no. 14, pp. 3809–3812, Jul. 2023.

S. Thomas, S. Razavian, W. Sun, B. F. Motlagh, **A. D. Kim**, Y. Wu, B. S. Williams, and A. Babakhani, "A 0.4-4 THz p-i-n Diode Frequency Multiplier in 90-nm SiGe BiCMOS." *IEEE Journal of Solid-State Circuits*, vol. 58, no. 9, pp. 2407–2420, Sep. 2023.

A. D. Kim, C. A. Curwen, Y. Wu, J. L. Reno, S. J. Addamane, and B. S. Williams, "Wavelength Scaling of Widely-Tunable Terahertz Quantum-Cascade Metasurface Lasers." *IEEE Journal of Microwaves*, vol. 3, no. 1, pp. 305–318, 2022.

Y. Shen, **A. D. Kim**, M. Shahili, C. A. Curwen, S. Addamane, J. L. Reno, B. S. Williams, "THz time-domain characterization of amplifying quantum-cascade metasurface." *Applied Physics Letters*, vol. 119, no. 18, p. 181108, 2021.

CHAPTER 1

Introduction

High-power, broadly-tunable, single-wavelength sources for spectroscopic applications are still lacking in the 1-10 THz range. A major application is gas sensing via absorption spectroscopy, as many polar molecular gases have strong rotational transitions in the THz region; in some cases better specificity and reduced spectral clutter is possible compared to the mid-infrared [1, 2]. At present, the two primary techniques for generation of tunable continuous-wave (cw) THz radiation are based on upconversion from the microwave using frequency multiplier chains (FMCs) and downconversion from the optical by using photoconductive photomixing [2–7]. Both of these techniques are fundamentally "electronic" and rely on the movement of free charge; as such their efficiency and output power roll-off due to transit time and parasitic effects at frequencies above 1 THz. Time-domain spectroscopy (TDS) has also been used in absorption spectroscopy to cover frequencies above 3 THz, but the low spectral resolution is often not suitable for high-resolution, gas-phase spectroscopic applications [8, 9]. Another important application for tunable cw THz sources is as a frequency-agile local oscillator in heterodyne receivers for astrophysics and space science. We dive deeper into this particular application in Section. 1.2.

1.1 Terahertz quantum-cascade lasers

Above ∼2 THz, electronic sources struggle to keep up with the large output power demands of spectroscopic and imaging applications. Optically pumped terahertz gas lasers can provide tens of mW output power across the 1–6 THz band, but are bulky, tabletop instruments whose emission frequencies are limited by available, discrete gas lines [10, 11]. However,

the recent emergence of quantum-cascade laser pumped THz gas lasers promises compact form factor and wide tunability [12–15]. Similarly, free-electron-lasers can generate kW-level

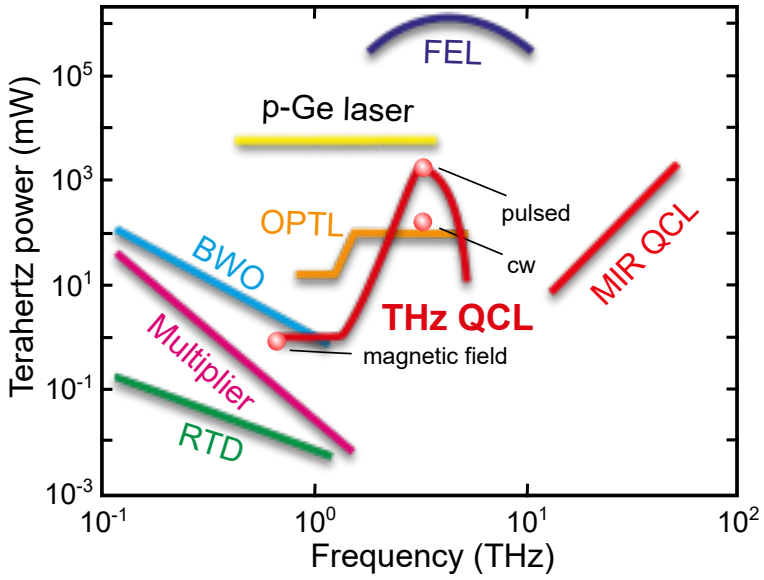

Figure 1.1: Survey of high power terahertz sources in relation to THz QCLs. THz QCL: Terahertz quantum-cascade laser. FEL: Free electron laser. p-Ge laser: p-doped germanium laser. OPTL: Optically pumped terahertz laser. BWO: Backward wave oscillator. Multiplier: solid state multiplier chains. RTD: Resonant tunneling diode. MIR QCL: Mid-infrared quantum-cascade laser. The figure is modified and reproduced from Ref. [16].

output powers but are impractical for most applications [17]. Another example is the p-doped germanium laser, which requires cryogenic cooling and magnetic fields, resulting in complex systems that discourage its use outside of research laboratories [18–20]. However, THz quantum-cascade lasers (QCLs), with their high power output and compact form factor, are promising candidates to fill the technological gap as applicable spectroscopic sources. Fig. 1.1 shows how the power output of other THz sources compare to that of the THz QCL.

QC-lasers are based upon gain that originates from intersubband transitions, i.e. stimulated emission between subband states within the conduction band of engineered heterostructure quantum wells. A simplified schematic of the carrier transport through the gain medium is shown in Fig. 1.2(a). Though there are several different approaches in designing the active region, the bandstructure is generally composed of an active stage, where a photon is emit-

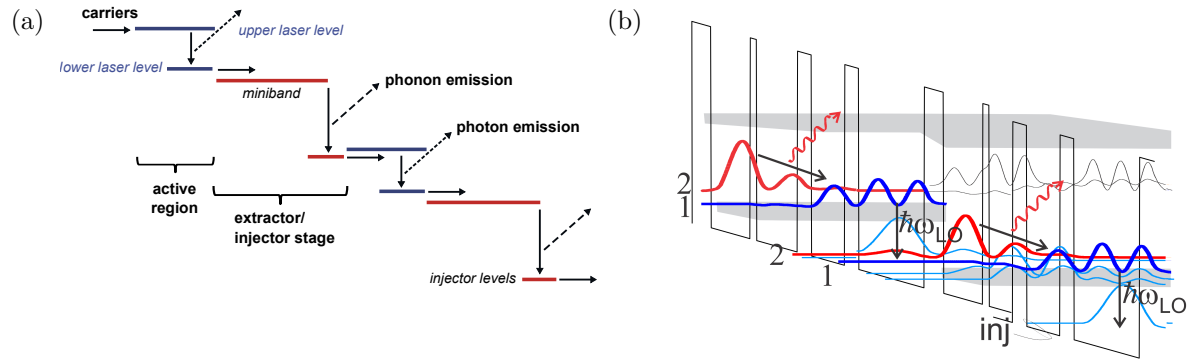

Figure 1.2: (a) Simplified schematic of the terahertz quantum-cascade bandstructure. (b) An actual bandstructure of a quantum-cascade active region similar to those used throughout this work. The figure in (a) is reproduced from [21]

ted, and an extraction/injection stage, where the carriers are delivered to the next module for photon emission [22]. The latter stage is typically facilitated by GaAs longitudinal-optical (LO) phonons — either directly or indirectly — resulting in very fast lower-state depopulation times. A representative band diagram of an active region used throughout this thesis is shown in Fig. 1.2(b), a hybrid bound-to-continuum resonant-phonon design based on Ref. [23]. Because the lasing transition energies are based on energy-level separations set by the heterostructure, there is great flexibility to engineer the QC gain material to provide amplification at the desired frequency. Various devices have been demonstrated at frequencies between 1.2-6.0 THz, typically with milliwatt power levels, but occasionally up to watt-level output [22, 24–27]. Operation is typically at cryogenic temperatures between 40-100 K, although recent advances have pushed operating temperatures up to 260 K in select devices [28].

1.1.1 Tunable terahertz QCLs

There have been several demonstrations of THz QC-lasers exhibiting extremely large gain bandwidths — often larger than 1 THz, and sometimes even octave spanning [29–31]. Despite this appealing broadband gain, the realization of tunable single-mode THz spectroscopic

sources tunable across large bandwidths has been unexpectedly challenging. Varying the temperature or injected current of a THz QC-laser typically provides fractional tuning of at most 1% — and usually much less due to the limited tuning index with temperature combined with a limited temperature budget [32–35]. One exception to this is a family of Vernier tuning approaches in coupled cavity lasers shown in Fig. 1.3(a), which has demonstrated up to ∼6% fractional tuning using a combination of Stark shift, cavity-pulling, and thermal control [36]. However, the broad tuning is characterized by mode-hops, with the single-mode continuous tuning typically available only over ranges of <1%.

Perhaps a more promising method is to use mechanically tuned external cavities, such as the Littrow configuration demonstrated in mid-infrared QC-lasers to obtain up to 39% fractional tuning [41]. However, this method is very challenging in the THz, since the subwavelength facets of metal-metal (MM) waveguides couple poorly to free-space, which makes antireflection coatings difficult to engineer. Nevertheless, tunable external cavity THz QC-lasers have been demonstrated using both Littrow cavity configurations and by mechanically changing the cavity length. Fig. 1.3(b) shows a demonstration of such a Littrow cavity, in which a Si lens was used at the waveguide facet to eliminate reflections and improve the beam quality incident on the grading. This resulted in 145 GHz of total tuning centered at 4.4 THz. Perhaps in a more simple configuration, a tuning mirror was placed on an SiO_2 AR-coated back-facet of a QCL, resulting in 90 GHz of tuning centered at 4.8 THz (see Fig. 1.3(c)) [38]. In a more unique imagination of the external cavity concept, a distributed feedback QCL is tuned by bringing an external mirror in close proximity to the grating, resulting in a coupled microcavity that can be tuned via its anti-crossing as illustrated in Fig. 1.3(d) [39]. A tuning range of 20 GHz was obtained centered around 3.41 THz. In another example, 40 GHz of tuning was achieved at 3.1 THz via NIR optical excitation of an electron-hole plasma to modulate the semiconductor index (see Fig. 1.3(e)) [42]. Despite these accomplishments, due to the mm-scale waveguide lengths required to provide enough gain, and difficulty in efficient external coupling, external-cavity configurations in THz QC-lasers have been limited to ∼4-5% fractional tuning — and a few GHz of mode-hop-free

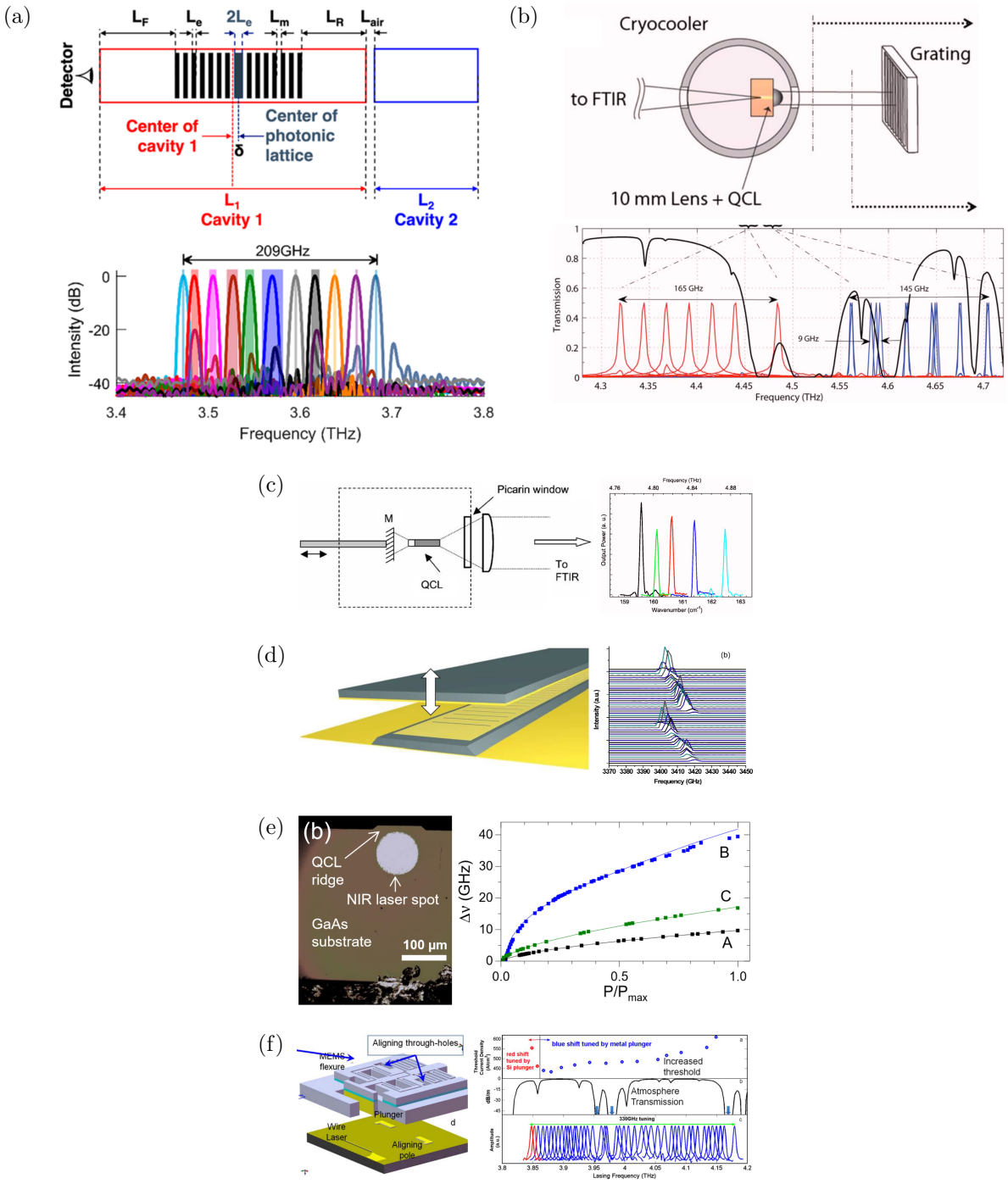

Figure 1.3: Survey of broadband tunable terahertz quantum cascade lasers. (b-d) are based on forming an external cavity. The figures are reproduced from [36–40].

tuning. In one notable departure of the external cavity approach, these challenges were avoided by instead manipulating, via MEMS, the fringing fields of a distributed-feedback

wire-laser, which achieved up to 8.6% fractional tuning (see Fig. 1.3(f)) [40, 43]. However, the broad tuning is likely accompanied by highly divergent beam-patterns and low power output due to the limitations of metal-metal waveguide architectures.

1.2 Terahertz QCLs for heterodyne spectroscopy

1.2.1 Terahertz astronomy

As a relatively unexplored frequency band, the terahertz regime — especially above ∼2 THz — has been a frontier in astronomical research for decades due the less matured technology available for astronomical observations. The significance of this band is highlighted by the presence of spectroscopic characteristics in the cosmic radiation that is important in understanding the mechanics of star and planet formation, the chemistry of the interstellar medium (ISM), and the evolution of galaxies (see Fig. 1.4(a)) [44–47]. As the dusty interstellar medium absorbs shorter wavelength radiation, it primarily cools through rotational and fine structure transitions in the THz range. However, this frequency band faces the additional challenge of Earth's atmospheric opacity at these frequencies, making terrestrial observations non-feasible and requiring measurements to be taken place beyond the Earth's troposphere via airborne instruments and balloon missions.

To highlight a couple examples, the spectral lines of neutral atomic oxygen at 4.745 THz [OI] and monodeuterated hydrogen at 2.675 THz [HD] have been of interest in terahertz astronomy due to their roles in tracing critical astrophysical processes. Oxygen, one of the most abundant elements in the universe, serves as a primary coolant in the warm, dense regions of interstellar clouds where star formation is active [44, 49–51]. Observations of this line provide essential data on the thermal dynamics within star-forming regions, facilitating detailed mapping and understanding of star formation mechanisms. Photodissociation regions in particular, being almost entirely composed of neutral gas, are very effectively studied by the OI line, providing information on the important physical characteristics of the region [49,51]. The HD line is crucial for probing the early universe and the evolutionary

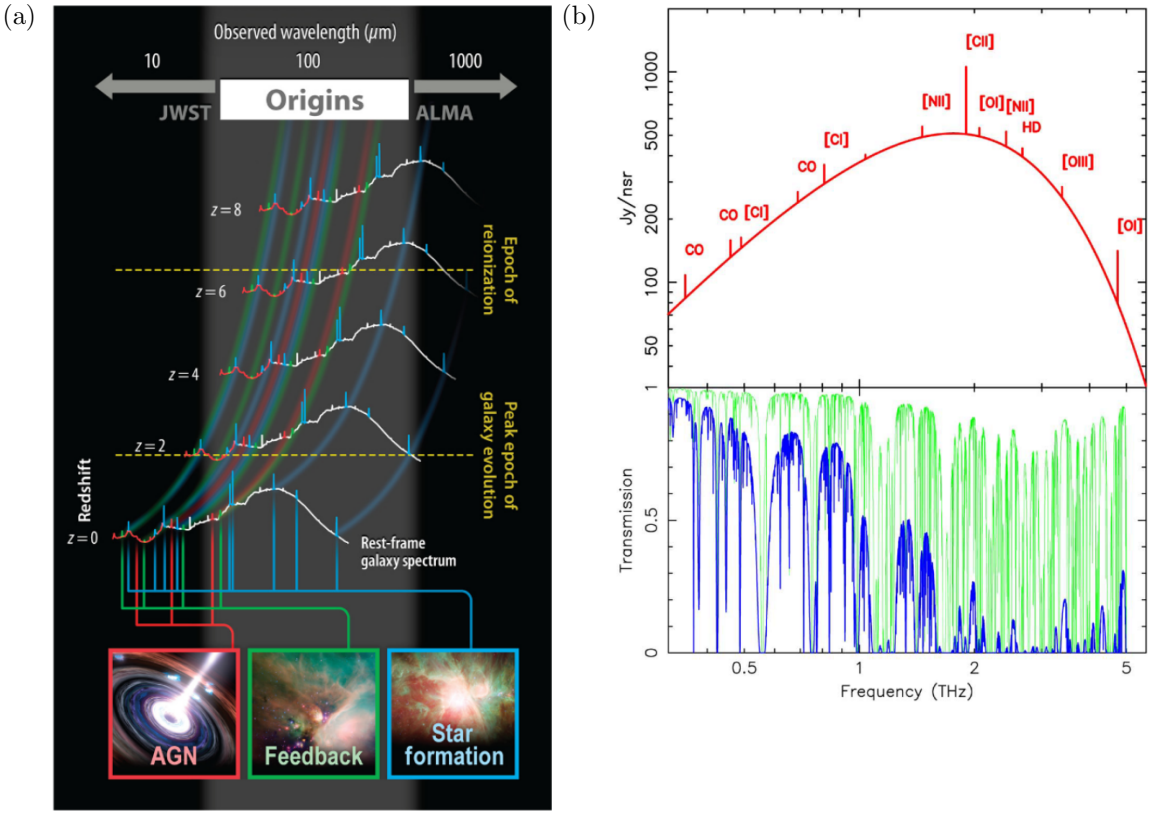

Figure 1.4: (a) Spectral lines emitted from various astrophysical phenomena, and the associated Doppler redshift with look-back time. The terahertz regime lies spectrally between JWST and ALMA, representing a key gap in wavelength coverage. The Origins Space Telescope (OST) is a prospective instrument geared toward filling this gap. (b) Select molecular and fine structure lines in the 0.3–5 THz range. The bottom spectra is the atmospheric transmission from Earth ground (blue) versus from the stratosphere (green). The figures are reproduced from [45, 48].

processes of stars and planetary systems. As deuterium is only destroyed in stellar processes — and never created — the HD line offers a unique measure of stellar activity and is an indicator of past star formation. Knowledge of H/D abundance in the ISM can reveal its history of astration, informing the evolution of primordial gases and the primordial abundance of deuterium. Additionally, HD is useful in assessing the mass distribution within protoplanetary disks, which is essential for constraining models for planet formation [52, 53]. The OI and HD lines are just two examples that demonstrate the insights THz astronomy

can provide, but indeed the band is populated by dozens of molecular and fine structure lines that may be astrophysically valuable, as illustrated in Fig. 1.4(b) [49, 54].

Advancements in THz astronomy require hybrid technological solutions that incorporate elements from both radio and infrared technologies, reflecting the unique position of THz radiation between these bands. In radio frequencies, the use of heterodyne receivers in space observations has been essential for high-resolution spectroscopy ($R = \lambda/\Delta\lambda \sim 10^6$). This technique is adopted to meet the velocity resolution requirements in THz observations to resolve the nuanced lineshapes and Doppler shifted components [51,55–58]. In heterodyne spectroscopy, a stable local-oscillator (LO) source is used in conjunction with a low-noise mixer, such as a cryogenically cooled hot-electron bolometer (HEB) or superconductor-insulator-superconductor (SIS) mixer, to down-convert the received "RF" signal into an intermediate frequency (IF) that can be electronically processed [59–62]. Schottky diode frequency-

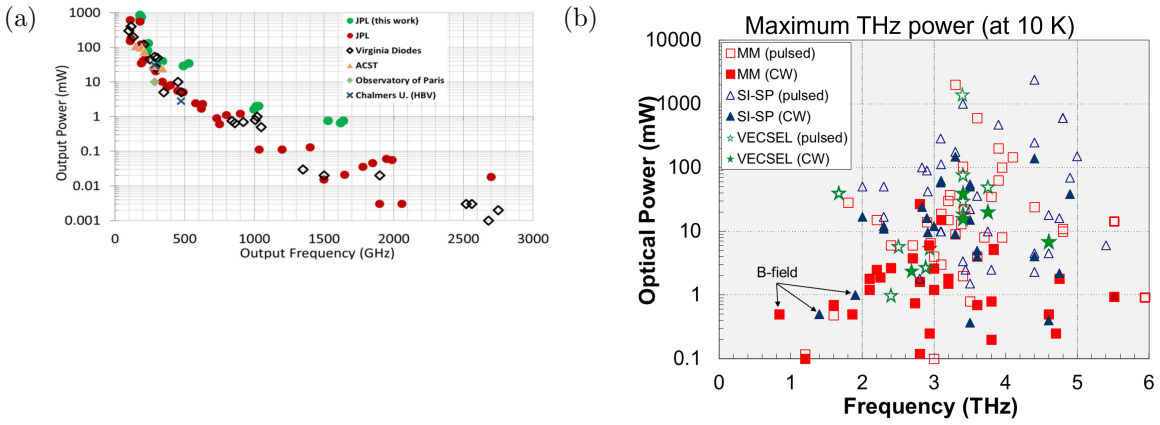

Figure 1.5: (a) Output power of state-of-the-art Schottky diode frequency multiplier chain sources. Reproduced from [6] (b) Output power of state-of-the-art THz quantum-cascade lasers. MM: metal-metal waveguide. SI-SP: semi-insulating surface-plasmon waveguide. VECSEL: vertical-external-cavity surface-emitting laser.

multiplier chains (FMCs) have been the leading THz local-oscillator source for decades due to their frequency stability (easily referenced to microwave frequency standards), sufficient power output, and compact form [6, 63–66]. However, power output decays rapidly with increasing frequency, and above ∼3 THz these sources struggle to provide sufficient power

to pump next-generation large format heterodyne mixers [55]. Fig. 1.5(a) shows the output power levels of state-of-the-art FMC sources. Generally, the power decays as f^{-3}, although there are continuing efforts to improve both the output power and conversion efficiency above 1 THz [6, 67]. On the other hand, THz QC-lasers begin to increase in optical output power above 2 THz. Fig. 1.5(b) shows the current state-of-the-art THz QC-lasers for various architectures including metal-metal (MM) waveguides, semi-insulating surface-plasmon (SI-SP) waveguides, and vertical-external-cavity surface-emitting lasers (VECSELs).

1.2.2 QCLs as local-oscillators

Above ~ 2 THz, quantum-cascade lasers are a promising alternative to fulfill the local-oscillator role. To date, there have been five different receivers built for heterodyne spectroscopy using a QC-laser as the local-oscillator. All five of these receivers were aimed at detecting the ground state fine structure transition of neutral oxygen, $^3P_1 \rightarrow {}^3P_2$, at 4.7448 THz. These five receivers are described below, in addition to the missions that featured them.

- **Stratospheric Terahertz Observatory 2 (STO-2)**: The STO-2 was a follow-up mission to the STO, a 14-day Antarctic flight that launched in January 2012 with a 1.4 THz channel and a 1.9 THz channel [73]. The STO-2 includes an additional channel at 4.74 THz. In total, there were two pixels at 1.4 THz [NII], two pixels at 1.9 THz [CII], and one pixel at 4.7 THz [OI]. Launched in December 8th, 2016, STO-2 was a 22-day Antarctic flight; a photograph of the gondola during a hang test is shown in Fig. 1.6(a). The 4.74 THz receiver includes a NbN HEB mixer and a 3rd order distributed feedback QC-laser (see Fig. 1.6(a)) developed by MIT [69,74–77]. The laser was mounted in a Stirling cryocooler and stabilized at 50 K. Had an output power of 0.25 mW and 0.7 W total power consumption. The QC-laser was phase-locked using a room-temperature superlattice harmonic mixer [78].

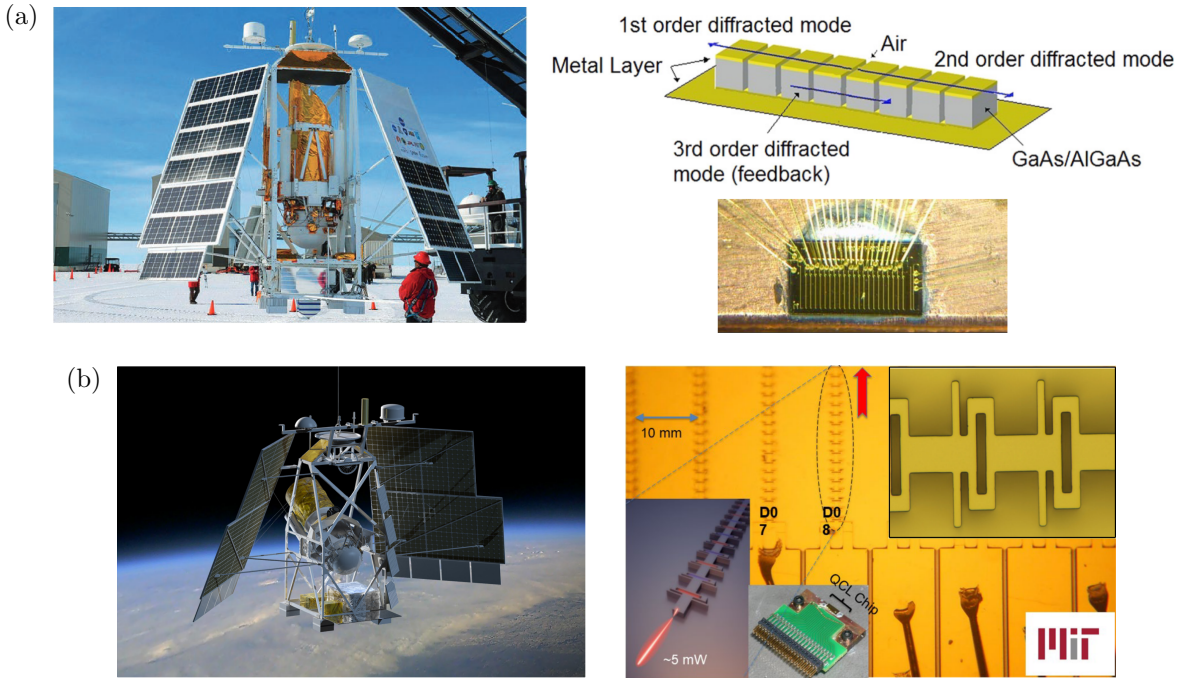

Figure 1.6: (a) STO-2 gondola hang test in Antarctica [68]. LO: 3rd-order distributed feedback QC-laser [69]. Microscope image credit to Delft University of Technology and SRON Netherlands Institute for Space Research. (b) Artist depiction of GUSTO gondola in flight (credit to NASA Jet Propulsion Laboratory). LO: Unidirectional antenna-coupled 3rd order distributed feedback QC-laser [70–72].

Unfortunately, due to a communication error, no data was collected for the 4.74 THz channel.

- **Galactic/Extragalactic ULDB Stratospheric Terahertz Observatory (GUSTO)**: A successor to the STO-2, GUSTO is a NASA balloon mission that launched on December 31st, 2023. Its flight lasted 57 days, 7 hours, and 38 minutes, setting a record for the longest NASA heavy-lift long-duration balloon flight in history [79]. An artistic depiction of the gondola is shown in Fig. 1.6(b). The observatory had the same three channels as STO-2, with the significant addition of 4x2 NbN HEB receiver arrays for each channel [80]. As described in Ref. [72], the five primary objectives for GUSTO are

1. Determine the constituents and life cycle of interstellar gas in the Milky Way
2. Witness the formation and destruction of star forming clouds.
3. Understand the dynamics and gas flow to and in the Galactic Center.
4. Understand the interplay between star formation, stellar winds and radiation, and the structure of the interstellar medium in the satellite galaxy known as the Large Magellanic Cloud (LMC)
5. Construct Milky Way and LMC templates for comparison with distant galaxies

The 4.7 THz receiver utilized a unidirectional antenna-coupled 3rd order DFB QC-laser, a more recent technology developed by MIT [70, 71]. The LO had an output power of ∼5 mW in continuous-wave at 50–70 K heatsink temperatures. The device also demonstrated record cw wall-plug efficiencies close to ∼1%. The high power output was necessary to sufficiently pump the 8-pixel receiver array. The laser was frequency stabilized using similar technology as in STO-2 [78,81]. Several DFBs were placed in an array to cover a wide bandwidth, as can be seen in Fig. 1.6(b), and each had an electrical tuning bandwidth of about 4 GHz.

- **The German REceiver for Astronomy at Terahertz frequencies (GREAT/upGREAT)**: A heterodyne spectrometer that was onboard the Stratospheric Observatory for Infrared Astronomy (SOFIA) since its early science flights in 2011, up until SOFIA was retired in late 2022. An image of the airborne observatory is shown in Fig. 1.7(a). The spectrometer initially had two channels: L1 (1.25–1.5 THz) and L2 (1.81–1.91 THz). Soon after, a third channel, M_a,

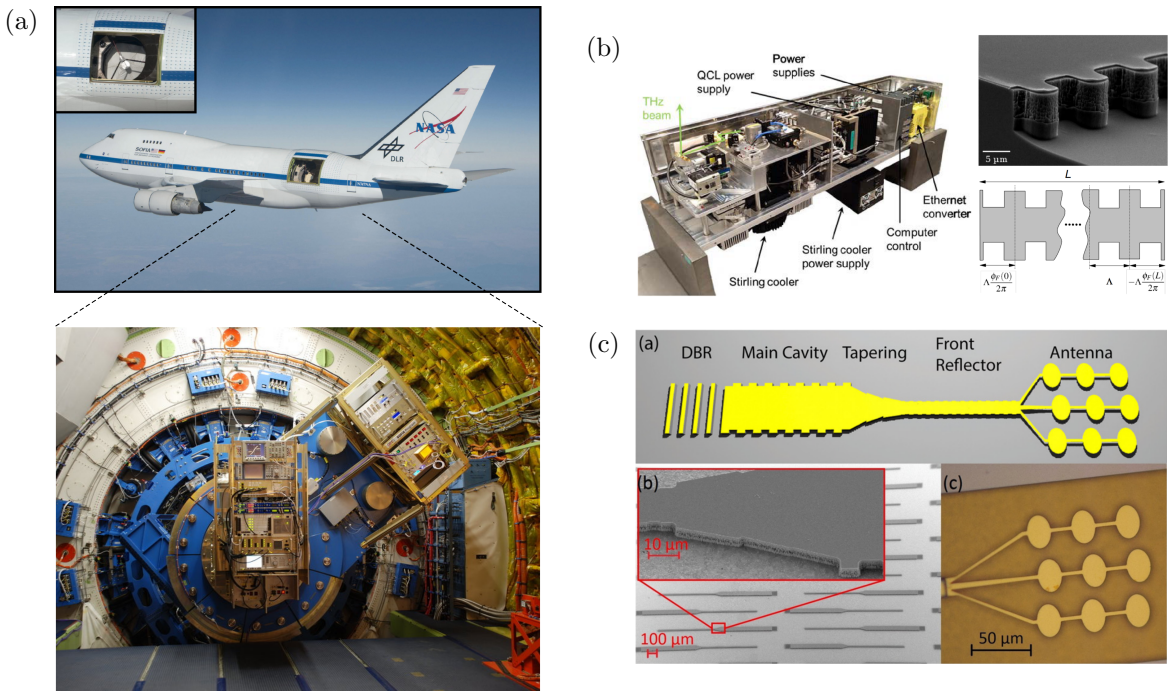

Figure 1.7: (a) SOFIA in flight. Inset shows the onboard 2.5 m infrared telescope. Below shows the GREAT spectrometer mounted on the instrument flange. Photos credit to NASA and Max Planck Institute for Radio Astronomy [82]. (b) LO box of the 4.74 THz receiver for the GREAT spectrometer. The LO is based on a lateral DFB grating for frequency selection [83, 84]. (c) 4.74 THz QCL LO for the high frequency array (HFA) in upGREAT. Based on a patch antenna coupled MM waveguide [85, 86].

was included aimed at 2.49–2.52 THz [82, 87]. But it wasn't until May of 2014 that a QC-laser based receiver was added, a single-pixel receiver designed to specifically probe the 4.74 THz [OI] line (see Fig. 1.7(b)); initial observations were aimed at planetary nebula NGC 7027, resolving the intricate $\sim$km/s-scale velocity structures in the outflow [84, 88, 89]. The LO was a surface-plasmon waveguide lateral distributed-feedback (lDFB) grating QCL supplied by the Institute of Optical Sensor Systems, German Aerospace Center (DLR) [83, 84]. The laser is mounted in a Stirling cryocooler that allows heatsink temperatures between 30 and 80 K. Electrical tuning of about 4 GHz was available, and above 1.2 mW output power with a high quality beam

profile (without correcting for cryostat window transmission and atmospheric absorption). In May 2016, a new 4.74 THz 1x7 heterodyne receiver array was installed as part of an upgraded set of receivers referred to as upGREAT [90, 91]. The LO for this receiver was supplied by Physikalisches Institut der Universität zu Köln (KOSMA) and ETH Zurich. The LO is based on a metal-metal waveguide integrated with a patch antenna array for surface emission as shown in Fig. 1.7(c) [85,86]. The laser had a cw power output of about 2.4 mW accompanied by a narrow single-lobed far-field beam. The device also showed good free-running stability, with free-running linewidths < 1 MHz and frequency drift of the same order.

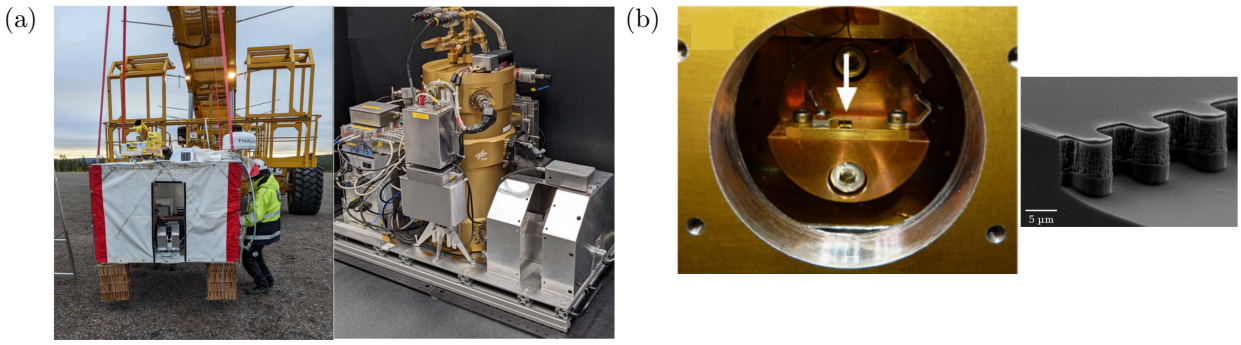

Figure 1.8: (a) OSAS-B gondola (left) and 4.7 THz receiver after successful recovery (right). (b) Photo of the QC-laser LO looking through cryostat window opening. The laser is based on a lateral DFB similar to that in the GREAT receiver. The SEM shows the lateral grating. Figures reproduced from [57].

- **The Oxygen Spectrometer for Atmospheric Science on a Balloon (OSAS-B)**: The first successful demonstration of 4.7 THz heterodyne spectroscopy on a balloon was took place on September 2022, launched from Esrange, Spain [57, 92]. A photograph of the gondola and receiver are shown in Fig. 1.8(a). The mission was aimed at probing neutral oxygen in Earth's mesosphere and lower thermosphere (MLT) region, helping study its chemical and physical dynamics. An

atmospheric study of neutral oxygen in the MLT region had been previously reported using the GREAT spectrometer in 2021 [58, 93]. As part of the European Hemera program, the balloon mission OSAS-B had the advantage of a higher altitude for negligible water absorption, and a wider range of elevation angles. The LO was a lDFB QC-laser similar to that in the 4.7 THz GREAT receiver and is pictured in Fig. 1.8(b). It has a power output between 1–2 mW with 0.6–1.0 W total power dissipation and operated between 58–64 K via a solid/liquid nitrogen stage. It features sub-MHz free-running linewidth, and an overall receiver spectral resolution of $R \sim 10^7$ — sufficient to resolve the spectral width of the oxygen line which is typically 20–35 MHz [57]. The OSAS-B was a significant testament to the legitimacy of a QCL-based balloon-borne heterodyne spectrometer, and the feasibility of a cryogenic frontend for short-to-medium duration flights.

While THz QCL-based heterodyne receivers for astronomy have been successfully demonstrated, there is still much room for improvement. This is because poor beam qualities, inefficiencies, cryogenic operating temperatures, and limited tuning bandwidths can make them less favorable than their FMC counterparts. This is why below 3 THz, FMCs are still the LO of choice for heterodyne receivers. However, THz QCLs have the potential to provide high quality beams with tens or hundreds of mW in output power — an crucial component for next-generation large-format receiver arrays with tens or hundreds of pixels [27, 55, 94].

1.3 Terahertz metasurface external-cavity lasers

The THz quantum-cascade vertical-external-cavity surface-emitting laser (QC-VECSEL) was first demonstrated in 2015 by Professor Williams' lab at UCLA [95]. The QC-VECSEL has demonstrated milliwatt level power with near-Gaussian beam patterns across frequencies

ranging from 1.76–5.72 THz [25]. While edge-emitting devices, such as metal-metal waveguides, produce heavily diffracted beams due to the sub-wavelength radiating aperture, the radiating aperture of the QC-VECSEL can be made much larger than the free-space wavelength, allowing for high quality beam patterns with highly scalable power output. The THz QC-VECSEL proves to be a promising candidate for a high-power local-oscillator, and as a source for other applications that benefit from high output powers and large tuning bandwidths such as hyperspectral imaging, multi-species gas spectroscopy, and optical coherence tomography [27, 96–100].

1.3.1 Basic principles of the QC-VECSEL

The external cavity is made up of an amplifying reflectarray metasurface and a highly reflective output coupler (OC). The VECSEL architecture circumvents the problems associated with the MM waveguide facets and the need for antireflective coatings which are inherently narrowband. The active metasurface is composed of an array of microcavity MM waveguide ridge antennas with subwavelength periodicity, loaded with THz QC gain material. In this way, the design exploits the temperature performance of the metal-metal structure via the TM modes of these sub-wavelength cavities for gain, while the lasing mode itself is that of the external plano-plano cavity in which a TEM_{00} fundamental Gaussian mode dominates.

A scanning electron microscope image of a typical metasurface is shown in Fig. 1.9(a), along with details of its unit cell cross-section. A circular area in the center of the metasurface is selectively biased by insulating all other regions of the metasurface during fabrication. This is partly to promote the lasing of the fundamental Gaussian mode in the external cavity. The bandstructure of a typical $GaAs/Al_xGa_{1-x}As$ QC gain material is shown in Fig. 1.9(a). The microcavity ridge antennas are similar in form to elongated microstrip patch antennas, and are characterized by a resonant mode where the vertical E-field has odd-symmetry underneath the metal contact ($w \approx \lambda_0/2n$, where λ_0 is the free-space wavelength). This mode is mostly composed of vertically oriented electric fields, which satisfy the intersubband selection rule for QC gain material. The sidewalls of the ridges can be thought of as narrow

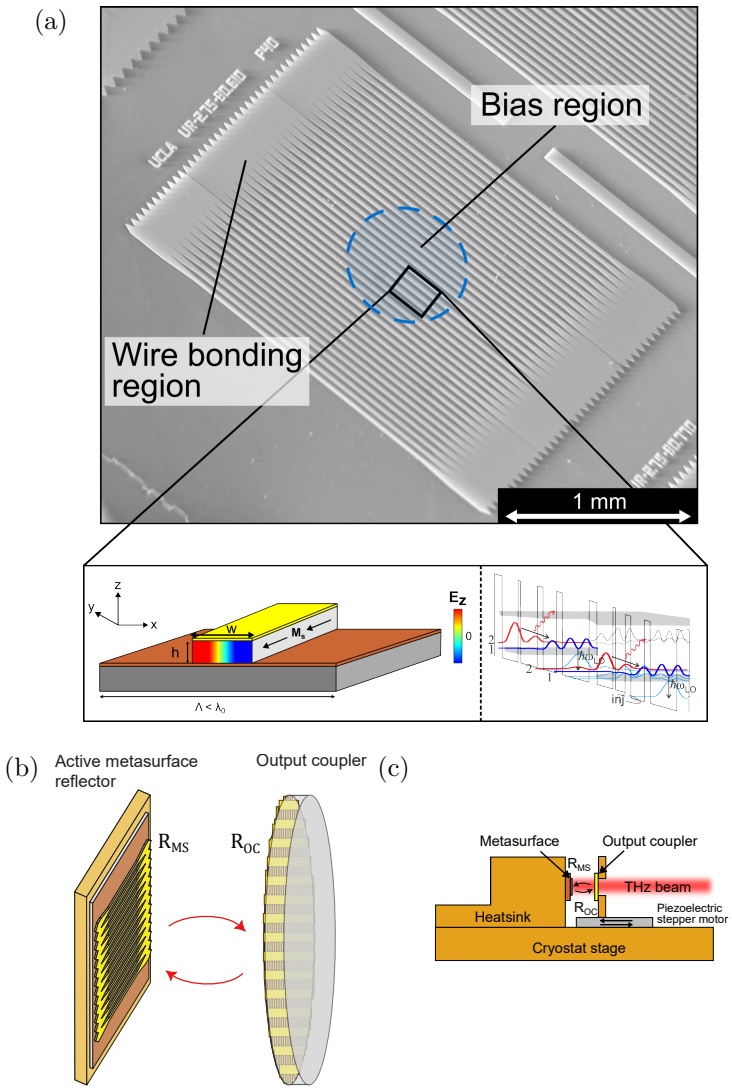

Figure 1.9: (a) Scanning electron microscopy image of a typical metasurface. The metasurface is composed of an array of metal-metal waveguide ridge antennas loaded with quantum-cascade gain material. A circular area in the center is selectively biased by patterning a layer of SiO_2 above the active region to encourage lasing of the TEM_{00} external-cavity mode. Below is a cross-sectional view of a unit cell vertical field profile and typical band structure typical band diagram of two periods of the GaAs/$Al_xGa_{1-x}As$ QC gain material that makes up the ridge antennas. (b) Illustration of the VECSEL architecture. (c) Schematic of the tunable VECSEL configuration. The metasurface chip is mounted onto a copper heatsink together with the OC on a piezoelectric stepper motor together on a cryostat stage.

slot antennas that radiate constructively in the surface normal direction in the presence of a ground plane [101]. An illustration of the overall VECSEL architecture is depicted in Fig. 1.9(b). A schematic of a tuning configuration is shown in Fig. 1.9(c).

1.3.2 Metasurface and cavity engineering

A key advantage of the QC-VECSEL architecture is that it opens up a much larger design space compared to more primitive structures — such as edge-emitting ridge lasers. Because the metasurface acts as an effective reflector, it can be electromagnetically engineered at the unit cell level to provide arbitrary reflection responses in both magnitude and phase — as is the spirit of the field of metasurfaces and reflectarrays [102–105]. A timeline of all the unique metasurface and cavity demonstrations of the QC-VECSEL since its invention is shown in Fig. 1.10. A brief summary of each design is provided below. All demonstrated QC-VECSELs after 2018 have been fully intra-cryostat. While it is not necessary for the VECSEL to be intra-cryostat, it has the benefits of removing intracavity window loss, circumventing window etalon effect, ease of alignment, and convenience of repeated use.

- *Focusing metasurface*: The metasurface reflection phase is spatially engineered as to provide a focusing response upon normal incidence. This is achieved by radially modulating the antenna width from the center of the bias area. The design allows for lower thresholds at longer cavity lengths, and is also more robust to cavity misalignment [106].

- *Polarimetric metasurface*: A metasurface with electrically switchable polarization states. Two electrically separate sets of antennas that reflect orthogonal linear polarization states are interleaved across the whole metasurface. The power output, beam quality, and frequency stay constant between the two polarization states [107].

- *TM_{03} metasurface*: A metasurface designed for maximizing power output, the antenna widths are 3x larger to be resonant with the $3\lambda/2$

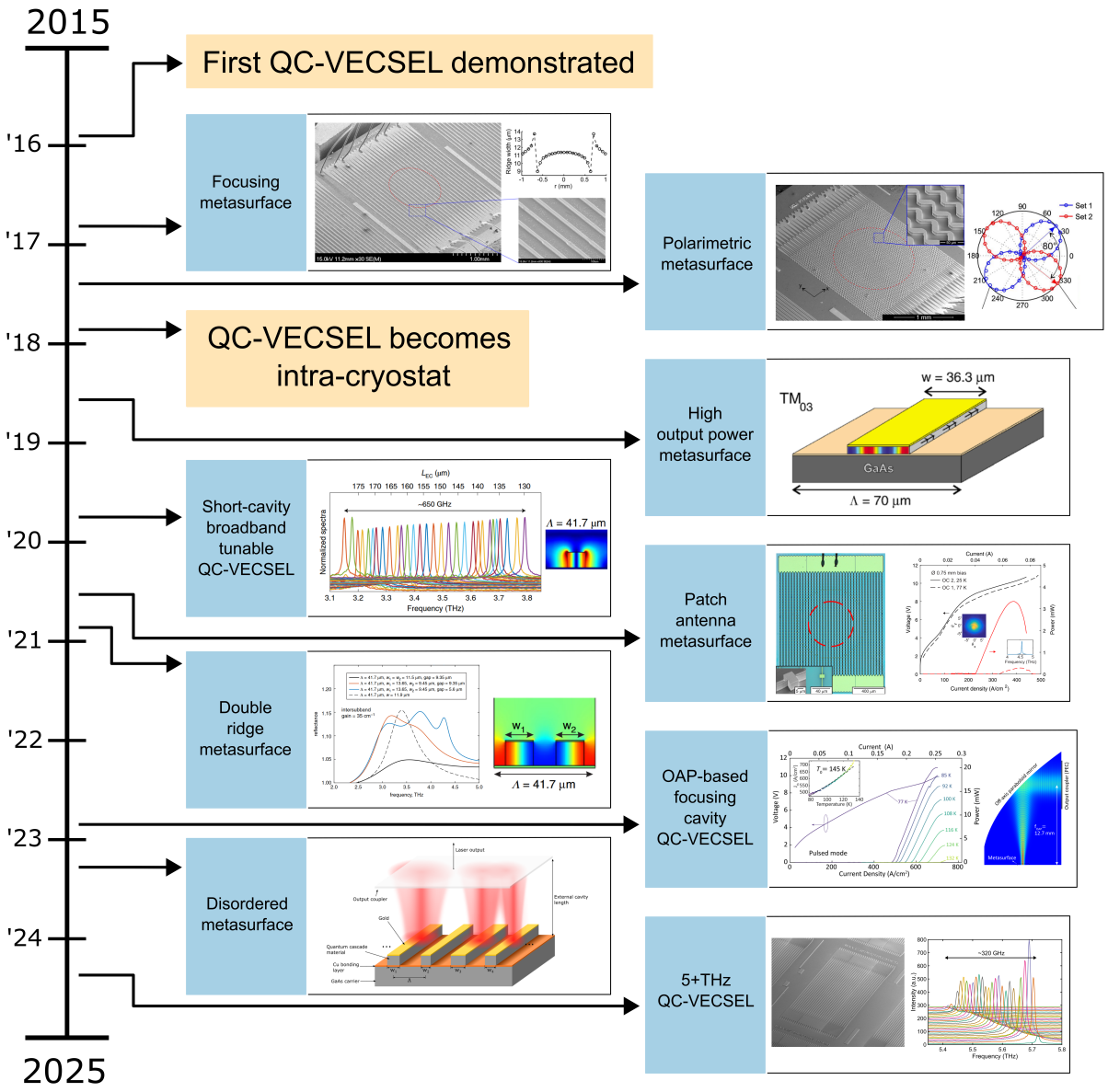

Figure 1.10: Timeline of various metasurface designs and cavity architectures for the QC-VECSEL since its first demonstration in 2015. In chronological order, the reported designs include the focusing metasurface [106], polarimetric metasurface [107], intra-cryostat QC-VECSEL [108], TM_{03} high power metasurface [24], short-cavity QC-VECSEL for broadband tunability [30], patch-antenna metasurface for low power consumption [109], double-ridge metasurface for broadband metasurface reflectance [110], OAP-based focusing QC-VECSEL [111], disordered metasurface [112], and the 5+THz QC-VECSEL [26]. All QC-VECSELs demonstrated after the first intra-cryostat report in 2017 have remained intra-cryostat.

mode, rather than the $\lambda/2$ mode. This results in a much higher radiative quality factor, allowing the use of more transmissive output couplers. Up to 1.35 W peak power output is achieved at 6 K heatsink temperature [24].

- *Broadband tunable QC-VECSEL*: The metasurface reflectance is spectrally broadened by reducing the periodicity. The external cavity length is reduced to the order of a wavelength, keeping the free-spectral-range of the cavity very large. This resulted in a 19% fractional tuning bandwidth centered around 3.5 THz [30].

- *Patch antenna metasurface*: Rather than ridges that extend the whole length of the metasurface, this metasurface is composed of rectangular patches of length L. This allows for a device that consumes much less power without having to reduce the size of the bias area — an action that would generally be counter to the VECSEL principle. Power consumption of less than 1 W was demonstrated [109].

- *Double-ridge metasurface*: Each unit cell houses a pair of coupled resonators based on the same microstrip antenna design. By deviating the widths of the two adjacent resonators, their natural frequencies are separated, and the broken symmetry cause perturbations of Bragg modes. This results in more complicated, but much broader reflectance spectra, resulting in lasing modes that spanned a 30% fractional bandwidth [110].

- *OAP cavity QC-VECSEL*: Instead of a plano-plano cavity, the external cavity is constructed with an off-axis-parabolic (OAP) mirror to focus light onto the metasurface bias area. This significantly reduces cavity diffraction loss, and allows for smaller bias diameters to curtail power dissipation. To date, this has resulted in the highest temperature

performance in a QC-VECSEL, demonstrating pulsed $T_{\max}$ between 132 and 145 K, depending on the output coupler used [111].

- *Disordered metasurface*: The widths of the metasurface antennas are pseudo-randomly varied to generate a metasurface with spatially disordered resonances. The resultant QC-VECSEL is extremely sensitive to cavity length, such that small cavity lengths (< 370 µm) result in multi-moding, while longer cavity lengths recover single-mode behavior [112].

- *5+THz metasurface*: The most recent effort of QC-VECSEL metasurface engineering — the device is wavelength-scaled to operate beyond 5 THz, an inherent challenge due to degradation of gain material, increase in material loss, and reduced radiative quality factor of the metasurface. After the successful demonstration of the QC active region, the subsequent QC-VECSEL showed > 1 mW power output and single-mode up to 5.72 THz [26].

1.3.3 Broadband tunability

Tuning of the emitted frequency (or wavelength) in the VECSEL architecture is achieved by mounting the OC on a piezoelectric stepper motor (ANPx311/RES/LT/HV - linear x-nanopositioner) on the cryogenic stage, allowing for a low-order longitudinal mode in the Fabry-Pérot (FP) cavity to be swept through the gain profile. Since the metasurface is optically thin, it is possible to reduce the cavity length to only a few tens or hundreds of microns (limited only by the height of the ridge antennas). If multiple longitudinal modes fall within the threshold gain bandwidth, the laser will mode-hop to an adjacent mode that competes for the same gain. In this situation, the tuning bandwidth is limited by the free-spectral-range (FSR) of the external cavity. As the OC is brought closer, the FSR increases, and fewer modes fall within the threshold gain bandwidth, as depicted in Fig. 1.11. If the FSR

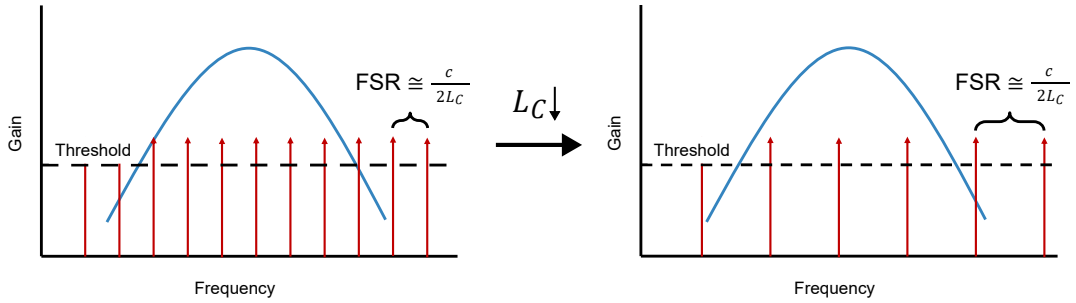

Figure 1.11: Simplified illustration of the longitudinal mode spacings in relation to the threshold gain bandwidth as the external cavity length is reduced. Reducing L_c until only a single longitudinal mode falls within the gain bandwidth is the principle behind broadband tuning in the QC-VECSEL.

is further increased until only a single mode falls within the threshold gain bandwidth, the tuning bandwidth becomes threshold-limited, and the laser will be extinguished on either end of the tuning range. This is the desirable regime for maximum tuning range, and is ultimately limited by the metasurface reflectance bandwidth; the gain material itself has proven to be very broadband ($>$ 1 THz in the 3–4 THz range), and designing a metasurface with an equally broad reflectance is a continuing effort [29, 31, 110]. It is also important to note that the longitudinal modes spacings deviate from an ideal Fabry-Pérot cavity due to the frequency-dependent reflection phase of the metasurface; this reduces the theoretical tuning range as well. A schematic of the tunable VECSEL configuration is shown in Fig. 1.9(c). In Ref. [30], it is shown that the VECSEL approach is highly effective for widely-tunable THz QC-lasers: tuning over a 650 GHz range around 3.5 THz.

CHAPTER 2

Wavelength scaling the metasurface in QC-VECSELs

2.1 Overview of metasurface design

The THz QC-VECSEL can be modeled as a simple two-mirror cavity with the metasurface and the OC being represented by a reflectance R_{MS} and R_{OC} respectively. If T is the single-trip transmittance of the external cavity, the threshold condition of the laser can be written as

$$R_{\mathrm{MS}} R_{\mathrm{OC}} T^2 = 1. \tag{2.1}$$

An analytical description for R_{MS} can be developed via two different perspectives: a field-amplitude model, and a transmission line model.

2.1.1 Field-amplitude model of the metasurface

The metasurface as a whole effectively acts as a single electromagnetic resonator centered at the design frequency of the half-wavelength microcavity mode, ω_{r}. If we treat the metasurface as a lumped-element, the circulating field amplitude of the effective resonator can be written as

$$\frac{\mathrm{d}}{\mathrm{d}t}(E(t)e^{j\omega t}) = \left[j\omega_{\mathrm{r}} - (\frac{1}{2\tau_{\mathrm{m}}} + \frac{1}{2\tau_{\mathrm{r}}}) \right] E(t)e^{j\omega t}, \tag{2.2}$$

where τ_{m} is the photon lifetime associated with material absorption loss, and τ_{r} is the radiative photon lifetime of the metasurface. When an external plane-wave, E_{in}, is incident on the metasurface, it becomes a driving term in the differential equation. Assuming time-harmonic

solutions of the field amplitude, we can write

$$\frac{\mathrm{d}E}{\mathrm{d}t} = \left[j(\omega_\mathrm{r} - \omega) - (\frac{1}{2\tau_\mathrm{m}} + \frac{1}{2\tau_\mathrm{r}}) \right] E + \frac{1}{\tau_\mathrm{r}} E_\mathrm{in}. \tag{2.3}$$

If the incident excitation field is at frequency ω, then the time-harmonic response for E can be written as

$$E = \frac{\tau_\mathrm{r}^{-1} E_\mathrm{in}}{j(\omega - \omega_\mathrm{r}) + \frac{1}{2}(\tau_\mathrm{m}^{-1} + \tau_\mathrm{r}^{-1})}. \tag{2.4}$$

The radiative photon lifetime τ_r describes the fraction of energy in the metasurface that is lost to radiation. In other words, it is tied to the radiative quality factor, Q_r, via the relation $Q_\mathrm{r} = \omega_\mathrm{r}\tau_\mathrm{r}$. As can be seen from Eq. (2.3), the smaller the Q_r, the larger the perturbation an external incident field will have on the resonator field.

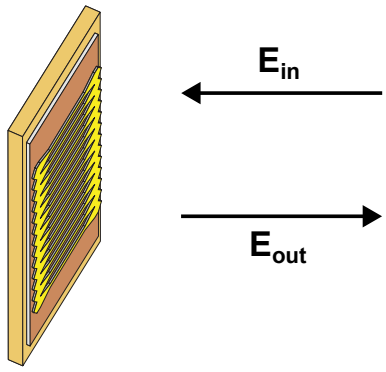

Figure 2.1: Schematic of the reflectance model used for the field-amplitude perspective

The reflection coefficient of the metasurface can be derived by determining the amplitude of the field that propagates away from the metasurface, as depicted in Fig. 2.1. Employing proper boundary conditions for continuity of the tangential electric field, we can write

$$E_\mathrm{out} = -E_\mathrm{in} + E. \tag{2.5}$$

This is fundamentally a statement of energy conservation, and can be produced from the equation

$$|E_\mathrm{in}|^2 \tau_\mathrm{r}^{-1} - |E_\mathrm{out}|^2 \tau_\mathrm{r}^{-1} = \frac{\mathrm{d}|E|^2}{\mathrm{d}t} + |E|^2 \tau_\mathrm{m}^{-1}. \tag{2.6}$$

With that established, we can write the reflection coefficient as

$$\begin{aligned}\Gamma_{\mathrm{MS}} &= \frac{E_{\mathrm{out}}}{E_{\mathrm{in}}} \\ &= \frac{-E_{\mathrm{in}} + E}{E_{\mathrm{in}}} \\ &= \frac{\frac{1}{2}(\tau_{\mathrm{r}}^{-1} - \tau_{\mathrm{m}}^{-1}) - j(\omega - \omega_{\mathrm{r}})}{\frac{1}{2}(\tau_{\mathrm{r}}^{-1} + \tau_{\mathrm{m}}^{-1}) + j(\omega - \omega_{\mathrm{r}})}.\end{aligned} \tag{2.7}$$

The final equation in Eq. (2.7) is a circle in the complex Γ_{MS} plane with respect to the parameter ω and is plotted in Fig. 2.2 for several different cases. In general, the complex reflectance at any frequency ω can be represented by the blue vector shown in the figure, $\Gamma_{\mathrm{MS}} = \sqrt{R_{\mathrm{MS}}} e^{j\phi_{\mathrm{MS}}}$. When $\tau_{\mathrm{m}}^{-1} > \tau_{\mathrm{r}}^{-1}$, the system is overcoupled. This means that the rate the electromagnetic energy radiates out of the resonator is much greater than the rate of energy lost in the material.

On the other hand, if $\tau_{\mathrm{m}}^{-1} < \tau_{\mathrm{r}}^{-1}$, the system is said to be undercoupled, and corresponds to a high-Q resonator. The overcoupled case is where the metasurface is designed to operate, intentionally keeping the radiative quality factor low as to prevent the metasurface to lase on its own. We can incorporate the notion of an active metasurface reflectance by relating τ_{m} to the gain coefficient such that

$$\tau_{\mathrm{m}}^{-1} = \Gamma v_g (g_{\mathrm{tr}} - g), \tag{2.8}$$

where Γ is the effective confinement factor of the metasurface mode to the gain material, v_g is the group velocity, and g_{tr} is the transparency gain defined as the gain required for unity reflectance. The confinement factor Γ is typically close to unity, and describes the fraction of the total energy that is being amplified by the active volume:

$$\Gamma_{\mathrm{act}} = \frac{\int_{\mathrm{act}} \varepsilon(\mathbf{r}) |E_z(\mathbf{r})|^2 \, dV}{\int_V \varepsilon(\mathbf{r}) |E(\mathbf{r})|^2 \, dV} \tag{2.9}$$

As gain is applied to the metasurface, the effective τ_{m}^{-1} becomes smaller, and the Γ_{MS} circle

in Fig. 2.2 grows in diameter. When $g = g_{\mathrm{tr}}$, the Γ_{MS} becomes a unit circle centered at the origin, and $|\Gamma_{\mathrm{MS}}| = 1$ for all ω (hence the name transparency gain). If gain is increased beyond g_{tr}, the decay rate becomes an amplification rate, represented by a negative value for τ_{m}^{-1}. In this case, the radius of the Γ_{MS} circle becomes larger than 1, and is also centered to the right of the origin. With this vector perspective, we can intuitively understand sweeping through the metasurface resonance as a full rotation of the Γ_{MS} circle from $-\pi$ to π, where the amplification is maximum at $\phi_{\mathrm{MS}} = 0$ (corresponding to $\omega = \omega_{\mathrm{r}}$), and $\Gamma_{\mathrm{MS}}(|\omega - \omega_{\mathrm{r}}| \to \infty) = -1$.

A special case depicted in Fig. 2.2 is for $\tau_{\mathrm{m}}^{-1} = \tau_{\mathrm{r}}^{-1}$, which is the case of critical coupling. The critical match between the material and radiative loss rates result in a zero reflectance at the resonant frequency, and a discontinuous reflection phase across the resonance. While the radiative quality factor of the metasurface is never made high enough for this to be a typical case, critical coupling has been observed due to strong intersubband absorption for a metasurface designed for around 2.3 THz [113].

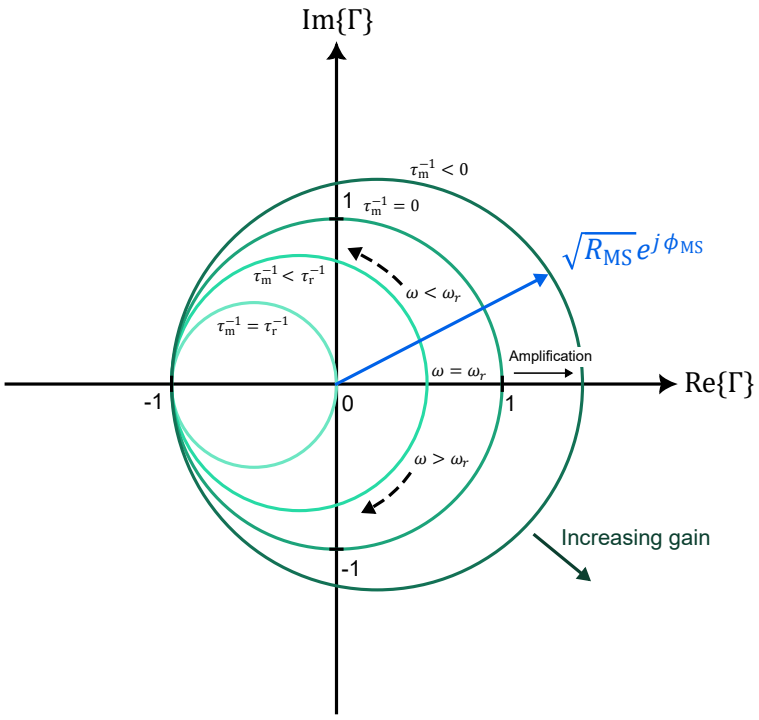

Figure 2.2: Representation of the metasurface reflection coefficient in the complex Γ_{MS} plane

Continuing the analysis from Eq. (2.7), we can separate the real and imaginary parts of the reflection coefficient and write

$$\Gamma_{\mathrm{MS}} = \frac{\frac{1}{4}\left(\tau_{\mathrm{r}}^{-2} - \tau_{\mathrm{m}}^{-2}\right) - (\omega - \omega_{\mathrm{r}})^2}{\frac{1}{4}\left(\tau_{\mathrm{r}}^{-1} + \tau_{\mathrm{m}}^{-1}\right)^2 + (\omega - \omega_{\mathrm{r}})^2} - j\frac{(\omega - \omega_{\mathrm{r}})\tau_{\mathrm{r}}^{-1}}{\frac{1}{4}\left(\tau_{\mathrm{r}}^{-1} + \tau_{\mathrm{m}}^{-1}\right)^2 + (\omega - \omega_{\mathrm{r}})^2}. \tag{2.10}$$

Then, the reflection phase is given by

$$\tan\phi_{\mathrm{MS}} = \frac{(\omega - \omega_{\mathrm{r}})\tau_{\mathrm{r}}^{-1}}{(\omega - \omega_{\mathrm{r}})^2 - \frac{1}{4}(\tau_{\mathrm{r}}^{-2} - \tau_{\mathrm{m}}^{-2})}, \tag{2.11}$$

and the reflectance can be written as

$$R_{\mathrm{MS}} = \frac{(\omega - \omega_{\mathrm{r}})^2 + \frac{1}{4}(\tau_{\mathrm{r}}^{-1} - \tau_{\mathrm{m}}^{-1})^2}{(\omega - \omega_{\mathrm{r}})^2 + \frac{1}{4}(\tau_{\mathrm{r}}^{-1} + \tau_{\mathrm{m}}^{-1})^2}. \tag{2.12}$$

The full frequency dependence of the metasurface reflectance is important to use for analyzing the VECSEL in a short-cavity or a cavity-tuning configuration, since the laser can operate detuned from the metasurface resonance due to the longitudinal mode selection of the external cavity. Nevertheless, we can obtain simplified expressions for the peak reflectance value as an additional tool for qualitative design principles. At resonance, $\omega = \omega_{\mathrm{r}}$, and using Eq. (2.8), Eq. (2.12) becomes

$$\begin{aligned} R_{\mathrm{MS}} &= \left(\frac{\tau_{\mathrm{r}}^{-1} - \tau_{\mathrm{m}}^{-1}}{\tau_{\mathrm{r}}^{-1} + \tau_{\mathrm{m}}^{-1}}\right)^2 \\ &= \left(\frac{1 - \tau_{\mathrm{r}}\Gamma v_g(g_{\mathrm{tr}} - g)}{1 + \tau_{\mathrm{r}}\Gamma v_g(g_{\mathrm{tr}} - g)}\right)^2. \end{aligned} \tag{2.13}$$

Since the metasurface is usually designed with $\tau_{\mathrm{r}} \gg \tau_{\mathrm{m}}$, the second term in the fraction becomes much less than one, and a Taylor series expansion for the reflectance centered at

g_{tr} can be written as

$$\begin{aligned} R_{\mathrm{MS}} &= 1 + 4\sum_{n=1}^{\infty}(-1)^n n(\tau_{\mathrm{r}}\Gamma v_g)^n(g_{\mathrm{tr}}-g)^n \\ &= 1 - 4\tau_{\mathrm{r}}\Gamma v_g(g_{\mathrm{tr}}-g) + 8(\tau_{\mathrm{r}}\Gamma v_g)^2(g_{\mathrm{tr}}-g)^2 - 12(\tau_{\mathrm{r}}\Gamma v_g)^3(g_{\mathrm{tr}}-g)^3 + \cdots \end{aligned} \tag{2.14}$$

Coincidentally, the first three terms in this expansion are identical to the first three terms in the expansion

$$\begin{aligned} e^{4\tau_{\mathrm{r}}\Gamma v_g(g_{\mathrm{tr}}-g)} &= \sum_{n=0}^{\infty}\frac{(-1)^n}{n!}(4\tau_{\mathrm{r}}\Gamma v_g)^n(g_{\mathrm{tr}}-g)^n \\ &= 1 - 4\tau_{\mathrm{r}}\Gamma v_g(g_{\mathrm{tr}}-g) + 8(\tau_{\mathrm{r}}\Gamma v_g)^2(g_{\mathrm{tr}}-g)^2 - \frac{64}{6}(\tau_{\mathrm{r}}\Gamma v_g)^3(g_{\mathrm{tr}}-g)^3 + \cdots \end{aligned} \tag{2.15}$$

The exponential is a much more mathematically and intuitively convenient form of the peak reflectance, since it is analogous to light amplification of a propagating wave over a distance — such as the form seen in the equations for a traditional diode laser. Hence, we can further define

$$\xi_0 = 4\tau_{\mathrm{r}}\Gamma v_g \tag{2.16}$$

as an effective gain interaction length at the metasurface resonance. Finally, for values of gain close to g_{tr}, we can write an approximation of the metasurface reflectance at resonance as

$$R_{\mathrm{MS}}(\omega = \omega_{\mathrm{r}}) \approx e^{\xi_0(g-g_{\mathrm{tr}})}. \tag{2.17}$$

2.1.2 Transmission line model of the metasurface

A simpler model can be established by treating the metasurface as a lumped element, and performing a transmission line treatment for the reflection coefficient [114, 115]. As depicted in Fig. 2.3, we consider a transmission line with characteristic admittance equal to that of the free space wave admittance $Y_0 = \sqrt{\epsilon_0/\mu_0}$, and terminated by a GLC load representing the metasurface. This is analogous to a plane-wave incident on the metasurface in free

space. Then, the reflection coefficient can be expressed as $\Gamma_{\mathrm{MS}} = (Y_0 - Y_L)/(Y_0 + Y_L)$, where

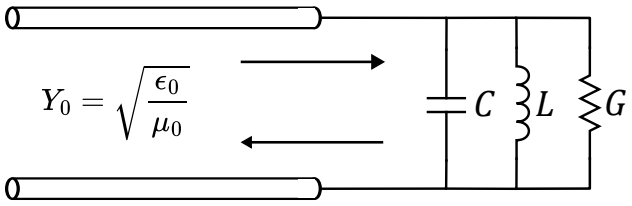

Figure 2.3: Schematic of a transmission line GLC model for the metasurface

$Y_L = j\omega C + (j\omega L)^{-1} + G$. Furthermore, the GLC circuit has a resonant frequency given by $\omega_r = 1/\sqrt{LC}$. Then, we can express the quality factor of the unloaded resonator as $Q_m = \omega_r C/G$, associated with the intrinsic material loss and gain of the active material. With the transmission line connected to a matched load, energy can be carried away from the resonator and can be described by a radiative quality factor equivalent to $Q_r = \omega_r C/Y_0$. The total quality factor can then be expressed as $Q_{\mathrm{tot}}^{-1} = Q_{\mathrm{m}}^{-1} + Q_{\mathrm{r}}^{-1}$. Relating this to lifetime parameters in Section 2.1.1, we can write $\tau_{\mathrm{m}}^{-1} = G/C$ and $\tau_{\mathrm{r}}^{-1} = Y_0/C$. The material and radiative quality factors are convenient figures of merit in the metasurface design process, since together they help describe the effective metasurface active reflectance. Some useful relations for these parameters are

$$Q_{\mathrm{m}} = \frac{\omega_r}{\Gamma v_g (g_{\mathrm{tr}} - g)} \tag{2.18}$$

and

$$Q_{\mathrm{r}} = \frac{\xi_0 \omega_{\mathrm{r}}}{4\Gamma v_g}. \tag{2.19}$$

In the same vein as Fig. 2.13, the peak reflectance can be expressed as

$$R_{\mathrm{MS}}(\omega = \omega_{\mathrm{r}}) = \left(\frac{Q_{\mathrm{m}} - Q_{\mathrm{r}}}{Q_{\mathrm{m}} + Q_{\mathrm{r}}} \right)^2, \tag{2.20}$$

producing an approximate peak reflectance that can be written as $R_{\mathrm{MS}}(\omega = \omega_{\mathrm{r}}) \approx e^{-4Q_{\mathrm{r}}/Q_{\mathrm{m}}}$.

2.1.3 Engineering the radiative quality factor

Using a cavity antenna model described in [101,115], the radiative quality factor of the ridge-antenna metasurface can be approximated in terms of more tangible design parameters:

$$Q_{\mathrm{r}} = \frac{n^2 w \pi \Lambda}{4 h \lambda_0} \approx \frac{n \pi \Lambda}{8h}, \tag{2.21}$$

where w is the antenna width, h is the active material thickness, and Λ is the periodicity of the metasurface. The periodicity must be sub-wavelength to operate in the metasurface regime and avoid higher-order Bragg surface modes (see details in Chapter 3). Additionally, the metasurface microresonators are intentionally designed to have low radiative quality factors such that they do not oscillate without the presence of strong feedback from an external cavity. Thus, the metasurface acts as an "amplifying mirror" that provides gain to the (ideally) TEM_{00} external-cavity mode, forcing the individual sub-cavities into an in-phase coherent supermode.

As suggested by Eq. (2.21), for a ridge metasurface, there are two primary ways to control the metasurface Q_{r}. One is to vary the height h of the QC material — a choice which will affect the number of QC-modules and required voltage. Increasing the height results in a lower Q_{r} since it increases the size of microstrip sidewalls that act as radiating apertures. The second is to vary the ridge period Λ (while being careful to remain in the subwavelength regime $\Lambda < \lambda_0$). This choice will affect the overall fill factor of active material, $F = w/\Lambda$, which will then determine the overall injection current required. This is illustrated by using a finite element method (FEM) solver to simulate the reflectance of the metasurface for two different periodicities — as shown in Figs. 2.4(a) and 2.4(b). The active region is modeled with a static dielectric constant and a spectrally flat gain curve. While this is not strictly accurate, it allows separate consideration of the metasurface from the underlying gain material. In general, the use of the full intersubband (ISB) expression for permittivity associated with the active region is necessary to capture strong coupling phenomenon, effects of detuning of the ISB transition from the metasurface, and phase tunability associated with

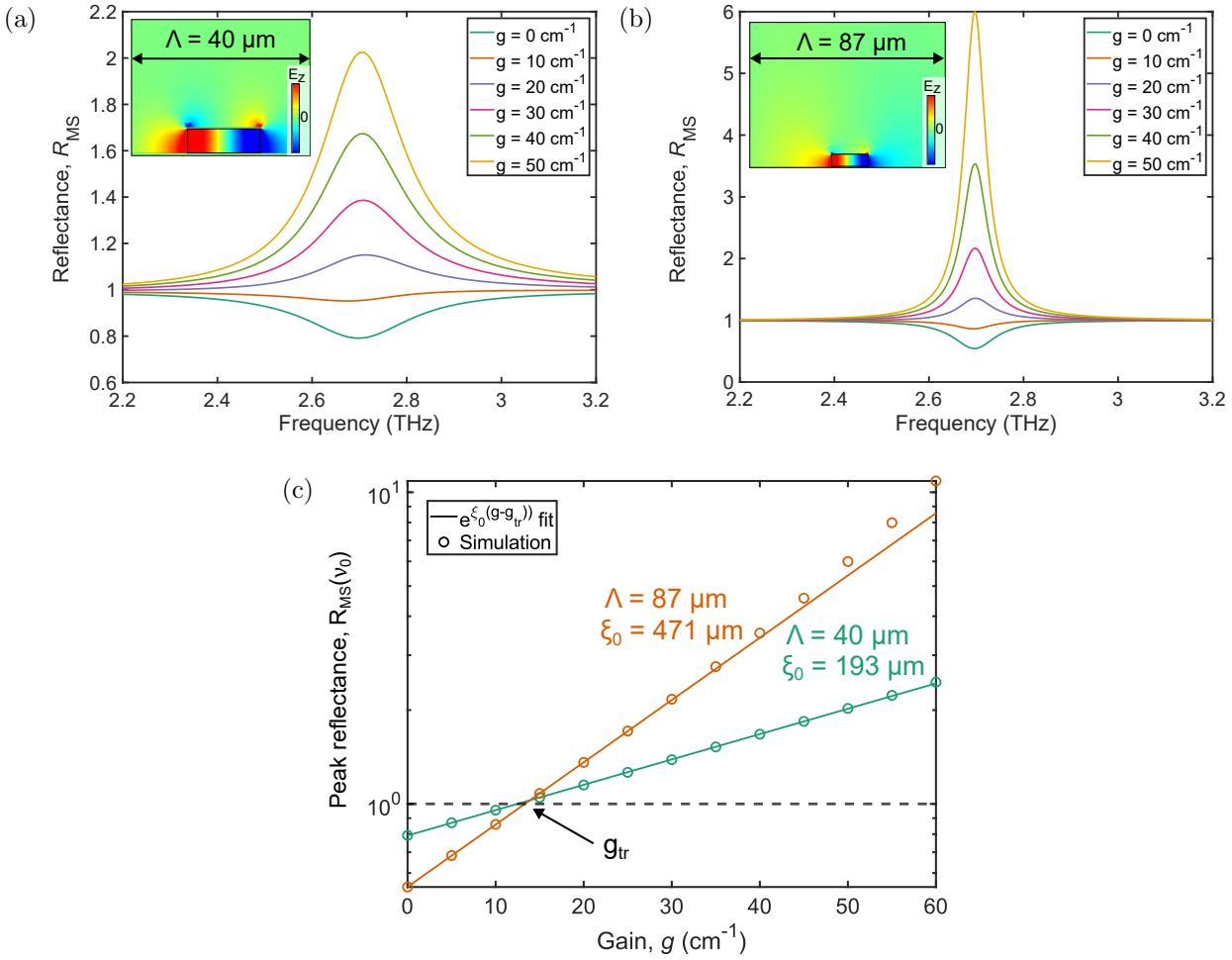

Figure 2.4: (a) Simulated 2.7 THz metasurface reflectance spectrum for various levels of applied gain (assuming a spectrally flat gain medium). The metasurface dimensions are $\Lambda = 40$ µm, $w = 14.9$ µm, and $h = 5$ µm. The only losses in the simulation are free-carrier losses in the metal. Inset: The simulated E_z profile in the metasurface unit cell, which is oriented to satisfy the intersubband selection rule for QC gain material. (b) Same simulation as (a) but with the period scaled up to $\Lambda = 87$ µm and width adjusted to $w = 14.6$ µm to keep the resonant frequency fixed. (c) Peak metasurface reflectance versus applied gain g. The solid line represents a fit using Eq. (2.17). The plot also indicates the transparency gain g_{tr}, which remains nearly unchanged for the two different periods.

the ISB transition [113]. The simulation only includes losses from the metal calculated via the Drude model — using free-carrier density $n_{\mathrm{Au}} = 5.9 \times 10^{22}$ cm^{-3} and scattering time $\tau_{\mathrm{Au}} = 39$ fs as input parameters [116]. The metasurfaces with $\Lambda = 87$ µm and $\Lambda = 40$ µm have

quality factors 25 and 10 respectively. The metasurface with larger Q_{r} will consequently have a larger ξ_0, conveying the stronger field enhancement in the microcavities. At high enough values of gain g, the metasurface itself will begin to approach the self-lasing condition ($Q_{\mathrm{m}} = -Q_{\mathrm{r}}$), and the reflectance curve will no longer obey Eq. 2.17 (see Fig. 2.4(c)). For a well designed VECSEL, the external-cavity mode will begin to lase and the gain will be clamped long before this self-oscillation condition is reached.

While a larger Q_{r} results in a larger active metasurface reflectance, it is accompanied by a reduction in reflectance bandwidth (Figs. 2.4(a) and 2.4(b)). Consequently, assuming $|Q_{\mathrm{m}}| \gg Q_{\mathrm{r}}$ and a spectrally flat material gain, the radiative quality factor determines the overall threshold gain bandwidth of the laser. Thus, for broadband tunability, it can be important to reduce the periodicity even further ($\Lambda < 0.5\lambda_0$), while paying attention to possible self-lasing dark modes that begin to appear (see Section 2.3.2). This strategy was employed in [30] to achieve 19% fractional tuning centered at 3.47 THz. However, reducing the periodicity of the metasurface comes at the cost of an increased fill factor, leading to larger power consumption for a given active area. To compensate, the metasurface bias area can be reduced. However, this must be done with care, since it can introduce additional losses due to the external-cavity mode spilling out of the active area in the transverse direction [113,114].

2.2 Wavelength scaling the ridge metasurface

2.2.1 Threshold gain bandwidth

If we begin with an existing design, scaling the metasurface QC-VECSEL operation to a new frequency seems simple in principle. Using a QC active material that produces gain at the desired frequency, we rescale the metasurface such that the half-wavelength condition is met within each ridge antenna: $w \approx \lambda_0/2n$. However, such scaling will also change other properties of the laser such as the threshold gain bandwidth and slope efficiency [25]. Consider a scaling factor S such that $\lambda_0 \to S\lambda_0$, $\Lambda \to S\Lambda$, and $w \to Sw$. For this analysis, we will consider first a fixed active region thickness, h, since this parameter is determined during

growth of the semiconductor has not been common within the THz QC-laser community to change h for different wavelengths. A separate analysis of the effect of h is performed in Section 2.4. The radiative quality factor scales as

$$Q_{\mathrm{r}} \rightarrow SQ_{\mathrm{r}}, \tag{2.22}$$

since the ratio of the radiating aperture height h to the wavelength is decreasing. With all other things equal, and assuming a spectrally flat gain medium, Eq. 2.22 suggests a threshold gain bandwidth that scales approximately as $\Delta\nu_{\mathrm{th}}/\nu_0 \rightarrow (\Delta\nu_{\mathrm{th}}/\nu_0)/S$, where $\Delta\nu_{\mathrm{th}}$ is the bandwidth of the metasurface reflectance spectrum for which $R_{\mathrm{MS}} > 1/R_{\mathrm{OC}}T^2$. However, it is important to also consider the scaling of the effective interaction length ξ_0, since it will have a significant impact on lasing threshold. Using Eq. 2.21, we can write the ξ_0 factor as

$$\xi_0 = \frac{\Gamma\lambda_0\Lambda}{4h};\ \xi_0 \rightarrow S^2\xi_0. \tag{2.23}$$

This quadratic dependence of ξ_0 with wavelength helps to compensate for the smaller QC-gain available at much lower frequencies (< 2 THz) [117–119]. On the other hand, at higher frequencies, ξ_0 can drop low enough to prevent lasing. This is exacerbated by increased free-carrier losses in the metal and additional losses from optical phonons as the photon energies approach the GaAs *Reststrahlen* band [120, 121] — though we exclude the latter from this section's analysis for simplicity. If we assume no round-trip diffraction losses, the threshold condition in (Eq. 2.1) can be interpreted as an active-metasurface reflection threshold, $R_{\mathrm{MS}}^{\mathrm{th}}(\nu) = 1/R_{\mathrm{OC}}$. Then, using a Lorentzian resonance model, we can express the fractional threshold gain bandwidth as

$$\frac{\Delta\nu_{\mathrm{th}}}{\nu_0} = \frac{1}{Q_{\mathrm{tot}}}\sqrt{\xi_0\frac{(g - g_{\mathrm{tr}})}{\ln R_{\mathrm{OC}}^{-1}} - 1}. \tag{2.24}$$

We evaluate the effect of wavelength scaling and R_{OC} on fractional bandwidth in Fig. 2.5(a). In order to consider this in isolation from the choice of active region, we choose to evaluate

these expressions for a value of $g = 30$ cm^{-1}. Because the FEM simulation only includes metallic losses, this value of g represents the net intersubband gain (in excess of any semiconductor or free-carrier losses). Indeed, in any real device, g depends upon many factors such as active region design, injection current, and temperature. Several trends are noted. First, we see that as the design frequency is increased, a more reflective OC is needed to achieve the same threshold gain bandwidth. The zero contour indicated by the dashed curve in Fig. 2.5(a) indicates where the metasurface reflectance threshold is equal to the reflectance at the resonant frequency. To circumvent this problem, higher Q_{r} metasurfaces can be designed, such as patch-based metasurfaces demonstrated in [109]. Second, we note that the effect of scaling on bandwidth depends greatly on the value of R_{OC}. For highly reflective OCs, the scaling of Q_{r} is canceled by the scaling of ξ_0, and the fractional bandwidth remains unchanged. However, for lower values of R_{OC} where the device is operating closer to threshold, the increase in Q_{r} results in a lower fractional bandwidth.

2.2.2 Slope efficiency

Wavelength scaling of the metasurface properties listed above will also have an important effect on the laser's slope efficiency. Using the formalism of [114], the slope efficiency of the QC-VECSEL can be written as

$$\frac{\mathrm{d}P}{\mathrm{d}I} = N_p \frac{h\nu}{e} \eta_{\mathrm{opt}} \eta_i \eta_{\mathrm{u}}, \tag{2.25}$$

where N_{p} is the number of QC periods, η_i is the internal quantum efficiency, and η_u is a modal uniformity factor that describes the modal intensity distribution of the microcavity resonance (for a ridge metasurface, $\eta_u \approx 0.66$) [122]. The metasurface design and choice of OC primarily affects the optical outcoupling efficiency η_{opt}; if we assume no round-trip transmission losses due to diffraction or the OC material, and a unity transverse confinement factor, we can approximate:

$$\eta_{\mathrm{opt}} \approx \frac{\ln\left(R_{\mathrm{OC}}^{-1}\right)}{\ln\left(R_{\mathrm{OC}}^{-1}\right) + \xi(\nu) g_{\mathrm{tr}}}. \tag{2.26}$$

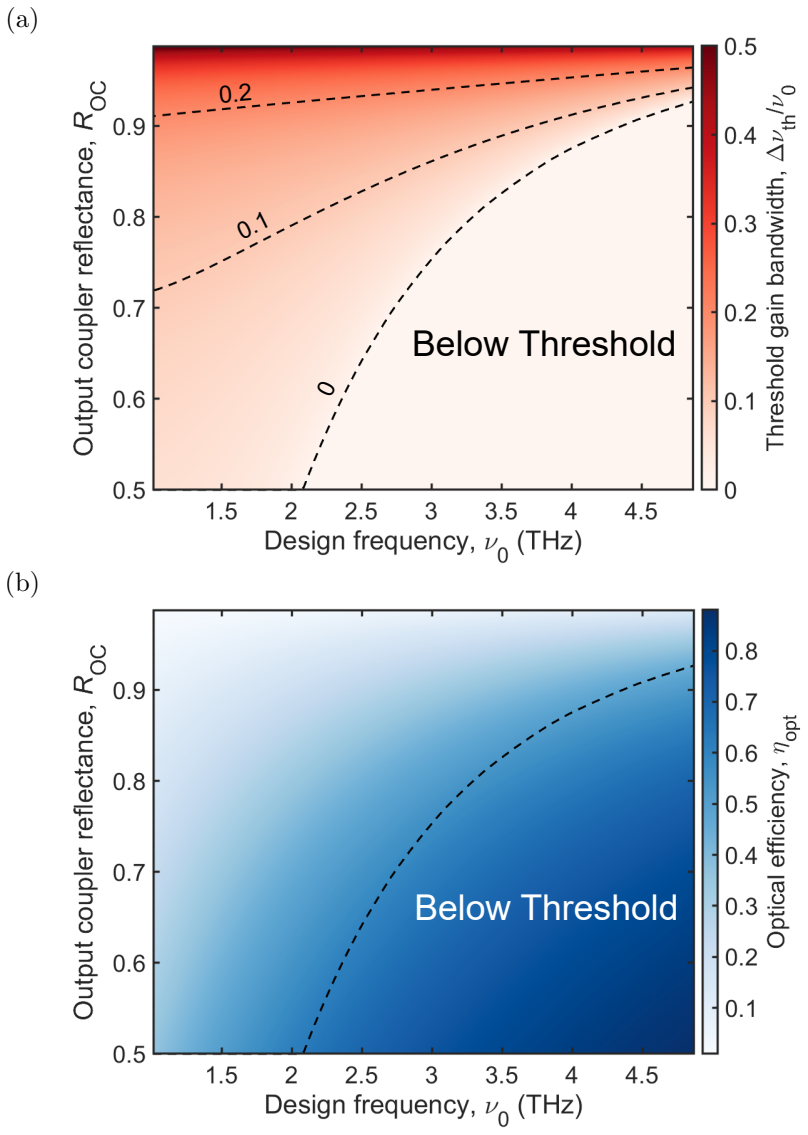

Figure 2.5: (a) Fractional threshold gain bandwidth versus metasurface design frequency and OC reflectance. The metasurface fill factor is fixed at 37% and active region thickness $h = 5$ µm. The values assume loss only from the metal. An arbitrary gain value of $g = 30$ cm^{-1} is applied to the active region. Select contours are shown as dashed curves. The zero contour indicates when the peak metasurface reflectance is at the threshold condition. (b) Change in optical efficiency η_{opt} at ν_0 for the same parameters used in (a). The same zero contour from (a) is drawn here to emphasize the threshold trade-off as the optical efficiency increases.

Therefore, the wavelength-scaling characteristic of the slope efficiency can be described by the photon energy and η_{opt}.

In order to better understand the effect of scaling on the slope efficiency, in Fig. 2.5(b) we plot the results of Eq. (2.26) for the same conditions as in Fig. 2.5(a). We immediately see that if R_{OC} is kept constant, the S^2 scaling of ξ_0 results in a strong reduction of η_{opt} at lower frequencies. Thus, to increase slope efficiency, a more transmissive OC can be used to combat the increased ξ_0. This is demonstrated in Fig. 2.5(b) for OC reflectances ranging from 0.5 to 1 at different design frequencies. As the OC reflectance is reduced, the optical efficiency increases due to the larger fraction of outcoupled radiation and vice versa. At the same time, the reduced ξ_0 at higher frequencies also increases η_{opt}. One way to interpret a smaller ξ_0 is that a larger fraction of the electric-field intensity is circulating in the external cavity, rather than confined to the metasurface microcavities, which results in more power being coupled out of the external cavity. Ultimately, there exists a significant trade-off between the threshold gain bandwidth and slope efficiency that depends on both the OC reflectance and design frequency. This is emphasized by the "below threshold" regime drawn on Fig. 2.5(b), which shows that the regions of highest efficiency are in fact inaccessible.

2.3 Wavelength scaling the patch metasurface

2.3.1 Ridge vs. patch metasurface overview

Most of this chapter details the 2-dimensional design space of the metasurface in which the structure is invariant along the longitudinal axis of the antennas. However, in general, the metasurface has a 3-dimensional design space. In 2020, a rectangular patch-based metasurface was demonstrated that aimed to reduce the fill-factor of the metasurface and thus minimize overall power dissipation of the laser [109]. The design is analogous to a microstrip patch antenna that is shorted along L from the connecting wires, which are needed for electrical connection. A comparison of the reflectance characteristic and geometry between the patch-based and ridge-based metasurface is shown in Fig. 2.6. The ridge metasurface can

be thought of as a special case of the patch metasurface in which L goes to infinity. As

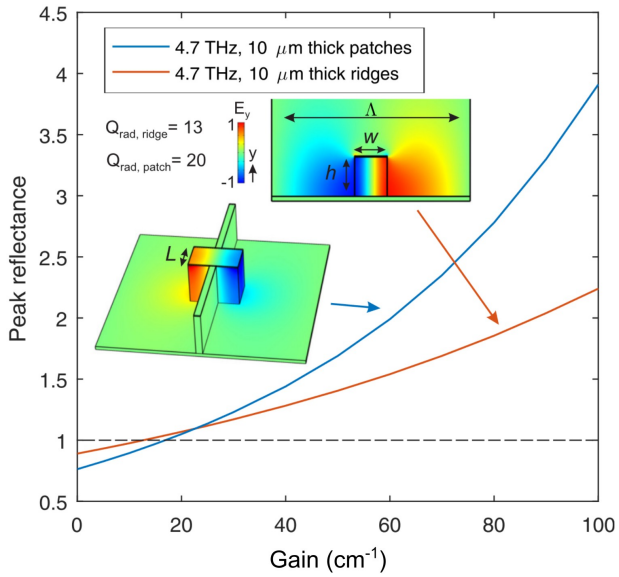

Figure 2.6: Simulated metasurface reflectance versus applied gain for a ridge-based and patch-based metasurface. The ridge dimensions are $\Lambda = 50$ µm and $w = 8.3$ µm. The patch dimensions are $\Lambda = 47$ µm, $w = 11.45$ µm, and $L = 7.5$ µm. Figure is reproduced from [109].

L is reduced, there are four important consequences: 1) The radiative quality factor Q_{r} increases. 2) The effective interaction length ξ increases. 3) The fill factor decreases. 4) The transparency gain g_{tr} increases. The first three effects are not inherently good or bad, but depend on the overall design. For higher frequency designs (4+ THz), reducing L helps compensate for the quadratic scaling of ξ with wavelength, helping maintain enough metasurface reflectance for sufficiently low threshold. Ridge-based metasurfaces fabricated for 4.7 THz were initially unsuccessful due to this reduced R_{MS}. However, reducing the active region thickness from 10 µm to 5 µm is another way to offset the reduced ξ, which allowed ridge-based metasurfaces to lase successfully without resorting to patch designs.

2.3.2 On the avoidance of self-lasing and undesirable modes

While patch-based metasurfaces designed at 4.6 THz showed great performance, those designed for lower frequencies (e.g. 2.7 THz) had a propensity to self-lase [109]. As with the modern metasurface structure, the tapered ends of the metasurface are designed, in part, to

discourage lasing of traveling waveguide modes of the microstrip antennas. However, this is not the only mechanism for self-lasing. The desired QC-VECSEL mode is the fundamental external cavity supermode enabled by the metasurface eigenmode in which each unit cell microcavity radiates in-phase at the TM_{01} cutoff frequency. When each unit cell is in-phase with its neighbors, the fringing fields of each microcavity add constructively in the far-field, and thus can support surface-radiation (see Fig. 2.7(a)). However, if each unit cell is out-of-phase with its neighbors, these fields add destructively, and the energy stays confined to the surface of the metasurface. This can be understood under the lens of Bloch's theorem and photonic crystals. Consider a uniform ridge metasurface that is periodic in x and invariant in y. Then, we can write the the electric field profile of a given eigenmode as

$$\mathbf{E}(x,z) = \mathbf{u}(x,z)e^{jk_x x}, \tag{2.27}$$

where $\mathbf{u}(x,z)$ is a periodic function that satisfies $\mathbf{u}(x,z) = \mathbf{u}(x+\Lambda,z)$, and $e^{jk_x x}$ is the plane-wave component with wavenumber k_x. Thus, we can understand the out-of-phase metasurface dark mode as an odd-symmetric Bloch state that corresponds to $k_x = \pi/\Lambda$, as depicted in Fig. 2.7(b). In other words, this mode exists on the edge of the first Brillouin zone. While there exists an even-symmetric counterpart, it is the odd-symmetric mode that competes with lasing, since it is strongly confined to the active material and has the same parity as the TM_{01} microcavity mode.

Performing an eigenfrequency study using COMSOL, the modal landscape of the metasurface versus periodicity is plotted in Fig. 2.8. The design under study is for a 2.7 THz uniform ridge metasurface with a 5 µm thick active region. Only the modes that have odd-symmetry and overlap with the gain material are shown. The solid curves represent the eigenfrequency, and the dashed lines represent the self-lasing threshold of the mode with the corresponding color. Note that the simulation was performed with scattering boundary conditions on the top boundary, and thus these threshold values are for a metasurface without the presence of an output coupler. The desired TM_{01} mode is given by the green curve, and remains relatively constant in frequency as the period is varied from 30 – 100

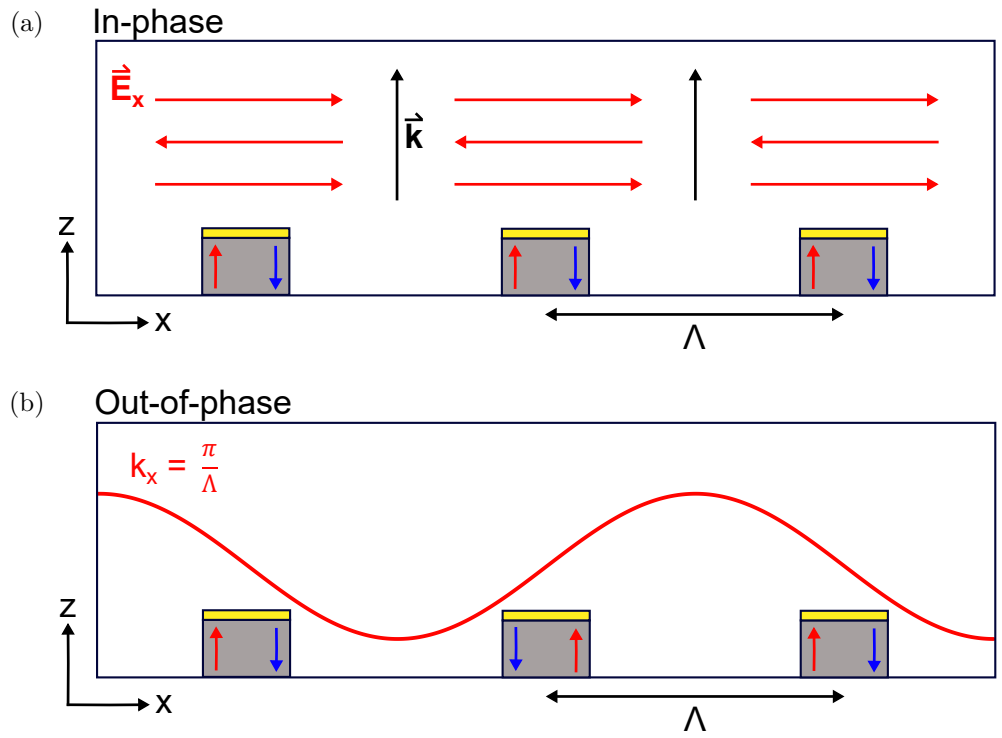

Figure 2.7: (a) Schematic of the desired metasurface mode in which each unit cell microcavity radiates in-phase with each other, resulting in constructive interference in the far-field. (b) The case in which each microcavity is out-of-phase with its neighbors. This is a surface-confined dark mode that can cause self-lasing of the metasurface.

µm. As intended, the self-lasing threshold for this mode is very high (> 100 cm^{-1}), and is a consequence of a low radiative quality factor for the microcavity resonance.

On the other hand, the eigenmode plotted in yellow has a self-lasing threshold that is very close to the transparency gain when the period is 50 µm or below. This is the aforementioned out-of-phase dark mode illustrated in Fig. 2.7(b), and only appears when the periodic boundary condition is set to the Brillouin zone edge (antiperiodic boundary conditions). Not only is the threshold low, but the eigenfrequency remains close to that of the desired mode. Fortunately, as the period gets larger, this parasitic dark mode diverges from the design frequency due to it anti-crossing with a corresponding anti-symmetric Bragg mode given by the purple curve. This mode again corresponds to the first order Bragg mode where $\Lambda = \lambda_0/2n_{eff}$, and is instead confined to the air outside the semiconductor ($n_{eff} \approx 1$).

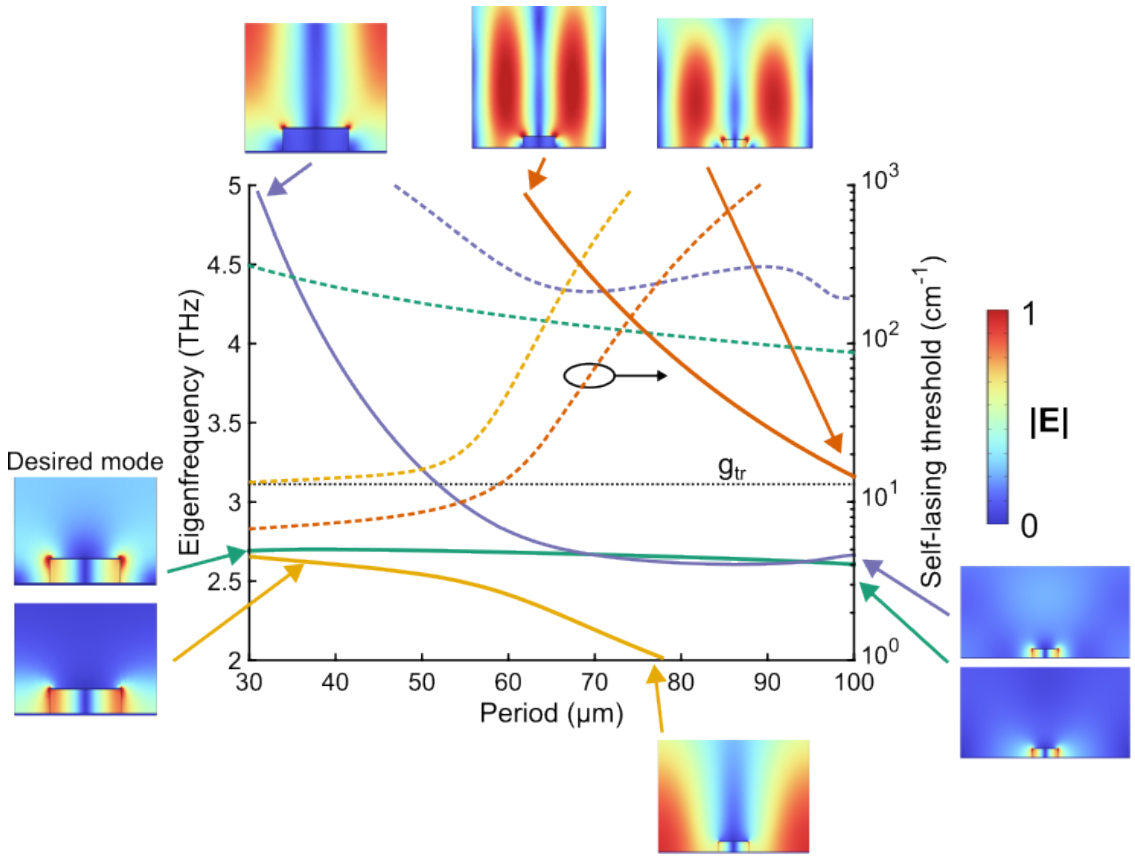

Figure 2.8: FEM simulated eigenfrequency of a 2D infinite metasurface versus period. This is equivalent to a uniform ridge-based metasurface. Each color corresponds to a different mode. The solid curves show the eigenfrequency, and the corresponding dashed lines are the self-lasing threshold. The green curve is the desired patch antenna mode for VECSEL operation.

Therefore, it is generally a good rule in the design of the metasurface to restrict the period such that $\Lambda > \lambda_0/2$.

The orange curve corresponds to the $\Lambda = \lambda$ Bragg mode, and anti-crosses with the desired mode when $\Lambda \approx 111$ μm. To avoid traversing into this regime of diffraction, a typical rule of thumb is to choose $\Lambda < 0.8\lambda_0$. However, as will be discussed in Chapter 3, the anti-crossing gap is a function of the radiative photon lifetimes of the desired mode and Bragg mode respectively, and thus can be exacerbated for higher frequency metasurface designs where the radiative quality factor of the metasurface drops. Fortunately, this mode is not a concern for self-lasing due to the higher threshold; this mode is localized in the air, not in

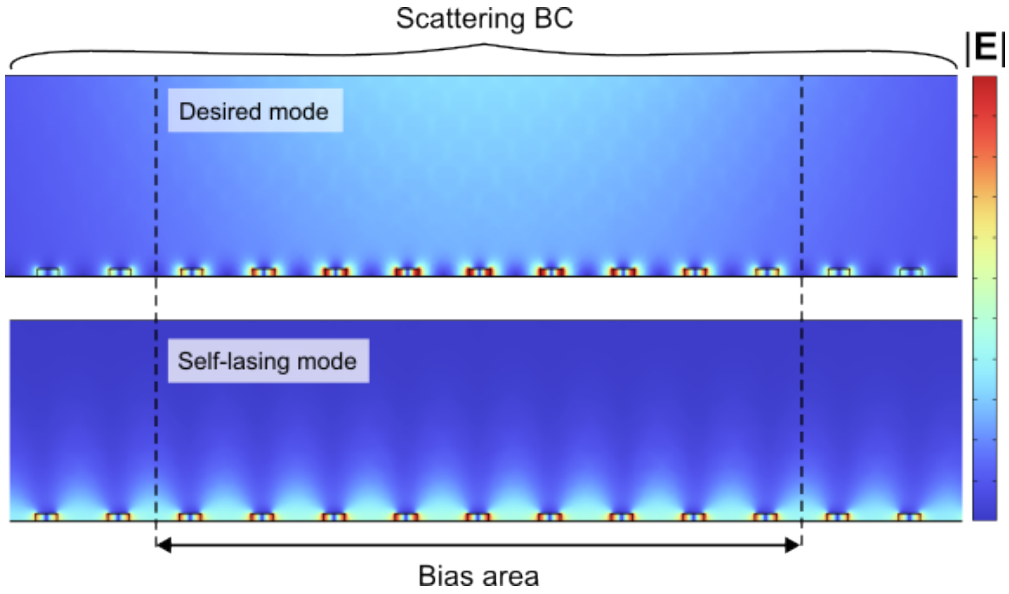

Figure 2.9: Eigenmode simulation of a 2D finite metasurface, illustrating the desired mode (top) and the self-lasing dark mode (bot). Only the antennas within the vertical dashed lines are biased.

the semiconductor.

Fig. 2.9 shows an eigenmode simulation of a finite metasurface for the case of $\Lambda = 50$ µm. The desired microstrip mode is resonant at 2.70 THz, while the self-lasing mode is resonant at 2.54 THz. Although the microstrip mode radiates to the surface normal, the self-lasing mode is localized to the surface and overlaps strongly with the active material. In the case of a finite metasurface, the threshold gain of the self-lasing mode is higher. This is because the Bragg mode is able to scatter out the edges of the metasurface, introducing a major loss mechanism that is not present when performing an infinite periodic simulation. For this simulation, the length of the bias area was 500 µm, and the total length of the metasurface was 1.5 mm. The threshold gain in this case is 29.5 cm^{-1}, compared to 16.0 cm^{-1} for the infinite case. This phenomenon helps suppress self-lasing in a real device, but can still act as an additional loss mechanism.

In testing fabricated devices, the rectangular patch-based metasurfaces were more susceptible to self-lasing. The rectangular patch metasurface has a modal landscape similar to that shown in Fig. 2.8, with a few notable distinctions. One, the dark mode stays closer in

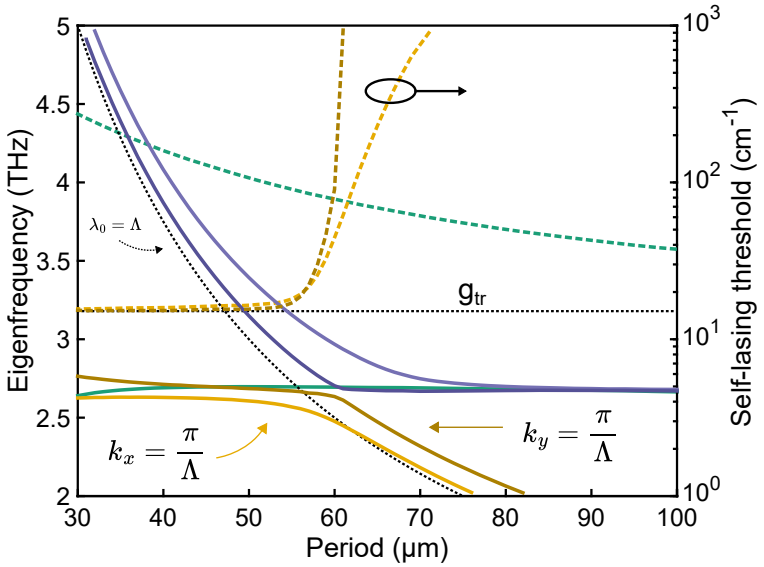

Figure 2.10: FEM simulated eigenfrequency of a 3D infinite metasurface versus period. This is equivalent to a uniform patch-based metasurface. Only the modes of interest are shown in this plot. The dark purple and dark yellow curves correspond to modes with in-plane momentum $k_y = \frac{\pi}{\Lambda}$ and $k_x = 0$. The light yellow and light purple curves correspond to modes with in-plane momentum $k_x = \frac{\pi}{\Lambda}$ and $k_y = 0$.

frequency to the desired mode for a wider range of periods, as can be seen in Fig. 2.10. Two, the additional periodicity in the y-direction means additional high quality factor dark modes associated with in-plane momentum in the y-direction. The higher quality factor of these parasitic modes will cause the lasing threshold of these modes to be lower, even for the case of a finite metasurface. This phenomenon most likely explains why uniform ridge metasurfaces designed at 2.7 THz resulted in successful VECSELs despite having a period equal to 40 µm or 50 µm, while patches with 50 µm period showed self-lasing. **Thus, to avoid the competition of self-lasing dark modes, it is important to keep the period greater than $\lambda_0/2$, particularly for the patch-based metasurface**.

2.4 Effect of active-region thickness on the metasurface

The analysis performed in Section 2.2 assumed a constant active region thickness h. In fact, the transparency gain g_{tr}, radiative quality factor Q_{r}, and the gain interaction length

ξ_0 all scale inversely with the active region thickness, which suggests we should consider modifying h as well. The combined effect on the fractional threshold gain bandwidth and slope efficiency is plotted in Fig. 2.11(a) for an exemplar metasurface design at 2.7 THz, once again assuming $g = 30$ cm^{-1}. The solid and dashed curves indicate an OC reflectance of 0.9 and 0.8 respectively. For a large OC reflectance, the fractional threshold gain bandwidth monotonically increases with h due to the broadening of the reflectance lineshape. The cutoff at $h = 2$ µm when $\Delta\nu_{\mathrm{th}}/\nu_0 = 0$ occurs due to the rapid increase of the transparency gain as h gets smaller (see Fig. 2.11(b)) and the applied gain can no longer compensate the material losses. This is roughly consistent with the thinnest reported QCLs that are 1.75 µm thick [123, 124]. As the OC reflectance gets weaker, the drop in R_{MS} with h, as illustrated in Fig. 2.11(b), begins to bring the laser below threshold. This is conveyed by the turning point in the fractional threshold gain bandwidth shown by the dashed curve in Fig. 2.11(a). This, in conjunction with Fig. 2.5, explains why VECSELs at 4.6 THz with a 10 µm thick active region required a special high-Q patch antenna design [109]. A 5 µm thick active region, on the other hand, was able to operate with a uniform-ridge design, as shown in the experimental survey in Section 2.6.

Additionally, Fig. 2.11 shows a monotonic increase of the slope efficiency with h. The $\mathrm{d}P/\mathrm{d}I$ values shown assume an ideal system in which $\eta_i = \eta_{\mathrm{u}} = 1$, and a QC period of 62 nm. The strong increase of slope efficiency with h is due to two effects. One, the reduced ξ improves the optical efficiency due to the reduced Q_{r} of the metasurface. Two, a thicker active region means a proportionally larger number of QC periods and thus more material gain. As expected, the slope efficiency increases as the OC gets more transmissive. However, there is an apparent trade-off with the threshold gain bandwidth for reasons similar to those explained in Section 2.2.

It is apparent that there may be advantages to using thicker active regions for device performance. However, a thicker active region will dissipate more electrical power and will be less efficient at heat removal, hindering cw performance. This is because the QC active material exhibits very small out-of-plane thermal conductivity ($\sim$5 W·m^{-1}·K^{-1}) due to

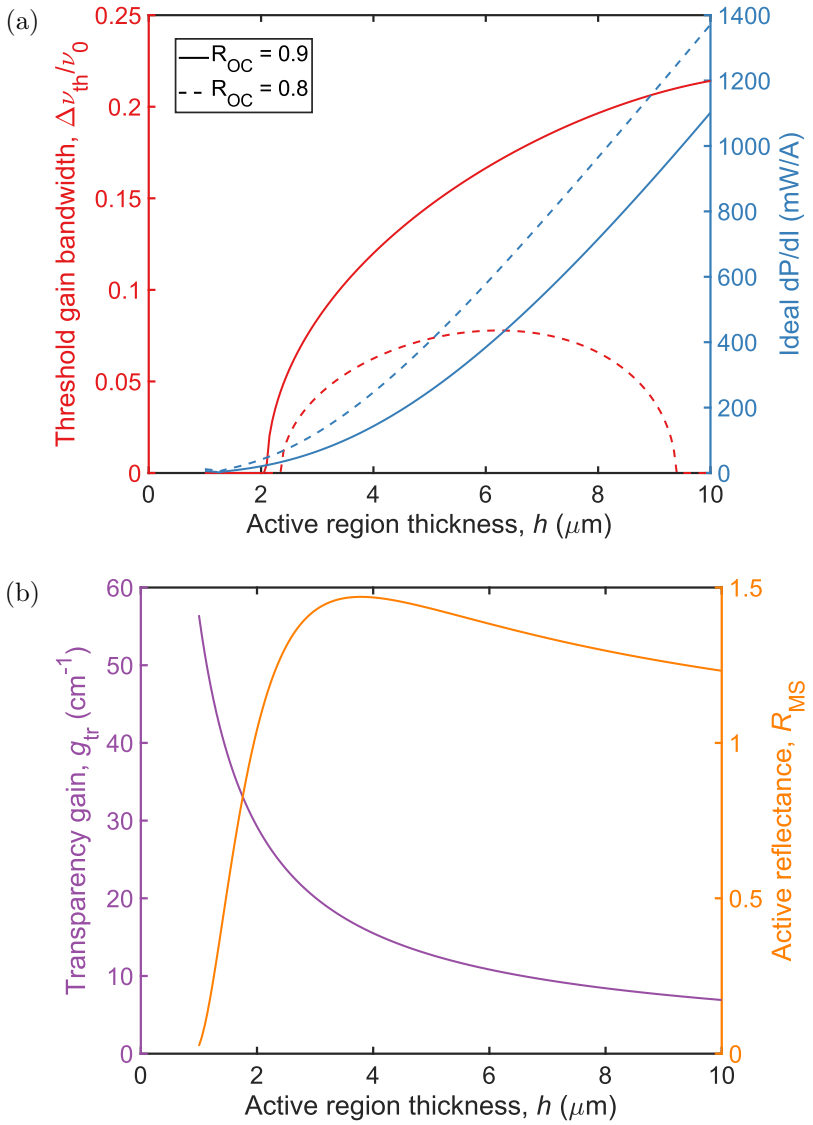

Figure 2.11: (a) Threshold gain bandwidth and ideal slope efficiency versus active region thickness. The values assume an applied gain of g = 30 cm^{-1} for a 2.7 THz VECSEL with w = 14.9 µm, Λ = 40 µm, and a 37% fill factor. The slope efficiency values assume a unity quantum efficiency and modal uniformity factor. It also assumes a quantum-cascade periodicity of 62 nm, which is typical for the active region designs used in this work. (b) The transparency gain and peak active-metasurface reflectance versus active region thickness. The transparency gain is inversely proportional to h. The peak reflectance reaches a maximum and begins to decay because the reduction in ξ starts to overcome the benefit of reduced material loss.

the large thermal boundary resistances of the GaAs/AlGaAs heterostructures [125, 126]. A previous demonstration showed an 18 K improvement in the cw maximum operating temperature when a 10 µm active region was reduced to 5 µm thick in a metal-metal waveguide laser [127]. The first reported QC-VECSEL with a 5 µm thick active region was a design nominally centered at 2.7 THz, and is detailed in Section 2.6.

2.5 Characteristics of single-mode tuning

While the analysis in the preceding section considered the threshold gain bandwidth of the QC-VECSEL, the actual selection and tuning of the lasing frequency is governed by the resonant modes of the external cavity. Given that the round-trip phase accumulation within the cavity must be an integer multiple of 2π, the longitudinal modes will occur at frequencies:

$$\nu_{\mathrm{m}} = \frac{c}{2L_{\mathrm{c}}}(m + \frac{\phi_{\mathrm{MS}}}{2\pi} + \frac{\phi_{\mathrm{OC}}}{2\pi}), \tag{2.28}$$

where L_{c} is the external cavity length, ϕ_{MS} is the metasurface reflection phase at ν_{m}, ϕ_{OC} is the OC reflection phase at ν_{m}, and m is a positive integer denoting the mode index. For now, we consider the OC to be "ideal", in that it exhibits a flat reflectance spectrum with a constant phase of $\phi_{\mathrm{MS}} = -\pi$. This condition is generally true for the metal-mesh OCs typically used for QC-VECSELs with reflectance $> 90\%$. On the other hand, the metasurface reflection phase spans 2π across its resonance. Fig. 2.12 shows a simulated reflection phase and group delay for a broadband metasurface designed at 2.7 THz. The result of Eq. (2.28) is plotted in Fig. 2.13(a) for the same metasurface parameters. The dispersion of the metasurface around the resonance causes a reduction in the FSR compared to an FP resonator. A small FSR can limit the tuning range of the laser, since the presence of more than one mode within the gain bandwidth can lead to mode-hopping as the cavity length is swept. Using Eq. 2.28, the FSR can be calculated as

$$\mathrm{FSR} \approx \frac{c}{2L_{\mathrm{c}}} \frac{1}{1 + \frac{c}{2L_{\mathrm{c}}}(\tau_{\mathrm{MS}} + \tau_{\mathrm{OC}})}, \tag{2.29}$$

where $\tau_{\mathrm{MS}} = -\mathrm{d}\phi_{\mathrm{MS}}/\mathrm{d}\omega$ and $\tau_{\mathrm{OC}} = -\mathrm{d}\phi_{\mathrm{OC}}/\mathrm{d}\omega$ is the group delay of the metasurface and OC respectively evaluated at the frequency of interest. The key conclusion is that a lower Q_{r} metasurface will have reduced group delay, and will lead to larger FSR values which maximize the single-mode tunable range.

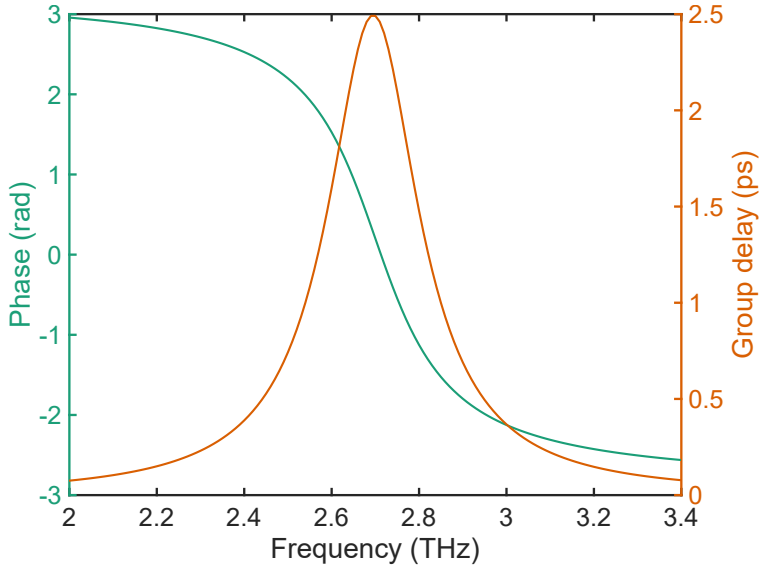

Figure 2.12: Simulated metasurface reflection phase and corresponding group delay.

The realizable single-mode tuning bandwidth of the QC-VECSEL is limited by either the threshold gain bandwidth $\Delta\nu_{\mathrm{th}}$, or the FSR of the external cavity — whichever is smaller. If the FSR is small enough that multiple allowable modes fall within the threshold gain bandwidth, it is possible for the laser to either mode-hop or lase in multi-mode operation before tuning through the available gain. Then, to achieve continuous single-mode tuning, the FSR of the external cavity must be large enough to only permit a single mode within $\Delta\nu_{\mathrm{th}}$.

In order to describe the interplay of these factors, we will consider an example case of a particular metasurface designed for amplification at 2.7 THz, with $h = 5$ µm, $w = 14.9$ µm, and $\Lambda = 40$ µm. Consider the plot in Fig. 2.13(a). The dotted lines correspond to the threshold gain bandwidth associated with this metasurface paired with an OC of reflectance $R_{\mathrm{OC}} = 0.95$. As an additional note, this gain bandwidth roughly corresponds

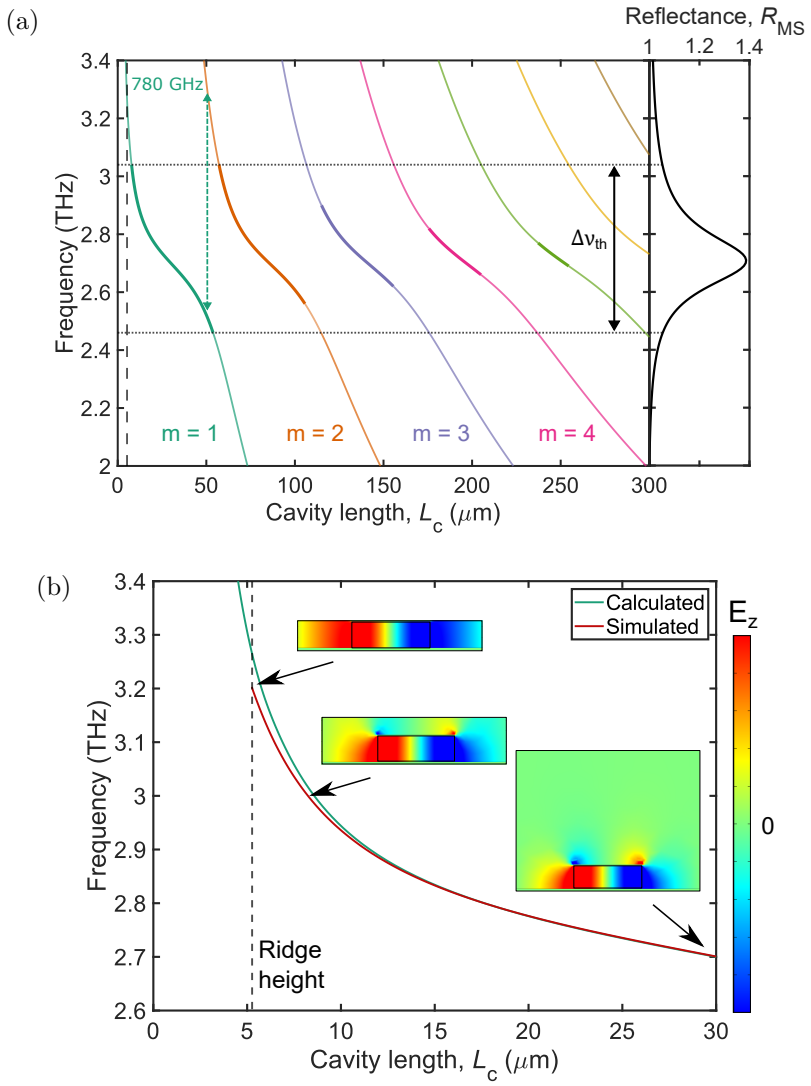

Figure 2.13: (a) Resonance condition of the QC-VECSEL versus the external cavity length. The horizontal dotted lines represent the threshold gain bandwidth. Interfaced to the right is the metasurface reflectance for an applied gain $g = 30$ cm^{-1}. The thicker lines indicate a single-mode tuning regime for the given threshold gain bandwidth. The green vertical dashed line shows the theoretical maximum tuning range of 780 GHz. (b) Simulated eigen-frequencies for small cavity lengths. The field profile of the unit cell is shown throughout the curve, demonstrating the perturbation of the microcavity mode profile. The vertical dashed line represents a practical limit of the cavity length. In this case, it is 5.25 µm, which is determined by the combined height of the active region and top metal contact.

with that measured from the QC-laser material grown by IQE plc of design RPC162-M3-2.7. Interfaced onto the plot is the simulated metasurface reflectance spectrum assuming a spectrally flat gain of $g = 30$ cm^{-1}; $\Delta\nu_{\text{th}}$ is the range over which $R_{\text{MS}} > R_{\text{OC}}^{-1}$. The thicker portion of the lines in Fig. 2.13(a) indicate the continuous single-mode tuning regimes for each mode index; these are the regions in which only a single longitudinal mode falls within $\Delta\nu_{\text{th}}$. For this particular example, we can see that operating on the $m = 2$ mode would allow for tuning through nearly all the available gain. As the cavity length grows longer, the device will lase on higher order modes, and the FSR-limited tuning range will decrease.

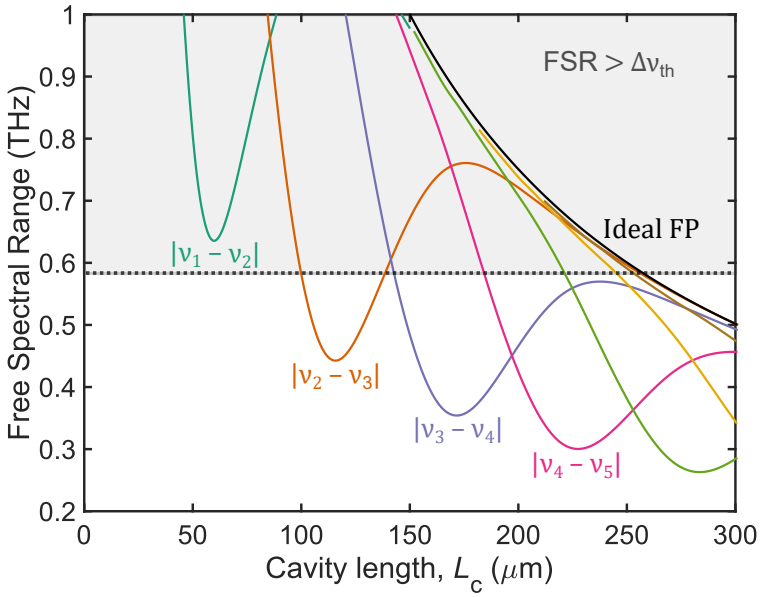

Figure 2.14: Calculated free-spectral-range (FSR) as a function of cavity length. Each curve shows the frequency difference between two adjacent modes. The black curve is the FSR for an ideal FP resonator. The grey shaded region indicates a regime where the FSR is greater than the threshold gain bandwidth.

If the cavity length is sufficiently reduced, it is possible to operate in the $m = 1$ mode of the external cavity. However, there are a couple factors to be considered. One, the physical limit of the cavity length (indicated by the dashed vertical line) is reached at 5.25 µm for the considered active region, including the top metal. Two, as the metal from the OC starts to interact with the metasurface near-field, the metasurface eigenmode will be perturbed. This

can be seen in Fig. 2.13(b), in which the simulated eigenfrequencies are plotted on top of the results from Eq. (2.28). The reduction in frequency can be attributed to the widening of the fringing fields as the OC gets closer, resulting in an effectively wider antenna. Even before this physical limit is reached however, one must take care to ensure the OC is perfectly parallel with the metasurface, otherwise higher order transverse modes can begin to lase, resulting in multimode operation and degraded beam patterns [30]. This effect can be suppressed using metasurfaces with small bias diameters.

The FSR between each adjacent mode is plotted in Fig. 2.14. The local minima locations shown in this plot are cavity lengths in which mode-hopping is most likely to occur. Indeed, the final limit to the tuning bandwidth is the FSR, since $\Delta\nu_{\text{th}}$ can always be increased by using a more reflective OC. For this metasurface, as was shown in Fig. 2.13, the FSR limited bandwidth is 780 GHz (27% fractional) as the laser is tuned through the $m = 1$ mode, which is less than half of that achieved with an ideal FP resonator (66% fractional for ideal FP cavity). If the metasurface is engineered with a smaller quality factor, the group delay is reduced, and the tuning range will approach the ideal limit.

2.6 Experimental survey of tunable QC-VECSELs

In this section, we present experimental data from five different tunable QC-VECSEL devices that cover various frequency bands between 1-6 THz. While these devices were not originally fabricated with the intention of making direct comparisons, they collectively illustrate some of the challenges associated with frequency scaling QC-VECSEL operation. While each of the metasurfaces in these devices use different GaAs/AlGaAs active regions designed for specific frequencies, they are all of the same type and based upon a 4-well hybrid bound-to-continuum/resonant-phonon design similar to that reported in [23]. A summary of the single-mode spectral coverage is shown in Fig. 2.15. The devices are labeled A-D in order of increasing frequency. Each set of spectra is collected using a fourier transform infrared (FTIR) spectrometer with a DTGS room-temperature detector. The output coupler position

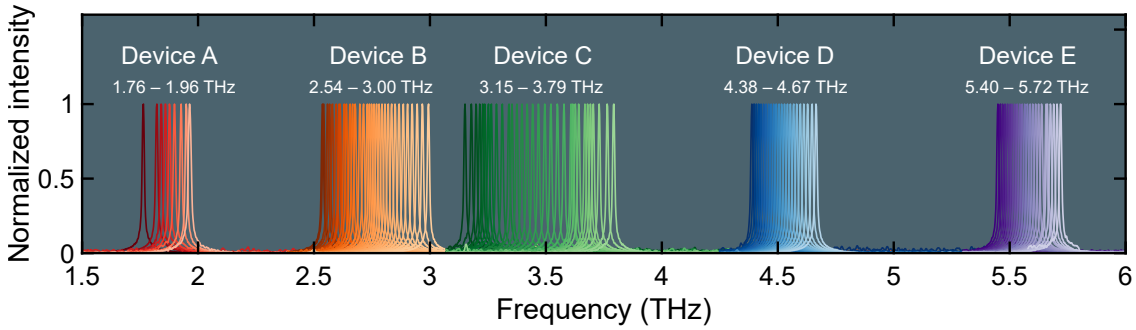

Figure 2.15: Summary of the spectral coverage of five representative QC-VECSELs measured in pulsed-mode as the cavity length is changed in real-time via piezoelectric control. All spectra are single-mode, with amplitudes normalized to unity. Spectra for devices A–D were collected at 77 K. Spectra for device E was collected at 5 K. Device A shows a tuning range of 1.76–1.96 THz. Device B shows a tuning range of 2.54–3.00 THz. Device C shows a tuning range of 3.15–3.79 THz. Device D shows a tuning range of 4.38–4.67 THz. Device E shows a tuning range of 5.40–5.72 THz.

is swept through an entire FSR using a piezoelectric stepper motor, and a spectrum is collected at each cavity step. A summary of key performance characteristics is shown in Table 2.1. Some of the listed parameters show a range of values due to the variation of these parameters as the laser is tuned. In particular, the output couplers have frequency-dependent reflectances due to FP oscillations caused by the substrate facets. The table lists the maximum achieved tuning range (fractional tuning shown in parenthesis), the nominal unit cell dimensions (fill factor in parenthesis), the threshold current density J_{th}, the dynamic range, the slope efficiency, and the reflectance of the output coupler R_{OC}. The dynamic range is quantified as $(J_{\mathrm{pk}} - J_{\mathrm{th}})/J_{\mathrm{pk}}$ from the device power-current-voltage curves, where J_{pk} is the current density at maximum power output. Fig. 2.16 shows a representative light-current-voltage (L-I-V) curve for devices A-E respectively, and Fig. 2.17 shows corresponding beam patterns taken at a particular cavity length. For each measurement, the laser is driven via a pulse generator, and the power is collected using a room-temperature pyroelectric detector calibrated with a thermopile. The inset of each L-I-V plot shows the lasing spectrum that corresponds to the collected data. The beam-pattern measurements show consistent high-quality single-mode beam profiles across the different devices. Additionally, measurements

Table 2.1: Summary of device performance in pulsed-mode operation

Device	A [117]	B	C [30]	D	E
Tuning range	1.76-1.96 THz (10.7% frac.)	2.54-3.00 THz (16.6% frac.)	3.15-3.79 THz (18.7% frac.)	4.38-4.67 THz (6.4% frac.)	5.40-5.72 THz (5.8% frac.)
h / w / Λ (µm)	10 / 20.9 / 75 (FF: 28%)	5 / 14.9 /40 (FF: 37%)	10 / 11.9 / 41.7 (FF: 29%)	5 / 8.6 / 30 (FF: 29%)	7 / 6.53 / 36 (FF: 18%)
J_{th} (A/cm^2)	424-444	570-630	500-560	404 @ 4.58 THz	750-1000
(J_{pk}-J_{th}) /J_{pk}	0.074 @ 1.95 THz	0.17-0.27	0.22-0.29	0.29 @ 4.58 THz	0.20-0.38
Slope efficiency (mW/A)	148 @ 1.95 THz	2.7-62.7	100-400	27.1 @ 4.58 THz	2.0 @ 5.69 THz
R_{OC}	0.94-0.98	0.98-0.995	0.92-0.98	0.93-0.98	∼0.99
Heatsink temp.	77 K	77 K	77 K	77 K	5 K

for devices A-D were taken at 77 K, while data for device E was collected at 5 K.

As a baseline, we will first detail the performance of Device C, which showed record single-mode tunability for a QC-VECSEL and was previously reported in [30]. The laser was able to tune single-mode from 3.15 to 3.79 THz, or 18.7% fractional, operating on the $m = 4$ mode. When the cavity length was made short enough for the device to operate on the $m = 2$ longitudinal mode, a much larger tuning bandwidth of 880 GHz was observed. However, at such small cavity lengths, the presence of higher-order transverse modes caused worse beam patterns and occasional multimoding throughout the tuning range. Still, it suggested that the particular active material had up to ∼1 THz gain bandwidth. The device also showed consistent tuning performance during cw operation. Although its power output was reduced by more than a factor of two compared to pulsed-mode operation, it was the highest cw power output that has been achieved at 77 K.

With all else equal, scaling to lower frequencies comes at the cost of a lower slope efficiency

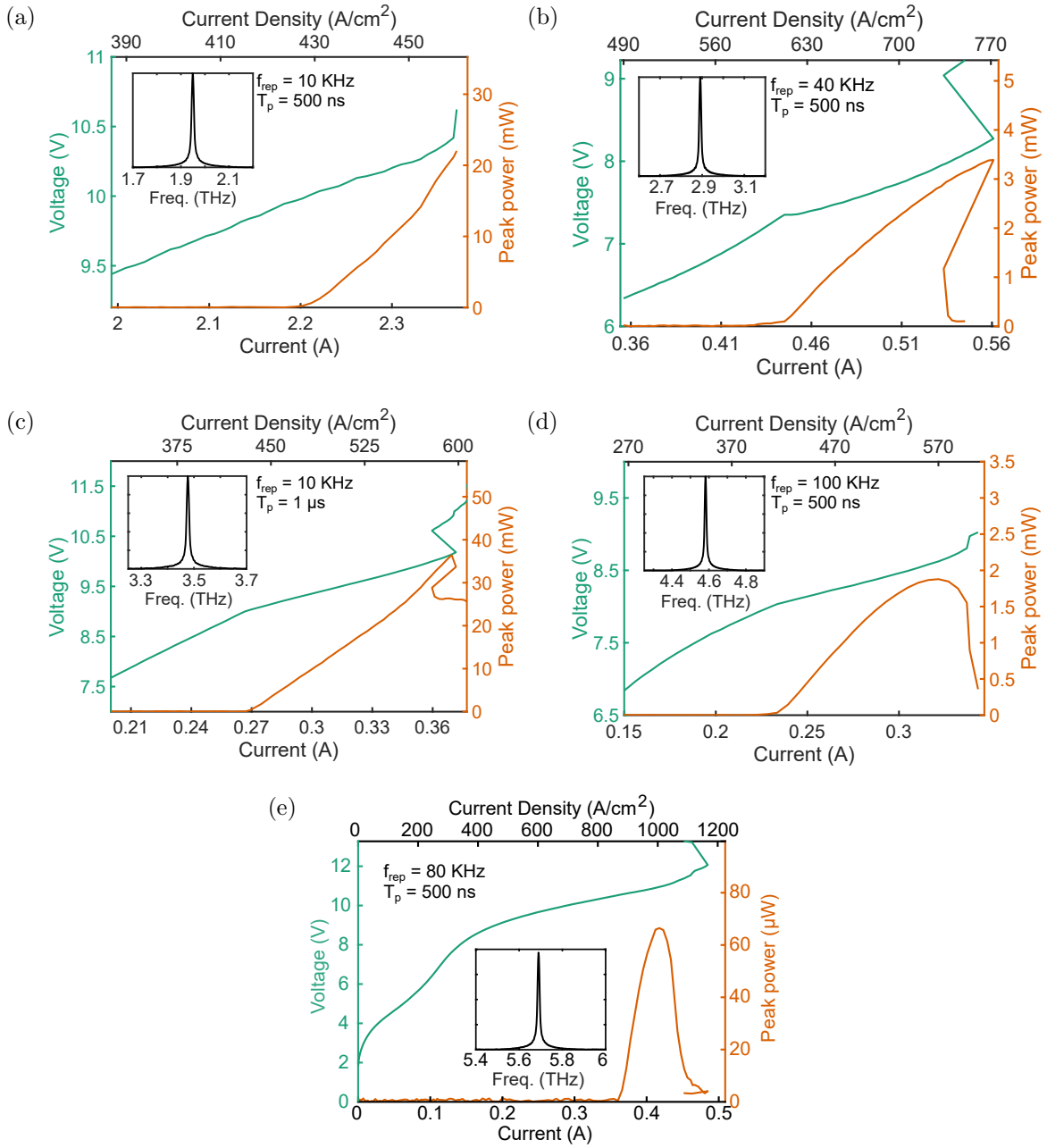

Figure 2.16: Representative power-current-voltage (L-I-V) curves for (a) Device A, (b) Device B, (c) Device C, (d) Device D, and (e) Device E. The measurements were performed in pulsed-mode operation. The repetition rate, f_{rep}, and pulse duration, T_{p}, is labeled for each L-I-V. Devices A–D were measured at 77 K, while Device E was measured at 5 K using LHe. The inset of each plot shows a corresponding FTIR measurement that shows the lasing frequency at which the data was collected.

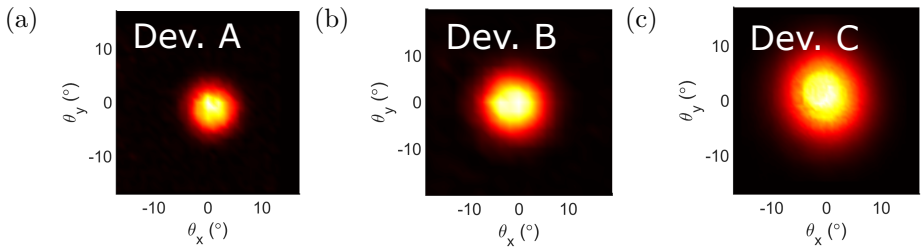

Figure 2.17: Radial beam pattern measurements for devices A–C. The VECSELs show a consistent single-mode Gaussian beam pattern for various wavelength-scaled devices.

due to the larger radiative quality factor. This is consistent with what we measured from Device B, a design centered at 2.7 THz. However, in anticipation of operating this device in cw, a 5 µm thick active region was used — a design choice not necessarily optimal for pulsed-mode operation [127]. In fact, according to Fig. 2.11(a), reducing h by half can reduce the slope efficiency by more than a factor of 5 depending on the value of R_{OC}. Furthermore, the thin active region results in a larger ξ_0, calling for a higher metasurface fill factor to maintain a Q_{r} small enough for broadband tuning. Again, to keep the power consumption low for cw operation, the bias diameter was kept at 0.5 mm. Fig. 2.16(b) shows a maximum power draw of 4.64 W. To maximize the tuning bandwidth, a large R_{OC} was used. The device demonstrated a fractional tuning bandwidth of 16.6%, covering the entire spectral band in which lasing from a metal-metal waveguide using the same active region was observed [127]. This tuning range of 460 GHz agrees closely with the simulations from Fig. 2.14 for a cavity that is tuned across the $m = 2$ mode index. The device also showed similar tuning performance in cw, as illustrated by the cw tuning spectrum in Fig. 2.18. The black dotted curve in the figure plots the atmospheric transmission at 30% relative humidity. Though the tuning performance remains relatively unchanged in cw, it comes with a reduction in power output due to the increased heating of the device. As the device heats up, the thermally activated LO-phonon scattering rate increases exponentially, increasing the current threshold of the laser. The influence of this heating on the laser power output is studied by biasing the laser with a pulser at increasingly longer pulse durations. As shown in Fig. 2.19, the power output decays with increasing pulse duration given a fixed repetition

rate of 40 KHz. An extrapolation of the trend suggests a 44% reduction in power in cw operation, and is consistent with the fact that the largest cw power measured was around 1.5 mW.

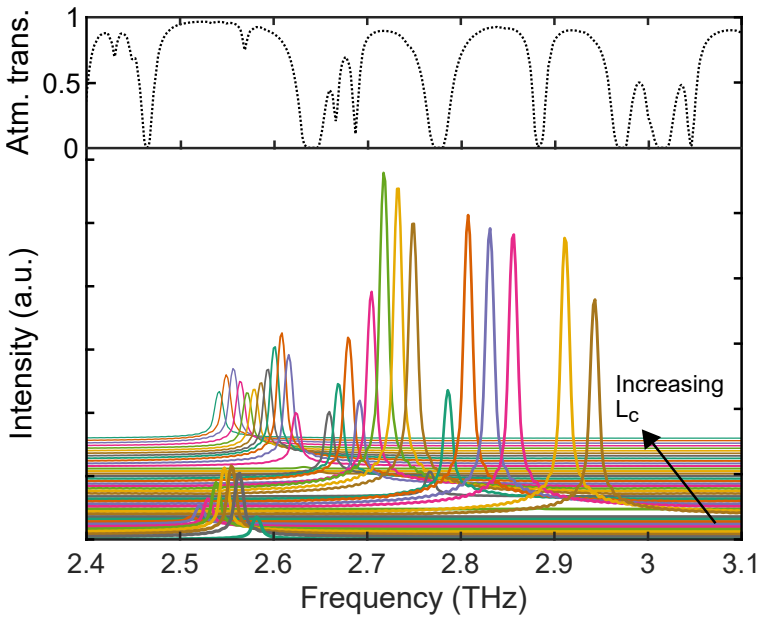

Figure 2.18: Continuous-wave tuning spectrum of Device B. The spectra are vertically stacked in the order in which the cavity length was tuned away from the metasurface. The spectrum spans about 430 GHz, resulting in a fractional tuning bandwidth of 15.8%. The dotted curve above the spectra is the atmospheric transmission spectrum at a 30% relative humidity. The output coupler used is Si-P10A4.

As the QC-VECSEL is scaled to the extreme ends of the spectrum (< 2 THz and > 4.5 THz), it becomes a challenge to maintain the same level of device performance. We detail here Device A [117] and D as representative devices at these extremes, with center frequencies 1.9 THz and 4.5 THz respectively. At the low end, the QC gain material is more difficult to engineer, since the small photon energies (8 meV at 2 THz) necessitate more closely spaced subbands that make selective pumping of the upper state more difficult [118, 128]. This makes population inversion more difficult to achieve, and introduces sub-threshold parasitic current channels, which increase the threshold current density. This explains why Device A has a dynamic range of 0.074, the smallest value reported in this survey. Furthermore,

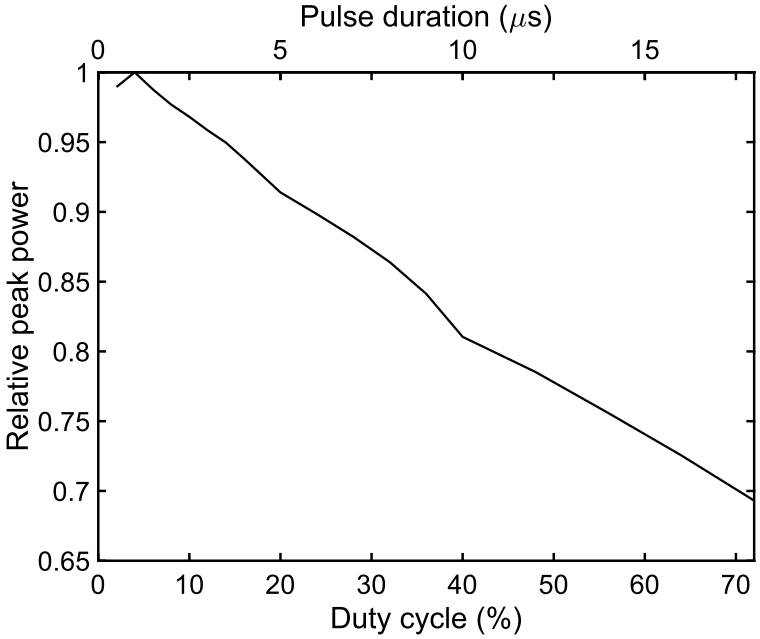

Figure 2.19: Relative peak power versus duty cycle for Device B. The laser is biased via a pulse generator at a 40 KHz repetition rate as the pulse width is stepped from 500 ns to 18 µs. The trend extrapolates to a ∼44% reduction in power output at cw.

the enhanced Q_{r} at this design frequency is associated with larger group delays, reducing the FSR near resonance. This resulted in a smaller tuning bandwidth of 200 GHz despite operating on the same $m = 4$ mode as Device C. Additionally, the large wavelength ($\lambda_0 =$ 150 µm at 2 THz) means that the bias area of the metasurface must be increased accordingly to preserve the transverse confinement factor of the external cavity Gaussian mode [114]. For Device A, the central bias circle was 1.5 mm in diameter. Since the current density does not scale with wavelength, a larger bias area means the device will consume more power. The *L-I-V* in Fig. 2.16(a) shows a maximum power consumption of 25 W, and cw operation was not possible. If the bias area is kept small, then the ill-confined beam will lead to large absorption losses in the unbiased area. This is exacerbated by the presence of a strong intersubband absorption feature at 1.9 THz at zero bias [113, 117].

At the other end of the spectrum, the reduced ξ_0 and Q_{r} make the metasurface struggle to provide sufficient gain. This is exacerbated by additional losses from optical phonons, as the

frequencies begin to approach the GaAs *Reststrahlen* band. This is especially problematic beyond 5 THz, thus a separate section (Section 3.3) is dedicated to discussing Device E at the end of the chapter. Nevertheless, attempts at realizing a 10 µm high ridge-based metasurface at 4.7 THz were unsuccessful, and relied on a high-Q patch-based metasurface to enhance the active metasurface reflectance [109]. However, these patch-based devices are much more narrowband, and can add more complexity to the fabrication. Using a 5 µm thick active region, the uniform ridge-based metasurface had a large enough metasurface reflectance to successfully lase. However, as predicted by Eq. (2.24), the threshold bandwidth is significantly reduced, and the device would fall below threshold before being able to tune through a full FSR of the external cavity. Consequently, the device showed a moderate tuning bandwidth of about 290 GHz, or 6.4% fractional.

2.7 Dependence of output coupler on frequency tuning

In this section, we explore the effects of varying the output coupler (OC) such as influence on tuning range and slope efficiency. We begin by briefly introducing the concept of the metal mesh OC, followed by a study of three different OCs using Device B as the device under test. The section ends with a unique case study of how the selection of OC is crucial for the polarization-switchable QC-VECSEL [107].

2.7.1 Designing the output coupler

The OCs are fabricated in-house by evaporating a metal mesh on either a z-cut quartz or high-resistivity Si substrate. The unit cell of the mesh is shown in the inset of Fig. 2.20. For the square mesh, P is the periodicity of the unit cell, and A is the width of the metal wires. For the circular mesh, P is the periodicity and D is the diameter of the holes. The density of the mesh controls the level of reflectance. The Fabry-Pérot etalon effect from the substrate can lead to a significant frequency dependence of the OC reflectance.

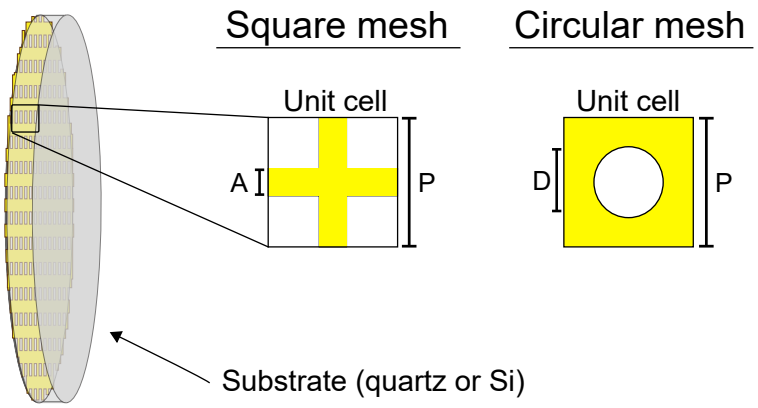

Figure 2.20: Illustration of the QC-VECSEL output couplers. The output coupler is based on an inductive mesh deposited on a quartz or Si substrate. Two primitive designs have been used: a square-based mesh and a circle-based mesh.

2.7.2 Uniform ridge metasurface

Three different output couplers are tested with Device B: two quartz substrates, and one Si substrate. The quartz thickness used is 100 µm thick, and the Si thickness is 280 µm. This leads to an FSR of about 700 GHz and 155 GHz respectively for the two substrates. Indeed, these values are on the order of the tuning range, and thus can dramatically affect the performance of the laser as the cavity is tuned. The larger index of the Si substrate will result in a high finesse etalon, and would be unsuitable for broadband tuning. Therefore, an etch-based anti-reflective coating was processed onto the Si substrate to reduce the fringe amplitude similar to that described in [129]. The transmission spectra of the OC designs used in this study are shown in Fig. 2.21. The figure shows both the relevant 2.5-3 THz window, and a zoomed out 1-5 THz window which better illustrates the FP oscillations. Both simulated and measured results are shown for the Si-P10A4 OC. The simulated results are shown for the Qtz-P13A3 and Qtz-P10A4 OC. Any small variation in the actual thickness of the substrate will manifest as a small horizontal shift of the simulated transmittance curve.

The choice of OC was observed to have a significant impact on the tuning bandwidth, threshold current density, dynamic range, and the slope efficiency. In particular, a *L-I-V* measurement was performed at each OC position as the cavity length was tuned, taking

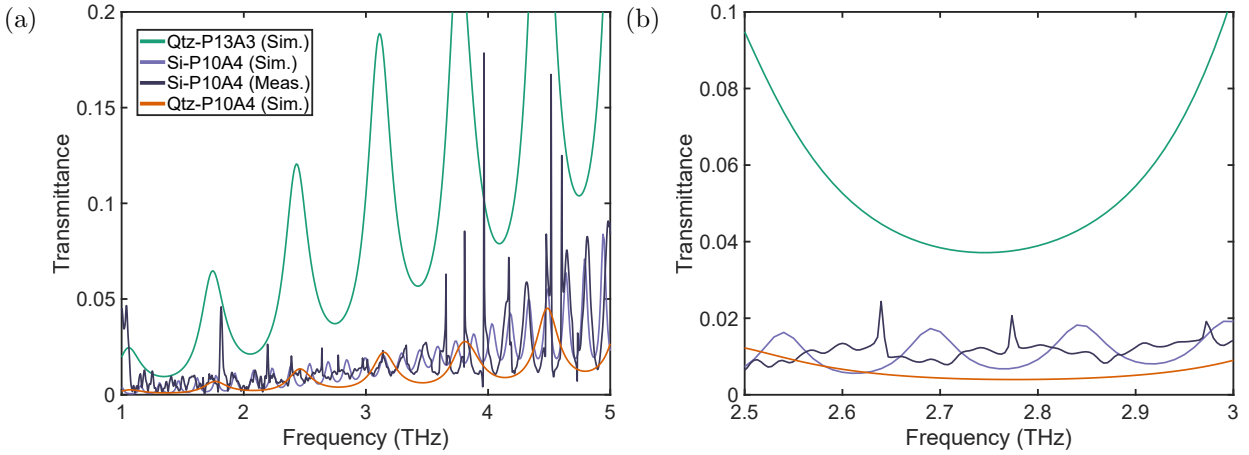

Figure 2.21: (a) Measured and simulated transmission spectra for the OCs designs used in this section. (b) is a zoomed window of the spectra shown in (a). For each OC spectrum, the mesh design is labeled, along with the corresponding substrates quartz (Qtz) or silicon (Si). P is the period of the unit cell, and A is the width of the metal lines. The Si substrate is 280 μm thick, and the quartz substrate is 100 μm thick.

note of the lasing frequency at each step. Looking at Fig. 2.22(a), we can see a general trend of increasing threshold for more transmissive OCs, which in turn results in a reduced dynamic range as can be seen in Fig. 2.22(b). It is apparent that the tuning bandwidth decreases with higher transmittance OCs as the tuning range switches from FSR-limited to threshold-limited. The Qtz-P13A3 showed a tuning range of 307 GHz. This was limited not by the FSR, but rather by the extinguished dynamic range at the extreme ends of the tuning spectrum — a consequence of the current threshold being driven up to the negative-differential-resistance limit. On the other hand, for the two P10A4 OCs, mode-hopping occurs before the dynamic range drops to zero, indicating that the tuning range was FSR limited.

Furthermore, as expected from Eq. (2.26), the more reflective OC is accompanied by a reduced slope efficiency (Fig. 2.22(c)). However, this is only generally true at the center of the metasurface resonance. We can see that for frequencies > 2.8 THz, the slope efficiency for Si-P10A4 increases rapidly, rivaling that of the more transmissive OC Qtz-P13A3. This is because the optical coupling efficiency η_{opt} increases significantly detuned from the meta-

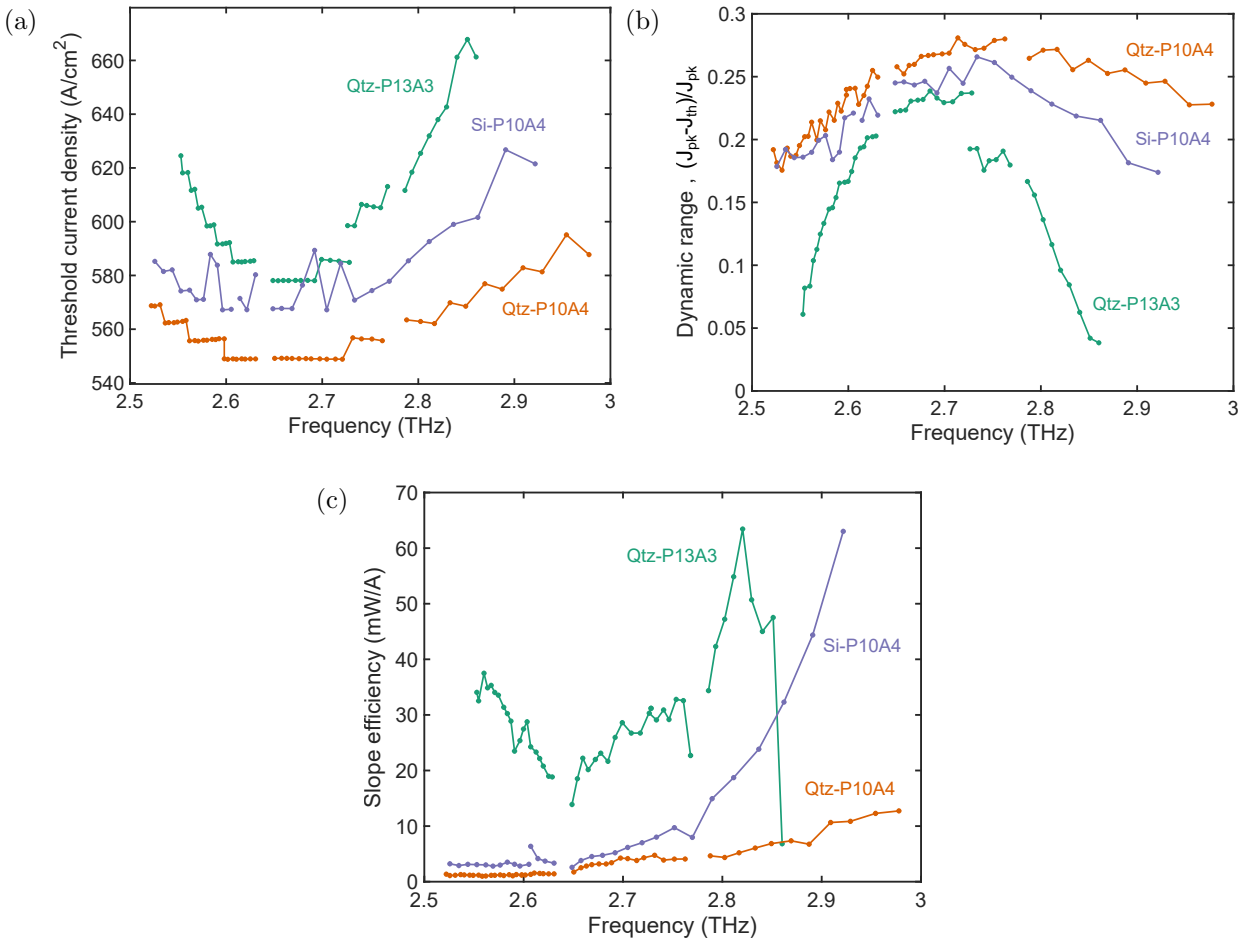

Figure 2.22: Measured (a) threshold current density, (b) dynamic range $(J_{pk} - J_{th})/J_{pk}$, and (c) slope efficiency as the external cavity length is swept, and the lasing frequency is correspondingly tuned. Each plot shows the results using three different output coupler designs.

surface resonance. This can be seen from Eq. (2.26), in which the term $\xi(\nu)$ decreases as ν is detuned from ν_0, and less of the intracavity VECSEL mode is confined within the microcavities. To compensate for the weaker gain interaction, the threshold current rises. However, if the OC reflectance is large enough such that the device remains above threshold, this will lead to an overall larger slope efficiency and power output. In the case of Qtz-P10A4, we see that the slope efficiency remains small even far from resonance. Although the the OC transmission spectra may suggest similar reflectance values between Si-P10A4 and Qtz-P10A4, the substantial difference in the threshold current values demonstrate that the Qtz-P10A4

still has a much higher reflectance. This, in conjunction with the smaller OC efficiency, explains why the slope efficiency remains much smaller than that of Si-P10A4 above 2.8 THz even though they share similar values near resonance. The lack of symmetry of the slope efficiency versus tuning is most likely because of the underlying gain spectrum of the active material. Measurements of the gain spectrum from the same active region fabricated into a nonresonant metal-metal waveguide laser suggest stronger gain at frequencies > 2.8 THz.

2.7.3 Special case: OC dependence of polarization-switchable metasurface

In 2017, a metasurface quantum-cascade laser with electrically switchable polarization that avoided the need for external moving elements and allowed for faster modulation speeds was demonstrated [107]. The metasurface is designed with two interleaved sets of antennas loaded with amplifying QC gain material, as shown in Figs. 2.23(a) and 2.23(b); each set of antennas amplifies either 45 degree or 135 degree linearly polarized light. Electrical switching between linearly polarized states is obtained, while the wavelength of light, power level, and Gaussian beam shape remains unchanged (see Fig. 2.23(c)). In the initial demonstration, the metasurface was mounted within a 77 K cryostat, and the output coupler mirror was placed externally. A 3 mm thick high-resistivity silicon cryostat window was used, and acted as a de facto intracavity etalon. This etalon acted to fix the cavity frequency, although it prevented continuous wavelength tuning. State-of-the-art QC-VECSELs have since been entirely intracryostat. In such a configuration, the polarimetric VECSEL has added complications. In this section, we demonstrate how the choice of OC can have a significant impact on the intracryostat polarimetric VECSEL.

Fig. 2.23(d) shows the simulated reflectance spectra of the metasurface. The plot on top shows the reflectance spectra when no gain is applied to either set of antennas. The plot below shows the result when 30 cm^{-1} of gain is applied to one set while the other remains passive. A co-polarization reflectance peak for the set with applied gain appears at 3.4 THz; this is the frequency in which the VECSEL is designed to operate. This is also the point in which all cross-polarization reflectance approaches zero. This would imply that operating in

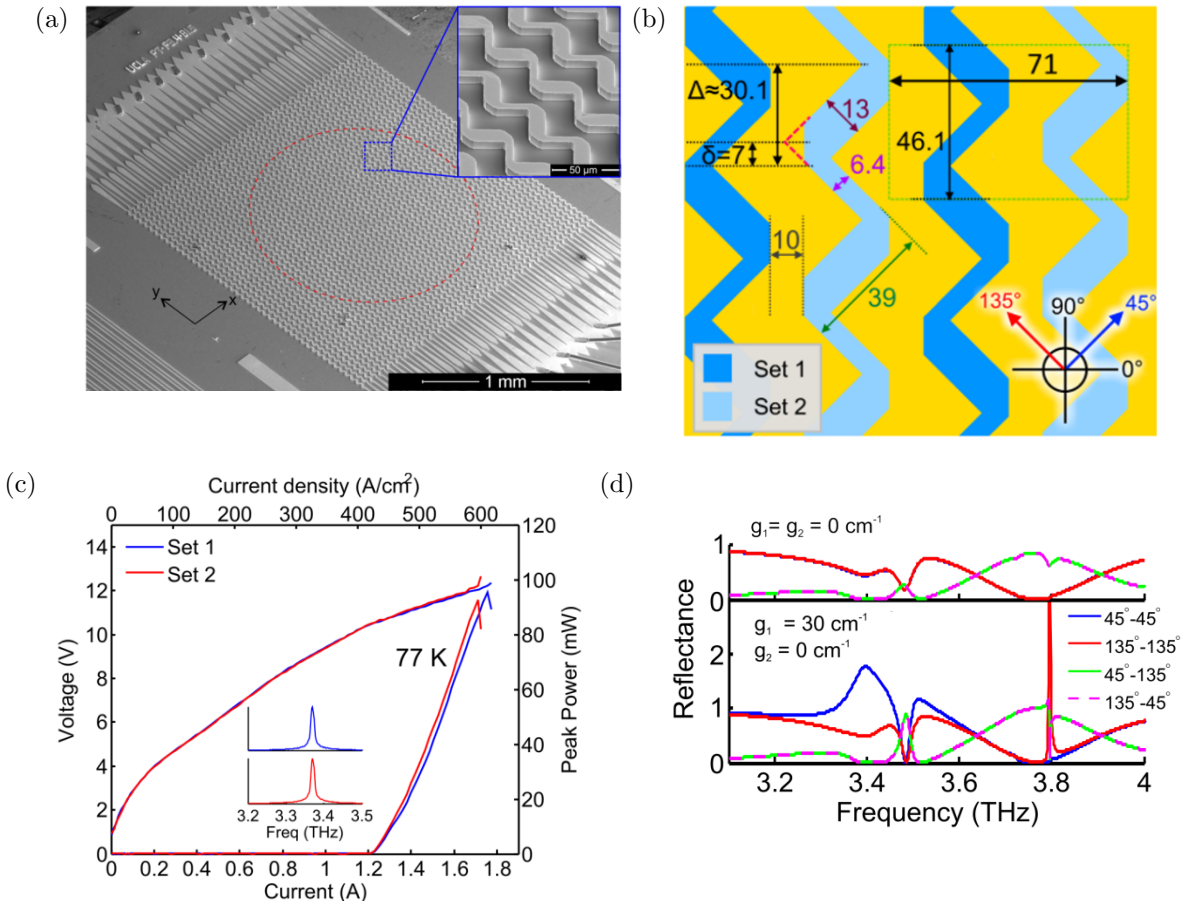

Figure 2.23: (a) SEM image of a metasurface with electrically switchable polarization state. (b) Geometry of the metasurface, showing the two electrically separate interdigitated sets of antennas. (c) Pulsed *L-I-V* curve for both sets of antennas. (d) Simulated reflectance spectra for both co-polarized and cross-polarized responses. The top spectra are when both sets of antennas are unbiased. The bottom spectra are when only one set of antennas is biased. These figures are reproduced from [107].

this frequency region would maximize the polarization purity of the output beam. However, the strong reflectance peak of the metasurface at 3.8 THz must also be considered. If the QC active material provides sufficient gain at this higher frequency, there exists the possibility of a competing mode lasing at ∼3.8 THz. This would be undesirable as it would have an adverse effect on the polarization purity of the output.

Fig. 2.24(a) shows the dependence of the cavity length on the frequency spectrum, axial ratio, and the axis of polarization of the output beam. A total of 11 different output coupler

positions were sampled. The cavity length is approximately 1.7 mm. Since the piezoelectric controller did not allow absolute position measurements, we are only able to infer the position by estimates based upon the observed free spectral range of the cavity. The frequency spectra on the right side of Fig. 2.24(a) shows how the spectra change as the OC is stepped away from the metasurface. As the cavity length changes, the lower frequency mode is observed to scan across a free spectral range of 90 GHz. As the cavity mode is tuned off resonance from the peak gain, a mode hop occurs. However, the removal of the intracavity etalon has resulted in the appearance of a competing mode near 3.75 THz at most cavity lengths, which likely corresponds to the simulated gain peak near 3.8 THz (in Fig. 2.23(d)). As the cavity length is varied, the observed polarization properties of the output beam are observed to vary. The left side of Fig. 2.24(a) plots the axial ratio and any changes in the axis of polarization corresponding to each sampled cavity length. The dotted lines in the figure illustrate which spectra is associated with the pair of data points.

While multiple factors can degrade the axial ratio, the primary concern must be towards deliberately suppressing the parasitic mode near 3.75 THz. It is noteworthy that any state in which the $\sim$3.75 THz mode is prominent does not have a large axial ratio. This is not surprising, since examination of Fig. 2.23(d) shows that the simulated gain peaks at 3.4 and 3.8 THz are expected to have nearly orthogonal polarizations. One way to suppress the undesired mode is by using an OC with a reflectance spectrum that only favors the desired frequency range. A measured transmittance spectrum of such an OC is shown in Fig. 2.24(b). At 3.4 THz, the OC transmittance is 12%. Meanwhile, at 3.75 THz, the transmittance is 42%. This makes the parasitic mode very lossy, and prevents lasing; QC-VECSELs have never been shown to lase with such low reflectance output couplers. On the other hand, a 12% transmittance roughly corresponds to 88% reflectance, which is sufficient for this metasurface. We observed that across any cavity length, the device remained single-mode near 3.4 THz. To ensure longitudinal modes are present near 3.75 THz, the cavity was made as long as 4 mm. The parasitic mode was never observed, and the lasing spectra for both sets is shown in Fig. 2.24(c). The axial ratio was 14 dB, and low axial ratio values seen in

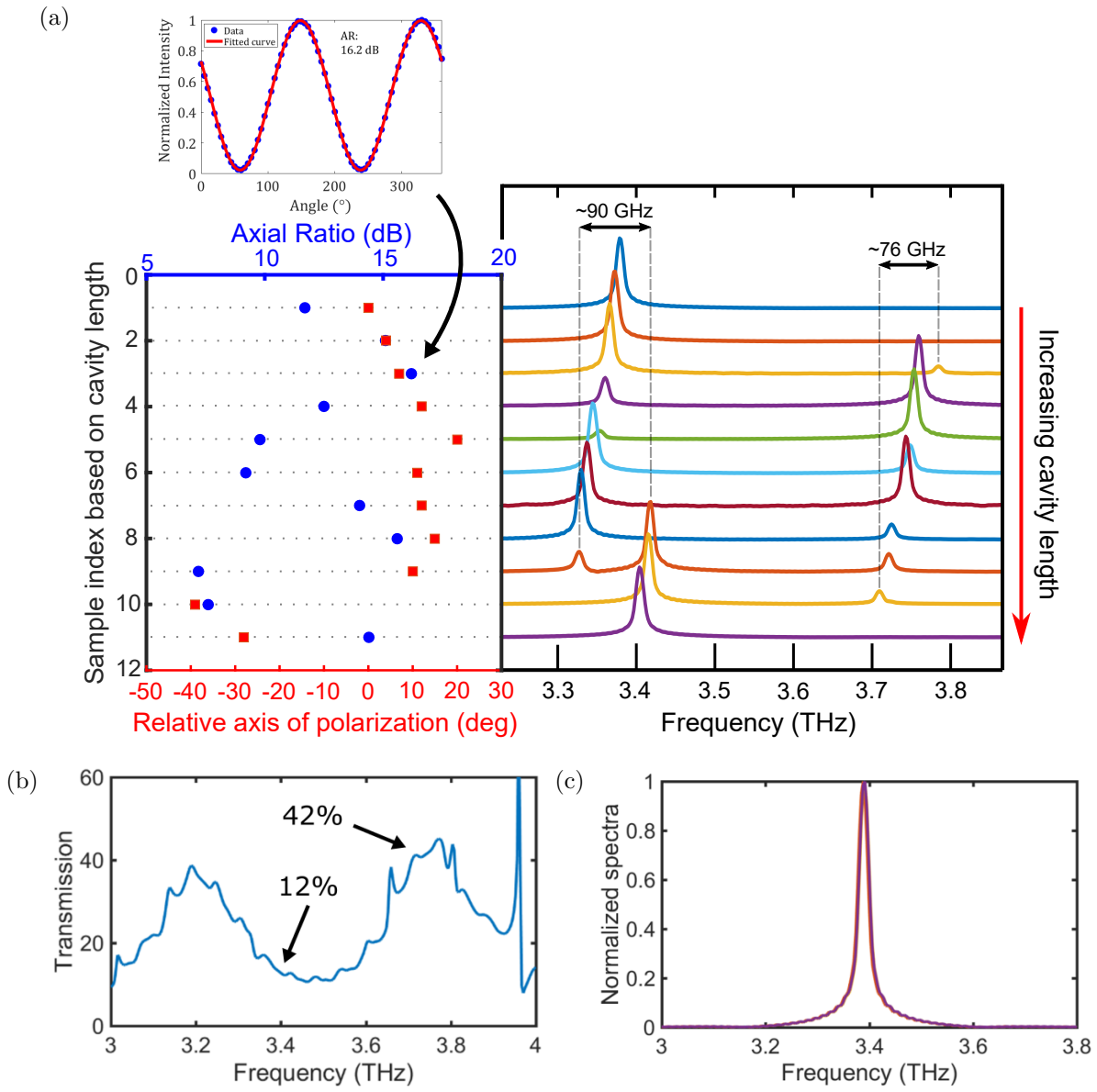

Figure 2.24: (a) Axial ratio and angle of polarization of emitted beam as the cavity length is varied. The corresponding spectra are shown on the right, with increasing cavity length going downward. The cavity length is approximately 1.7 mm. (b) Measured OC transmittance spectrum used to eliminate parasitic mode. (c) Measured emission spectra of both sets of antennas after the OC from (b) is used.

Fig. 2.24(a) were not observed. Thus, the output coupler was used not only as a partially transmitting mirror for light output, but also as a filter to discourage lasing of undesired modes.

CHAPTER 3

Designing metasurfaces for beyond 5 THz

As detailed in Section 1.2, QCLs are alternative LO candidates at frequencies beyond 2 THz; they have been used in the GREAT spectrometer and GUSTO/STO-2 to observe [OI] lines at 4.74 THz. However, beyond 5 THz, there is a technological gap in LO candidates, despite the regime being populated by astrophysically interesting lines such as [NIII] (5.23 THz), [SI] (5.32 THz), [FeI] (5.52 THz), [OIII] (5.79 THz), and [FeIII] (5.8 THz) [54].

The first demonstration of a THz QCL operating in continuous-wave above 5 THz was in 2022, with a maximum operating temperature of 15 K at 5.26 THz [130]. Since then, a metal-metal ridge waveguide operating up to 5.71 THz with a maximum operating temperature of 68 K was demonstrated [131]. The results were obtained by careful design of a GaAs/AlGaAs quantum-cascade active region, as well as the waveguide itself to minimize losses. Fig. 3.1 shows its power-current-voltage characteristics operating in both pulsed and cw at various temperatures. In cw, the device showed a maximum output power of 1 mW at 45 K, which was the lowest temperature able to be achieved using a Stirling cooler. The devices demonstrated broadband gain with various lasing modes observed spanning from $4.76 - 6.03$ THz in pulsed mode operation, and $4.95 - 5.71$ THz in cw.

In this section, we detail the design considerations and challenges associated with realizing a QC-VECSEL at higher frequencies. With access to a suitable active region, incorporating it into the QC-VECSEL architecture is a natural progression to realize a technology more suitable for a local oscillator, as it comes with the benefits of single-mode operation, scalable power output, high beam-quality, and frequency tunability [25].

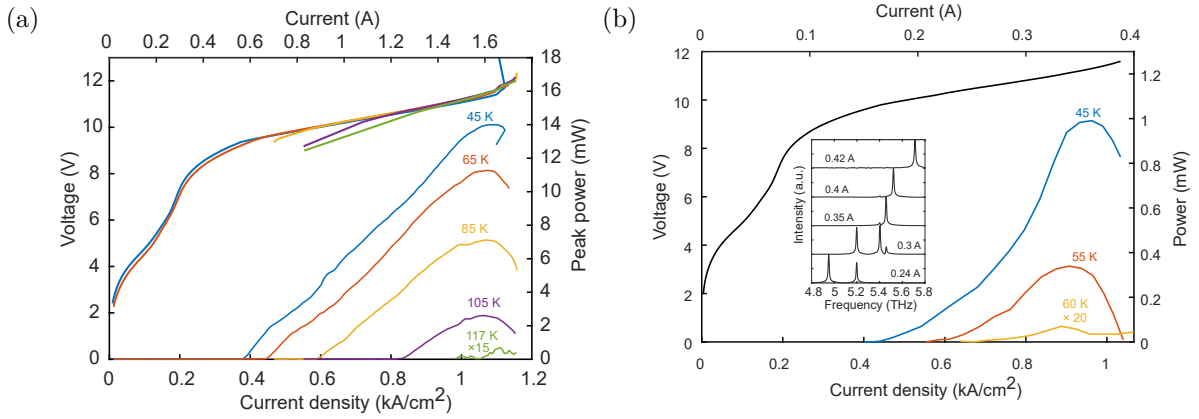

Figure 3.1: (a) Pulsed mode *L-I-V* curve of a 2 mm × 75 µm MM waveguide showing $T_{\max}$ of 117 K (b) Continuous-wave *L-I-V* of a 0.5 mm × 75 µm MM waveguide showing $T_{\max}$ of 60 K. The inset shows the cw spectra at 45 K. The figures are reproduced from [131] for the VB1401 D2 design.

3.1 Transparency gain and net amplification

3.1.1 The *Reststrahlen* band

To design QCLs above 5 THz, it becomes important to address the reduced gain and increased losses due to proximity to the *Reststrahlen* band of GaAs. This band is associated with strong reflection and absorption due to optical-phonon resonances in the 8-9 THz range. For the QC active region, the reduced gain is a consequence of increased thermally-activated electron-optical-phonon scattering of electrons from the upper state. This scattering rate is approximated as $\tau_{u\to l}^{-1} \approx W_{\text{hot}} \exp\{-(E_{\text{LO}} - h\nu)/(k_{\text{B}}T_{\text{e}})\}$. The closer the photon energy of the laser transition is to the longitudinal-optical (LO) phonon energy of GaAs — which is about 36 meV — the less in-plane momentum an upper-state electron needs to nonradiatively scatter down to the lower states.

Secondly, higher frequency also comes with increased material losses. This is primarily due to the rapidly increasing loss from GaAs TO and LO phonons, in addition to intersubband absorption in the active region. While the latter can be mitigated by proper QC design, as was demonstrated in Ref. [131], the former is an intrinsic property of the material

and cannot be eliminated. Using a multi-oscillator model, detailed in Refs. [120, 121], the complex permittivity of GaAs in the vicinity of the *Reststrahlen* band can be written as

$$\epsilon(\nu) = \frac{(\epsilon_0 - \epsilon_\infty)\nu_{\mathrm{TO}}^2}{\nu_{\mathrm{TO}}^2 - \nu^2 + 2i\nu\Gamma_{\mathrm{PH}}} + \frac{(\epsilon_\infty - \epsilon_{\mathrm{UV}})\nu_{\mathrm{VIS}}^2}{\nu_{\mathrm{VIS}}^2 - \nu^2 + 2i\nu\Gamma_{\mathrm{VIS}}} + \epsilon_{\mathrm{UV}}, \tag{3.1}$$

where ϵ_0 is the DC value, ϵ_∞ is the infrared value, ϵ_{UV} is the ultraviolet value, ν_{TO} is the transverse-optical (TO) phonon resonant frequency, ν_{VIS} is the visible oscillator frequency, Γ_{PH} is the damping coefficient of the optical phonons, and Γ_{VIS} is that of the visible. Using

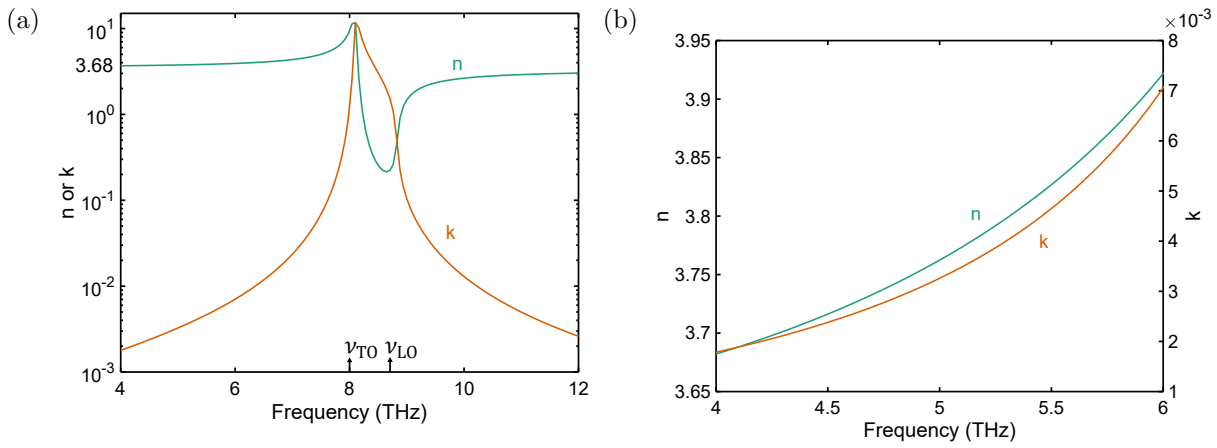

Figure 3.2: (a) Real and imaginary component of GaAs refractive index based on phonon oscillator model detailed in Ref. [120, 121]. (b) Zoomed in window in linear scale.

values $\epsilon_0 = 12.9$, $\epsilon_\infty = 10.86$, $\epsilon_{\mathrm{UV}} = 4.5$, $\nu_{\mathrm{TO}} = 270$ cm^{-1}, $\nu_{\mathrm{VIS}} = 23000$ cm^{-1}, $\Gamma_{\mathrm{PH}} = 0.8$, and $\Gamma_{\mathrm{VIS}} = 1$, the real and imaginary part of the refractive index is plotted in Fig. 3.2; n and k are defined as $\sqrt{\epsilon} = n - jk$. Plotting the zoomed window from 4–6 THz, Fig. 3.2(b) shows how much both n and k can vary in the frequency range of interest. Scaling the QC-VECSEL from 4 to 6 THz results in an increase in the material extinction coefficient by more than a factor of three. The zoomed window also shows the importance of incorporating the phonon absorption model into electromagnetic simulations in the design of a metasurface, since the index starts to significantly divert from the DC value of $\epsilon_0 = 12.9$.

3.1.2 Metasurface transparency gain and reflectance

In principle, scaling the metasurface to operate at higher frequencies is a straightforward matter of scaling the metasurface dimensions (e.g. width, period, height) by the wavelength. However, the solution is not so straightforward since losses and gain do not scale favorably. In particular, metallic loss makes it undesirable to scale down the metasurface active region thickness; however, if it is not scaled down, the radiative quality factor of the metasurface drops significantly, which in turn reduces the effective gain interaction length, ξ. This is exacerbated by the fact that ξ scales quadratically with wavelength, as was shown in Eq. (2.23). Ultimately, this results in a weaker metasurface amplification per reflection, and

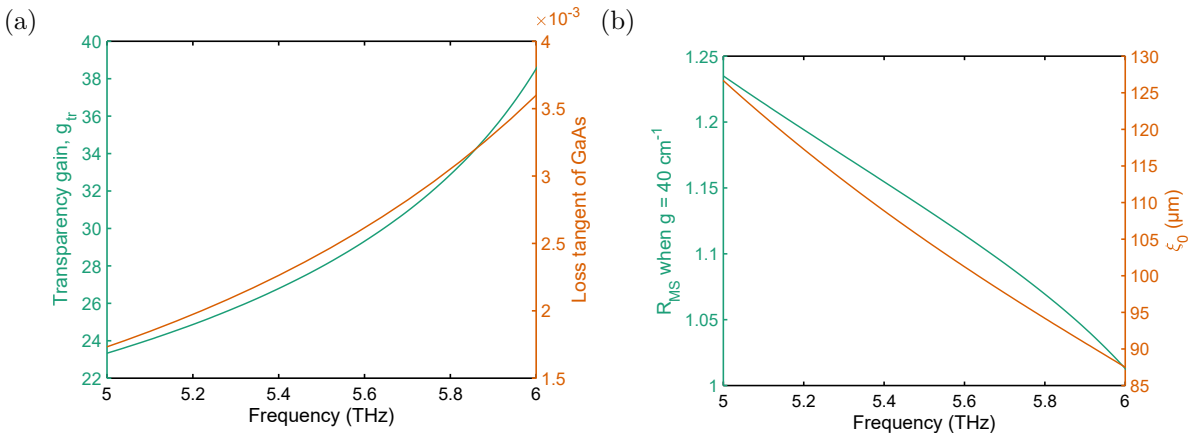

Figure 3.3: (a) Metasurface transparency gain versus design frequency. The fill factor is fixed at 15% to keep the period relative to the wavelength roughly constant. The material loss tangent is superimposed as reference. (b) The corresponding peak metasurface reflectance and effective interaction length versus design frequency. The reflectance values assume a flat gain of 40 cm^{-1}.

thus higher lasing thresholds. Fig. 3.3(a) shows the transparency gain of a metasurface as the design frequency is swept from 5 to 6 THz for a fixed active region height (7 μm) and a fixed fill factor (15%). The loss tangent of the underlying GaAs is superimposed for reference. The concomitant metasurface peak reflectance is plotted in Fig. 3.3(b), along with ξ_0. The reflectance values assume 40 cm^{-1} of spectrally flat gain is supplied by the material. The reduced R_{MS} demands more reflective OCs to maintain the same threshold gain — which,

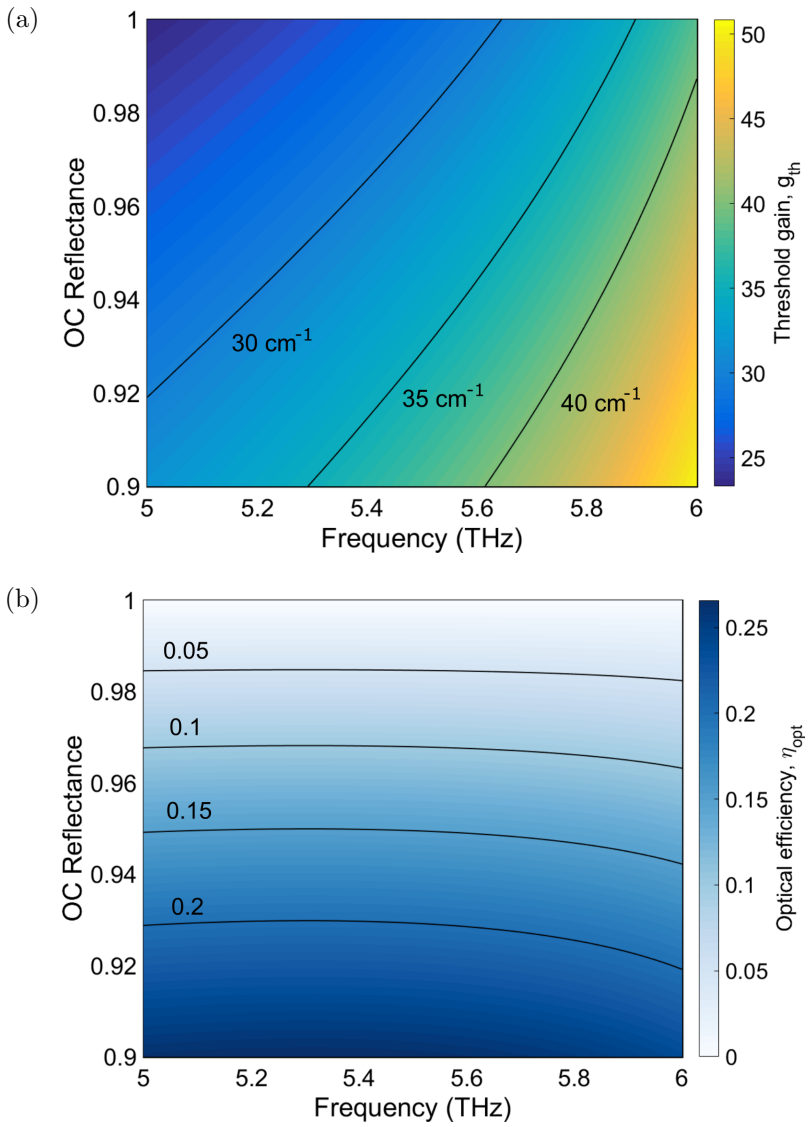

Figure 3.4: (a) Threshold gain versus OC reflectance and designed resonant frequency for a uniform ridge metasurface. The fill factor is fixed at 15%. The external cavity transmission is assumed to be unity. (b) Corresponding optical efficiency of the simulation performed in (a). The optical efficiency values refer only to what is obtained at the metasurface resonant frequency.

in turn, can result in lower power output. The color plot in Fig. 3.4(a) shows how g_{th} varies with both design frequency and OC reflectance. Contour lines are shown for $g_{\text{th}} = 30$ cm^{-1}, $g_{\text{th}} = 35$ cm^{-1}, and $g_{\text{th}} = 40$ cm^{-1}. For a given R_{OC}, the threshold increases rapidly due to both the increasing g_{tr} and decreasing R_{MS}. The accompanying color plot in Fig. 3.4(b)

shows the corresponding tradeoff with optical efficiency. Any reduction in efficiency due to absorption loss in the OC is not included. Note that these values are only for when the VECSEL operates at exactly the metasurface resonant frequency, and can substantially increase when the laser is detuned from resonance.

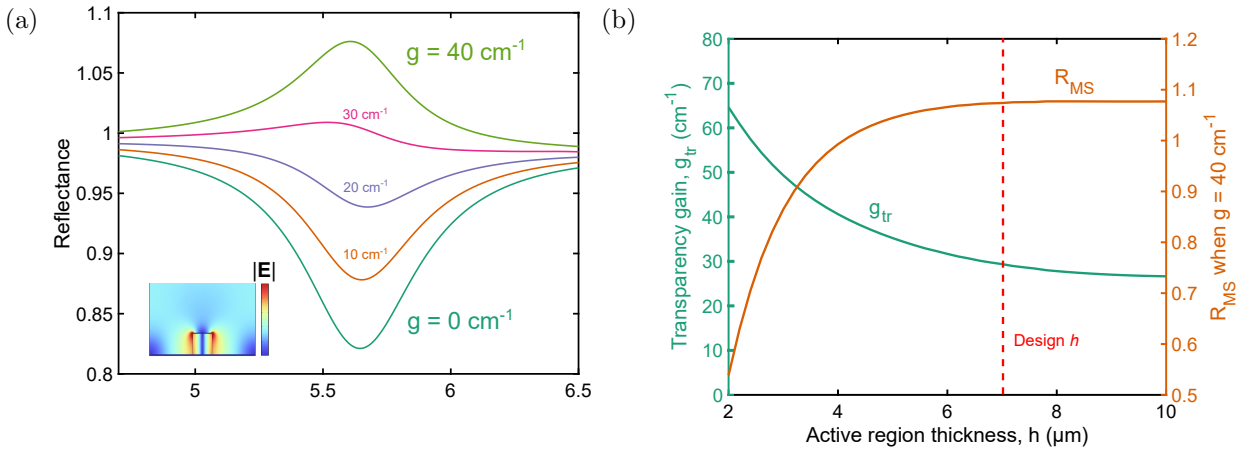

Figure 3.5: (a) Metasurface reflectance spectra for various levels of applied gain. Nominal design frequency is 5.65 THz. Parameters used are: $w = 6.53$ µm, $h = 7$ µm, and $\Lambda = 36$ µm. (b) Variation of transparency gain and peak metasurface reflectance versus active region thickness for the design shown in (a). The reflectance values assume an applied gain of 40 cm^{-1}.

If the active region height is scaled down in attempt to preserve the radiative quality factor of the metasurface, the metallic losses cause the transparency gain to be further reduced. This phenomenon was discussed in Section 2.4, but garners particular importance when designing beyond 5 THz due to the much larger g_{tr}. Consider a metasurface with a nominal design frequency of 5.65 THz. The reflectance spectra for various levels of applied gain are shown in Fig. 3.5(a). When the active region height is reduced from 10 to 2 µm, the g_{tr} and R_{MS} monotonically worsen, as depicted in Fig. 3.5. This occurs because the increase in g_{tr} as the thickness is reduced always outweighs the increase of radiative quality factor, which would aim to increase metasurface reflectance. However, if the thickness is made too large, the diminishing quality factor begins to have additional consequences. If h was wavelength scaled from the 4.7 THz design of Device D (from Section 2.6), then it

would result in a thickness of about 4 µm. Instead, the active growth thickness is increased to 7 µm, in which no further increase would be beneficial. Then, the accompanying issues acssociated with a low radiative quality factor are separately addressed.

3.2 Coupling to surface-propagating modes

When the active region thickness is not wavelength-scaled down with the other dimensions of the metasurface, the radiative quality factor scales down proportionally according to Eq. (2.21). Besides the reduced R_{MS}, the low Q_{r} increases the coupling strength with a surface-propagating mode associated with the second order Bragg condition, $\Lambda = \lambda_0$. Fig. 3.6 shows the eigenfrequency mapping with periodicity for four eigenmodes of an infinite uniform ridge metasurface. The solid curves correspond to frequency, and the color-corresponding dashed curves are the respective self-lasing thresholds. The green curve is the desired metasurface mode. As the period is increased, this mode hybridizes with the anti-symmetric Bragg mode (orange curve) and forms an anti-crossing. The importance of avoiding this regime of diffraction has been known, and has typically resulted in a rule of thumb stating $\Lambda < 0.8\lambda_0$. However, because the anti-crossing gap scales with Q_{r}, the restriction on Λ must be tightened.

To reveal the detrimental effects of coupling to the surface-propagating mode, it is not sufficient to perform a periodic simulation. This is because the energy in a surface-propagating wave in an infinite periodic structure is stored on the surface, and would produce a misleading large quality factor. However, in a realistic finite metasurface, like that illustrated in Fig. 3.7(a), surface-propagating energy is lost at the edges. A simulation is performed for a 1 mm long metasurface with a central 0.5 mm bias region. The threshold gain, assuming a PEC output coupler, is plotted for the case of both a 5 µm and 7 µm thick active region in Fig. 3.7(b). Initially, the threshold gain slowly decays due to the gradually increasing metasurface reflectance with larger period. However, as the period gets past ∼40 µm, the threshold gain begins to rapidly increase. The critical period at which this occurs is different

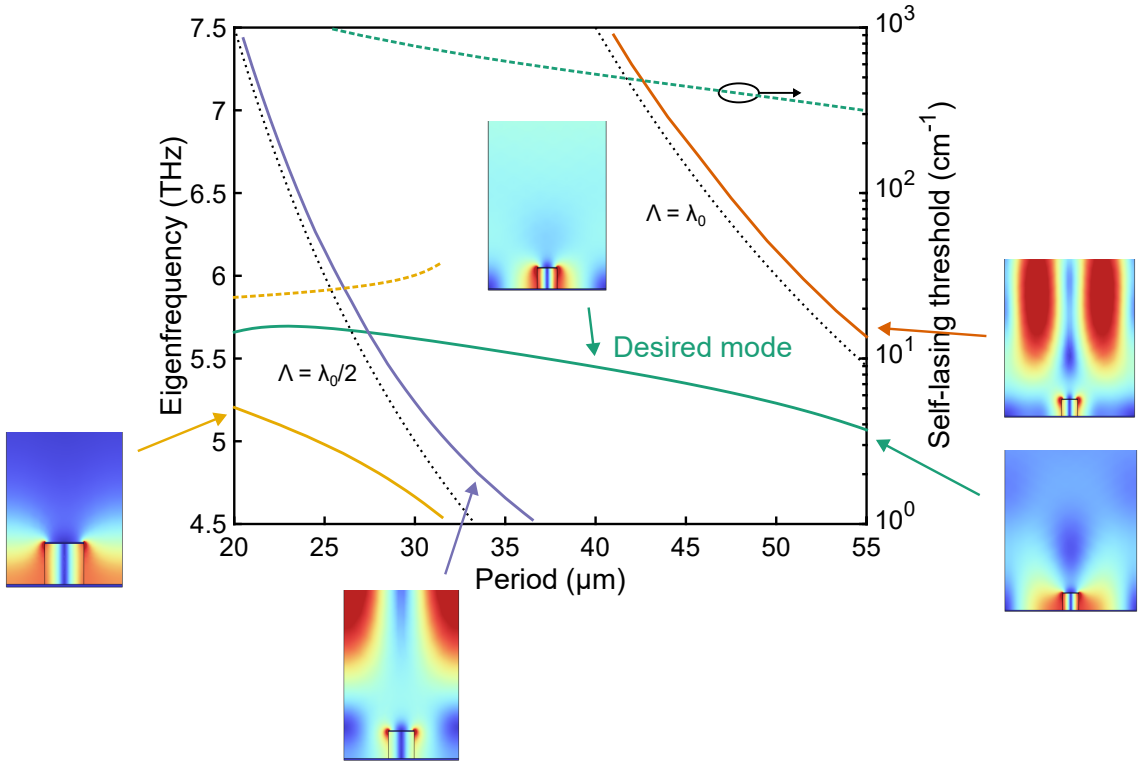

Figure 3.6: FEM simulation of eigenfrequency versus period for four eigenmodes of interest. The top boundary is set to be a scattering boundary condition. The dashed lines of the corresponding colors represent the self-lasing threshold. The green curve is the desired metasurface mode. The orange curve corresponds to the surface-progating mode that couples with the desired mode. The yellow curve shows the anti-symmetric dark mode detailed in Section 2.3.2.

between the two active region thicknesses because of the difference in the coupling strength between the desired VECSEL mode and the surface-propagating mode. In other words, the threshold gain before this critical period is limited by the material losses. A simulation is shown in Fig. 3.7(c) for the 7 μm case in which excess loss is added to the unbiased ridges. We can see that the inclusion of extra loss only has an effect in the smaller period regions, since beyond $\Lambda \sim 40$ μm, the threshold becomes limited by the surface-propagating mode and less dependent on material losses.

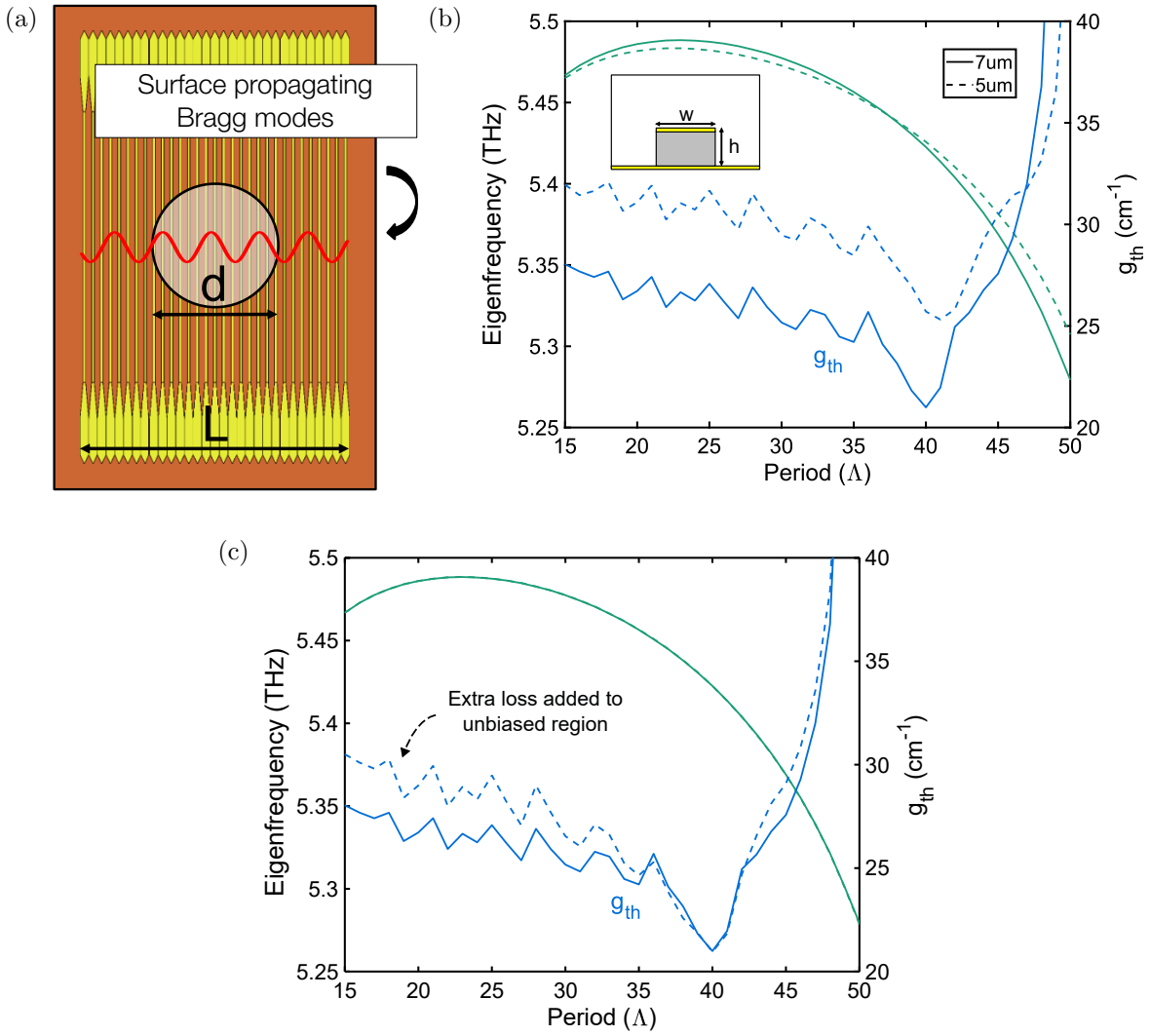

Figure 3.7: (a) Schematic of a metasurface labeling the bias diameter, d, and the metasurface length, L. The red waveform depicts the surface-propagating mode that extends beyond the bias region and scatters at the edges of the metasurface. (b) FEM simulation of a finite dimension VECSEL for the case of $h = 7$ µm and $h = 5$ µm. Both the eigenfrequency and threshold gain are plotted as a function of the period. The top boundary is set as a PEC boundary condition. The parameters used are $w = 6.72$ µm, $d = 0.5$ mm, and $L = 1.0$ mm. (c) FEM simulation of a finite VECSEL for $h = 7$ µm and additional loss added to the unbiased ridges. The solid curve is the same as that in (a) and shown for reference.

3.3 Experimental results

A series of metasurfaces designed for 5+THz operation were fabricated with periodicities ranging from 36–44 µm. Five different metasurfaces with $\Lambda \geq 40$ µm were tested as VECSELs and all five failed to demonstrate any signs of lasing. All tests were attempted at LHe temperatures with a short tunable cavity architecture. This is most likely due to the excess loss from coupling to surface-propagating modes as described in Section 3.2. The only successful metasurfaces that were tested had $\Lambda = 36$ µm, which is about 65% of the free space wavelength. This section presents the results obtained from the two devices, Device E and Device F. A summary of the device characteristics is presented in Table 3.1.

Table 3.1: 5+THz device characteristics for results shown in Section 3.3

Device	Design ν	w / h / Λ (µm)	Bias diam.	Tuning range	Output coupler
E	5.65 THz	6.53 / 7 / 36 (FF:18%)	0.540 mm	5.40 - 5.72 THz	0.99 (OC 1)
F	5.45 THz	6.81 / 7 / 36 (FF:19%)	0.540 mm	5.35 - 5.60 THz	0.976 - 0.983 (OC 2)

3.3.1 Device E: 5.65 THz design

Device E has a nominal design frequency of 5.65 THz. The antenna width is 6.53 µm and the period is 36 µm, resulting in a fill factor of 18%. The metasurface is incorporated into a tunable VECSEL configuration using a piezoelectric stepper motor as described in Section 2.6. The cavity length is made to be as short as possible, and is limited by the height of the wirebonds. A series of spectra is collected using an FTIR as the output coupler is discretely stepped away from the metasurface. The attocube motor controller voltage was set to 55 V, which heuristically corresponds to about 1 µm steps. Fig. 3.8(a) shows the tuning characteristic as the cavity length is swept across three FSRs. For each longitudinal order, the tuning was limited by the thresold gain bandwidth, and mode-hopping was never

observed. The arrows indicate regions in which lasing was extinguished — such spectra are not plotted in this figure, and plotting is resumed as soon as measurable spectra are detected. Surprisingly, the continuous tuning bandwidth was smaller for the shortest cavity lengths. The longitudinal order $m = m_0$ corresponds to the smallest longitudinal order that was experimentally achievable. The widest tuning bandwidth was achieved by stepping the output coupler out to $m = m_0 + 2$, in which ∼320 Hz (5.8% fractional) of tuning was observed. This result is separately plotted in Fig. 3.8(b).

A representative *L-I-V* curve at the maximum power output frequency (5.59 THz) within the $m = m_0+2$ tuning range is shown in Fig. 3.8(c). The laser was driven with 80 kHz pulses at 4% duty cycle. The pulser was electrically gated at 5 Hz. The measured threshold current density is 867 mA/cm^2. The maximum power output, correcting for the 41% transmission of the 3 mm thick HDPE window, was measured to be 66 µW. The power was measured with a pyroelectric detector (label: Gentec A) separately calibrated against a thermopile using a 3.4 THz VECSEL with higher output power. Additionally, a representative *L-I-V* curve is shown in Fig. 3.8(d) when the device is operated in the $m = m_0$ longitudinal order. When the cavity length is made too short, higher-order transverse modes begin to lase, and the device demonstrates multi-moding. This comes with worse beam shapes and less power collected [30].

The threshold current density is extracted from the IV curves as the device is tuned and is plotted against emission frequency in Fig. 3.9(a). The threshold is observed to increase monotonically with frequency. Since the output coupler reflectance spectrum is quite flat, as can be seen in Fig. 3.9(b), the changing threshold is primarily due to the metasurface reflectance lineshape. The data suggests the reflectance peak is closer to 5.5 THz, rather than the nominal 5.65 THz design frequency. As the laser is detuned, the threshold increases due to the decreasing R_{MS}, and consequently a higher power output. The lack of symmetry in the threshold plot can be explained by insufficient gain at lower frequencies. Although broadband gain was demonstrated for this material spanning from 4.76–6.03 THz, they were obtained by MM waveguides which had much lower thresholds. This allowed the MM

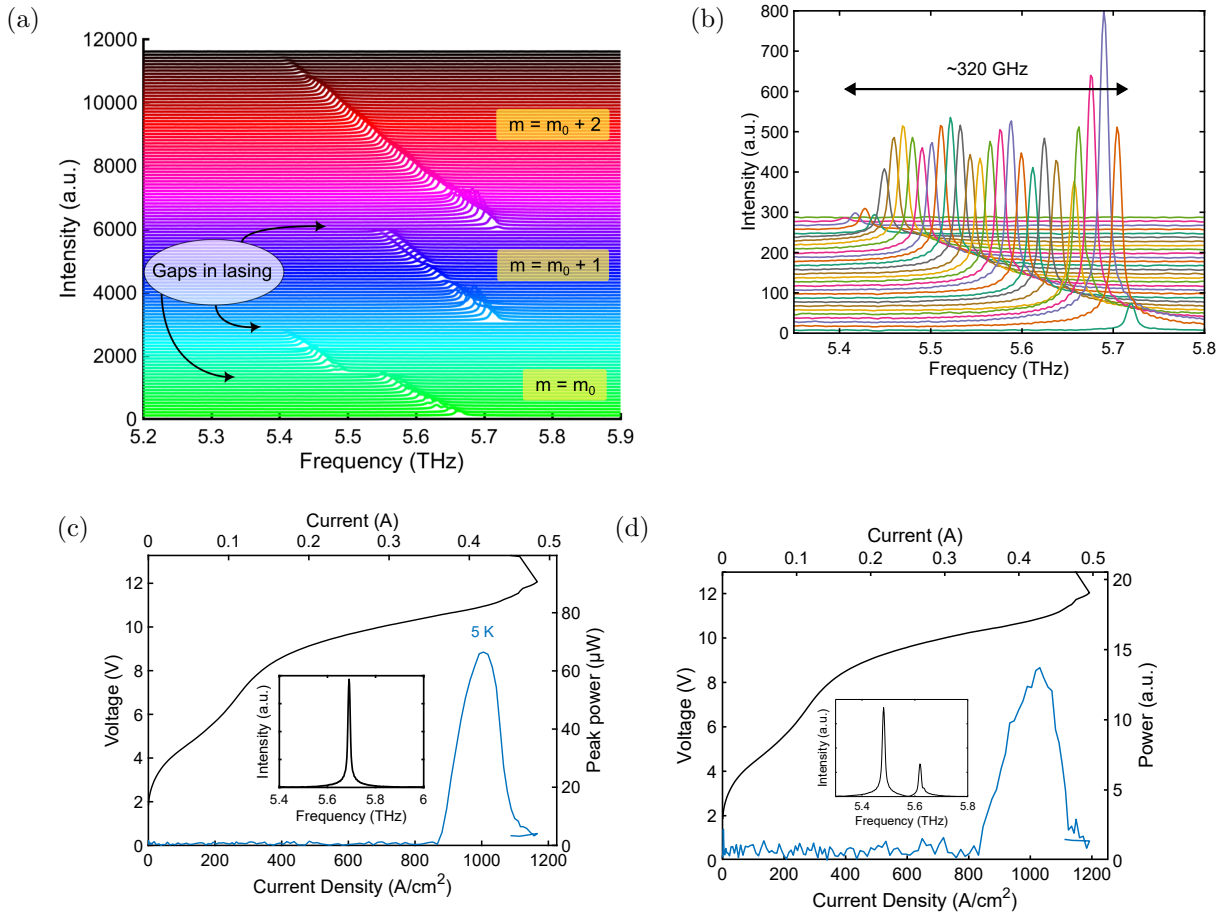

Figure 3.8: (a) Tuning spectra of Device E over three longitudinal mode orders. Starting from bottom up, lasing spectra are sequentially collected as the output coupler is stepped incrementally away from the metasurface using an attocube piezoelectric stepper motor and controller. The attocube controller voltage is set to 55 V, which has heuristically corresponded to ~ 1 µm. The arrows point to regions where the laser was extinguished and are not shown in this plot. (b) Tuning spectra of the $m = m_0 + 2$ mode shown in (a). A 320 GHz tuning bandwidth is achieved. (c) Representative *L-I-V* curve at $m = m_0 + 2$. (d) Representative *L-I-V* curve at $m = m_0$. Data shown in this figure is collected at 5 K heatsink temperature and in pulsed mode operation (4% duty cycle at 80 kHz repetition rate).

waveguides to operate at a lower bias where the gain is peaked at lower frequencies [131].

A set of temperature dependent *L-I-V* is collected, and a $T_{\max}$ of 50 K is measured in pulsed mode. The temperature values refer to the heatsink temperature as the device was warmed up by evacuating the LHe from the cryostat reservoir. Fitting the data to the

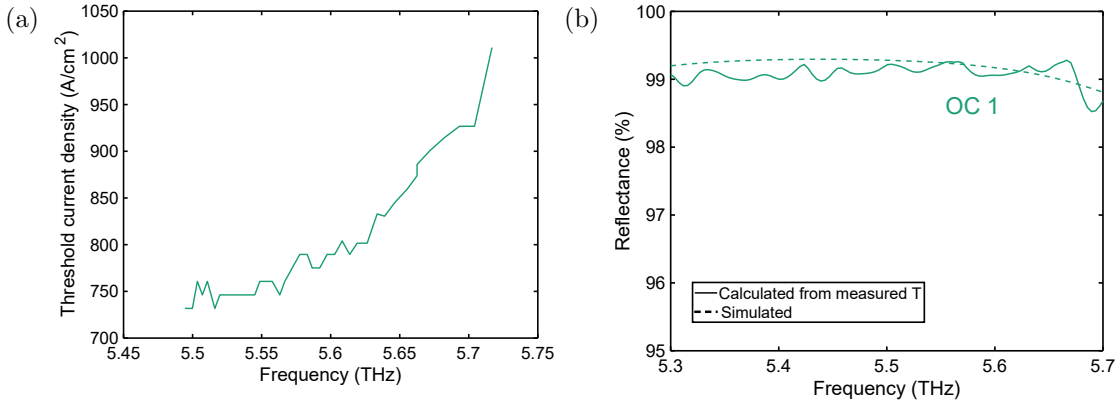

Figure 3.9: (a) Threshold current density versus emission frequency as the cavity length. The threshold values are extracted from the collected IV curves as the device is tuned. (b) Reflectance spectrum of OC 1. The dashed curve shows simulated values. The solid curve is obtained from calculating the reflectance based on a measured transmittance spectra and simulated absorptance.

empirical relation $J_{\text{th}} = J_0 \exp(T/T_0)$, as performed in Fig. 3.10(b), we obtain $T_0 = 161$ K and $J_0 = 726$ mA/cm^2. For comparison, the MM waveguide had $T_{\text{max}} = 117$ K and characteristic temperature $T_0 = 63$ K. The difference in T_{max} between the VECSEL and the waveguide laser is 67 K. Though this difference is expected due to the higher loss present in the VECSEL, the difference is larger than previously observed devices at 2.7 THz and 3.4 THz [108], which had differences of 41 THz and below. This suggests that the VECSEL architecture above 5 THz fundamentally has more loss beyond just the increased material losses — possible reasons for which were discussed in the preceding sections. Additionally, in the provided temperature range, the peak power has a nearly linear relationship with temperature. This is a result of the threshold having an approximate linear relationship with temperature in this range, while the slope efficiency remains relatively unchanged.

3.3.2 Device F: 5.45 THz design

Device F was observed to have a higher power output at the expense of a smaller tuning bandwidth. The metasurface has an identical period of $\Lambda = 36$ µm but a smaller antenna width of 6.81 µm which aims at a nominal resonant frequency of 5.45 THz. The simulated

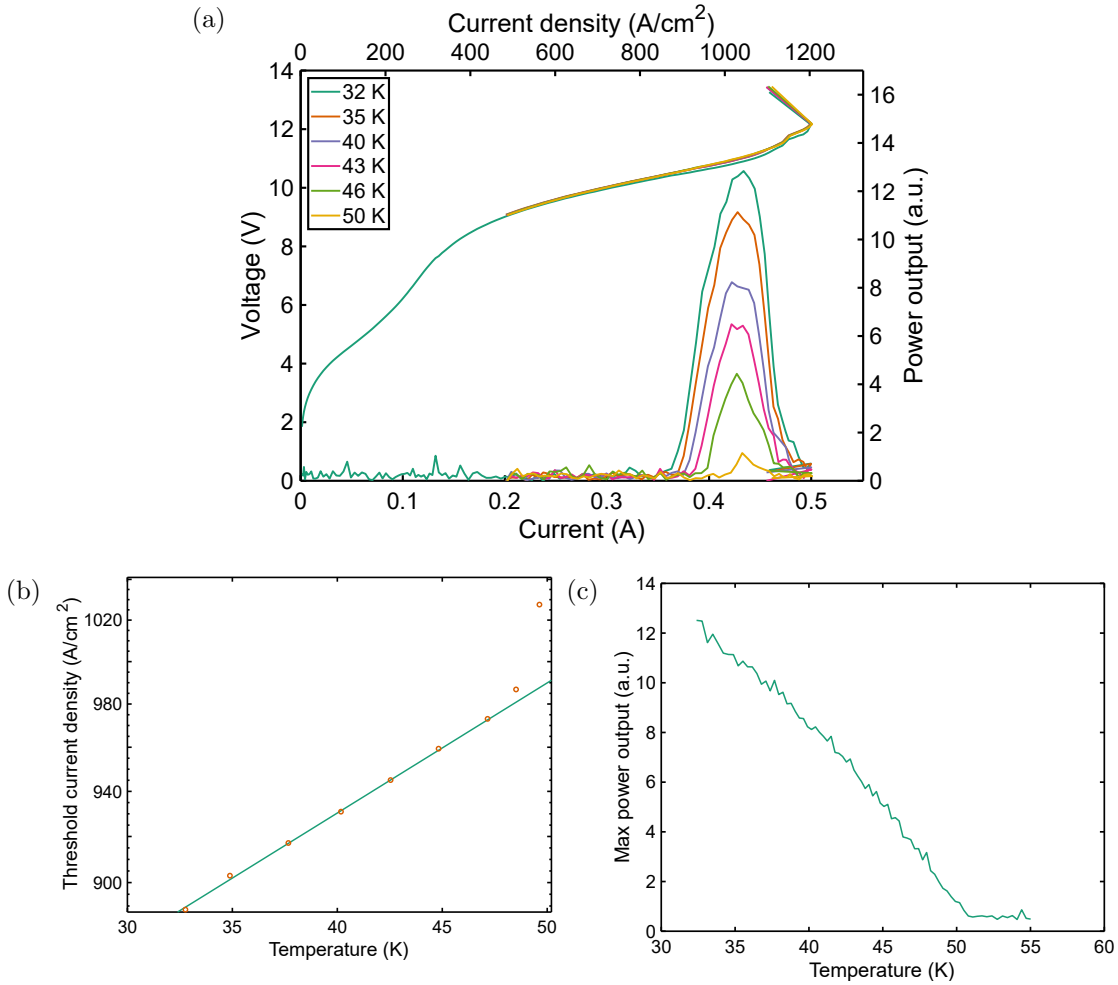

Figure 3.10: (a) Temperature dependent *L-I-V* curves in pulsed mode operation (4% duty cycle at 80 kHz repetition rate). Maximum operating temperature is 50 K. $T_0 = 161$ K and $J_0 = 726$ mA/cm^2. (b) Measured threshold current density as a function of heatsink temperature. (c) Relative power output as a function of heatsink temperature.

reflectance spectra are shown in Fig. 3.11(a). A peak power output of 1.3 mW is measured at 5.52 THz. Fig. 3.11(b) shows the *L-I-V* curve in pulsed mode with 10 kHz repetition rate and 1 µs pulse width. A tuning range of ∼250 GHz is observed ranging from 5.35 THz to 5.6 THz. A relative power output versus emission frequency is plotted from the FTIR data and is shown in Fig. 3.12(a). Again, the tuning bandwidth is threshold-limited, and no mode-hopping was observed. The dips in the power correspond to water absorption lines as can be seen from the superimposed HITRAN data of transmission through water vapor at

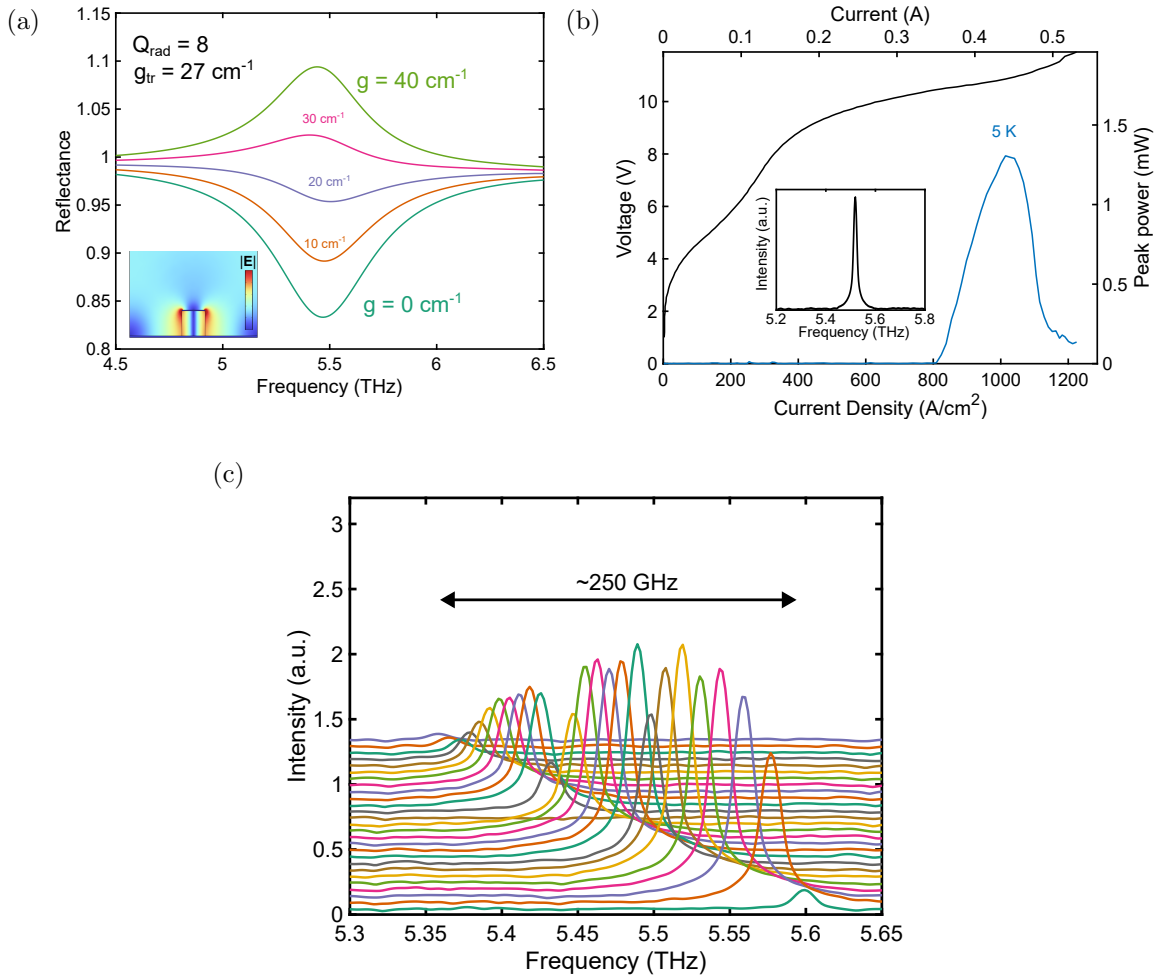

Figure 3.11: (a) Reflectance spectra for various levels of applied gain for a nominal design frequency of 5.45 THz. The inset shows the electric field magnitude of a unit cell. (b) Device F *L-I-V* curve corresponding to 5.52 THz emission frequency collected at 5 K heatsink temperature. A peak power of 1.3 mW is obtained correcting for the 41% transmission of the cryostat HDPE window. (c) Tuning spectra for Device F showing a tuning range between 5.35–5.60 THz, corresponding to a 250 GHz tuning bandwidth

30% RH. The power output initially grows with frequency as the laser is detuned from the metasurface resonance towards regions with smaller ξ and thus higher slope efficiency. The power then eventually decays and lasing is extinguished due to the increasing threshold. This is exacerbated by the decrease in OC reflectance (OC 2) above 5.5 THz (see Fig. 3.12(b)). While a full threshold mapping with frequency was not collected for this device, Fig. 3.12(c) shows a few representative *L-I-V* curves with their corresponding spectra (Fig. 3.12(d))

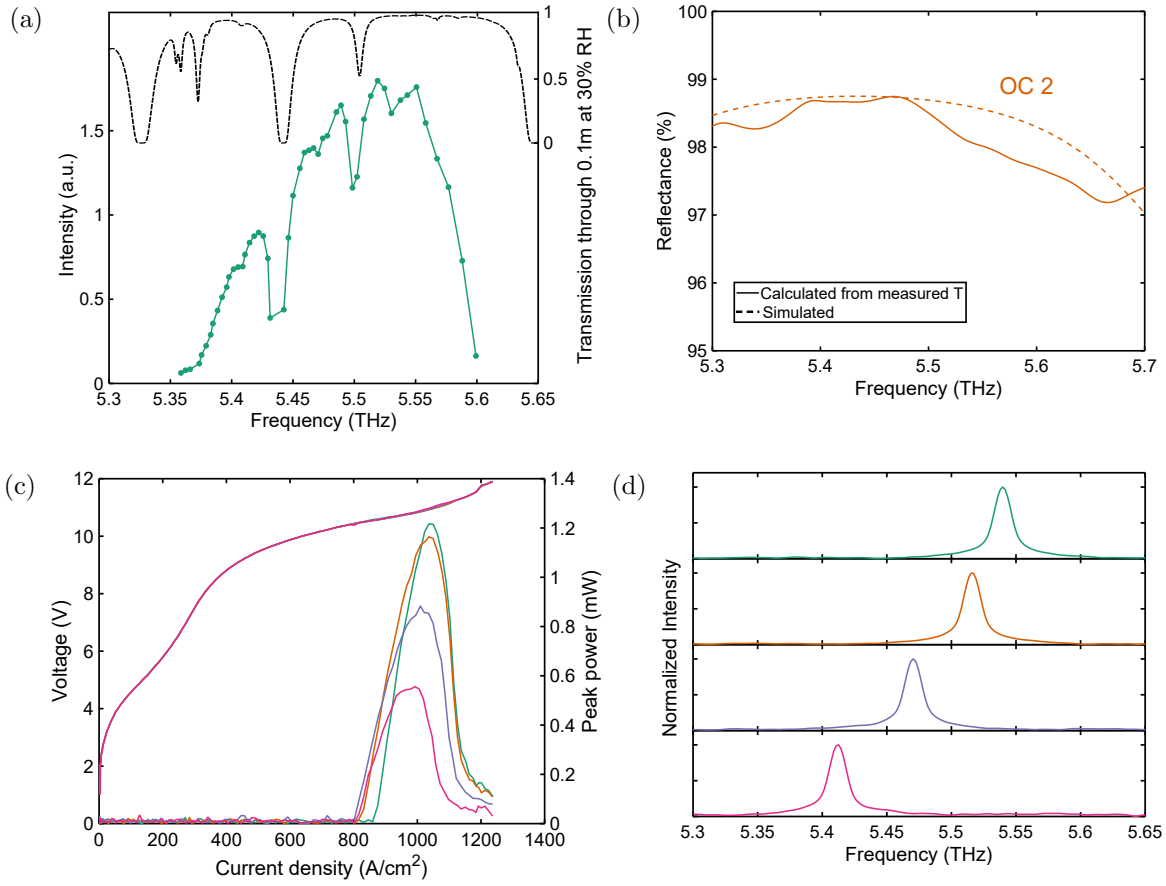

Figure 3.12: (a) Relative intensity versus emission frequency measured via FTIR. A water transmission spectrum produced from HITRAN data is superimposed on the graph. The dips in the power spectrum agree well the water absorption lines. (b) Reflectance spectrum of OC 2. The dashed curve is a simulation including loss in the metal and quartz substrate. The solid curve is calculated from a measured transmittance and a simulated absorption spectrum. (c) *L-I-V* curves for select points in the tuning bandwidth. The curves are color-coded with their corresponding emission spectrum shown in (d).

throughout the tuning bandwidth. Once again, the threshold is seen to increase with emission frequency. The $T_{\max}$ for this device was measured to be roughly 47 K, as demonstrated in Fig. 3.13. It is probable that the $T_{\max}$ may be closer to that of Device E if the pulse width used was 500 ns rather than 1 µs. Nevertheless, the max power output of Device F was a factor of 20 higher than Device E. Yet, the $T_{\max}$ is roughly the same. This means that Device F has inherently less loss associated with the metasurface, and most likely stems from the smaller

antenna width that reduces the surface-mode coupling. This allows a higher transmissive OC to increase the slope efficiency, but still maintaining the same overall cavity losses.

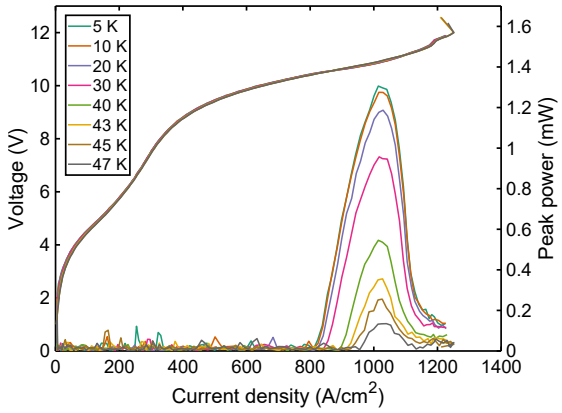

Figure 3.13: Temperature dependent *L-I-V* curves for Device F in pulsed mode operation with a 10 kHz repetition rate and 1 µs pulse width.

A few beam profile cross-sections are measured at various cavity lengths in both X and Y directions, where X is the direction of the metasurface periodicity. The 1D cuts are shown in Fig. 3.14. The top row corresponds to the x-cuts, and the bottom row corresponds to the y-cuts. The measurements are performed using a pyroelectric detector (label: Gentec A) with a 1 mm diameter pinhole aperture mounted on a travel stage that is translated manually via a micrometer. The detector is about 3 ∈ away from the lasing aperture. Each row shows beam profiles for increasing cavity length from left to right, roughly separated by half-wavelength distances. The beam shapes improve as the cavity length gets longer, because the thresholds of higher-order transverse modes increase faster than that of the fundamental. The ideal FWHM of a Gaussian beam at a wavelength of 55 µm is about 5.8 mm assuming a unity M^2. At the $m = m_0 + 2$ longitudinal order, the measured FWHM along the x-direction is 7.34 mm, and 5.80 mm in the y-direction. The beam has slight asymmetry, with the x-direction having a wider beam. This can be explained by the direction of periodicity being along x, causing any diffraction-associated beam degradation to only be along this direction.

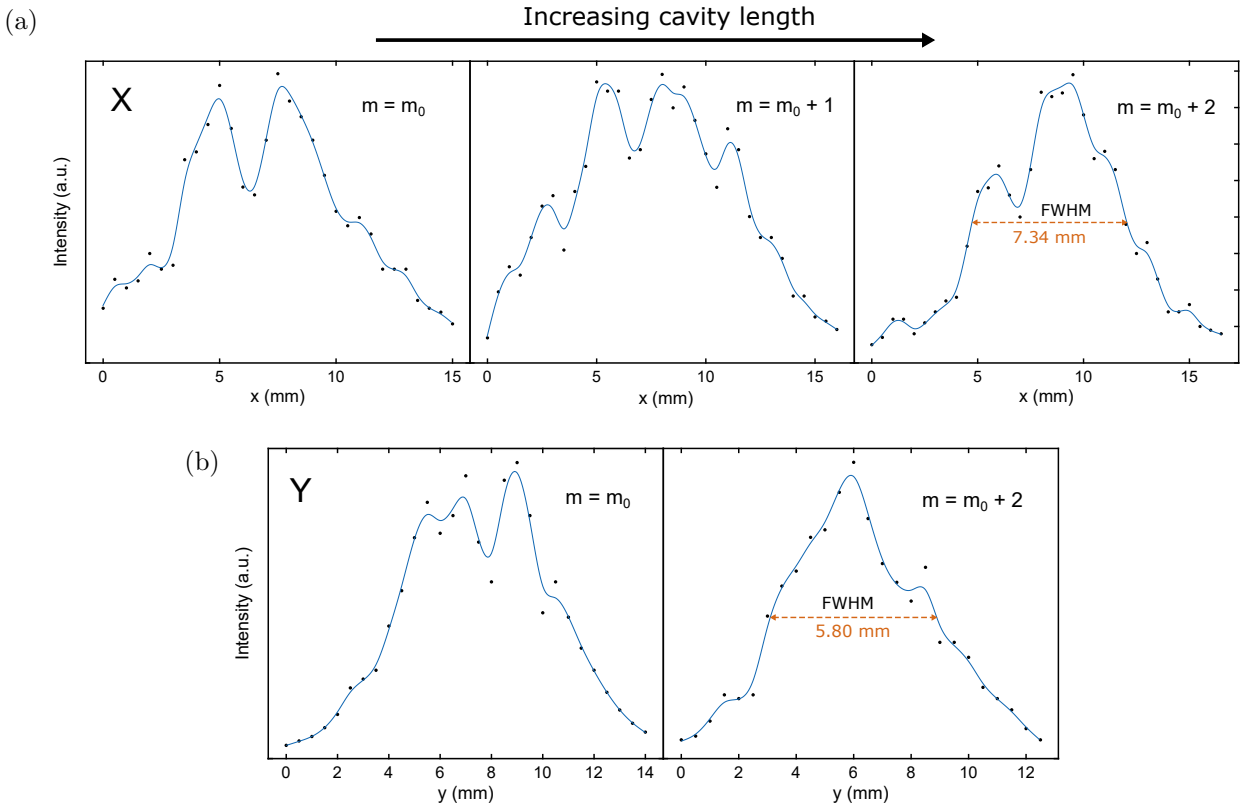

Figure 3.14: 1-dimensional intensity profile of Device F. The top row is the profile in x, which is the direction of metasurface periodicity. The bottom row is the profile in y. From left to right is increasing cavity length by longitudinal orders; m_0 corresponds to the smallest longitudinal order and the shortest cavity length. The orange arrow in the $m = m_0 + 2$ case labels the full-width half-maximum of the beam profile.

3.4 Discussion and future designs

To optimize the QC-VECSEL, we must first understand what factors are limiting its performance in terms of overarching parameters. Consider the case of the MM waveguide demonstrated in Fig. 3.1(a). The slope efficiency of the laser can be approximated using Eq. (2.25), where

$$\eta_{\text{opt}} = \frac{\alpha_{\text{m}}}{\alpha_{\text{m}} + \alpha_{\text{w}}}, \tag{3.2}$$

where α_{m} and α_{w} are the mirror and waveguide losses respectively. At 45 K, the pulsed threshold current density is 383 mA/cm^2, corresponding to a threshold current of 575 mA.

Using standard formalism for a homogeneously broadened gain medium, we can write the relationship between threshold gain and threshold current density as

$$J_{\mathrm{th}} = \frac{g_{\mathrm{th}} e L_{\mathrm{p}}}{\sigma \tau_{\mathrm{eff}}} + J_{\mathrm{leak}}, \tag{3.3}$$

where L_{p} is the length of each QC module, σ is the stimulated emission cross-section, τ_{eff} is the effective population inversion lifetime, and J_{leak} is the sub-threshold leakage current of the device [114]. The threshold gain of a symmetrical MM ridge laser, assuming unity confinement factor, can be written as

$$g_{\mathrm{th}} = \frac{1}{L} \ln R_{\mathrm{MM}}^{-1} + \alpha_{\mathrm{w}}, \tag{3.4}$$

where L is the length of the ridge, and R_{MM} is the reflectance of each facet. The first term in Eq. (3.4) is equal to the mirror loss, α_{m}. Based on information provided in Ref. [131], we obtain $\alpha_{\mathrm{w}} = 21.2$ cm^{-1} and $\alpha_{\mathrm{m}} = 2.81$ cm^{-1}, which assumed a simulated R_{MM} value of 0.57 for a 75 µm wide MM facet. This results in a threshold gain of $g_{\mathrm{th}} = 24.0$ cm^{-1}, and an optical efficiency of $\eta_{\mathrm{opt}} = 0.12$. The measured slope-efficiency at 45 K is about 14.1 mW/A. However, taking into account the power output from the other facet, and transmission through a 3 mm thick HDPE window, the slope-efficiency is closer to $\mathrm{d}P/\mathrm{d}I = 56.4$ mW. Then, using Eq. (2.25), we can approximate the internal quantum-efficiency as $\eta_{\mathrm{i}} = 0.17$, assuming $N_{\mathrm{p}} = 127$ and $\nu = 5.45$ THz.

We now ascertain the theoretical limits of the QC-VECSEL performance based on the MM waveguide results and compare it to the experiment. The main difference is in the optical efficiency, which for a QC-VECSEL, is given by Eq. 2.26. Assuming an internal quantum efficiency of $\eta_i = 0.17$, and negligible leakage current J_{th}, we can simulate the QC-VECSEL slope efficiency versus R_{OC}. The plot in Fig. 3.15(a) includes levels of transparency gain larger than the initial simulated value of $g_{\mathrm{tr}} = 27$ cm^{-1} to better understand how the presence of additional loss will affect the overall device performance. For a high reflectance OC, the slope efficiency is less sensitive to changes in g_{tr}. Indeed, the slope efficiency is maximized if

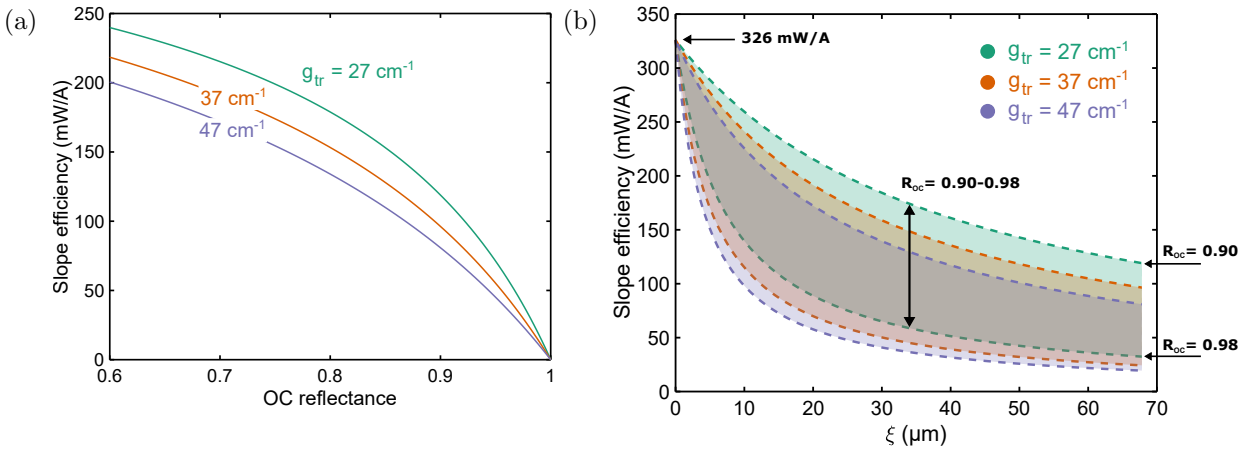

Figure 3.15: (a) Simulated slope efficiency versus OC reflectance for $g_{\mathrm{tr}} = 27$ cm^{-1}, 37 cm^{-1}, and 47 cm^{-1} for Device F. Other input parameters are $N_{\mathrm{p}} = 127$, $\nu = 5.45$ THz, and $\eta_i = 0.17$. (b) Slope efficiency versus ξ for various g_{tr} and R_{OC} ranging from 0.90 to 0.98. The slope efficiency when $\xi = 0$ corresponds to the theoretical maximum achieved by a unity optical efficiency.

the optical efficiency is unity, which occurs when R_{OC} is zero. Alternatively, the efficiency increases as the VECSEL is detuned from the metasurface resonance due to the reduction in ξ. This is shown in Fig. 3.15(b) depicting the slope efficiency as ξ is varied from 0 to 68 µm (corresponding to the peak ξ_0 for the metasurface in Device F). A theoretical maximum of 326 mW/A is calculated for this design. Unfortunately, such a value is inaccessible in reality since it requires either zero material loss, or infinite gain. The slope efficiency for Device F is about 19 mW/A, which corresponds to an optical efficiency of $\eta_{\mathrm{opt}} = 0.06$. This is significantly lower than the MM waveguide which had a slope efficiency of 56.4 mW. This is because an unexpectedly large threshold gain forced the use of very high reflectance OCs, which drastically reduces η_{opt}. This combined effect is readily observed in the simulated power output shown in Fig. 3.16(a), where a large g_{tr} limits both how transmissive the OC can be, and how much power is out-coupled. The experimental results suggest g_{tr} values closer to 47 cm^{-1}. Fig. 3.16(b) illustrates how the power output and WPE changes with detuning. It also demonstrates how the tuning bandwidth is affected by the choice of R_{OC}, since a high R_{OC} can tolerate small ξ. However, when g_{tr} is large, the maximum power

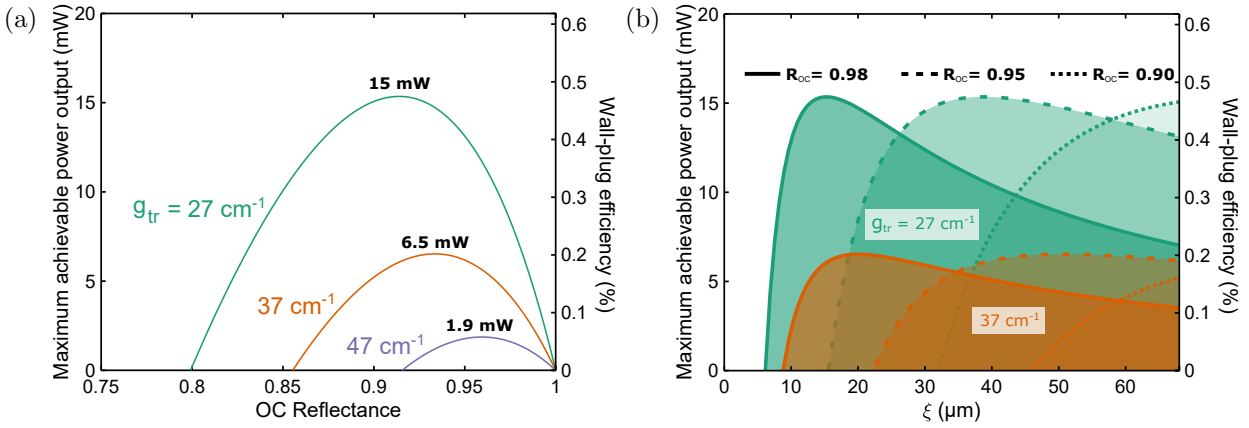

Figure 3.16: (a) Simulated maximum achievable power output versus OC reflectance for Device F. The input parameters are the same as those used in Fig. 3.15. A maximum current of $I_{\max} = 435$ mA is assumed based on the measured I-V. (b) Simulated maximum achievable power output versus ξ for $g_{\text{tr}} = 27$ cm^{-1} and 37 cm^{-1} for OC reflectances $R_{\text{OC}} = 0.98$, 0.95, and 0.90.

output becomes less dependent on R_{OC}, since the gain threshold becomes dominated by metasurface losses.

The simulations show that Device F power output and WPE may be improved by an order of magnitude. This QC-VECSEL had a lower slope efficiency than the MM waveguide laser, yet also had a higher threshold current density. This makes clear that the most important factor in improving the 5+THz QC-VECSEL performance is to overcome the excess losses introduced by the architecture including coupling to surface modes as described in Section 3.2, and external cavity diffraction loss. Steps towards this goal include smaller period metasurfaces, focusing metasurfaces [106], and OAP-cavity VECSELs [111].

CHAPTER 4

Terahertz self-mixing interferometry and study of optical feedback

4.1 Introduction

4.1.1 Basic principle of the self-mixing effect

Self-mixing (SM) interferometry within terahertz (THz) quantum-cascade lasers (QCLs) has garnered significant attention in the past decade for various sensing applications. In SM interferometry, the output beam of a laser is intentionally reinjected back into the laser cavity, which coherently perturbs both the amplitude and phase of the intra-cavity field. The reinjected beam contains information regarding its journey, which it then imparts onto the laser's measurable properties such as its power output and terminal voltage. When the feedback power is sufficiently low, the effect can be understood by the vector diagram shown in Fig. 4.1. If $\mathbf{E}_0$ represents the intracavity field, then the reinjected radiation $\mathbf{E}_{\mathrm{FB}}$ acts as a perturbation of the intrinsic intracavity field. Then, the in-phase component of the reinjected field, $E_{\mathrm{FB}} \cos \phi_{\mathrm{FB}}$, acts as an amplitude modulation term, while the quadrature component, $E_{\mathrm{FB}} \sin \phi_{\mathrm{FB}}$, acts as a frequency modulation. While this is an intuitive way to understand the self-mixing effect, it begins to lose its validity at higher levels of feedback due to the more complex nonlinear dynamics induced by the amplitude-phase coupling of the laser.

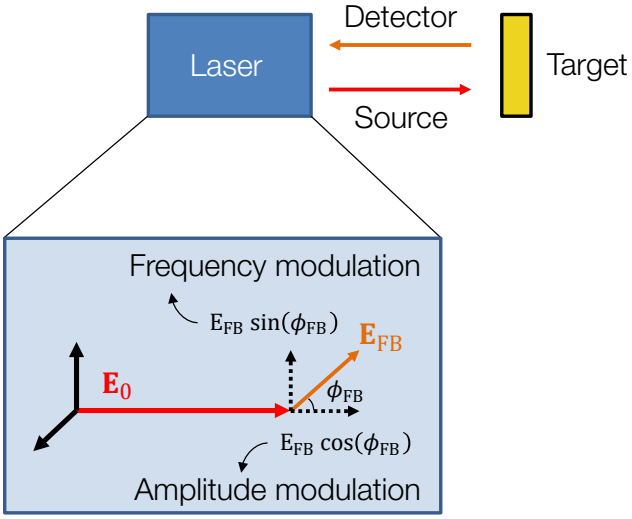

Figure 4.1: Simplified schematic of the self-mixing physical principle.

4.1.2 Applications: sensing

One of the ubiquitous applications of self-mixing interferometry is in sensing. This is because the SM response is fast, and fundamentally limited by the relevant laser electron and photon lifetimes (typically tens of picoseconds at most). Additionally, the sensing is coherent, and can be extremely sensitive ($\sim 10^{-8}$). For these reasons, SM interferometry has been particularly attractive in the THz due to the lack of convenient room-temperature fast detectors. With this technique, sensing applications become achievable using THz QC-lasers without the need for a separate detector.

One of the first set of demonstrations was in THz imaging, where SM was used to perform long distance imaging, real-time imaging, and depth-resolved sensing [132–139]. Fig. 4.2 showcases a couple examples of imaging of obscured objects and highly resolved features in coins. A notable demonstration is shown in Fig. 4.2(b) in which the fast nature of SM interferometry is used by incorporating a fast scanning mirror in reflection mode imaging to obtain cm-scale images at Hz level rates.

SM has also been used to demonstrate material characterization, gas spectroscopy, and near-field microscopy [134, 136, 140–152]. A few examples are shown in Fig. 4.3. Because SM

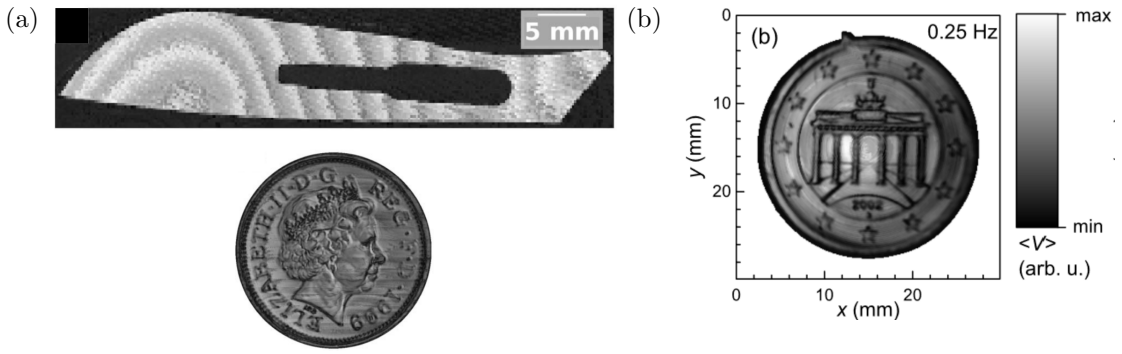

Figure 4.2: (a) Self-mixing image of a scalpel obscured by a polyethylene FedEx envelope, and a high-resolution image of a British coin. (b) SM image of German coin obtained in reflection mode using a fast scanning mirror. The image was collected in 4 seconds. Figures reproduced from [132, 133].

enables coherent sensing, it has been used to distinguish between different plastics by obtaining the full complex permittivity values (Fig. 4.3(a)). SM interferometry was also used to perform gas spectroscopy by frequency tuning the QC-laser across a methanol absorption line via current sweeping (Fig. 4.3(b)). This technique produced spectral resolution on the order of $\nu/\Delta\nu \sim 10^6$ — comparable to that obtained with a LHe cooled Ge:Ga photoconductive detector. There were also demonstrations of using SM for near-field microscopy/nanoscopy. In one particular demonstration, a Pt tip was used in proximity of the sample to realize a scattering-type scanning near-field optical microscopy system (s-SNOM), achieving 60–70 nm in-plane spatial resolution (Fig. 4.3(c)). Another unique demonstration of SM was in a pump-probe reflection-mode setup to image photogenerated carrier density in n-type Si. Fig. 4.3(d) shows a CCD image of the near-IR pump on the left, followed by a raster-scan THz SM image on the right.

Early demonstrations of SM in THz QC-lasers included displacement sensing and velocimetry. These applications in metrology have been extensively explored in the visible and infrared, and such demonstrations establish the proof-of-concept for THz QC-lasers as SM sensors [153, 154]. Perhaps in the most straightforward experimental setup, a SM signal can be obtained with the sample target mounted on a translating stage or a speaker to provide

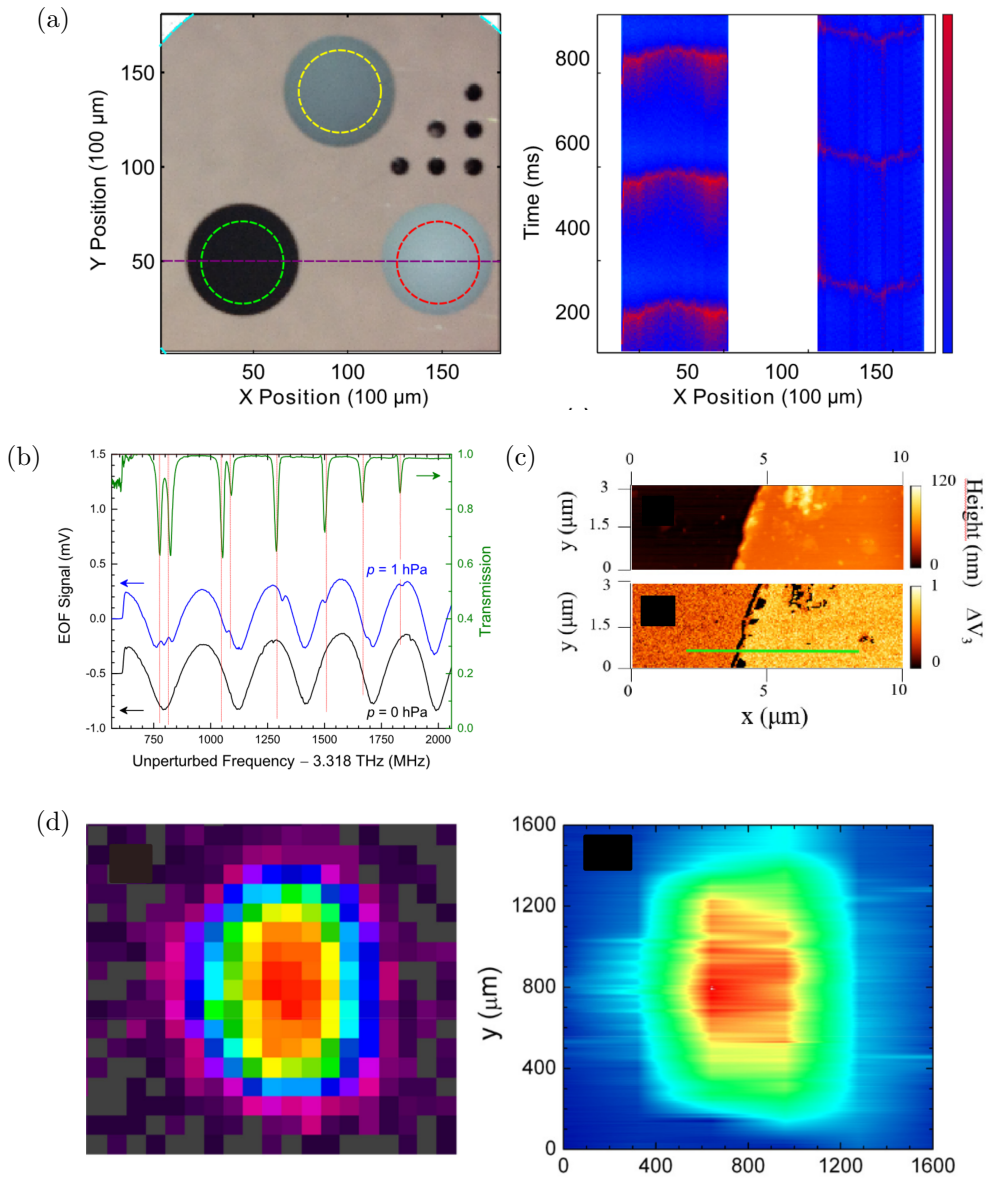

Figure 4.3: (a) Photograph of three different plastics and corresponding self-mixing signals along the horizontal dashed line. (b) Self-mixing signal through a gas cell filled with methanol at 1 hPa and zero pressure. The green curve shows the transmittance spectrum of the gas. (c) s-SNOM image obtained via self-mixing from back-scattered radiation from Pt tip. (d) CCD image of IR pump beam (left) illuminated on a Si sample and corresponding THz SM image (right). Figures reproduced from [140–143].

external cavity length modulation (see Fig. 4.4(a)). Because the total phase accumulation in the external cavity is given by $\phi_0 = \omega_0 \tau_{\text{ext}} = 2\omega_0 L_{\text{ext}}/c$, the information of the sample's rela-

tive position is imprinted in the terminal voltage of the QC-laser. Using the same principle, it is also possible to obtain information on the speed of the external target, as illustrated by the sample data shown in Fig. 4.4(b). While SM in the terahertz will always have worse displacement resolution due to its longer wavelength, the advantage of terahertz is its ability to transmit through plastics, fabrics, and other non-polar materials.

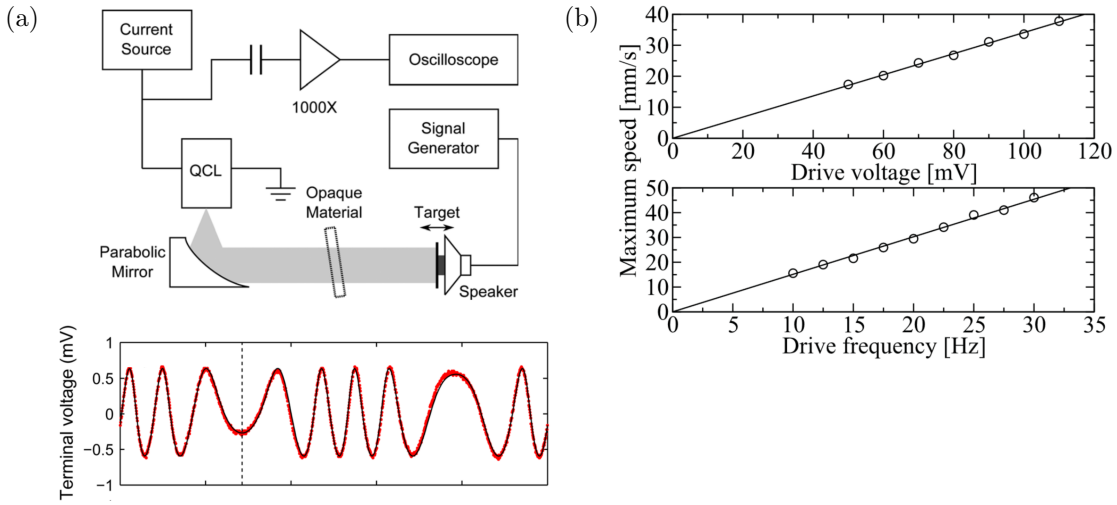

Figure 4.4: (a) Schematic of a self-mixing interferometer for displacement sensing. The data below shows an SM signal obtained with a black cloth placed in the path of the beam. (b) Speed of an oscillating speaker obtained from SM signals from a nearly identical setup as that shown in (a). Figures reproduced from [134, 144].

4.1.3 Applications: self-characterization

Beyond sensing, SM has been used for laser self-characterization [155–158]. This is because the laser response to optical feedback is dependent on key laser parameters such as the linewidth enhancement factor (LEF), laser linewidth, and the emission spectrum. In the case of Fig. 4.5(a), the SM signal morphology was directly used to measure the LEF of a THz QC-laser, obtaining values between 0 and 0.5 depending on the laser bias point. This was the first demonstration of measuring α of a THz QC-laser, and came soon after the initial demonstration in the mid-IR regime [158]. The LEF in particular has gotten a lot of attention, since it has been shown to play a key role in optical frequency comb generation

in THz QCLs [159–161]. In the mid-IR, SM was also used to measure the laser linewidth by monitoring the fringe durations of the SM signal via an oscilloscope and calculating phase noise (see Fig. 4.5(b)). One important demonstration in the THz was a measurement of the laser emission spectrum that performed comparably to a Fourier transform infrared (FTIR) spectrometer. With a simpler optical setup, and a detection speed not limited by slow pyroelectric detectors, SM can be an attractive alternative to FTIRs for measuring emission spectra, especially since it has shown to work with multimode emissions (see Fig. 4.5(c)).

Self-mixing is an important tool towards studying the effect that optical feedback can have on the laser itself. Depending on the feedback conditions, and the type of semiconductor laser, optical feedback is known to cause the laser to mode hop, multi-mode, stabilize, destabilize, or even drive the laser into chaos [162–172]. Due to extremely fast gain recovery times, and near-zero LEFs, QCLs have been shown to be particularly stable under optical feedback compared to conventional diode lasers [173]. Nonetheless, optical feedback has been shown to have a significant effect for frequency comb operation and stability in THz QC-lasers [166, 174, 175]. The intentional or accidental presence of feedback must always be considered for THz QC-lasers, since there are no readily available optical isolators in the 1–10 THz range. To date, almost all demonstrations of SM interferometry in THz QCLs has been performed via surface-plasmon waveguide edge-emitting lasers, which were favored over metal-metal waveguide lasers because of their larger waveguide mode, which eased optical coupling upon retroreflection [22].

For the THz QC-VECSEL, influence of optical feedback in previous experiments have been observed, primarily as a parasitic feature due to difficulties in avoiding the phenomenon in optical systems. For instance, there was evidence of optical feedback modulating injection locking bandwidths in both optical injection-locking and RF injection-locking schemes, as well as triggering multi-mode oscillation from a nominally single-mode QC-VECSEL [174, 176].

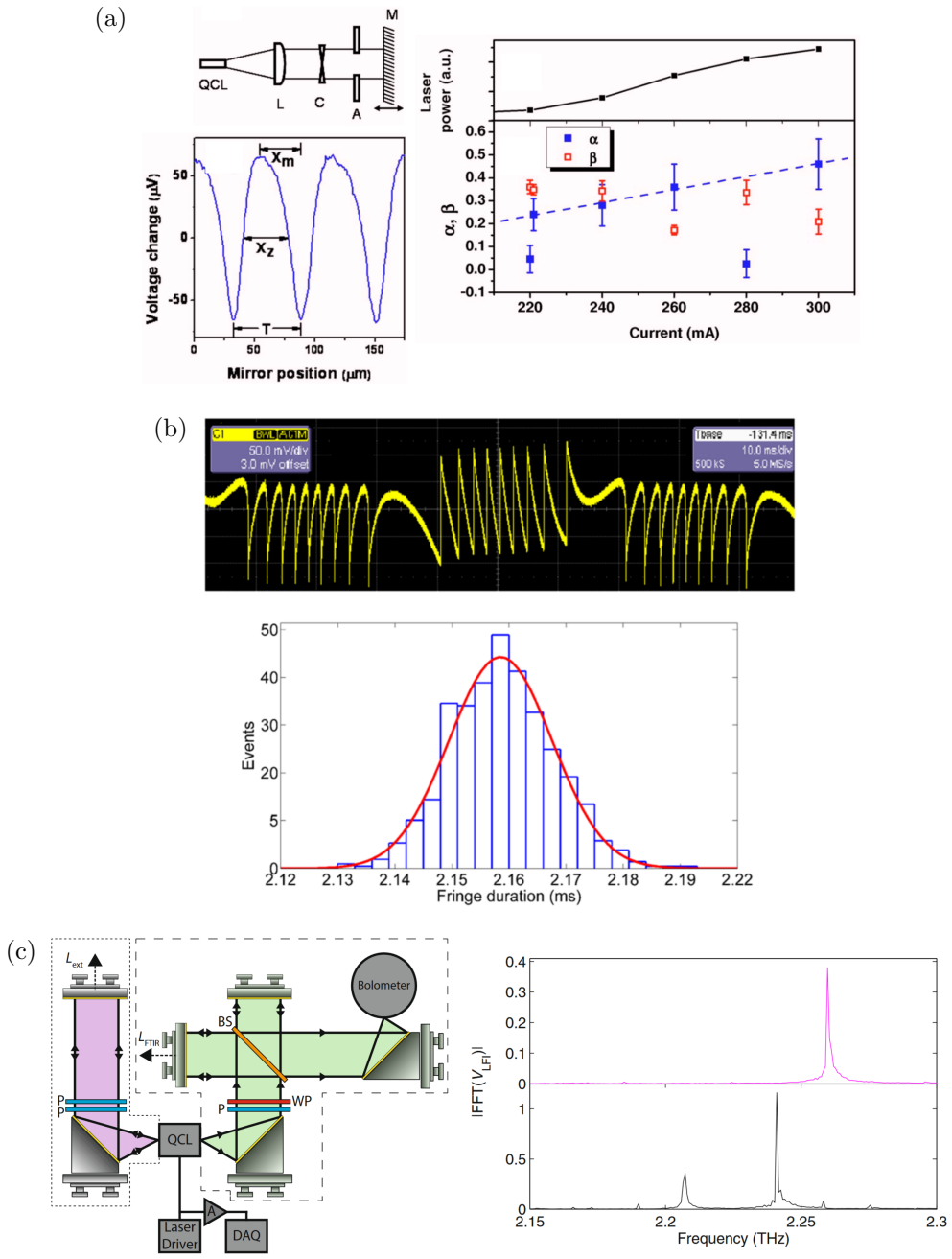

Figure 4.5: (a) Measurements of linewidth enhancement factor α of a THz QC-laser obtained from self-mixing voltage waveforms. (b) Measurements of phase noise via self-mixing signals from a mid-IR QC-laser. (c) Optical setup and results of a self-mixing based interferometer for measuring emission spectra of a THz QC-laser. The results are compared with a FTIR. Figures reproduced from [155–157].

4.1.4 Regimes of operation

In a famous 1986 paper by Tkach and Chraplyvy, a 1.55 µm InGaAsP distributed feedback (DFB) laser was shown to operate in five distinct regimes of optical feedback [162]. The distinctions between these regimes have been found to be present across semiconductor lasers in general, and have since become commonplace descriptions for lasers under optical feedback [149, 177–180]. These regimes include:

- **Regime I**: the lowest level of feedback, with injected power ratios on the scale of -80 dB. This is also associated with Acket feedback parameter $C \ll 1$. In this regime, the self-mixing signal is nearly a perfect sinusoid, and the amplitude scales linearly with feedback strength. The laser linewidth is broadened or narrowed depending on the phase of the feedback, but remains single-mode.
- **Regime II**: the so-called moderate feedback regime ($C > 1$). The regime depends on both the feedback strength and the external cavity length. It is characterized by mode-hopping the apparent splitting of emission lines that results from it. The SM signal is no longer sinusoidal, and instead has regions of bistability.
- **Regime III**: at higher levels of feedback, the regime ceases to depend on the external cavity length, and single-mode stability is recovered. The injected power ratio is on the scale of -45 dB, and $C \gg 1$. However, the laser remains dependent on the phase of feedback.
- **Regime IV**: a regime often denoted by "coherence collapse", in which the laser develops sidemodes and diminishes the coherence length of the laser. The injected power ratio exceeds -40 dB. This regime is also characterized by chaos dynamics and chaotic instabilities. However, such a phenomenon has yet to be observed in QC-lasers.

- **Regime V**: beyond -10 dB of feedback, the external optical feedback system resembles that of a long external cavity laser, and the feedback is no longer a mere perturbation to the laser. This results in a return of high stability with narrow linewidths.

The transition points between these regimes is well described by the well-known T-C diagram shown in Fig. 4.6(a). The initial two regimes depend on both the feedback power ratio and external cavity length. However, as the feedback power increases, the regimes start to lose dependency on the external cavity length. It is important in any self-mixing system to determine what regime the device operates in, since it can have significant impact on the spectral behavior of the laser emission.

While the behavior of semiconductor lasers under optical feedback has been well studied for decades, the quantum-cascade laser warrants its own study. In the context of self-mixing, QC-lasers are unique in a couple of ways. One, thanks to the ultrafast phonon scattering mechanism, the gain recovery times in QC active regions are on the order of 1–10 picoseconds, more than two orders of magnitude smaller than that of interband lasers [159,181,182]. This results in an absence of relaxation oscillations because these transient oscillations between the carrier and photon densities become overdamped by the ultrafast carrier dynamics [183,184]. Two, QC-lasers have been predicted to have near-zero linewidth enhancement factors (LEF) due to the symmetric gain profile arising from intersubband transitions [185, 186]. This hasn't necessarily held true in experiments for mid-IR QC-lasers, but measurements of LEF in THz QC-lasers were significantly smaller ($|\alpha| < 1$) than that of interband lasers which have typical LEF values between 1 and 5 [160, 187–195]. For these reasons, QC-lasers have been predicted to be very stable against optical feedback [173]. There has been several efforts in the past decade to investigate the stability of QC-lasers, mostly in the mid-IR, in addition to recent reports revealing indications of chaos dynamics [167, 172, 196–199]. In a particular work by Jumpertz et al., the T-C diagram was modified to match what was observed in a 5.6 µm DFB mid-IR QC-laser [165]. The regime diagram is shown in Fig. 4.6(b) and corresponding spectral characteristics in Fig. 4.6(c). The study demonstrated much smaller

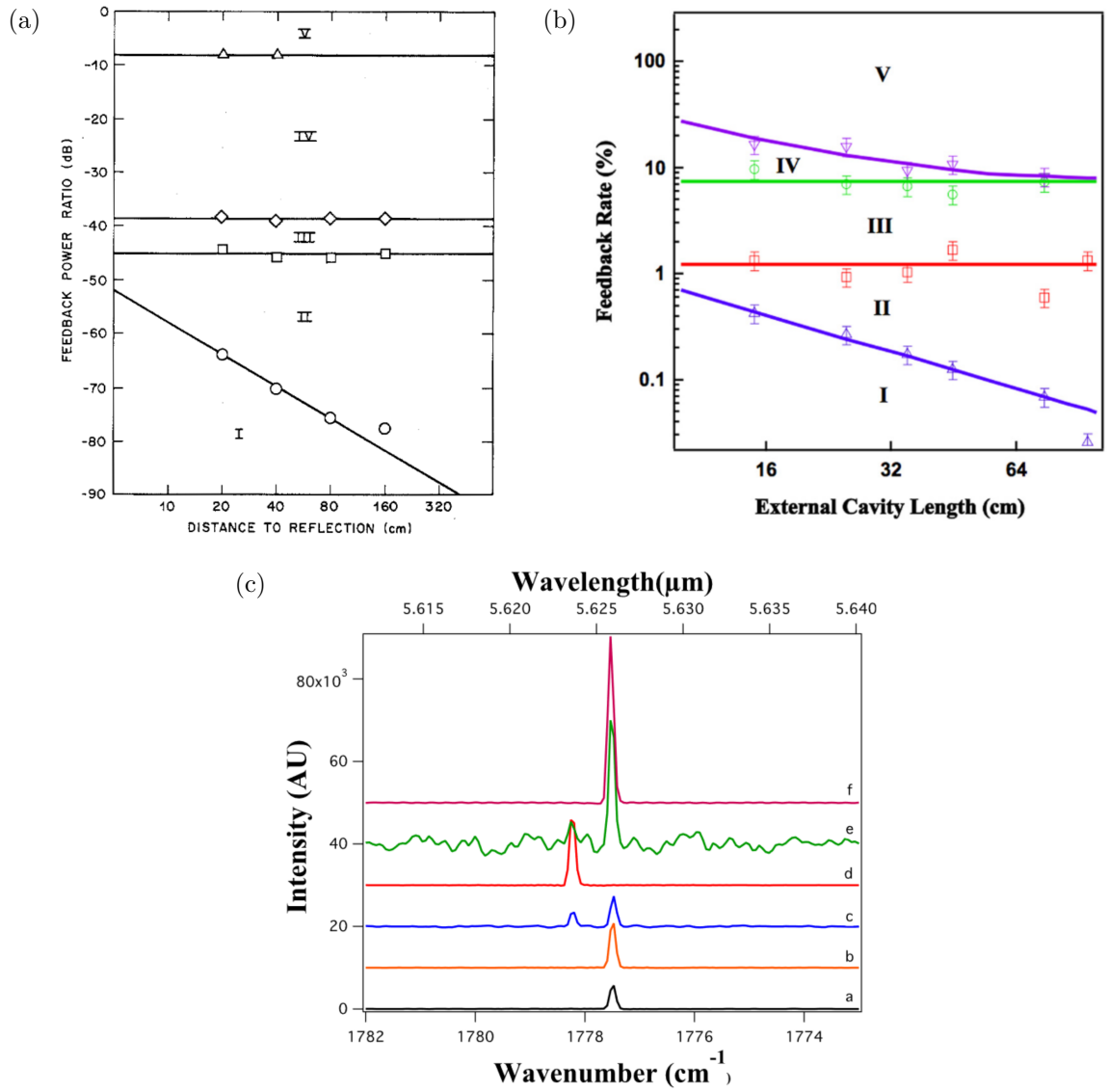

Figure 4.6: (a) T-C diagram showing the five different regimes of optical feedback. (b) Similar regime diagram as (a), but for a 5.6 μm mid-IR QC-laser. (c) Emission spectra corresponding to the five feedback regimes. The bottom spectrum is for the free-running case, followed by the feedback regimes starting from the bottom up. Figures reproduced from [162, 165].

windows of instability (Regime IV) that progressively get smaller for longer external cavity lengths. Likewise, the stable regimes are observed to be much broader with respect to the feedback strength.

Optical feedback dynamics in THz QC-lasers has been relatively unexplored, and to date,

there have been no signs of coherence collapse or chaos from these devices. However, recent studies by Qi et al. revealed evidence of feedback induced self-pulsations due to the beating between the internal laser cavity and external cavity modes [166, 171]. These periodic pulsations associated with the external cavity modes seem to be a potential avenue for feedback induced instability in THz QC-lasers as opposed to undamped relaxation oscillations in interband lasers.

4.2 Theoretical model for self-mixing in QC-VECSELs

A theoretical model for self-mixing that includes the effect of the metasurface resonance can be established by adapting the three-mirror model [178,200]. While a Lang-Kobayashi-based reduced rate equation model can provide a complete time-dependent picture, the three-mirror model can arrive at analytical steady-state solutions that are in good agreement with experiment [157, 166, 201]. This is especially true in THz quantum-cascade lasers because these devices have been shown to remain stable across a wide range of feedback levels [173].

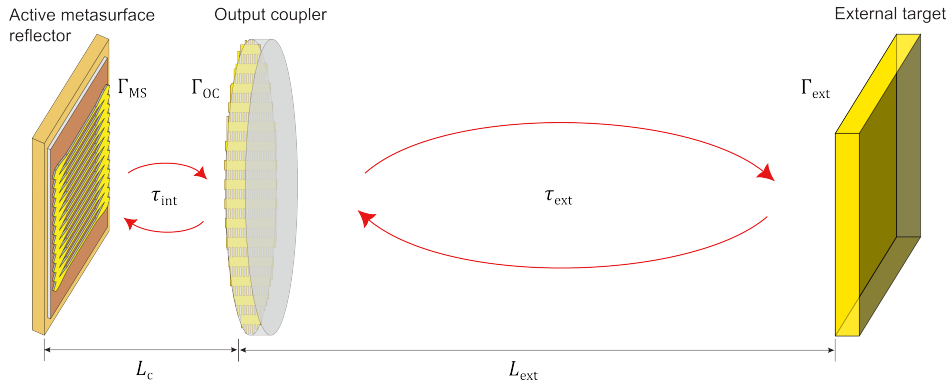

Figure 4.7: Schematic of the three-mirror model including the QC-VECSEL. Γ_{MS}, Γ_{OC}, and Γ_{ext} are the reflection coefficients of the metasurface, output coupler, and external target respectively. τ_{int} and τ_{ext} are the internal and external cavity round-trip times. L_c is the VECSEL cavity length, and L_{ext} is the external feedback cavity length.

Consider the three-mirror Fabry-Pérot cavity shown in Fig. 4.7. The reflection coefficients of each mirror is given by Γ_{MS}, Γ_{OC}, and Γ_{ext} respectively. If light transmitted through the

output coupler undergoes n round-trips (RTs) in the external feedback cavity, we can write an effective reflection coefficient at the output coupler facet that subsumes the effect of the external cavity:

$$\Gamma_{\text{eff}}(\omega) = \Gamma_{\text{OC}} + (1 - R_{\text{OC}}) \sum_{i=1}^{n} \epsilon_i \Gamma_{\text{OC}}^{i-1} \Gamma_{\text{ext}}^{i} e^{-j2ikL_{\text{ext}}}. \tag{4.1}$$

If we assume the reflection phases $\phi_{\text{OC}} \approx \phi_{\text{ext}} \approx \pi$, and write

$$\kappa_i = \epsilon_i \left(\frac{1 - R_{\text{OC}}}{R_{\text{OC}}} \right) \left(\sqrt{R_{\text{ext}} R_{\text{OC}}} \right)^i \tag{4.2}$$

as the coupling strength associated with the i^{th} RT, we can further write

$$\Gamma_{\text{eff}}(\omega) = \sqrt{R_{\text{OC}}} e^{j\pi} \left(1 + \sum_{i=1}^{n} \kappa_i e^{-j2ikL_{\text{ext}}} \right), \tag{4.3}$$

where ϵ_i is the total field attenuation in the external cavity, and L_{ext} is the length of the external cavity. These expressions assume an infinitely thin output coupler substrate, but can easily be modified otherwise by including additional phase terms in the exponential. If desired, the reflection phase ϕ_{ext} can be kept general inside the complex exponential to account for arbitrary external targets. Such is the basis for SM sensors for material characterization and analysis [151,152]. Although the common simplification from this point is to neglect all feedback contributions beyond the first RT ($n = 1$), we find experimentally that this is not a valid approximation for self-mixing in the QC-VECSEL. Thus, we will continue subsequent analyses without loss of generality to n RTs in the external feedback cavity.

To incorporate the result of Eq. (4.3) into subsequent analyses, we must arrive at expressions for the magnitude and phase of the complex-valued function. If we define the bracketed term as γ_{FB}, and assuming $\kappa_i \ll 1$, we can write

$$|\gamma_{\text{FB}}|^2 \approx 1 + 2 \sum_{i=1}^{n} \kappa_i \cos\left(2ikL_{\text{ext}}\right) \tag{4.4}$$

and

$$\angle\gamma_{\mathrm{FB}} \approx -\sum_{i=1}^{n} \kappa_i \sin\left(2ikL_{\mathrm{ext}}\right), \tag{4.5}$$

leading to the useful results

$$R_{\mathrm{eff}} \approx R_{\mathrm{OC}} \left(1 + 2\sum_{i=1}^{n} \kappa_i \cos\left(2ikL_{\mathrm{ext}}\right)\right) \tag{4.6}$$

and

$$\phi_{\mathrm{eff}} \approx \pi - \sum_{i=1}^{n} \kappa_i \sin\left(2ikL_{\mathrm{ext}}\right), \tag{4.7}$$

With this, we can express the resonance condition of the laser cavity as

$$\frac{2\omega L_{\mathrm{c}}}{c} - \phi_{\mathrm{MS}}(\omega, n) - \phi_{\mathrm{eff}} = 0, \tag{4.8}$$

where ϕ_{MS} and ϕ_{eff} represent the reflection phase of the metasurface and effective mirror respectively. Comparing this to the resonance condition for the case without external feedback, we can further write

$$0 = \frac{2L_{\mathrm{c}}}{c}\Delta\omega - \Delta\phi_{\mathrm{MS}} - \angle\gamma_{\mathrm{FB}}, \tag{4.9}$$

where $\Delta\omega = \omega - \omega_0$, $\Delta\phi_{\mathrm{MS}}$ is the change in the metasurface reflection phase, and ω_0 is the emission frequency of the laser without feedback. Going forward, we continue to assume $\kappa_i \ll 1$. Also, we make an additional assumption that the metasurface reflectivity Γ_{MS} is given by a Lorentz oscillator model. We know the first assumption is valid due to the large reflectance of the output coupler ($R_{\mathrm{OC}} > \sim$90%), as will be shown in Section 4.4. For the latter assumption, we can see from Fig. 4.8 that the reflectance and reflection phase of the metasurface obtained via full-wave finite-element (FEM) simulation (COMSOL Multiphysics) matches very closely to an analytical Lorentz oscillator model over its entire bandwidth and for various levels of applied gain. Thus, we can write the metasurface reflection coefficient as

$$\Gamma_{\mathrm{MS}} \approx \frac{\frac{1}{4}\left(\tau_{\mathrm{r}}^{-2} - \tau_{\mathrm{m}}^{-2}\right) - (\omega - \omega_{\mathrm{r}})^2 - j\tau_{\mathrm{r}}^{-1}(\omega - \omega_{\mathrm{r}})}{\frac{1}{4}\left(\tau_{\mathrm{r}}^{-1} + \tau_{\mathrm{m}}^{-1}\right)^2 + (\omega - \omega_r)^2}, \tag{4.10}$$

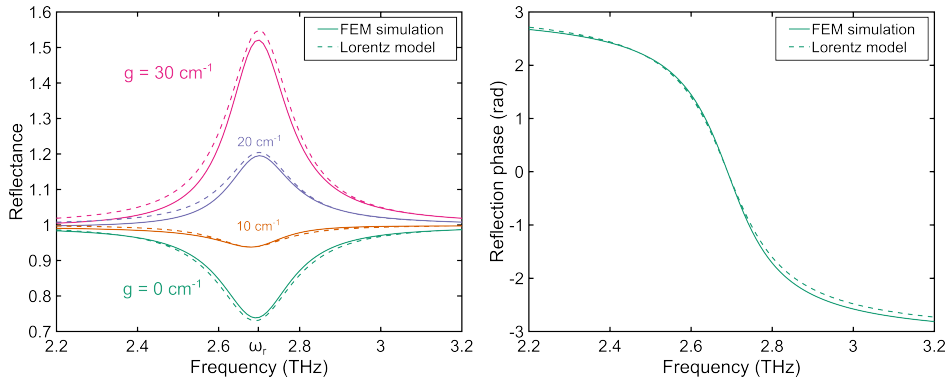

Figure 4.8: The metasurface reflectance (left) and reflection phase (right) for the device used in this work. The solid lines are from a full-wave FEM simulation. The dashed lines are based on an analytical Lorentz oscillator model. Reflectance is shown for various levels of applied material gain to compensate for losses.

which provides a reflection phase given by

$$\tan\phi_{\mathrm{MS}} = \frac{\tau_{\mathrm{r}}^{-1}(\omega-\omega_{\mathrm{r}})}{(\omega-\omega_{\mathrm{r}})^2 - \frac{1}{4}\left(\tau_{\mathrm{r}}^{-2}-\tau_{\mathrm{m}}^{-2}\right)}, \tag{4.11}$$

where τ_{r} is the photon lifetime associated with the radiative loss of the metasurface itself, τ_{m} is the photon lifetime associated with the material loss, and ω_{r} is the resonant frequency of the metasurface.

To explicitly bring out the amplitude-phase coupling in the laser, we can write the change in the metasurface reflection phase evaluated at ω_0 as

$$\Delta\phi_{\mathrm{MS}} = \left[\frac{\partial\phi_{\mathrm{MS}}}{\partial\omega}\Delta\omega + \frac{\partial\phi_{\mathrm{MS}}}{\partial n}\Delta n\right]_{\omega_0}. \tag{4.12}$$

If we assume $\tau_r^{-1} \gg \tau_m^{-1}$, which is typically true since the metasurface is deliberately designed to have a low radiative quality factor, we can use Eq. (4.11) to write

$$\begin{aligned}\frac{\partial\phi_{\mathrm{MS}}}{\partial\omega} &= -\frac{\tau_{\mathrm{r}}^{-1}}{(\omega_0-\omega_{\mathrm{r}})^2 + \frac{1}{4}\tau_{\mathrm{r}}^{-2}} \\ &= -2\pi\mathcal{L}(\omega_0),\end{aligned} \tag{4.13}$$

where $\mathcal{L}(\omega)$ is the Lorentzian lineshape given by

$$\mathcal{L}(\omega) = \frac{1}{2\pi} \frac{\tau_r^{-1}}{(\omega - \omega_{\mathrm{r}})^2 + \frac{1}{4}\tau_r^{-2}}. \tag{4.14}$$

For the subsequent term in Eq. (4.12), we can write

$$\begin{aligned} \frac{\partial \phi_{\mathrm{MS}}}{\partial n} &= \frac{\partial \phi_{\mathrm{MS}}}{\partial \omega_{\mathrm{r}}} \frac{\partial \omega_{\mathrm{r}}}{\partial n} \\ &= (-\frac{\partial \phi_{\mathrm{MS}}}{\partial \omega})(-\frac{\omega_{\mathrm{r}}}{n}) \\ &= -2\pi \mathcal{L}(\omega_0) \cdot \frac{\omega_{\mathrm{r}}}{n}. \end{aligned} \tag{4.15}$$

This leads to a simplified expression for the change in the metasurface reflection phase,

$$\Delta\phi_{\mathrm{MS}} = -2\pi \mathcal{L}(\omega_0) \left(\Delta\omega + \frac{\omega_{\mathrm{r}}}{n} \Delta n \right). \tag{4.16}$$

In general, the index is a function of both the frequency and carrier density in the material. In other words,

$$\Delta n = \frac{\partial n}{\partial N} \Delta N + \frac{\partial n}{\partial \omega} \Delta\omega, \tag{4.17}$$

where N is the carrier concentration. We now introduce the Henry's linewidth enhancement factor, α, which represents a coupling between the index and gain in the material enforced by the Kramers-Kronig relation. The factor can be written as

$$\alpha = -\frac{2\omega}{c} \frac{\partial n / \partial N}{\partial g / \partial N}. \tag{4.18}$$

This allows us to write

$$\frac{\partial n}{\partial N} \Delta N = -\frac{\alpha c}{2\omega_0} \Delta g. \tag{4.19}$$

To develop an expression for the change in the gain, consider the threshold gain of the

VECSEL in the presence of feedback:

$$g_{\mathrm{th}} = -\frac{1}{\xi}\ln\left(T^2 R_{\mathrm{MS}} R_{\mathrm{eff}}\right). \tag{4.20}$$

Plugging in Eq. (4.6), this becomes

$$g_{\mathrm{th}} \approx g_{\mathrm{th},0} - \frac{2}{\xi}\sum_{i=1}^{n}\kappa_i \cos\left(2ikL_{\mathrm{ext}}\right), \tag{4.21}$$

where $g_{\mathrm{th},0}$ is the threshold gain of the solitary laser.

Plugging everything back into Eq. 4.9, and rearranging terms, we arrive at an intuitive form of the phase equation:

$$0 = \tau_{\mathrm{int}}\Delta\omega + \underbrace{\left(\sum_{i=1}^{n}\kappa_i \sin(2ikL_{\mathrm{ext}})\right)}_{\text{FM term}} + \underbrace{\frac{\omega_{\mathrm{r}}}{\omega_0}\alpha\left(\sum_{i=1}^{n}\kappa_i \cos(2ikL_{\mathrm{ext}})\right)}_{\text{AM term}}, \tag{4.22}$$

where

$$\tau_{\mathrm{int}} = \frac{2L_{\mathrm{c}}}{c} + 2\pi\mathcal{L}(\omega_0) + 2\pi\mathcal{L}(\omega_0)\frac{\omega_{\mathrm{r}}}{n}\frac{\partial n}{\partial\omega}, \tag{4.23}$$

and represents the RT time of the VECSEL cavity. In general, the RT time includes the group delay associated with the metasurface dispersion in addition to the material dispersion. The second term in the rhs of Eq. (4.22) is the phase contribution from the feedback-induced frequency-modulation (FM) of the laser. The third term is the phase contribution from the feedback-induced amplitude-modulation (AM) of the laser. Note that this term is a consequence of a finite LEF which results in an amplitude-phase coupling inside the oscillator and is an integral part of self-mixing phenomena. However, the factor $\omega_{\mathrm{r}}/\omega_0$ in the AM term is not a factor that appears in conventional ridge lasers, but appears in the VECSEL analysis due to the single-mode detunability away from the metasurface peak reflectance via the Fabry-Pérot VECSEL cavity mode. This detuning factor contributes to an effective linewidth enhancement factor of the laser which we define as $\alpha_{\mathrm{eff}} \coloneqq (\omega_{\mathrm{r}}/\omega_0)\alpha$. This dependence is not unique to the VECSEL, and is a result of the frequency dependence of the LEF due to the

odd-symmetric phase profile [202, 203]. In fact, the material LEF is itself also frequency dependent, and so the full dependence on α_{eff} with detuning is not known.

Defining $\phi_{\text{FB}} \coloneqq \omega\tau_{\text{ext}}$ and $\phi_0 \coloneqq \omega_0\tau_{\text{ext}}$, Eq. (4.22) can be rearranged into the more practical and familiar form of the generalized Adler phase equation,

$$0 = \phi_{\text{FB}} - \phi_0 + \sum_{i=1}^{n} \left[C_i \sin\left(i\phi_{\text{FB}} + \arctan(\alpha_{\text{eff}})\right)\right], \tag{4.24}$$

where

$$C_i = \kappa_i \sqrt{1+\alpha_{\text{eff}}^2}\frac{\tau_{\text{ext}}}{\tau_{\text{int}}}. \tag{4.25}$$

For a single RT, the parameter C_i reduces to the familiar Acket parameter, C, which subsumes the various feedback variables and can succinctly describe the regimes of operation of a self-mixing system [180, 204]. Therefore, the parameter C_i is an extension of the Acket parameter that describes the feedback level associated with the i^{th} RT of the external cavity. While Eq. (4.24) describes the perturbation of the emission frequency due to feedback, the SM signal can be obtained from the terminal voltage V_{SM} of the laser at constant current injection due to the modulation of the threshold gain. If we assume $V_{\text{SM}} \propto (N - N_{\text{th}})$, then

$$V_{\text{SM}} \propto -\frac{2}{\xi}\sum_{i=1}^{n} \kappa_i \cos(i\phi_{\text{FB}}). \tag{4.26}$$

Note that this is also a frequency dependent quantity given by $\xi = (c/n)2\pi\mathcal{L}(\omega)$, since it follows from the Lorentzian lineshape of the metasurface amplification.

In the simple case of a single RT ($i = 1$), the SM theory and signal morphology is well documented and understood [153, 154, 178, 205]. Fig. 4.9(a) shows the relationship between ϕ_{FB} and ϕ_0 this case. Without any optical feedback, the two phase terms are equivalent, since the laser frequency is not perturbed. As optical feedback is introduced, the laser frequency — and consequently the phase difference — is modulated. Beyond $C = C_1 = 1$, the phase relation becomes multi-valued. At this point, the system moves beyond the weak feedback regime, as described in Section 4.1.4. Specifically, phase relation forms regions with three

possible solutions, of which only two are stable. A few representative cases for the SM signal are illustrated in Fig. 4.9(b). For the SM signal morphology, larger coupling levels manifest as a departure from a sinusoid, and eventually produces jump points to the next stable phase point. Another important consequence of a coupling level beyond $C = 1$ is the DC offset that is produced, and the amplitude of the SM waveform is no longer well-defined, despite what the form in Eq. (4.26) would suggest. Larger values of α also has a big impact on the signal, causing asymmetric tilts and affecting the jump behavior. The case for $\alpha = 0$, $\alpha = 0.5$, and $\alpha = 1$ are shown in Fig. 4.9(b).

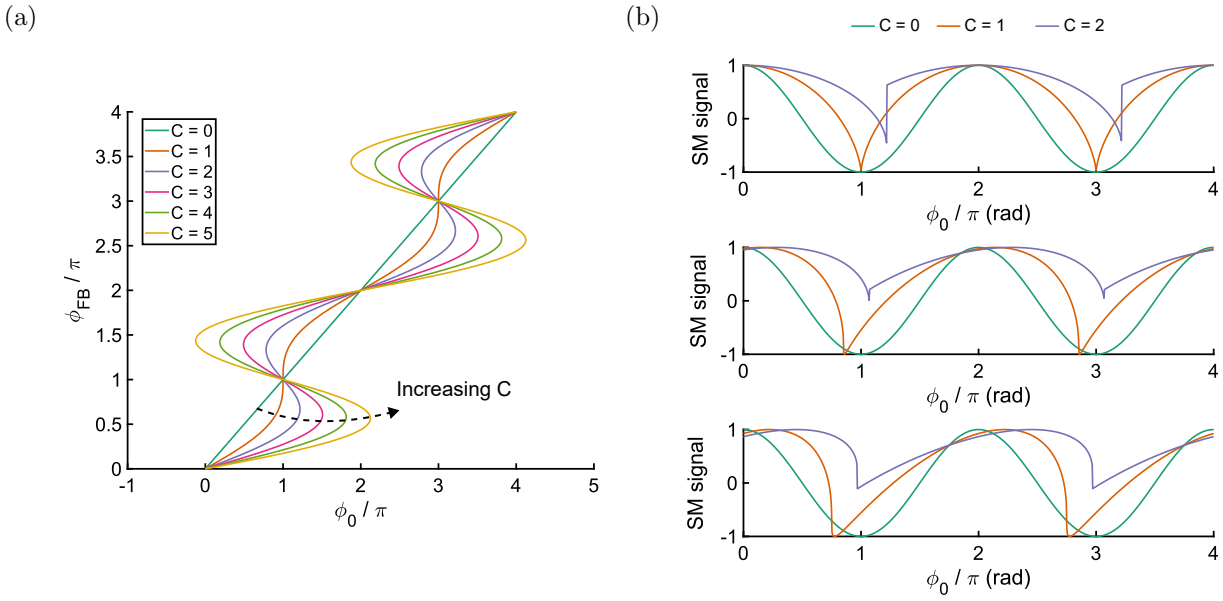

Figure 4.9: (a) Feedback phase relation for the single-bounce case. The Acket parameter C is varied from 0 to 5. (b) Calculated SM signals for a few representative cases. Starting from top to bottom, the assumed LEFs are $\alpha = 0$, $\alpha = 0.5$, and $\alpha = 1$.

For the case of $n = 2$, the phase relations become significantly more complicated. In an ideal system, the feedback level from the second RT, C_2, is not independent, and would have a fixed relationship to C_1. However, in experiment, non-idealities in alignment, optical components, and diffraction prevent constraining the value of C_2 in such ways. Some illustrative examples of the $n = 2$ case, based on the relation provided in Eq. (4.24), are shown

in Fig. 4.10. In particular, we demonstrate the relationship between ϕ_{FB} and ϕ_0 for the case of varying C_2 for a given C_1. Fig. 4.10(a) illustrates the case for $C_1 = 0$, and Fig. 4.10(b) shows the case for $C_1 = 1$. If we only consider reflections from the second RT, the self-mixing dynamics resemble the conventional case, but with two main distinctions. One, the periodicity is cut by half, resulting in a period of π. In an optical system such as that of Fig. 4.7, this will manifest as a $\lambda/4$ spatial periodicity of the self-mixing fringes as the external target is translated. Two, the phase relation steps into the regime of multistability sooner than the case of a single RT, resulting in a bistable regime for $0.5 < C_2 < 2.3$. The presence of multiple RTs in the self-mixing analysis precludes the simple delineation of feedback regimes based on a single feedback parameter [153, 205–207]. Thus, for the purposes of this work, we classify the weak feedback regime as the set of C_i n-tuples that maintain bijectivity of the phase relation in Eq. (4.24). The case for $n = 2$ is illustrated in Fig. 4.10(c). As ϕ_{FB} becomes multi-valued, the system enters the moderate feedback regime, typically characterized by mode-hopping instabilities, multimoding, and hysteresis [159, 162, 165].

A few representative self-mixing voltage waveforms according to Eq. (4.26) are calculated in Fig. 4.11 for the case of $n = 2$. Fig. 4.11(a) shows the case for $\alpha = 0$, and Fig. 4.11(b) shows the case for $\alpha = 0.5$. When both C_1 and C_2 are present, the self-mixing waveform features fringes that don't necessarily peak at the same value. Additionally, fringes appear every π when C_2 is non-zero. These features are indicative of the multi-bounce self-mixing effect and is experimentally demonstrated in Section 4.4. As the feedback strength gets larger, the waveform develops discontinuities associated with the path-dependence of ϕ_{FB} with respect to ϕ_0. Additionally, comparing Fig. 4.11(a) and 4.11(b) illustrates the effect of the LEF on the SM signal morphology; a non-zero α breaks the symmetry and produces a tilt to the signal.

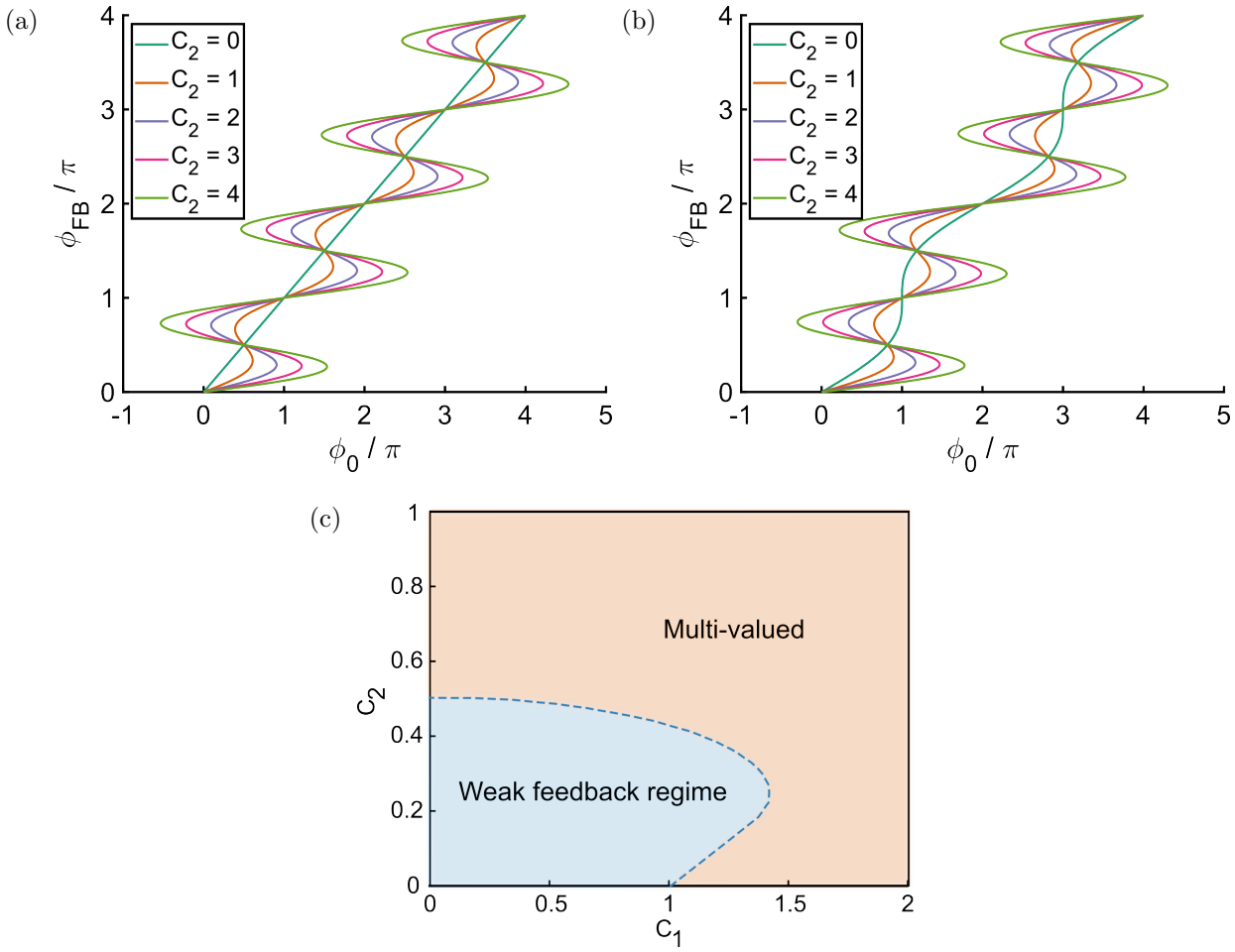

Figure 4.10: (a) Feedback phase relation for $C_1 = 0$, and varying C_2 from 0 to 4. (b) Feedback phase relation for $C_1 = 1$, and varying C_2 from 0 to 4. (c) Mapping of the weak feedback regime in the C_1-C_2 plane. Outside this regime, the phase relation becomes multi-valued and enters the moderate feedback regime.

4.3 Experimental methods

4.3.1 Device under test

The QC-VECSEL used in this work is based on an elliptical patch metasurface that couples to surface-incident radiation. The electric field profile of a unit cell is illustrated in Fig. 4.12(a). The patches are composed of 5-µm-thick QC gain material based on a 4-well phonon-depopulation design grown by IQE plc and was featured in Ref. [127]. The epitaxial

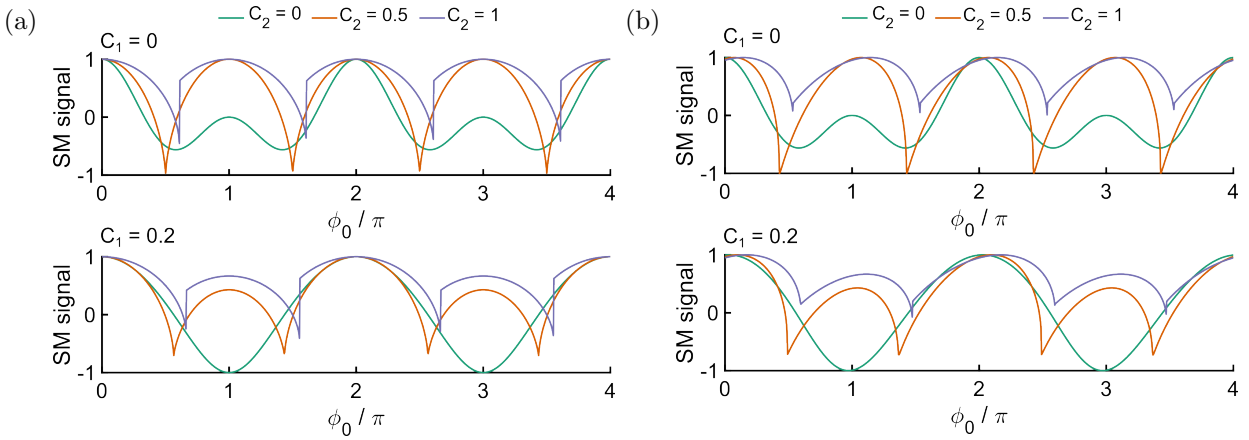

Figure 4.11: (a) Calculated SM voltage signals for $C_1 = 0$ and $C_1 = 0.2$ as C_2 is varied and $\alpha_{\text{eff}} = 0$. (b) Same as (a) but for $\alpha_{\text{eff}} = 0.5$.

growth is 80 repetitions of the layer sequence given, in Å, by 106/**20**/106/**37**/88/**40**/<u>172</u>/**51** (GaAs/$\mathbf{Al_{0.15}Ga_{0.45}As}$), where the middle 88 Å of the underlined layer is nominally doped at 5×10^{16} cm^{-3}. A microscope image of the entire metasurface and a corresponding SEM image of a single patch are shown in Fig. 4.12(b). The period of the patch array is 50 µm, and the major and minor axes of the ellipse are 21.4 µm and 14.6 µm respectively. Only patches within a central circular area with a diameter of 0.75 mm are biased, so as to preferentially pump the fundamental Gaussian mode of the VECSEL cavity. The output coupler is based on a metallic mesh evaporated on a quartz substrate to give a reflectance of $|\Gamma_{\text{OC}}|^2 = 0.95$. The output coupler is fixed and clamped onto the metasurface die copper submount with a 1 mm thick copper spacer, which eliminates any instabilities or thermal drift associated with a kinematic mount. The laser has a single mode emission peak at 2.80 THz and peak output power of 0.5 mW with threshold current of 385 mA and max current of 460 mA (Fig. 4.12(c)). The laser is driven in continuous-wave mode by a low noise (3 nA/$\sqrt{\text{Hz}}$) current source from Wavelength Electronics (QCL OEM1000+) and is cooled with liquid nitrogen to 77 K inside a cryostat with a TPX window.

Table 4.1: Parameter symbols and their descriptions for VECSEL SM model

Parameter symbol	Description	Units
Γ_{MS}	Metasurface reflection coefficient	1
Γ_{ext}	External target reflection coefficient	1
Γ_{OC}	Output coupler reflection coefficient	1
Γ_{eff}	Effective reflection coefficient	1
τ_{ext}	RT time of external feedback cavity	s
τ_{int}	RT time of VECSEL cavity	s
τ_{MS}	Metasurface group delay ($\tau_{\mathrm{MS}} = 2\pi\mathcal{L}(\omega)$)	s
ϕ_0	Intrinsic phase accumulation in external cavity, ($\phi_0 = \omega_0\tau_{\mathrm{ext}}$)	rad
ϕ_{FB}	Feedback phase accumulation in external cavity, $\phi_{\mathrm{FB}} = \omega\tau_{\mathrm{ext}}$	rad
ϵ_i	Field attenuation factor for the i^{th} round-trip	1
κ_i	Feedback strength for the i^{th} round-trip	1
α_{eff}	Effective linewidth enhancement factor of the metasurface	1
C_i	Feedback level for the i^{th} round-trip	1
L_{c}	VECSEL cavity length	m
L_{ext}	Length of the external feedback cavity	m
τ_{r}	Radiative photon lifetime of the metasurface	s
τ_{m}	Non-radiative photon lifetime of the metasurface	s
R_{MS}	Metasurface reflectance	1
R_{OC}	Output coupler reflectance	1
ξ	Effective gain interaction length of the metasurface	m
ω_0	Intrinsic frequency of the laser without optical feedback	rad/s
ω_{r}	Resonant frequency of the metasurface	rad/s
ω	Frequency of the laser with optical feedback	rad/s
g_{th}	Threshold gain of the laser with feedback	cm^{-1}
$g_{\mathrm{th},0}$	Threshold gain of the laser without feedback	cm^{-1}
V_{SM}	RT time of external feedback cavity	V

4.3.2 Fixed cavity mount

A fixed output coupler mount configuration for the QC-VECSEL has the advantage of long-term stability at the cost of frequency tunability. It also has the advantage of a small form factor, since the OC mount can be directly screwed down with the copper submount that houses the metasurface. A CAD drawing is illustrated in Fig. 4.13(a). The OC is placed directly on top of the mounting bracket, and clipped in place with PELCO SEMClip$^{\mathrm{TM}}$ clips.

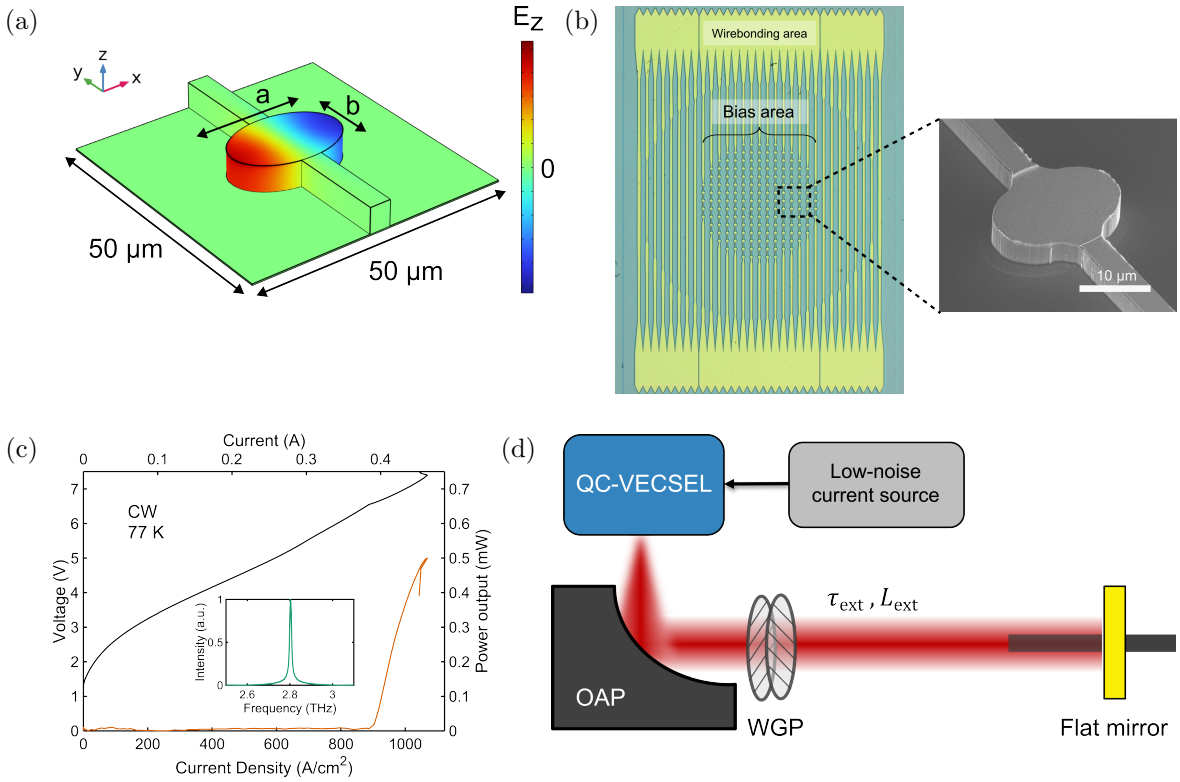

Figure 4.12: (a) Simulated electric field profile of the metasurface unit cell. The period of the metasurface is 50 μm in both x and y dimensions. The dimensions of the ellipse are given by $a = 21.4$ μm and $b = 14.6$ μm. (b) Optical microscope image of the full metasurface, and an SEM image of a single patch. The patches are selectively biased in a circular bias area in the center of the metasurface. (c) Power-current-voltage measurement of the device under test in continuous-wave operation at 77 K. The inset shows the emission spectrum obtained from an FTIR. (d) Schematic of the experimental setup. Crossed wire-grid polarizers are used whenever additional attenuation is desired.

We note, however, that only a single clip was used to secure the OC in the device under test due to the OC piece being too small. The two clearance holes in the OC mount are aligned with those of the copper submount so that the two copper pieces are screwed down together to the copper heatsink. As a result, the cavity length is directly determined by the thickness of the copper mount.

As a demonstration of its long time-scale stability, IVs of the device taken about a year apart are compared in Fig. 4.13(b). Though the two IVs don't exactly overlap due to some

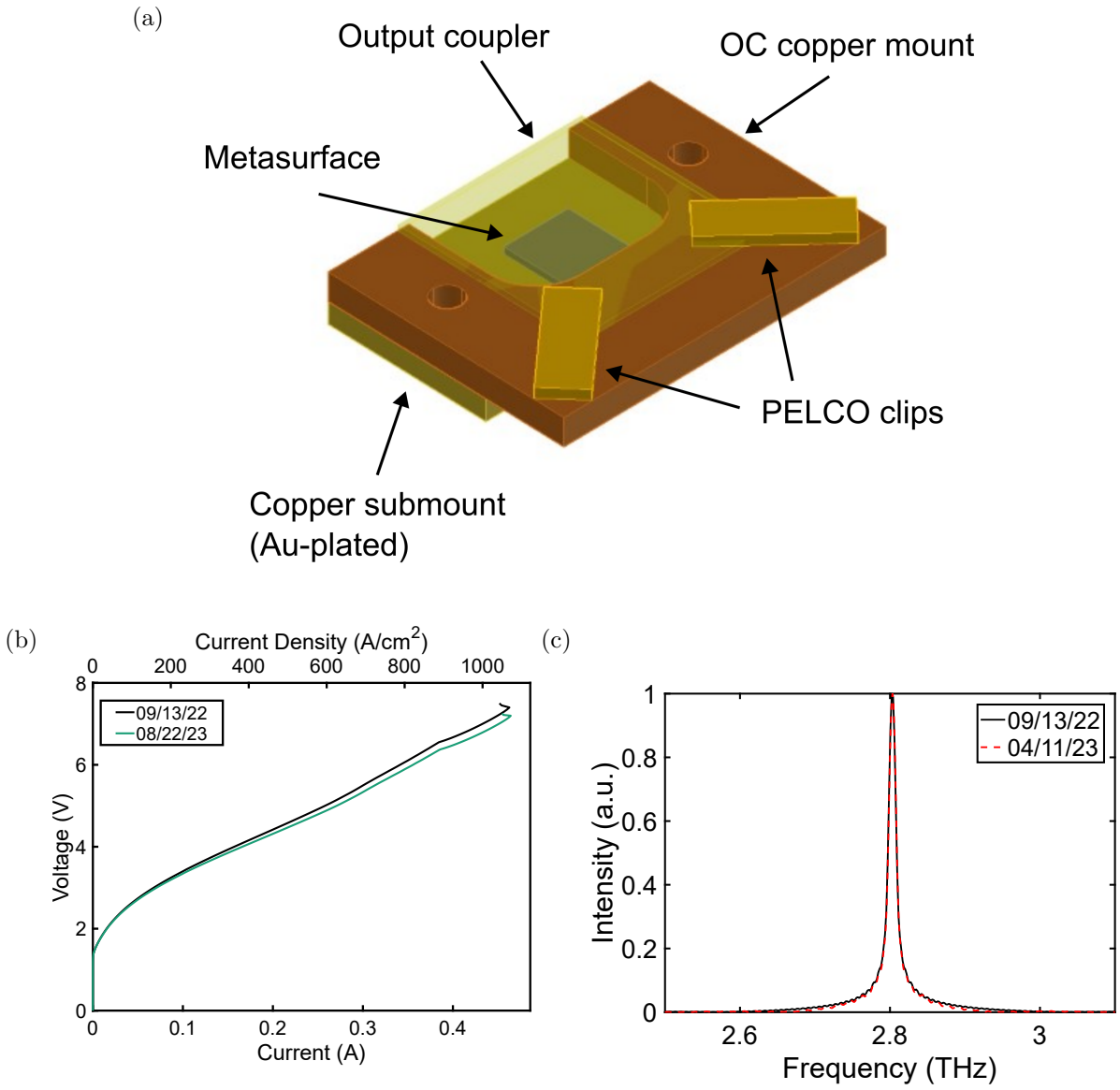

Figure 4.13: (a) CAD drawing of the QC-VECSEL fixed cavity architecture.

change in series resistance, it is noteworthy that the threshold current has remained the same. Performing a similar comparison with the emission spectra over about a seven month period, we find that the measured lasing frequencies are indistinguishable (based on an FTIR measurement with 7.5 GHz resolution). The overlapping spectra plots are shown in Fig. 4.13(c). We note that the device was never removed from the cryostat during these time periods, and the device was seldom exposed to atmosphere. However, it went through

multiple thermal cycles every week, as the device was used regularly for optical feedback studies. Although there is a lack of comparative data in longevity for kinematic mount configurations, the heuristic study shown here can attest to the robustness of the fixed cavity mount.

A potential problem in the fixed cavity architecture is the inherit assumption that the metasurface is perfectly parallel to the copper submount surface. This is not necessarily true, since unevenness in the indium solder during die attach can cause a slight angle. This can be accounted for by placing metallic shims between the OC mount and the submount. Fortunately, for the device under test, the cavity was already aligned without the need for shims.

4.3.3 Optical setup

Light leaving the laser is collimated by a 4" effective focal length f/2 off-axis parabolic (OAP) mirror and reflects off a flat mirror mounted on a 25 mm translation stage (Thorlabs MTS25-Z8), allowing for stepping the external cavity length. Moving the translation stage along a fixed rail mount allows for cavity extension from 10 to 80 cm while maintaining the alignment between the two mirrors. The laser emission frequency being near the edge of an atmospheric transmission window necessitates the use of a nitrogen purge enclosure in which relative humidity is reduced to $\sim$1%. Dual wire-grid polarizers (Microtech G30-S) in the collimated beam path are used whenever additional attenuation is desired.

As the translation stage reduces the external cavity length, the SM signal can be recorded as the ac component of the QCL terminal voltage. This signal can be simply acquired using a benchtop multimeter, as was done for the results in Section 4.4. We also employed the conventional method of lock-in detection with an optical chopper (modulated at 200 Hz), which was used for data presented in Section 4.5. However, as will be discussed in Section 4.6, these measurements were accompanied by unexpectedly large noise at higher feedback levels. In response we employed an alternate method, detailed in Section 4.7, involving lock-in differential resistance detection made using small-signal modulation of the current source

with a 100 kHz sinusoidal signal.

4.4 Multi-bounce self-mixing results

Without any intentional effort to produce the phenomenon, the experimentally observed SM voltage signal consistently demonstrated feedback coupling from light that underwent two RTs in the external cavity. In fact, when the external cavity length was made sufficiently short ($L_{\text{ext}} < 40$ cm), we observed SM signals that were dominated by the second RT ($C_2 \gg C_1$). An example of such a signal is shown in Fig. 4.14(a) for a cavity length of 17.8 cm. Fitting the data to Eq. (4.24) and Eq. (4.26) with appropriate normalization, we obtain $C_2 = 0.56 \pm 0.09$ and $\alpha_{\text{eff}} = 0.8 \pm 0.3$. The value of α_{eff} is consistent with previously reported SM measurements of the LEF in THz QCLs, ranging from -0.2 to $+1$ [144, 155].

Based on the fit parameters, we can quantify both the total field attenuation, ϵ, and the coupling strength using Eq. (4.25). The attenuation factor includes loss from the cryostat window, diffraction, and the mismatch of the spatial mode of the reinjected field. The internal RT time can be calculated from the known laser cavity length ($L_{\text{c}} = 1.0$ mm) and the simulated metasurface group delay. We obtain an attenuation coefficient of $\epsilon \approx 0.072$, which results in a coupling strength of 3.6×10^{-3}. A recent work by Keeley et al. reported an attenuation coefficient of $\epsilon = 0.0033$ when using a SP waveguide emitting at 3.4 THz [208]. Assuming a facet reflectivity of 33%, the obtained coupling strength is 3.8×10^{-3} — almost identical to that obtained with the VECSEL [209]. At first, the large output coupler reflectances required for the VECSEL may suggest the architecture is not well-suited for SM interferometry. However, the high beam-quality does well to compensate by reducing the amount of reinjected power lost to diffraction and modal-mismatch. Fig. 4.14(b) illustrates this by comparing the κ vs R_{OC} curves for the respective attenuation coefficients for the SP waveguide and the VECSEL. In fact, while the maximum achievable κ for the SP waveguide is fixed, the VECSEL has some freedom in moving along this curve. VECSELs with OC reflectance as low as 82% have been demonstrated, which would correspond to

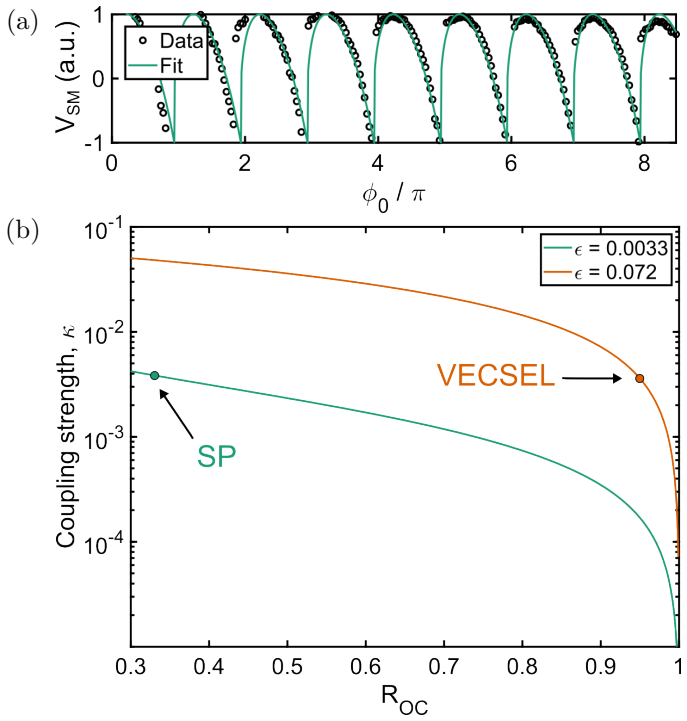

Figure 4.14: (a) Normalized SM voltage signal. The green curve is a fit to the collected data based on Eq. (4.24) and Eq. (4.26). The extracted parameters are $C_1 \approx 0$, $C_2 = 0.56 \pm 0.09$, and $\alpha_{\text{eff}} = 0.77 \pm 0.26$. (b) Coupling strength, κ, versus output coupler reflectance. The green curve corresponds to a surface-plasmon waveguide laser. The orange curve corresponds to the QC-VECSEL. The labeled points show exactly the point of operation.

$\kappa = 1.3 \times 10^{-2}$ [24]. Conversely, the reflectance can be made to be larger to reduce the laser's sensitivity to optical feedback.

4.5 Asymmetric cavity test

The observation of multiple RTs in the external cavity as shown in Section 4.4 warrants further investigation of the influence of optical alignment. The external target is deliberately misaligned by an angle θ, and a SM signal is collected over a 500 μm translational scan. Fig. 4.15(a) illustrates (to scale) a ray trace up to the second RT for a target misalignment angle of $\theta = 2°$. It is evident that in such an asymmetric cavity, the feedback ray from the first RT is displaced further from the initial source compared to the feedback from the

second RT. This will cause the coupling strength from the second RT to be more robust to target misalignment. This effect remains true in general for all odd-numbered versus even-numbered RTs, but higher-order contributions were observed to be much weaker and are not considered in this work [210, 211].

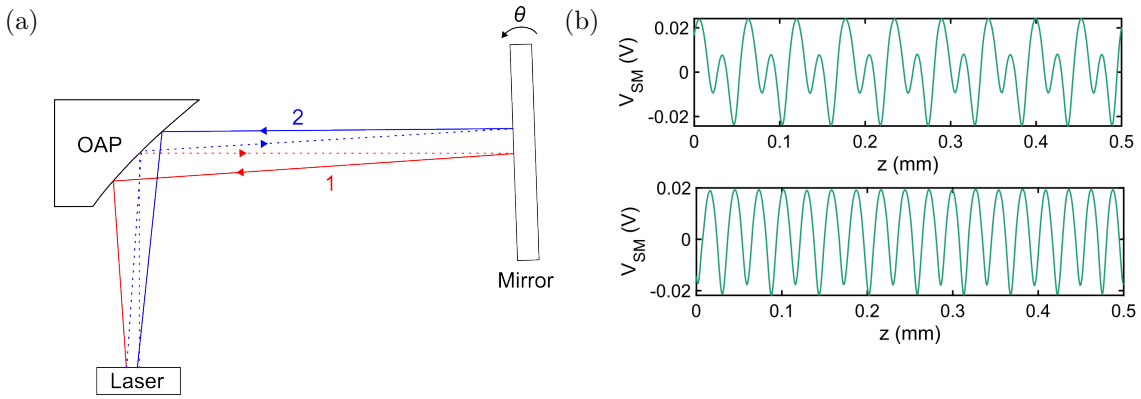

Figure 4.15: (a) Ray tracing of the optical setup for a misaligned external target. The red trace corresponds to the first round-trip beam, and the blue trace corresponds to the second round-trip beam. The dotted portions of the path represent rays traveling away from the laser. The solid portions are rays traveling towards the laser. (b) Measured self-mixing voltage signals. The bottom signal is obtained when the mirror is rotated 2 degrees toward the laser.

Fig. 4.15(b) shows two SM signals obtained at an external cavity length of 30 cm. The top plot shows the case for when the target is close to perfectly aligned, and the contribution from the first and second RTs are comparable. The bottom plot was obtained by misaligning the mirror 2° off normal, which results in a SM signal that is dominated by the second RT as indicated by the near-$\lambda/4$ periodicity. Although it was left out in the analysis performed in Section 4.2 for simplicity, in general there can be additional phase offsets between each round-trip due to varied propagation lengths in an imperfectly aligned system. The multi-bounce SM equations from Eq. (4.24) and Eq. (4.26) can be respectively modified to include this generalization:

$$0 = \phi_{\mathrm{FB}} - \phi_0 + \sum_{i=1}^{n} \left[C_i \sin\left(i\phi_{\mathrm{FB}} + \arctan(\alpha_{\mathrm{eff}}) + \delta_i \right) \right], \tag{4.27}$$

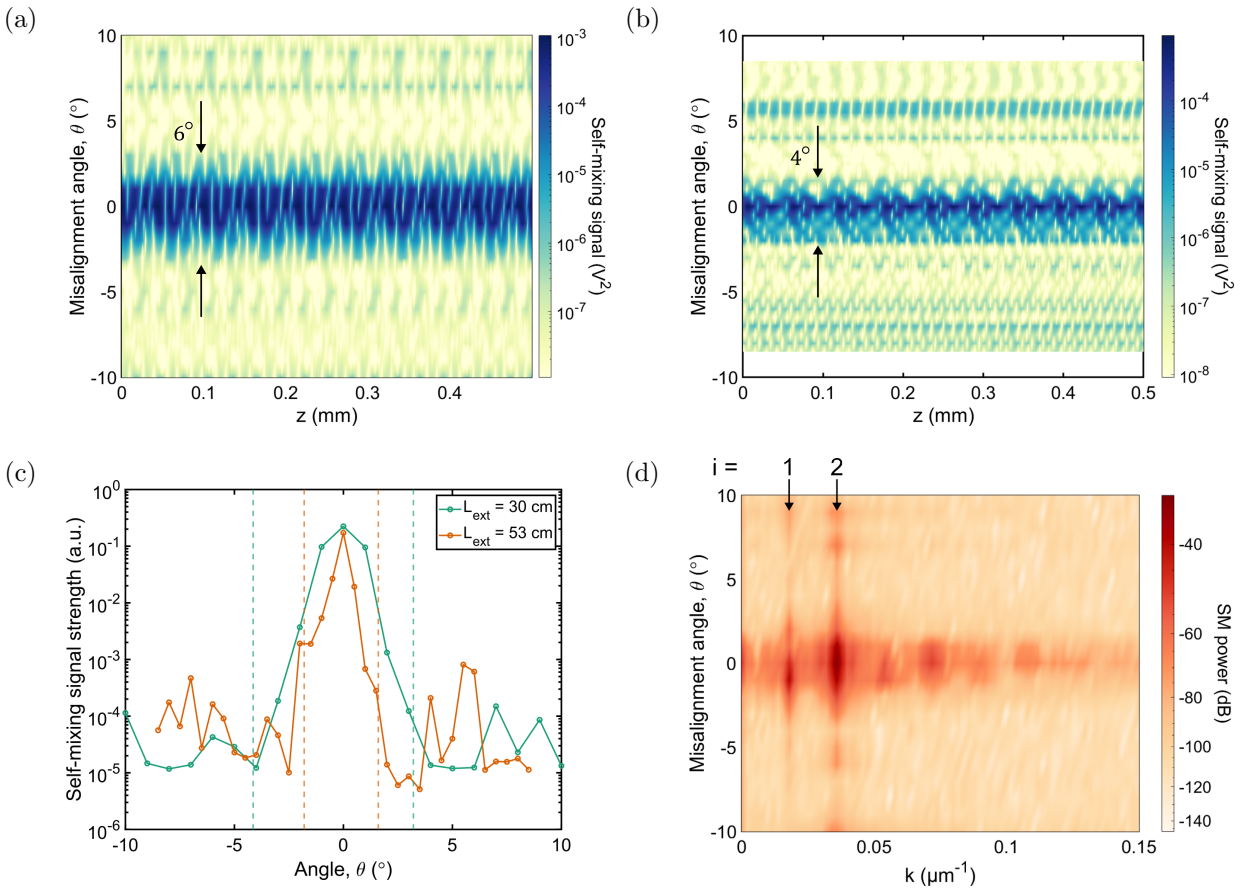

Figure 4.16: (a) Self-mixing signal power as a function of relative target mirror position and target misalignment angle, θ. The external cavity length is approximately 30 cm. (b) Same measurement as (a), but taken at an external cavity length of 53 cm. (c) Energy in the SM signal as a function of relative mirror angle for two different cavity lengths. The vertical dashed lines represent the angles that correspond to reflections incident at the physical edges of the OAP. (d) Spatial Fourier transform of the SM signal when $L_{\text{ext}} = 30$ cm, corresponding to the data in (a). The arrows indicate the spatial frequencies that correspond to the first and second round-trip.

and

$$V_{\text{SM}} \propto -\frac{2}{\xi}\sum_{i=1}^{n}\kappa_i \cos(i\phi_{\text{FB}} + \delta_i), \tag{4.28}$$

where δ_i is an arbitrary phase term to account for any extra relative phase differences between higher order RT terms. Data was collected across a range of misalignment angles from $-10°$ to $10°$, and the SM signal power is plotted as a function of relative mirror position for two

external cavity lengths, $L_{\text{ext}} = 30$ cm and $L_{\text{ext}} = 53$ cm (Figs. 4.16(a) and 4.16(b)). To better visualize the range of accepted misalignment angles, the total energy of the SM signal for each case is calculated in Fig. 4.16(c). The vertical dashed lines correspond to the mirror angles that would result in the initial ray walking off the boundaries of the OAP (which has inherent asymmetry). In contrast to SM interferometry with edge-emitting lasers, the SM signal strength from the VECSEL appears to be significantly tolerant to target misalignment. This is due to two reasons. First, the output coupler serves as a large flat mirror that the initial ray can reflect off of to undergo secondary RTs. Second, the high beam-quality reduces the diffraction loss in the external cavity that would otherwise significantly attenuate the power from the second RT. The contribution from the second RT can be seen in Fig. 4.16(d), where the spatial Fourier transform is plotted against the relative misalignment angles for the case of $L_{\text{ext}} = 30$ cm. The spatial frequency labeled $i = 2$ corresponds to the component that is periodic with $\lambda/4$, and remains relatively independent of the angle until it approaches the physical edges of the OAP. One interesting observation is the spectral broadening of the higher order RT components. We speculate that this is caused by, in part, the higher sensitivity of higher order bounces in generating regions of multistability for lower feedback levels C_i as suggested by the model in Fig. 4.10.

4.6 Self-mixing enhanced voltage instability

4.6.1 Detection sensitivity with an optical chopper

For higher signal-to-noise ratios, and faster signal acquisition, it is customary to implement an optical chopper for lock-in detection in a THz SM interferometric system [134, 155]. However, in experiments, moments of enhanced noise at the modulation frequency regimes accessible by the optical chopper (< 1 kHz) were observed. Fig. 4.17(a) shows a representative SM signal obtained with an optical chopper and lock-in detection. The chopping frequency was set at 100 Hz, and $L_{\text{ext}} = 17.8$ cm. Without any added attenuation, the coupling strength was large enough to be beyond weak coupling. However, as can be seen, the

SM signal is too noisy for any analysis. At first, this was suspected to be due to inaccurate positional readings of the translational stage. However, if this was true, this problem should be indifferent to the feedback strength. Instead, we found the noise to improve at lower levels of feedback, and furthermore, depend on how long it had been since the dewar was last cooled (further discussed in the subsequent section). Additionally, the stage is specified to have a minimum repeatable increment of 0.8 um, which is 0.75% of the emission wavelength.

To quantify a SM detection sensitivity, three wire-grid polarizers were used: two Microtech G30-S polarizers and an InfraSpecs FIR-MIR P03. The Microtech polarizers have nominal transmission of 97%, and a nominal extinction ratio of 74:1. Therefore, these polarizers alone could not sufficiently extinguish the SM signal. The InfraSpecs polarizer has a nominal transmission of 80%, and a nominal extinction ratio of >8000:1. The order orientation of the polarizers is depicted in Fig. 4.17(a). The initial polarizer was oriented for maximum transmission of the outgoing beam as to enforce the correct polarization state for all reinjected radiation to couple to the metasurface. This optical setup, assuming an ideally polarized source, allows for power attenuation ranging from -40 dB to -128 dB. We define ϵ_a as the factor of ϵ_1 in Eq. (4.2) associated with attenuation added by the crossed polarizers in a single RT. In general, ϵ_i also includes coupling loss due to the cryostat window, diffraction loss, misalignment, atmospheric absorption, and spatial mode mismatch at reinjection. In log scale, the SM signal amplitude versus the power attenuation factor, ϵ_a^2 can be fitted to a line as shown in Fig. 4.17(c). The minimum detectable SM signal occurs at -49 dB of added attenuation. Unlike the results obtained by Keeley et al. with the ridge waveguide laser, the noise floor here was limited by the voltage instability of the QC-VECSEL rather than current noise from the laser driver [208].

4.6.2 Investigation of voltage instability due to output coupler vibrations

To investigate this further, we monitored the terminal voltage of the device in the frequency domain via an oscilloscope. Without the presence of optical feedback, a particular tone at $\sim$920 Hz was always visible, as shown in Fig. 4.18(a). The fact that this tone is visible

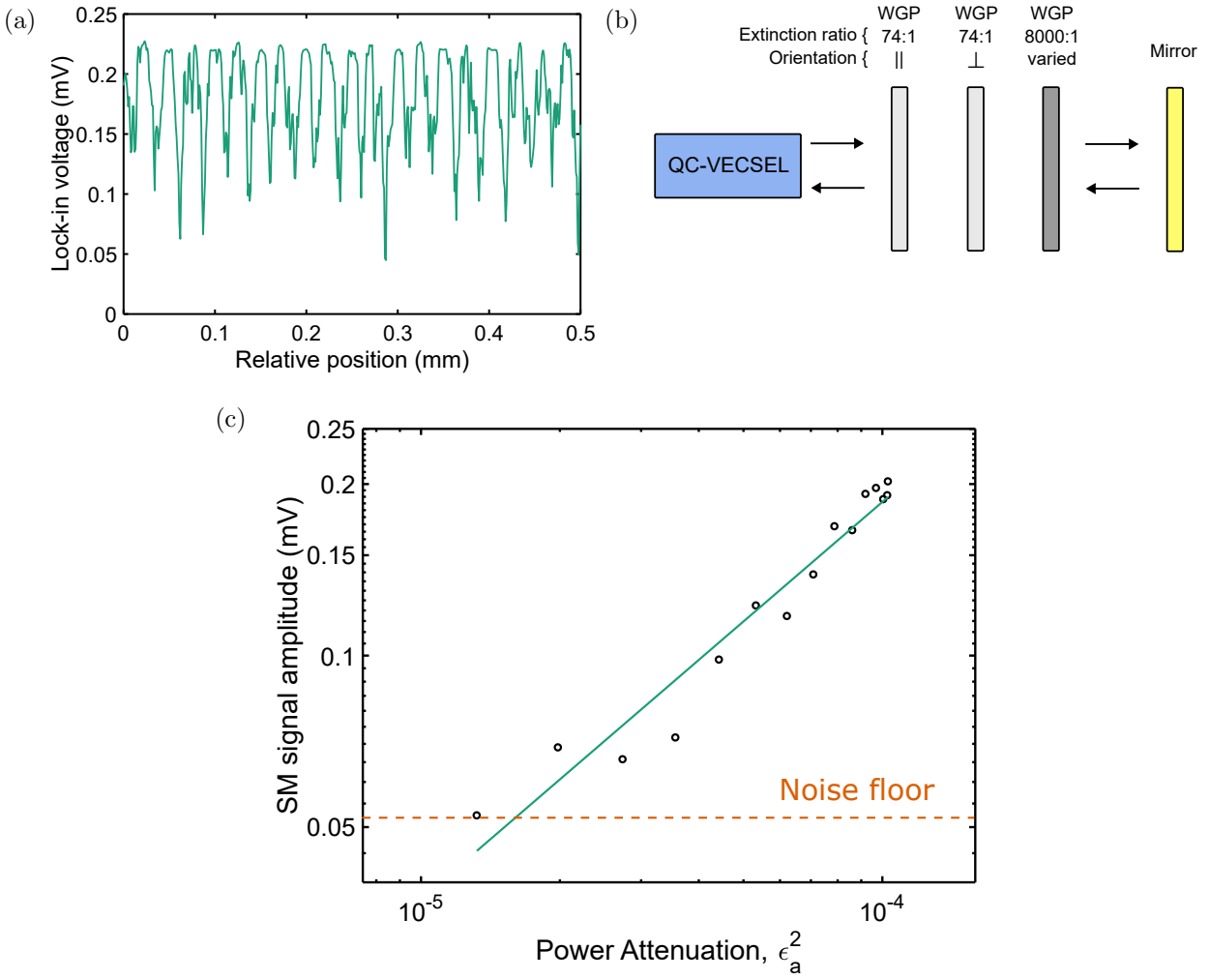

Figure 4.17: (a) Self-mixing signal measured with lock-in detection referenced to an optical chopper at 100 Hz. Relevant parameters: $L_{\text{ext}} = 17.8$ cm, $I = 400$ mA, $\Delta z = 2$ µm. (b) Simplified schematic of the optical path showing the order and orientation of the three polarizers used in the measurements for SM detection sensitivity (c) SM signal amplitude versus added power attenuation. -49 dB is the most amount of power attenuated by the crossed polarizers before a SM signal could no longer be discerned. $L_{\text{ext}} = 40.6$ cm

with the external mirror completely removed proves that this tone cannot be generated by vibrations of the external mirror. Instead, this tone is likely caused by the mechanical resonance of the quartz output coupler, and can vary depending on the thermo-mechanical state of the device. However, when optical feedback is introduced, this tone is amplified, and additional harmonics are generated due to the nonlinearity introduced by self-mixing at

large feedback levels (Fig. 4.18(b)).

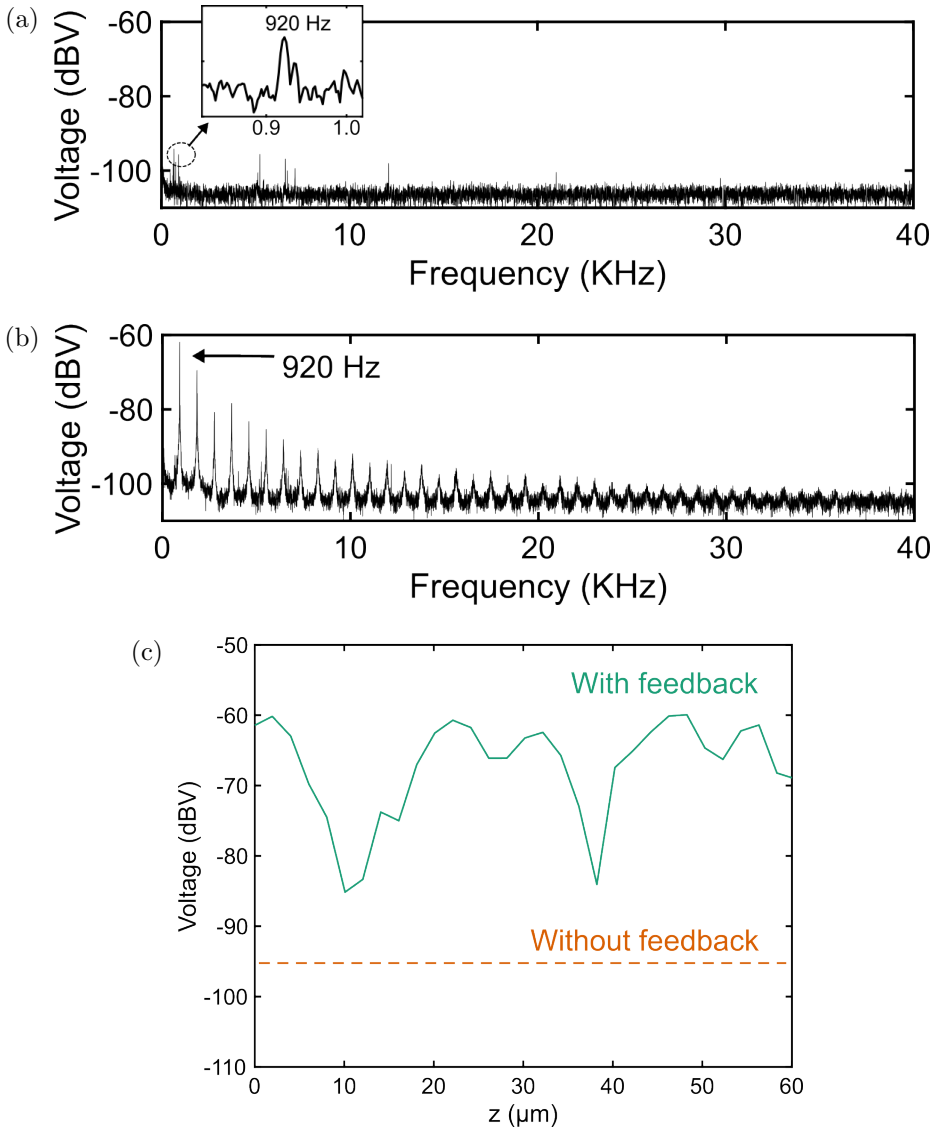

Figure 4.18: (a) AC-coupled averaged voltage spectrum of the device biased at 410 mA without optical feedback. The inset shows a resonance at ∼920 Hz. The spectrum is collected with a span of 40 KHz and a resolution bandwidth of 300 mHz. (b) Same conditions as (a), but with the presence of feedback. The harmonic tones are separated by 920 Hz. (c) Strength of the 920 Hz tone versus target mirror position. The orange dashed line shows the no feedback case as reference.

Additionally, we find that across all bias points and external cavity lengths, the presence of feedback always amplified the voltage instability. Fig. 4.18(c) plots the peak of the 920 Hz tone as the target mirror is swept across a half wavelength. Without feedback, the strength

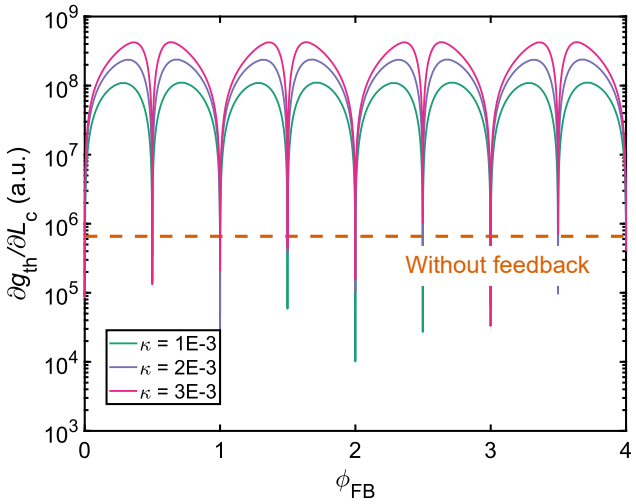

Figure 4.19: Simulated threshold sensitivity to internal cavity length as a function of feedback phase. The assumed values for the plots are: $Q_r = 24.5$, $L_c = 1$ mm, $L_{ext} = 23$ cm, and $\partial g_{th,0}/\partial f = 4.4$ cm^{-1}THz^{-1}. Three different coupling strengths are chosen: $\kappa = 1 \cdot 10^{-3}$, $\kappa = 2 \cdot 10^{-3}$, and $\kappa = 3 \cdot 10^{-3}$.

of the tone is measured to be -96 dBV with a 300 mHz resolution bandwidth. With feedback, the peak ranges from -85 dBV to -60 dBV, once again with a $\lambda/4$ periodicity. These results can be predicted based on the model established in Section 4.2. The mechanical vibration of the output coupler can be represented as small perturbations to L_c. The corresponding perturbations to the SM voltage can be written as

$$\frac{\partial V_{SM}}{\partial L_c} \propto \frac{\partial g_{th}}{\partial L_c} = \frac{\partial g_{th}}{\partial \omega}\frac{\partial \omega}{\partial L_c}, \tag{4.29}$$

where

$$\frac{\partial g_{th}}{\partial \omega} = \frac{\partial g_{th,0}}{\partial \omega} + \frac{2}{\xi}\sum_{i=1}^{n} i\kappa_i \tau_{ext} \sin(i\phi_{FB}), \tag{4.30}$$

and

$$\frac{\partial \omega}{\partial L_c} = -\frac{2\omega/c}{2L_c/c + \tau_{MS} + \sum_{i=1}^{n} i\kappa_i \tau_{ext} \cos(i\phi_{FB})}. \tag{4.31}$$

The first term in Eq. (4.30) corresponds to the changes in threshold gain due to perturbations in the emission frequency without feedback. This can come from the frequency dependence

of the metasurface resonance, output coupler reflectance, and the material gain lineshape. The frequency instability due to L_c for various feedback conditions is given by Eq. (4.31) and can be experimentally observed [212]. The expression suggests that the frequency stability can always be made better or worse depending on the feedback phase. However, in the case of the voltage stability, the perturbations to the threshold gain and the emission frequency are coupled, resulting in a more complicated dynamic. A set of simulated curves for $\partial g_{\mathrm{th}}/\partial L_c$ is shown in Fig. 4.19 for various levels of coupling strength. To be consistent with the experimental setup, we use the values $Q_r = 24.5$, $L_c = 1$ mm, $L_{\mathrm{ext}} = 23$ cm, and $\partial g_{\mathrm{th},0}/\partial f = 4.4$ cm^{-1}THz^{-1}. The latter parameter is estimated from the frequency dependence of the output coupler, since the spectrally dependent reflectance will vary the intrinsic lasing threshold. The plots verify the possibility for optical feedback to predominately exacerbate the instability of the laser terminal voltage — even by several orders of magnitude.

4.7 Self-mixing interferometry via small-signal modulation

4.7.1 Self-mixing voltage signal

Due to the phenomenon observed in Section 4.6, it is important that any SM interferometric system using the QC-VECSEL is configured to measure its signals spectrally far from the mechanical noise regime. This is especially true for higher levels of feedback. One way to achieve this is via small-signal modulation of the current source. Because the intrinsic frequency of the laser is a function of injected current, modulating the current modulates the intrinsic phase, $\phi_0 = \omega_0 \tau_{\mathrm{ext}}$. In other words, the current modulated SM signal can be written as

$$V'_{\mathrm{SM}} = \frac{\mathrm{d}V_{\mathrm{SM}}}{\mathrm{d}I} = \frac{\mathrm{d}V_{\mathrm{SM}}}{\mathrm{d}\phi_{\mathrm{FB}}} \frac{\mathrm{d}\phi_{\mathrm{FB}}}{\mathrm{d}\phi_0} \frac{\mathrm{d}\phi_0}{\mathrm{d}I}. \tag{4.32}$$

Each factor in the rhs is given by

$$\begin{aligned}\frac{\mathrm{d}V_{\mathrm{SM}}}{\mathrm{d}\phi_{\mathrm{FB}}} &= \frac{2}{\xi}\sum_{i=1}^{n} i\kappa_i \sin\left(i\phi_{\mathrm{FB}}\right) \\ \frac{\mathrm{d}\phi_{\mathrm{FB}}}{\mathrm{d}\phi_0} &= \frac{1}{1+\sum_{i=1}^{n} iC_i \cos(i\phi_{\mathrm{FB}} + \arctan(\alpha_{\mathrm{eff}}))} \\ \frac{\mathrm{d}\phi_0}{\mathrm{d}I} &= \tau_{\mathrm{ext}}\frac{\mathrm{d}\omega_0}{\mathrm{d}I}.\end{aligned} \tag{4.33}$$

Plugging these equations back in, we arrive at a modified SM voltage signal given by

$$V'_{\mathrm{SM}} \propto \frac{2}{\xi}\frac{d\omega_0}{dI}\frac{\tau_{\mathrm{int}}}{\sqrt{1+\alpha_{\mathrm{eff}}^2}}\frac{\sum_{i=1}^{n} iC_i \sin(i\phi_{\mathrm{FB}})}{1+\sum_{i=1}^{n} iC_i \cos(i\phi_{\mathrm{FB}} + \arctan(\alpha_{\mathrm{eff}}))}\Delta I. \tag{4.34}$$

While V_{SM} is a signal produced by feedback induced changes in the threshold gain, V'_{SM} is the signal produced by feedback induced changes in the differential resistance associated with photon-assisted transport. We modulate the current source by 0.80 mA peak-to-peak at 100 kHz (limited by the bandwidth of our lock-in amplifier). This current modulation corresponds to a frequency modulation of ∼13.5 MHz/mA [212] of the laser mode. At an external cavity length of 61 cm, this corresponds to a phase modulation of $\Delta\phi_0 = 0.09\pi$.

4.7.2 Measurement of electrical tuning range

As a proof of concept of the measurement technique, the modulated SM signal is collected as the current is swept across the dynamic range. With the external mirror fixed, a SM signal is produced by the change in emission frequency with electrical bias point. That is,

$$\frac{\Delta\phi_0}{\Delta I} = \frac{\Delta\omega_0}{\Delta I}\frac{2L_{\mathrm{ext}}}{c}. \tag{4.35}$$

As shown in Fig. 4.20(a), the measurement is repeated for reduced cavity lengths in increments of 5 µm which will act as a horizontal shift of the relative phase; the curves are vertically offset for visual clarity. Additionally, each curve is a result of taking the difference between a current sweep with and without feedback to only show the contribution from the

self-mixing (Fig. 4.20(b) shows the differential resistance versus current without the presence of feedback). We can see that in each curve, there is a sharp dip at $I = 382mA$, corresponding to the laser threshold. Before threshold, the signal is flat bf — indeed, there cannot be any SM signals when the device is not lasing. After threshold, however, SM oscillations begin to appear.

There are two key observations to highlight. First, the signal morphology is different than what is usually observed in SL interferometry. This is because the waveform is given by V'_{SM} from Eq. (4.34), rather than the more familiar form in Eq. (4.26). A simulated sample waveform is shown in Fig. 4.21 for the case of two RTs, $C_1 = 0.2$, and $\alpha = 0.5$. We can see that these waveforms are more tangent-like than they are sinusoidal, and higher levels of feedback are marked by infinite discontinuities. The second key observation is the aperiodicity of the signal with current. If frequency tuning was linear with current, then the observed SM signal will be periodic throughout the dynamic range. Instead, the oscillations are faster near and far from threshold, and slower in the middle sections of the dynamic range. When the local tuning coefficient is small, the SM amplitude is also reduced since the signal is proportional to $\mathrm{d}\omega_0/\mathrm{d}I$, as shown in Eq. (4.34). This, in part, is why each subsequent curve in Fig. 4.20(a) is not exactly a phase-shifted copy of one with a different L_{ext}. Overall, the signal morphology can be quite complicated, since it is influenced by the changing coupling strength with bias, the changing linewidth enhancement factor with bias, and possible changes in coupling strength with L_{ext} that can arise from an imperfectly aligned system.

It is no surprise the tuning isn't perfectly linear, and in fact the results agree closely with what was directly observed using a mixer for a QC-VECSEL fabricated from the same active region [212]. Nevertheless, by counting fringes, the tuning range can be estimated. The waveforms show six total fringes, corresponding to $\Delta\phi_0 = 6\pi$ for the two RT case. For $L_{\mathrm{ext}} = 53$ cm, this results in a total tuning range of $\Delta\nu \approx 843$ MHz. With a dynamic range of 62.3 mA, this corresponds to an average tuning coefficient of 13.5 MH/mA. This range is consistent with what is commonly observed for THz QC-lasers, owing to the blue-shift of

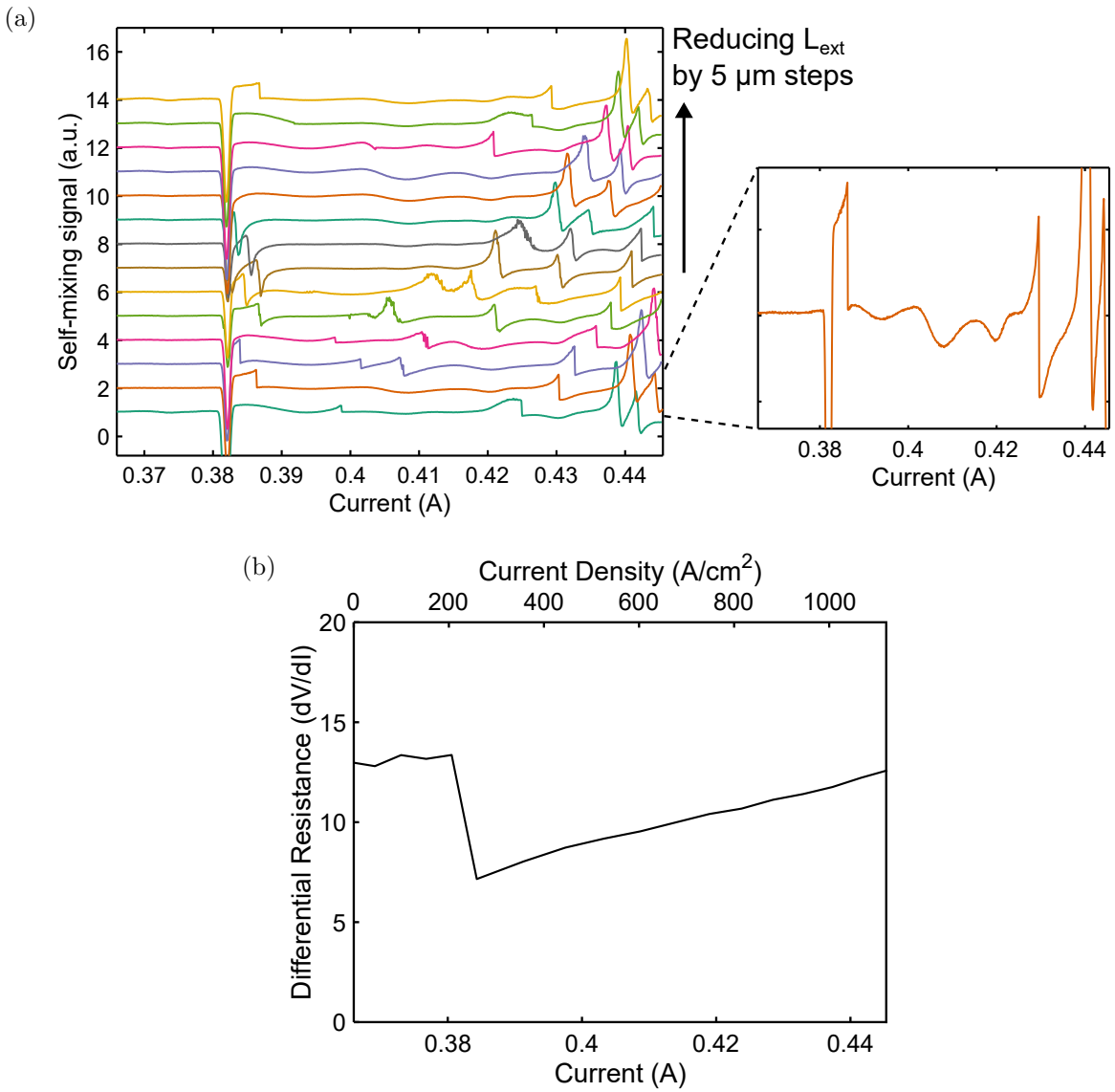

Figure 4.20: (a) Self-mixing signal from current sweep using small-signal current modulation technique. Starting from bottom up, each curve is separated by 5 μm decrements of the external cavity length. The plots are obtained by taking the difference between with and without feedback. The adjacent plot is a zoomed window of a single curve, more clearly showing the oscillations throughout the dynamic range. (b) Differential resistance versus bias current. The sharp drop indicates the lasing threshold at 382 mA.

the gain peak of the active material [32, 213, 214].

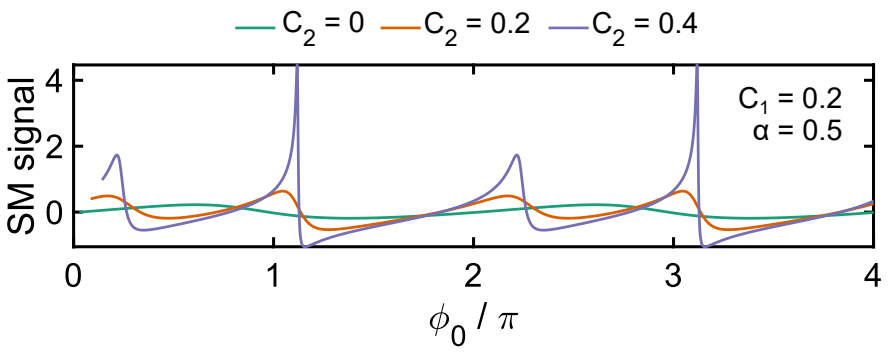

Figure 4.21: Simulated self-mixing signals based on the small-signal current modulation technique for the case of two roundtrips. The plots assume fixed values $C_1 = 0.2$ and $\alpha = 0.5$ as C_2 is varied.

4.7.3 Identifying weak and moderate feedback regimes

While this alternate measurement scheme was motivated by operating away from mechanical noise, it comes with two additional benefits. One, modulation at higher frequencies allows faster lock-in detection and faster data acquisition rates. Two, signals corresponding to the moderate feedback regime become easily identifiable due to infinite discontinuities in differential resistance at the jump points (see Fig. 4.10). Fig. 4.22(a) shows an SM signal collected in the weak feedback regime, and one collected in the moderate feedback regime. The feedback level was controlled via crossed polarizers, allowing for additional RT field attenuation, ϵ_a, all the way down to the noise floor. Fig. 4.22(b) plots the maximum slope of the SM signal as the feedback level is gradually increased. The curvature follows from Eq. (4.34), but eventually saturates due to the discrete step size in z. Nevertheless, since our step size is much smaller than the periodicity ($\Delta z = 1$ μm), it allows us to easily identify excursions into the moderate feedback regime. We find that despite the large reflectance of the output coupler, the VECSEL is susceptible to moderate levels of feedback for cavity lengths up to 81 cm. Additionally, the relative feedback contributions from the first and second RT can vary significantly with attenuation and cavity length.

The color plots in Fig. 4.22(c) illustrate the obtained V'_{SM} signal for various levels of added attenuation. The three color plots, from left to right, show the case for $L_{\mathrm{ext}} = 41$

cm, $L_{\text{ext}} = 61$ cm, and $L_{\text{ext}} = 81$ cm respectively. The horizontal dashed line indicate the border between weak and moderate feedback regimes. When the feedback level is high, and the cavity length is sufficiently short, the SM signals appear to be dominated by the second RT term. However, as further attenuation is added, C_1 becomes much larger than C_2, and the signal begins to recover $\lambda/2$ periodicity because the second RT term is attenuated by ϵ_a^2. Finally, as the external cavity length is further extended, the diffracted loss experienced by the second RT beam becomes large enough that its effects become extinguished. We also note that the device was biased near threshold, but these trends were similar across different bias points of the laser. These color plots exemplify the distinct behavior of a QC-VECSEL SM interferometer under various feedback conditions. Much of the well-developed analytical and analog processing techniques only work when higher-order RT reflections can be ignored [134, 153, 155, 179, 215–217]. Therefore, extra care must be taken in the interpretation and processing of SM signals acquired from these devices.

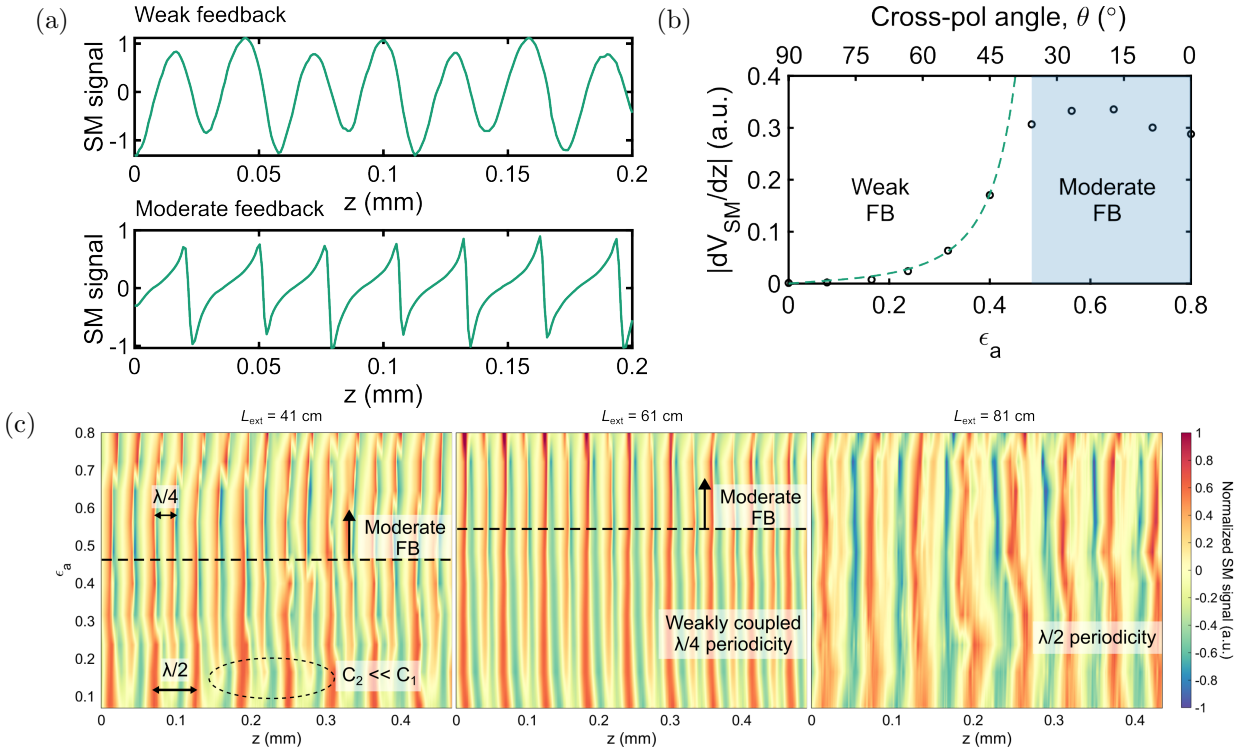

Figure 4.22: (a) Measured self-mixing signals according to Eq. (4.34) in the weak feedback regime and the moderate feedback regime. (b) Maximum differential voltage as a function of field attenuation. The dashed curve show a trajectory according to Eq. (4.34). The blue shaded region corresponds to the moderate feedback regime. (c) Color plots of the SM signal for various levels of additional field attenuation via crossed-polarizers. The horizontal dashed lines indicate the approximate border between weak and moderate feedback. The dashed oval indicates a region where the feedback contribution from the second RT is much smaller compared to the first. The three color plots show data obtained for three different external cavity lengths: $L_{\text{ext}} = 41$ cm, $L_{\text{ext}} = 61$ cm, and $L_{\text{ext}} = 81$ cm.

CHAPTER 5

Conclusion

5.1 Metasurface engineering for the QC-VECSEL

It has been demonstrated that the QC-VECSEL as a broadband tuning source can be designed to occupy bands throughout the 1.76–5.72 THz range, all while maintaining high quality beam patterns and output powers of a few to tens of milliwatts. The technology promises to fill a gap that concerns fields such as tunable absorption spectroscopy and frequency-agile heterodyne spectroscopy. The accomplishments detailed in this thesis make significant strides towards this goal. They include:

- Establishing fundamental wavelength scaling rules for the QC-VECSEL metasurface. Scaling the metasurface is not as straightforward as proportionally scaling the entire geometry. This is because both material loss and gain do not scale favorably, and the metasurface thickness has additional consequences in thermal performance for continuous-wave operation. For frequencies below 3 THz, the metasurface gain interaction length ξ increases, reducing the outcoupling efficiency of the VECSEL. This can be mitigated by reducing the metasurface period, but reducing it below $\lambda_0/2$ can introduce self-lasing dark modes. For frequencies above 4 THz, ξ drops significantly due to the quadratic dependence with wavelength, and increases the lasing threshold. This is exacerbated by increased losses due to closer proximity to the *Reststrahlen* band. Additionally, the low radiative quality factors result in larger coupling factors with lossy surface propagating modes of the metasurface. For such metasurfaces, high reflectance

output couplers are needed. Additionally, it is important to forgo scaling down the metasurface thickness in order to curtail increased waveguide losses.

- Demonstration of broadband tunable QC-VECSELs centered at 2.77 THz, 4.53 THz, and 5.56 THz. This includes the demonstration of the highest frequency emission from a QC-VECSEL to date, measured at 5.72 THz. The metasurfaces were designed using a combination of theoretical models detailed in this thesis and finite-element-method COMSOL simulations. The metasurfaces were fabricated in the UCLA Nanolab and — in part — the UCSB Nanofabrication facility. Information on fabrication processes is found in Appendix B.

Indeed, there are multiple paths for future improvement. First, more work must be done to realize devices with optimized combinations of active region, output coupler, metasurface quality factor, and cavity, in order to obtain higher output powers in continuous-wave mode across the 1.5-6 THz band. By operating in the $m = 1$ or $m = 2$ mode of optimized low-Q metasurface devices, fractional tuning ranges of $\sim$30% should be achievable. This would allow full coverage of the 1.5–6 THz range with just 4–5 devices.

Second, there is much room for improvement of the intracryostat cavity tuning mechanism. For example, one could envision replacing the piezoelectric motor with an integrated MEMS output coupler mirror that would rapidly scan the cavity over an FSR at kilohertz rates. Such a device would be similar to swept-wavelength VCSELs and could have applications in time-resolved laser absorption spectroscopy and swept-source optical coherence tomography [218, 219]. Another promising approach would be metasurface output coupler mirrors with optoelectronic control of the reflection phase, due to their fast modulation speeds (>100 MHz) and lack of moving parts [220, 221]. To be suitable to use with the VECSEL, such a metasurface output coupler would need to be partially transmitting, and have sufficiently low loss so that reflectances >90% could be obtained across the tuning band.

Third, to be suitable for high-resolution spectroscopy, instrumentation effort must be spent on stabilization. Due to mechanical vibrations, the QC-VECSEL has free-running linewidths on the order of 50 MHz, more than an order of magnitude higher than those

demonstrated by monolithic devices. Both phase locking and optical injection locking of the QC-VECSEL with stable electronic sources have since been reported [176, 212]. These demonstrations were important to establish validity of the architecture as potential sources for high-resolution applications. The stability can also be improved by using longer cavity lengths, such as that of the OAP-based cavity, which showed free-running linewidths on the order of tens of kilohertz [111]. Indeed, the challenge will be how to combine this with the movable OCs required for broadband tunability.

5.2 Study of self-mixing and optical feedback in the QC-VECSEL

Self-mixing interferometry is studied for the first time in the THz QC-VECSEL, and new phenomenology is observed. Key accomplishments and findings in this thesis include:

- A theoretical model for self-mixing in the QC-VECSEL is established. The model is a modified Lang-Kobayashi steady-state model that includes the QC-VECSEL round-trip phase condition, and a generalization to multiple round-trips. The established model allows extraction of key fitting parameters for self-mixing signals such as coupling strength and effective linewidth enhancement factor of the gain-loaded metasurface.

- Observation of multi-bounce self-mixing prevalent in a large range of feedback conditions. Such phenomenon has not been reported in conventional ridge waveguide THz QCLs. This can be understood as a consequence of the VECSEL's excellent beam quality, large millimeter-scale emitting aperture, and the fact that the output coupler is a large flat mirror which allows multiple round trips to survive in the feedback cavity.

- Observation of feedback-induced voltage instability of QC-VECSEL self-mixing signals. The instability of the device terminal voltage associated with vibrations of the output coupler is enhanced by optical feedback. Such phenomenon agrees

with the theoretical models and demonstrates the importance of addressing this excess noise in any QC-VECSEL self-mixing system.

- An alternative self-mixing detection scheme is demonstrated involving small-signal current modulation and lock-in detection. The electrical modulation, rather than conventional optical chopper systems, allow for lock-in referencing far from the enhanced noise regimes for the QC-VECSEL. Such a detection scheme also allows for much faster detection, with detection speeds only limited by the driver bandwidth and RC time constants of the biasing circuit.

The QC-VECSEL has the potential to be a powerful SM sensor. The combination of excellent beam pattern with the ability to choose the output coupler reflectance, allows one to deliberately reach high feedback coupling strengths, and obtain the concomitant high sensitivity. Being able to modify the feedback sensitivity with choice of OC is a unique feature of the VECSEL and is a potential avenue for future study. Furthermore, QC-VECSELs have been shown to exhibit broadband single-mode tunability ($\sim$19%) by using ultrashort cavities with piezoelectrically tunable lengths [25,30]. Such a laser is potentially equipped to perform broadband SM interferometry for hyperspectral or 3D depth resolved imaging, solid-state or multi-species gas-phase spectroscopy, and measurement of complex refractive indices in the THz band. The device may also serve as a versatile platform for self-characterization and studying feedback effects across the gain bandwidth.

Whether as standalone devices, or as part of a hybrid electronic-photonic system, the metasurface VECSEL approach is a significant step towards realizing THz QC-lasers' long-promised potential as practical spectroscopic tools.

APPENDIX A

Appendix: Active region information

The gain material is grown on a GaAs wafer via molecular-beam epitaxy. Device B uses a wafer grown by IQE plc, and the others use wafers grown by Sandia National Laboratories. The GaAs/AlGaAs growth sequence for each device featured in this dissertation is listed below. The values are provided in angstroms, and the bold values indicate the AlGaAs barriers. Each growth has a nominal doping level of 5×10^{16} cm^{-3} in the underlined layer.

Table A.1: Active region label and growth sequence for each device featured in this dissertation.

Name	Wafer	Growth sequence	Repetitions
Device A [117]	VA1032	113/**21**/103/**37**/88/**40**/<u>177</u>/**54**	150
Device B [25]	IQE1002256	106/**20**/106/**37**/88/**40**/<u>172</u>/**51**	80
Device C [30]	VB0739	103/**17**/107/**37**/88/**37**/<u>172</u>/**51**	163
Device D [25]	VB1247	95/**14**/110/**18**/85/**31**/<u>162</u>/**37**	89
Device E [26]	VB1401	86/**17**/97/**28**/75/**31**/<u>147</u>/**40**	127
Device F [26]	VB1401	86/**17**/97/**28**/75/**31**/<u>147</u>/**40**	127
SMI Device [200]	IQE1002256	106/**20**/106/**37**/88/**40**/<u>172</u>/**51**	80

APPENDIX B

Appendix: Metasurface fabrication process

Some variation in the fabrication flow exists between the six devices featured in this dissertation. In this section, the most up to date fabrication flow is provided.

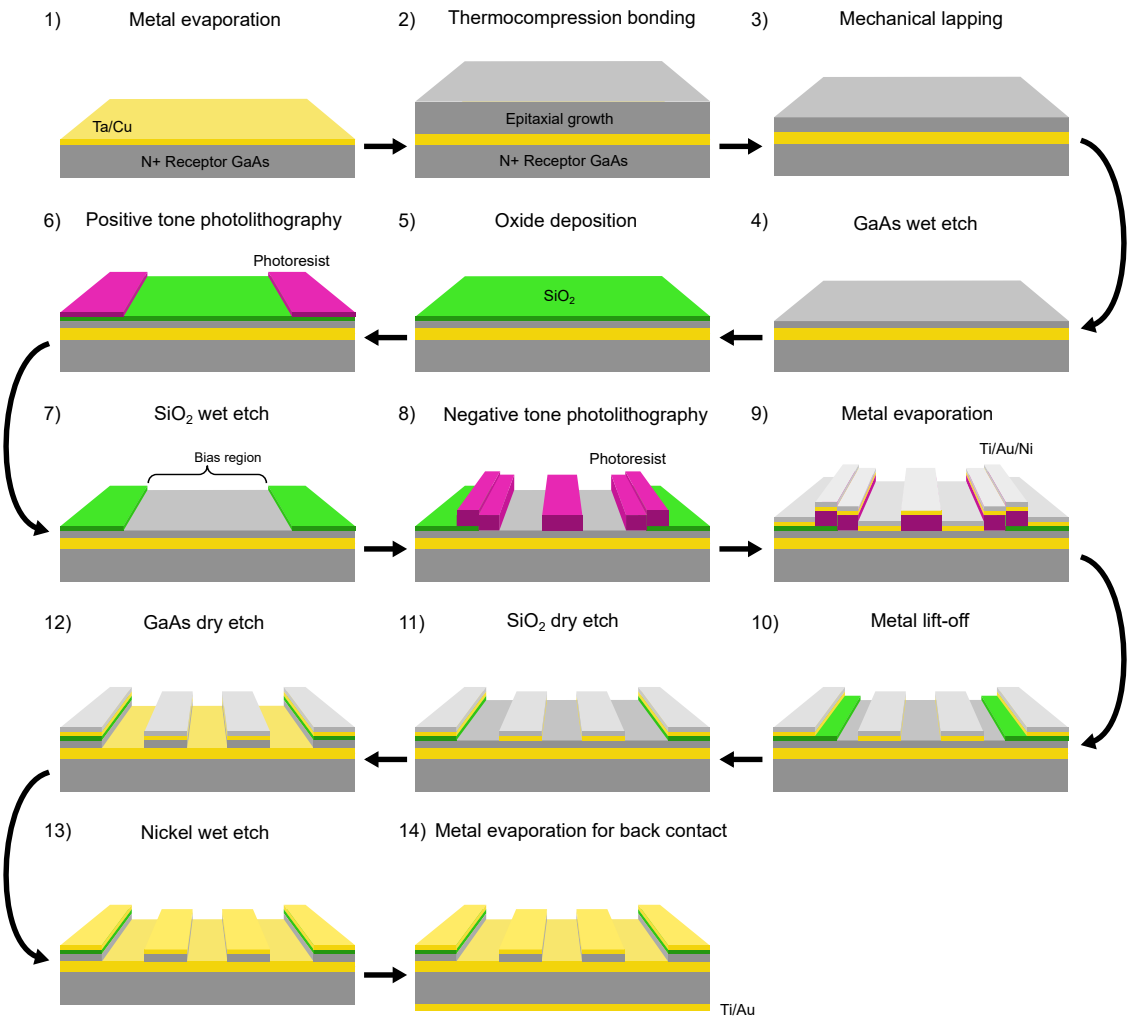

Figure B.1: Metasurface fabrication flow

1. Metal evaporation of 10/300 nm Ta/Au on epitaxial wafer and N+ GaAs receptor wafer. The wafers are cleaved into ∼1 cm square pieces.

2. Thermocompression bonding of the epitaxy piece and the receptor piece. The bonding is performed using the Karl Suss SB 8e bonder at 350°C for 1 hour followed by a 1 hour anneal.

3. The epitaxial substrate is thinned down via mechanical lapping until about 50 µm of the substrate remains.

4. The remaining substrate is removed with a citric acid selective wet etch, which stops on a 100 nm thick $Al_{0.55}Ga_{0.45}As$ layer. The citric acid solution is a 4:1 volumetric ratio of citric acid solution to hydrogen peroxide. Afterwards, the etch-stop layer is removed via a brief dip into hydrofluoric acid. Additionally, because the metasurface has areas that we wish to selectively bias, the 100 nm doped layer that caps the QC stack is removed. This layer is wet etched with a 490/3/5 volumetric ratio of water, hydrogen peroxide, and ammonium hydroxide.

5. A ∼200 nm film of SiO_2 is deposited via PECVD.

6. Photolithography is performed using positive tone AZ 5214 photoresist to define the bias region. The photoresist is spun at 3500 rpm, soft baked at 105°C for 1 minute, developed in a 1:5 solution of AZ 400 and water for 40 seconds, and hard baked at 150°C for 3 minutes.

7. The SiO_2 is wet etched using buffered oxide etch (BOE). The bias region is defined in this step.

8. Photolithography is performed using negative tone AZ nLOF 2020 photoresist to define the metasurface antennas. The photoresist is spun at 3500 rpm, soft baked at 110°C for 1.5 minutes, post-exposure

baked at 110°C for 1 minute, and developed in AZ 300 MIF for 1 minute.

9. Metal evaporation composed of 15/200/250 nm Ti/Au/Ni. The Ni layer acts as a self-aligning mask for the subsequent dry etch.

10. SiO_2 dry etch using fluorine based ICP-RIE (STS AOE recipe: OXIDAPIC).

11. Dry etch of the GaAs/AlGaAs QC active region via chlorine based ICP-RIE (PlasmaTherm SLR 770). The gases used include 50 sccm BCl_3, 3 sccm Cl_2, and 3 sccm N_2.

12. The remaining Ni is then removed with a commercial Nickel etchant (Nickel Etchant TFB).

13. Metal evaporation of a 15/300 nm Ti/Au film on the backside of the receptor piece to define the back contact.

APPENDIX C

Appendix: More on improving QC-VECSEL efficiency

For a uniform ridge based metasurface, the output power of the QC-VECSEL can be written as

$$P_{out} = N_p \frac{h\nu}{e} \underbrace{\frac{\tau_{\text{eff}}}{\tau_2 + \tau_{\text{eff}}}}_{\eta_i} \underbrace{\frac{\ln\left(R_{\text{OC}}^{-1}\right)}{\ln\left(R_{\text{OC}}^{-1}\right) + \xi(\nu) g_{\text{tr}}} \frac{T_{\text{OC}}}{1 - R_{\text{OC}}}}_{\eta_{\text{opt}}} \underbrace{\frac{\left(\int\limits_{\text{act}} |E_z|^2 \, dA\right)^2}{A_{\text{act}} \int\limits_{\text{act}} |E_z|^4 \, dA}}_{\eta_{\text{u}}} (I - I_{\text{th}}) \,, \tag{C.1}$$

where N_p is the number of quantum-cascade periods, τ_{eff} is the effective population inversion lifetime that accounts for a non-unity injection efficiency, τ_2 is the non-radiative relaxation time of the lower lasing level, R_{OC} is the reflectance of the output coupler, ξ is the metasurface effective gain interaction length, g_{tr} is the metasurface transparency gain, T_{OC} is the transmittance of the output coupler, A_{act} is the cross-sectional area of the active antennas, E_z is the electric field in the antennas oriented in the direction that satisfies the intersubband selection rule, and I_{th} is the threshold current.

The terms in Eq. C.1 can be grouped into key parameters. Parameter η_i is the internal quantum efficiency, which reflects both the non-unity injection efficiency into the upper lasing level, and the non-zero relaxation time of the lower lasing level. Parameter η_{opt} is the optical efficiency, which quantifies the fraction of total energy lost to outcoupled radiation. This term also includes the output coupler efficiency which takes into account any material losses within the OC. Lastly, the parameter η_{u} is the modal uniformity factor. Since the field profile inside the radiating antennas is based on an anti-symmetric half-wavelength resonance, the field pattern has a null in the center of the ridge, and the field intensity throughout the active

material is not spatially uniform. Therefore, these regions of low intensity result in excess current that does not contribute as much to stimulated emission. The modal uniformity factor for the basic patch antenna is exactly $\eta_{\mathrm{u}} = \frac{2}{3}$, assuming a spatially uniform field incident on the metasurface.

Based on Eq. C.1, the equation for WPE above threshold can be written:

$$\mathrm{WPE} = \underbrace{\frac{N_p h\nu}{eV}}_{\eta_V} \eta_i \eta_{opt} \eta_u \underbrace{\frac{I - I_{th}}{I}}_{\eta_I}, \tag{C.2}$$

where η_V can be defined as a voltage efficiency, and η_I as a current efficiency. The internal quantum efficiency, η_{i}, is purely dictated by the active region design and growth quality. The primary design considerations for the metasurface and VECSEL are the optical efficiency, η_{opt}, and the lasing threshold, I_{th}. How these parameters relate to the overall design, and the trade-offs between the two, are the driving points of Chapters 2 and 3. In this appendix, we briefly address the auxiliary sources of reduced wall-plug efficiency, such as the active region voltage defect, parasitic voltage drops, non-unity modal uniformity factor, and non-unity OC efficiency.

C.1 Voltage efficiency

Above threshold, the voltage across the device can be written as

$$V = N_{\mathrm{p}}(\frac{h\nu}{e} + \Delta_{\mathrm{inj}}) + V_{\mathrm{p}} \tag{C.3}$$

where $h\nu$ is the laser transition energy, Δ_{inj} is the active region voltage defect (the net voltage drop per module in the QC active region that does not contribute to radiation), and V_{p} subsumes all parasitic voltage drops due to parasitic resistances in the entire biasing circuit. As illustrated in Fig. C.1, we can decompose the total measured voltage drop, in

order of high to low potential, into

$$V = IR_{\mathrm{D+}} + IR_{\mathrm{top}} + V_{\mathrm{sb}} + V_{\mathrm{QC}} + IR_{\mathrm{con}} + IR_{\mathrm{sub}} + IR_{\mathrm{In}} + IR_{\mathrm{Cu}} + IR_{\mathrm{D\text{-}}}. \tag{C.4}$$

An explanation of each term is given below:

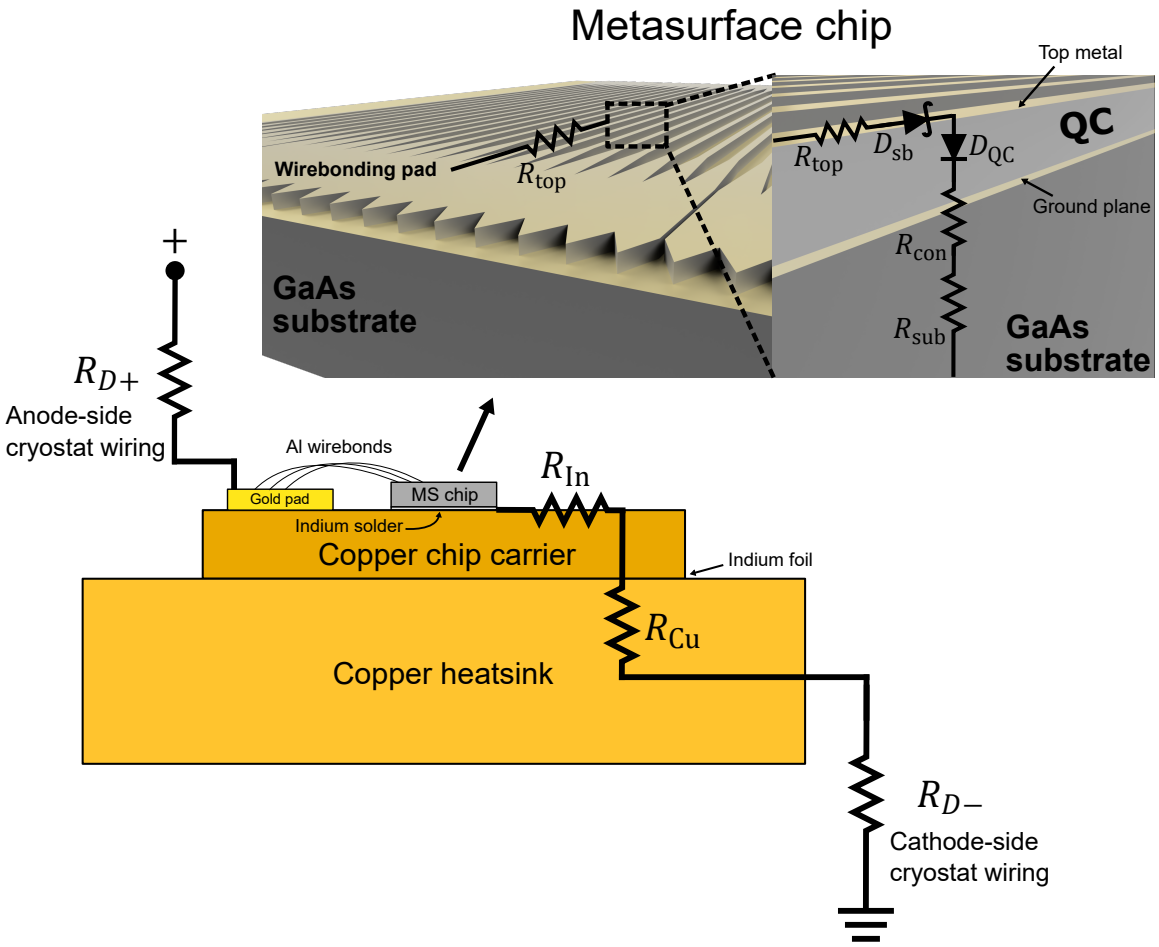

Figure C.1: Schematic of the entire biasing circuit for the QC-VECSEL. The metasurface chip illustration shows a simplified circuit model that includes the various contributions to the overall voltage. The inset shows the metasurface antenna cross-section that includes the top metal, QC active region, ground plane, and the n+ GaAs substrate.

- $\mathbf{R}_{\mathrm{D+}}$: The anode-side wiring external to the metasurface which include the wirebonds, gold pad, SMA connectors and cryostat feedthrough.

- $\mathbf{R}_{\text{top}}$: Parasitic resistance of the top Ti/Au film between the wire-bonding pad and the metasurface bias region. The thickness of the Au film is 200 nm — such a thickness maintains resistivity values close to bulk values [222]. At 80 K, close to typical operating temperature of the QC-VECSEL, the resistivity of gold is $0.48 \times 10^{-8}\ \Omega\,\text{m}$ [223]. This results in a sheet resistance of 24 mΩ per square. The equivalent R_{top} will then depend on the length and width of the antennas, and the number of periods within the bias region.

- $\mathbf{V}_{\text{sb}}$: The forward voltage of the Schottky barrier formed by the top metal and the QC active region interface. This can be measured using the well-known $C - V$ method, which takes advantage of the linear $1/C^2$ vs V relationship of the Schottky diode given by $1/C^2 = 2(V_{\text{sb}} - V_{\text{a}})/q\epsilon N_d$, where V_{sb} is the built-in potential. Because the built-in potential depends on the doping concentration, the measured V_{sb} have ranged from 0.64 V to 0.73 V across various QC epitaxial wafers.

- $\mathbf{V}_{\text{QC}}$: The total voltage drop across the QC active region. This can be written as $V_{\text{QC}} = N_{\text{p}}(h\nu/e + \Delta_{\text{inj}})$. The voltage defect, Δ_{inj}, is not necessarily a parasitic term, but corresponds to the energy separation between the lower lasing level and the injector level. However, since this potential difference does not directly generate photons, it is a source of reduced WPE. The value of Δ_{inj} depends on the active region design, but is typically around 36 mV or greater for the designs used in this dissertation.

- $\mathbf{R}_{\text{con}}$: The contact resistance of the non-alloyed ohmic contact at the interface between the QC material and the ground plane. These ohmic contacts, formed by a highly doped n++ GaAs layer and a thin low-temperature grown cap layer, have proven to be high per-

formance contacts with specific contact resistances on the order of $\rho_c = 10^{-7}\ \Omega\,\mathrm{cm}^2$ [224].

- $\mathbf{R}_{\mathrm{sub}}$: Resistance of the n+ GaAs receptor substrate. The receptor substrate is doped on the order of $10^{18}\ \mathrm{cm}^{-3}$ and has a thickness of 500 µm. Based on the typical active areas of the metasurface ($\sim\ 10^{-3}\ \mathrm{cm}^2$), the substrate resistance proves to be relatively negligible ($R_{\mathrm{sub}} \ll 1\ \Omega$).

- $\mathbf{R}_{\mathrm{In}}$: Net resistance of the ohmic contact between the n+ GaAs receptor substrate and the Ti/Au back contact, and the indium solder joint that is used to solder the metasurface chip onto an OFHC copper chip carrier. The dominant contribution is most likely the back-side ohmic contact, since no special treatment is performed.

- $\mathbf{R}_{\mathrm{Cu}}$: Bulk resistance of the copper chip carrier and the copper heatsink. At 80 K, the bulk resistivity of copper is $0.2 \times 10^{-8}\ \Omega\,\mathrm{m}$. Since copper is a great conductor, and the current path length is at most a couple centimeters, R_{Cu} should be quite negligible.

- $\mathbf{R}_{\mathrm{D\text{-}}}$: The cathode-side wiring of the cryostat which includes connection to a female SMA outer conductor, a male-to-male SMA cable, and finally the cryostat feedthrough.

As a representative example of the parasitic voltage drops observed in a typical fabricated metasurface, consider the *L-I-V* of Device B shown in Fig. C.2(a). At the bias point generating maximum power output, the voltage across the device (measured at the cryostat SMA feedthrough) is 8.48 V. The QC active region design shows 54 mV/module at design bias based on *nextnano* non-equilibrium Green's function (NEGF) simulations, which implies a voltage defect of $\Delta_{\mathrm{inf}} \approx 43$ meV. There are a total of 80 modules, resulting in a total $V_{\mathrm{QC}} = 4.32$ V, which corresponds to a voltage efficiency of $\eta_V = 0.11$ and a total of 4.16 V in parasitic voltage drop external to the active region. A separate metasurface chip from

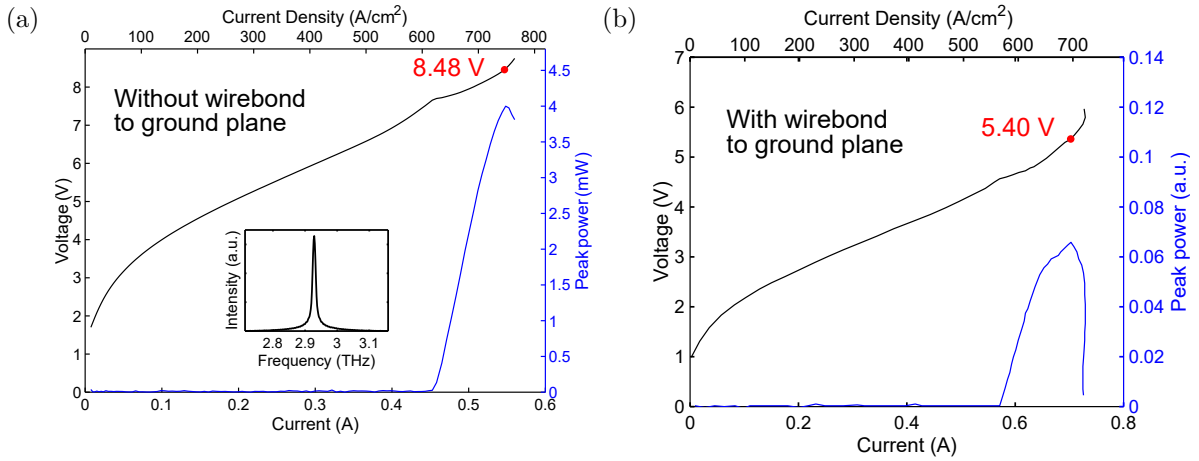

Figure C.2: (a) *L-I-V* characteristic of Device B at 77 K using a highly reflective Si P10-A4 output coupler. There are no wirebonds to the ground plane, and the device is biased through the GaAs substrate. The measured voltage at maximum power output is 8.48 V (b) *L-I-V* characteristics of a different device from the same wafer in which there were wirebonds to the ground plane, circumventing biasing through the substrate and back-side contact. The measured voltage at maximum power output is 5.40 V. Measurement in (b) credit to Chris Curwen.

the same active region in which the ground plane was directly wirebonded to the copper chip carrier demonstrated a bias voltage of about 5.4 V, as shown in Fig. C.2(b). This is a 3.08 V difference in the bias voltage with and without wirebonding to the ground plane — by far the largest source of parasitic voltage drop in the circuit. This is due to the poor ohmic contact formed by the GaAs receptor substrate and the back-side gold contact, which forms a reverse-biased Schottky diode. Since the GaAs substrate doping is on the order of 10^{18} cm^{-3}, the breakdown voltage of this junction can indeed be a few volts [225].

With wirebonding to the ground plane, the voltage efficiency is brought up to $\eta_V = 0.17$. Additionally, we know that the forward voltage of the top metal Schottky contact contributes about 0.7 V. This Schottky contact is not trivial to remove, since any attempt at forming an ohmic contact may introduce additional waveguide loss to the metasurface mode. Nevertheless, taking into account the Schottky voltage, this leaves about 0.38 V remaining, which is distributed among the remaining parasitics: $R_{\mathrm{D+}}$, R_{top}, R_{con}, R_{Cu}, and

$R_{\text{D-}}$. Based on the estimated sheet resistance of 24 mΩ for the top metal, the total voltage drop from R_{top} in Device B is approximately 0.1 V. This may be improved by wirebonding from both ends of the metasurface antennas, rather than biasing from just a single side as depicted in Fig. C.1. Nevertheless, the maximum achievable voltage efficiency is primarily limited by the active region itself. For the case of Device B, removing all parasitic voltages will still result in a non-unity voltage efficiency of $\eta_V = 0.21$, due to the large voltage defect relative to the photon energy at 2.7 THz ($h\nu \approx 11.2$ meV).

C.2 Output coupler efficiency

The QC-VECSEL output coupler is typically an inductive gold mesh evaporated on a quartz or Si substrate as described in Section 2.7.1. The periodicity and width of the metal mesh, along with the substrate, determine the overall reflectance. While high-resistivity Si can have up to an order of magnitude smaller absorption coefficient in the terahertz, the quartz substrates used are typically very thin (100 μm), allowing the loss from the substrate to be quite small [226]. Therefore, the primary source of loss from the OC is the free carrier loss in the metal mesh. When the transmittance of the OC is small, it becomes comparable to the absorbance, resulting in a low OC efficiency. The OC efficiency can be written as

$$\eta_{\text{OC}} = \frac{T_{\text{OC}}}{1 - R_{\text{OC}}} \tag{C.5}$$

A simulation of the OC reflectance and corresponding efficiency for four different mesh dimensions are shown in Fig. C.3. Each OC has a 10 µm period mesh with circular holes. From highest to lowest reflectance, the diameters shown are 3 µm, 4 µm, 5 µm, and 6 µm. Free-carrier losses are included in the simulation using the Drude model based on the parameters $n_{\text{Au}} = 5.9 \times 10^{22}$ cm^{-3} and $\tau_{\text{Au}} = 39$ fs. The material losses matter less for lower reflectance OCs since a much smaller fraction of the overall transmitted radiation is lost to the material. However, when the OC reflectance is high, the OC efficiency can drop below 10%.

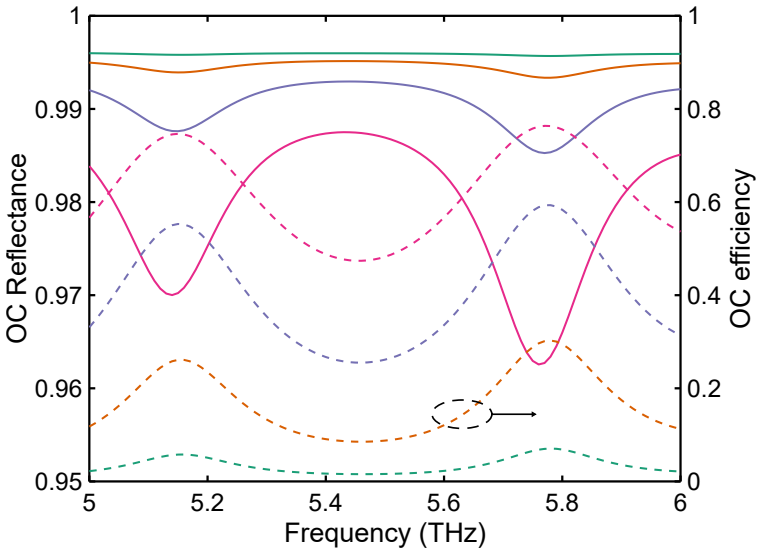

Figure C.3: Simulated output coupler reflectance and corresponding efficiency. Each color represents a different metal mesh. From highest to lowest reflectance, the OC designs are: P10-D3, P10-D4, P10-D5, and P10-D6, where P10 refers to the 10 µm period of the mesh, and D# refers to the diameter of the circular holes in microns.

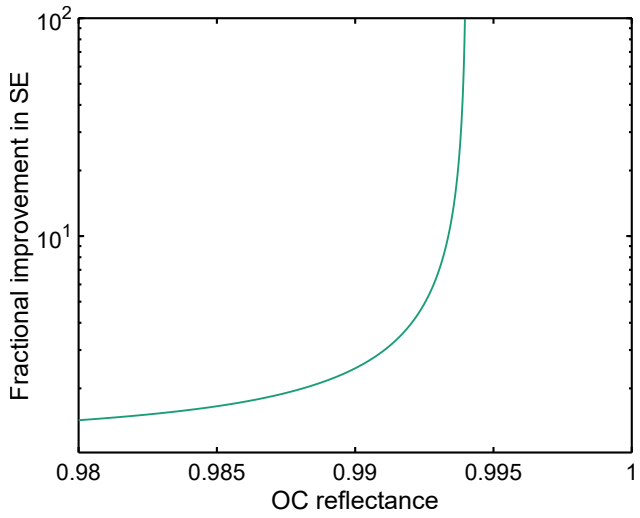

Figure C.4: Fractional improvement in slope efficiency versus reflectance for an output coupler with no material losses.

An all-dielectric output coupler based on high-contrast gratings (HCG), similar to those used in VCSEL technology, can be used to circumvent metal losses [227]. An HCG based high-resistivity Si OC will have near zero absorption, and dramatically improve the OC

efficiency for high reflectance designs. The fractional improvement in slope efficiency is illustrated in Fig. C.4 as a function of OC reflectance, in comparison to an OC with 0.6% absorption obtained from simulation.

C.3 Modal uniformity

The modal uniformity factor in Eq. C.1 refers to the non-uniform electric-field profile along the active region in the antennas. For an ideal half-wavelength microcavity mode with a plane wave incident on the metasurface, the modal uniformity factor is $\eta_u = 2/3$. This factor has an adverse effect on the wall-plug efficiency because the regions of lower electric-field amplitude contribute less stimulated emission while still drawing current. Figure C.5(a) shows a schematic and simulation of the antenna after removing w_g of active material from the center such that $\frac{w_g}{w} = 0.5$. The two vertical black lines show the boundary between QC material and air. The black curve shows the electric field magnitude distributed across the cavity.

The result of removing active material can be characterized by its effect on the modal uniformity η_u, transparency gain g_{tr}, effective interaction length ξ, and the material fill factor. Indeed, as the $\frac{w_g}{w}$ ratio increases, the modal uniformity factor approaches unity. However, due to the reduction in the amount of gain material overlap with the microcavity mode, the transparency gain increases. This trade-off becomes increasingly more sensitive as the air gap increases due to the air gap approaching regions of higher electric field magnitude. Based on the analysis, an air gap of $w_g = \frac{1}{2}w$ is chosen as the recommended design. This design leads to an increase of modal uniformity factor from $\eta_u = 0.66$ to $\eta_u = 0.95$ — a 44% increase in the wall-plug efficiency — while only increasing the transparency gain from $g_{tr} = 12.62$ cm^{-1} to $g_{tr} = 12.97$ cm^{-1}. However, the actual fabrication of such a design must be considered. The fabrication of this device will need to involve a polymer, such as benzocyclobutene (BCB), to temporarily fill in the gap for the top metallization. In the case where BCB is taken in place of the air gap, the extra loss from the BCB results in a

larger transparency gain for a given $\frac{w_g}{w}$. Nevertheless, at the chosen design, the inclusion of BCB still only increases the transparency gain to $g_{tr} = 14.14$ cm^{-1}, which is still a perhaps manageable 12% increase of the transparency gain.

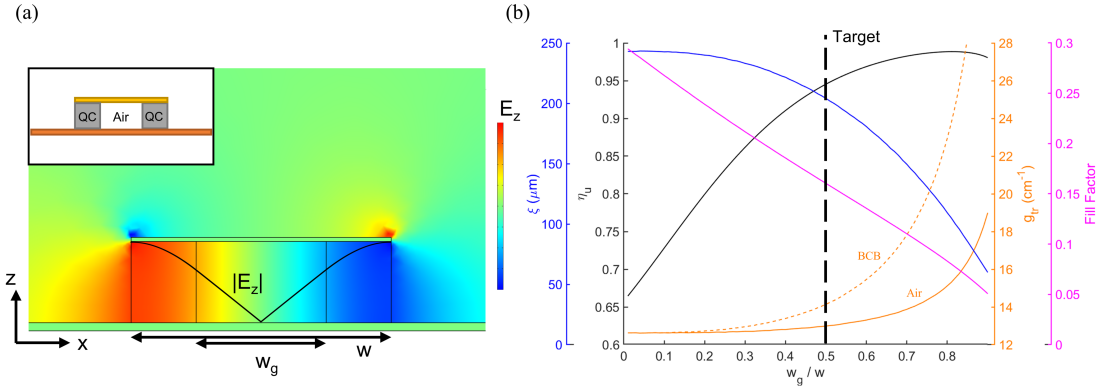

Figure C.5: (a) A COMSOL simulation of the metasurface antenna for $w_g = \frac{1}{2}w$. The vertical bars represent the air-QC boundary. The black curve shows the electric field magnitude in the z-direction across the width of the antenna. The inset is a schematic of the proposed design. (b) A plot showing how η_u, g_{tr}, ξ, and fill factor vary with increasing $\frac{w_g}{w}$. The transparency gain is plotted for the cases with and without BCB in place of the air gap. The other parameters remain almost unchanged with the introduction of BCB. The vertical dashed bar indicates the target design, $w_g = \frac{1}{2}w$. At this target design, $\eta_u = 0.95$, $g_{tr}^{\text{air}} = 12.97$ cm^{-1}, $g_{tr}^{\text{BCB}} = 14.14$ cm^{-1}, $\xi = 204$ μm, and fill factor = 0.16.

Another benefit arises from the reduction in material fill factor. At the target design, the fill factor is reduced by about 50%, which corresponds to an equal reduction in the threshold current. For continuous-wave operation, this reduction in current will result in less overall power dissipation. This may be another mechanism in which increasing the modal uniformity factor will increase the wall-plug efficiency. Furthermore, removing QC material from the antenna cavity also changes the effective index of the medium. Both air and BCB have indices close to unity, reducing the effective index as the gap increases. Because the antenna mode has a resonance condition of $f \approx \frac{c}{2n_{\text{eff}}w}$, the width of the antenna must increase to compensate for the reduction in effective index. This contributes to a change in radiative quality factor, shown by the fitting parameter ξ. A summary of the results of varying $\frac{w_g}{w}$ is

illustrated in Figure C.5(b).

C.4 Summary of efficiency metrics

As a qualitative insight into what limits the wall-plug efficiency of the THz QC-VECSEL, we can compare the performance of Device B (2.7 THz) with Device C (3.5 THz), which showed the best performance. Table C.1 shows a summary of the individual parameters that compose the wall-plug efficiency (see Eq.C.2) for Device C. The product $\eta_i\eta_{\text{opt}}$ is obtained from measurements of the slope efficiency, while the individual contributions are not known. Since the frequency tuning of the QC-VECSEL includes detuning from the metasurface resonance, the device performance can vary significantly when operated on and off resonance; efficiency parameters for both cases are included in the table. The target values are ideal values that provide a sense of how far the realized device is from theoretical maximums. Device C demonstrated the highest performance in efficiency and power output for a QC-VECSEL thus far, and serves as a good benchmark for other. wavelength-scaled devices.

The corresponding summary for Device B is shown in Table C.2. The *L-I-V* characteristic of the device when operating on and off resonance is shown in Fig. C.6. It is apparent that the under-performing parameters for Device B are η_V and $\eta_i\eta_{\text{opt}}$. The former can be improved by 50% simply by wirebonding directly to the metasurface ground plane as described in Section C.1. The latter most likely has room for improvement in both η_i and η_{opt}. At lower frequencies, the internal quantum efficiency can drop due to difficulties associated with selective injection and extraction of the upper and lower lasing levels respectively. Additionally, due to the 5 µm thickness of the active region and lower wavelength, the metasurface ξ is about 4× larger than that of Device B, substantially reducing η_{opt}. Overall, a 3.8× increase can be expected for the $\eta_i\eta_{\text{opt}}$ product for a unity quantum efficiency and a sufficiently reduced metasurface ξ factor.

The summary for Device F (5.48 THz center frequency) is shown in Table C.3. This device had wirebonds that connected directly to the ground plane, resulting in voltage efficiencies

only limited by the QC active region design; *nextnano* simulations show 84 mV/module when biased at max gain. With 127 modules, this results in a total of 10.67 V — nearly identical to the observed values. As detailed in Section 3.4, the primary factor that curtailed performance in the 5+THz devices was the unexpectedly high transparency gain which caused thresholds much higher than the metal-metal waveguide lasers from the same active material. These challenges manifest in a reduced η_I and η_{opt}, as can be seen in the table. Fortunately, the target values show that there is much room for improvement, and future designs aim to improve the slope efficiency by at least an order of magnitude.

Table C.1: Device C (3.5 THz center frequency) summary of measured and target efficiency values. Data is produced from measurements shown in Ref. [30].

Param.	Exp. value (pulsed 77 K) near resonance	Exp. value (pulsed 77 K) off resonance	Target	Comments
ν	3.40 THz	3.72 THz	—	Two frequencies obtained from two different cavity lengths from the same device.
N_p	163	163	—	Number of modules in active region is set during epitaxial growth.
T_OC	2%	6%	—	Due to finite absorption loss in the output coupler, the OC reflectance is not exactly $1 - T_\mathrm{OC}$. Simulations show absorbance close to 0.6%.
$\mathrm{d}P/\mathrm{d}I$	200 mW/A	480 mW/A	1.2 kW/A	Target value comes from simultaneous improvement of η_i, η_opt, and η_u.
V_max	10.1 V	10.1 V	8.2 V	This voltage is measured at the bias point with maximum output power.
I_th	286 mA	314 mA	180 mA	Target value is based on the threshold obtained from a metal-metal waveguide ridge laser.
I_max	437 mA	437 mA	—	Max current based on measured current at the bias point with maximum output power.
$\boldsymbol{\eta_V}$	0.23	0.25	0.29	Target value assumes an active region with 50 mV/module obtained from *nextnano* simulations.
$\boldsymbol{\eta_I}$	0.35	0.28	0.56	Target value is based on what was measured from a metal-metal waveguide of the same epitaxial growth.
$\boldsymbol{\eta_i\eta_\mathrm{opt}}$	0.13	0.32	0.57	The target value is assuming no excess cavity losses and a lossless OC.
$\boldsymbol{\eta_\mathrm{u}}$	0.66	0.66	0.95	Not measured, but based on simulation (see Section C.3).
WPE	0.31% (0.7%)	1.1% (1.5%)	8.8%	The measured WPE is lower than the product of all the efficiency subcomponents due to slope-efficiency roll-off. The value obtained by taking the product is in parenthesis. Target WPE is the product of all the target efficiency parameters.

Table C.2: Device B (2.77 THz center frequency) summary of measured and target efficiency values [30].

Param.	Exp. value (pulsed 77 K) near resonance	Exp. value (pulsed 77 K) off resonance	Target	Comments
ν	2.66 THz	2.93 THz	—	Two frequencies obtained from two different cavity lengths from the same device.
N_p	80	80	—	Number of modules in active region is set during epitaxial growth.
T_OC	1%	1.5%	—	Due to finite absorption loss in the output coupler, the OC reflectance is not exactly $1 - T_\mathrm{OC}$. Simulations show absorbance close to 0.6%.
$\mathrm{d}P/\mathrm{d}I$	4.6 mW/A	54 mW/A	226 mW/A	Target value comes from simultaneous improvement of η_i, η_opt, and η_u.
V_max	8.48 V	8.48 V	4.32 V	This voltage is measured at the bias point with maximum output power.
I_th	410 mA	453 mA	371 mA	Target value is based on the threshold obtained from a metal-metal waveguide ridge laser.
I_max	563 mA	550 mA	—	Max current based on measured current at the bias point with maximum output power.
$\boldsymbol{\eta_V}$	0.11	0.11	0.21	Target value assumes an active region with 54 mV/module obtained from *nextnano* simulations.
$\boldsymbol{\eta_I}$	0.27	0.18	0.41	Target value is based on what was measured from a metal-metal waveguide of the same epitaxial growth.
$\boldsymbol{\eta_i\eta_\mathrm{opt}}$	0.008	0.084	0.32	The target value is assuming no excess cavity losses and a lossless OC.
$\boldsymbol{\eta_\mathrm{u}}$	0.66	0.66	0.95	Not measured, but based on simulation (see Section C.3).
WPE	0.011% (0.014%)	0.084% (0.11%)	2.6%	The measured WPE is lower than the product of all the efficiency subcomponents due to slope-efficiency roll-off. The value obtained by taking the product is in parenthesis. Target WPE is the product of all the target efficiency parameters.

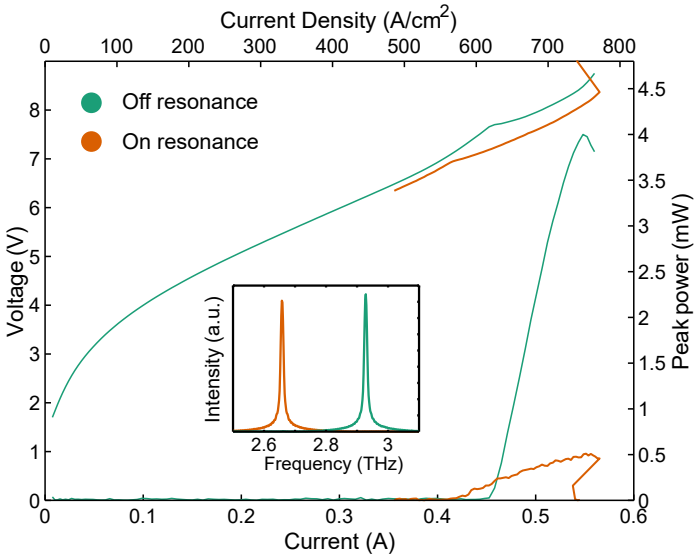

Figure C.6: *L-I-V* characteristic of Device B operating on and off the metasurface resonance. When the laser is detuned from the metasurface resonance, both the slope efficiency and threshold current are increased. The inset shows the measured FTIR spectra of the laser for both cases.

Table C.3: Device F (5.48 THz center frequency) summary of measured and target efficiency values. Data used to calculate table values are from Section 3.3.2.

Param.	Exp. value (pulsed 5 K) near resonance	Exp. value (pulsed 5 K) off resonance	Target	Comments
ν	5.42 THz	5.52 THz	—	Two frequencies obtained from two different cavity lengths from the same device.
N_p	127	127	—	Number of modules in active region is set during epitaxial growth.
T_OC	0.68%	1.1%	—	Due to finite absorption loss in the output coupler, the OC reflectance is not exactly $1 - T_\mathrm{OC}$. Simulations show absorbance close to 0.6%.
$\mathrm{d}P/\mathrm{d}I$	9.6 mW/A	21 mW/A	937 mW/A	Target value comes from simultaneous improvement of η_i, η_opt, and η_u.
V_max	10.80 V	10.86 V	10.67 V	This voltage is measured at the bias point with maximum output power.
I_th	347 mA	350 mA	165 mA	Target value is based on the threshold obtained from a metal-metal waveguide ridge laser.
I_max	424 mA	439 mA	—	Max current based on measured current at the bias point with maximum output power.
$\boldsymbol{\eta_V}$	0.26	0.27	0.27	Target value assumes an active region with 84 mV/module obtained from *nextnano* simulations.
$\boldsymbol{\eta_I}$	0.18	0.20	0.62	Target value is based on what was measured from a metal-metal waveguide of the same epitaxial growth.
$\boldsymbol{\eta_i\eta_\mathrm{opt}}$	0.005	0.011	0.11	The target value is assuming no excess cavity losses and a lossless OC.
$\boldsymbol{\eta_\mathrm{u}}$	0.66	0.66	0.95	Not measured, but based on simulation (see Section C.3).
WPE	0.012% (0.015%)	0.027% (0.039%)	1.7%	The measured WPE is lower than the product of all the efficiency subcomponents due to slope-efficiency roll-off. The value obtained by taking the product is in parenthesis. Target WPE is the product of all the target efficiency parameters.

REFERENCES

[1] M. Naftaly, N. Vieweg, and A. Deninger, "Industrial Applications of Terahertz Sensing: State of Play," *Sensors*, vol. 19, no. 19, p. 4203, Jan. 2019.

[2] I. R. Medvedev, C. F. Neese, G. M. Plummer, and F. C. D. Lucia, "Submillimeter spectroscopy for chemical analysis with absolute specificity," *Optics Letters*, vol. 35, no. 10, pp. 1533–1535, May 2010.

[3] I. R. Medvedev, M. Behnke, and F. C. De Lucia, "Fast analysis of gases in the submillimeter/terahertz with "absolute" specificity," *Applied Physics Letters*, vol. 86, no. 15, p. 154105, Apr. 2005.

[4] J. C. Pearson, B. J. Drouin, A. Maestrini, I. Mehdi, J. Ward, R. H. Lin, S. Yu, J. J. Gill, B. Thomas, C. Lee, G. Chattopadhyay, E. Schlecht, F. W. Maiwald, P. F. Goldsmith, and P. Siegel, "Demonstration of a room temperature 2.48–2.75 THz coherent spectroscopy source," *Review of Scientific Instruments*, vol. 82, no. 9, p. 093105, Sep. 2011.

[5] A. D'Arco, A. D'Arco, A. D'Arco, D. Rocco, F. P. Magboo, C. Moffa, G. D. Ventura, G. D. Ventura, G. D. Ventura, A. Marcelli, A. Marcelli, L. Palumbo, L. Palumbo, L. Mattiello, S. Lupi, S. Lupi, M. Petrarca, and M. Petrarca, "Terahertz continuous wave spectroscopy: a portable advanced method for atmospheric gas sensing," *Optics Express*, vol. 30, no. 11, pp. 19 005–19 016, May 2022.

[6] J. V. Siles, K. B. Cooper, C. Lee, R. H. Lin, G. Chattopadhyay, and I. Mehdi, "A New Generation of Room-Temperature Frequency-Multiplied Sources With up to 10× Higher Output Power in the 160-GHz–1.6-THz Range," *IEEE Transactions on Terahertz Science and Technology*, vol. 8, no. 6, pp. 596–604, Nov. 2018.

[7] S. Preu, G. H. Döhler, S. Malzer, L. J. Wang, and A. C. Gossard, "Tunable, continuous-wave Terahertz photomixer sources and applications," *Journal of Applied Physics*, vol. 109, no. 6, p. 061301, Mar. 2011.

[8] R. M. Smith and M. A. Arnold, "Selectivity of Terahertz Gas-Phase Spectroscopy," *Analytical Chemistry*, vol. 87, no. 21, pp. 10 679–10 683, Nov. 2015.

[9] D. Mittleman, R. Jacobsen, R. Neelamani, R. Baraniuk, and M. Nuss, "Gas sensing using terahertz time-domain spectroscopy," *Applied Physics B*, vol. 67, no. 3, pp. 379–390, Sep. 1998.

[10] G. Dodel, "On the history of far-infrared (FIR) gas lasers: Thirty-five years of research and application," *Infrared Physics & Technology*, vol. 40, no. 3, pp. 127–139, Jun. 1999.

[11] K. Zhong, W. Shi, D. Xu, P. Liu, Y. Wang, J. Mei, C. Yan, S. Fu, and J. Yao, "Optically pumped terahertz sources," *Science China Technological Sciences*, vol. 60, no. 12, pp. 1801–1818, Dec. 2017.

[12] P. Chevalier, A. Amirzhan, F. Wang, M. Piccardo, S. G. Johnson, F. Capasso, and H. O. Everitt, "Widely tunable compact terahertz gas lasers," *Science*, vol. 366, no. 6467, pp. 856–860, Nov. 2019.

[13] A. Amirzhan, P. Chevalier, J. Rowlette, H. T. Stinson, M. Pushkarsky, T. Day, H. O. Everitt, and F. Capasso, "A quantum cascade laser-pumped molecular laser tunable over 1 THz," *APL Photonics*, vol. 7, no. 1, p. 016107, Jan. 2022.

[14] M.-H. Mammez, Z. Buchanan, O. Pirali, M.-A. Martin-Drumel, J. Turut, G. Ducournau, S. Eliet, F. Hindle, S. Barbieri, P. Roy, G. Mouret, and J.-F. Lampin, "Optically Pumped Terahertz Molecular Laser: Gain Factor and Validation up to 5.5 THz," *Advanced Photonics Research*, vol. 3, no. 4, p. 2100263, 2022.

[15] A. Pagies, G. Ducournau, and J.-F. Lampin, "Low-threshold terahertz molecular laser optically pumped by a quantum cascade laser," *APL Photonics*, vol. 1, no. 3, p. 031302, Jun. 2016.

[16] M. Brandstetter, C. Deutsch, M. Krall, and K. Unterrainer, "Instant imaging with terahertz lasers - News," May 2015.

[17] P. Tan, J. Huang, K. Liu, Y. Xiong, and M. Fan, "Terahertz radiation sources based on free electron lasers and their applications," *Science China Information Sciences*, vol. 55, no. 1, pp. 1–15, Jan. 2012.

[18] H.-W. Hübers, S. G. Pavlov, and V. N. Shastin, "Terahertz lasers based on germanium and silicon," *Semiconductor Science and Technology*, vol. 20, no. 7, p. S211, Jun. 2005.

[19] E. Bründermann, D. R. Chamberlin, and E. E. Haller, "High duty cycle and continuous terahertz emission from germanium," *Applied Physics Letters*, vol. 76, no. 21, pp. 2991–2993, May 2000.

[20] P. Shumyatsky and R. R. Alfano, "Terahertz sources," *Journal of Biomedical Optics*, vol. 16, no. 3, p. 033001, Mar. 2011.

[21] S. Makhlouf, O. Cojocari, M. Hofmann, T. Nagatsuma, S. Preu, N. Weimann, H.-W. Hübers, and A. Stöhr, "Terahertz Sources and Receivers: From the past to the Future," May 2023.

[22] B. S. Williams, "Terahertz quantum-cascade lasers," *Nature Photonics*, vol. 1, no. 9, pp. 517–525, Sep. 2007.

[23] M. I. Amanti, G. Scalari, R. Terazzi, M. Fischer, M. Beck, J. Faist, A. Rudra, P. Gallo, and E. Kapon, "Bound-to-continuum terahertz quantum cascade laser with a single-quantum-well phonon extraction/injection stage," *New Journal of Physics*, vol. 11, no. 12, p. 125022, Dec. 2009.

[24] C. A. Curwen, J. L. Reno, and B. S. Williams, "Terahertz quantum cascade VECSEL with watt-level output power," *Applied Physics Letters*, vol. 113, no. 1, p. 011104, Jul. 2018.

[25] A. D. Kim, C. A. Curwen, Y. Wu, J. L. Reno, S. J. Addamane, and B. S. Williams, "Wavelength Scaling of Widely-Tunable Terahertz Quantum-Cascade Metasurface Lasers," *IEEE Journal of Microwaves*, vol. 3, no. 1, pp. 305–318, Jan. 2023.

[26] A. D. Kim, M. Shahili, S. Addamane, C. A. Curwen, J. H. Kawamura, and B. S. Williams, "Metasurface-based terahertz quantum-cascade lasers operating beyond 5 THz," in *33rd International Symposium on Space Terahertz Technology*, Apr. 2024.

[27] L. Gao, C. Feng, and X. Zhao, "Recent developments in terahertz quantum cascade lasers for practical applications," *Nanotechnology Reviews*, vol. 12, no. 1, Jan. 2023.

[28] A. Khalatpour, A. K. Paulsen, C. Deimert, Z. R. Wasilewski, and Q. Hu, "High-power portable terahertz laser systems," *Nature Photonics*, vol. 15, no. 1, pp. 16–20, Jan. 2021.

[29] M. Rösch, G. Scalari, M. Beck, and J. Faist, "Octave-spanning semiconductor laser," *Nature Photonics*, vol. 9, no. 1, pp. 42–47, Jan. 2015.

[30] C. A. Curwen, J. L. Reno, and B. S. Williams, "Broadband continuous single-mode tuning of a short-cavity quantum-cascade VECSEL," *Nature Photonics*, vol. 13, no. 12, pp. 855–859, Dec. 2019.

[31] G. Scalari, M. I. Amanti, C. Walther, R. Terazzi, M. Beck, and J. Faist, "Broadband THz lasing from a photon-phonon quantum cascade structure," *Optics Express*, vol. 18, no. 8, pp. 8043–8052, Apr. 2010.

[32] M. S. Vitiello and A. Tredicucci, "Tunable Emission in THz Quantum Cascade Lasers," *IEEE Transactions on Terahertz Science and Technology*, vol. 1, no. 1, pp. 76–84, Sep. 2011.

[33] A. Barkan, F. K. Tittel, D. M. Mittleman, R. Dengler, P. H. Siegel, G. Scalari, L. Ajili, J. Faist, H. E. Beere, E. H. Linfield, A. G. Davies, and D. A. Ritchie, "Linewidth and tuning characteristics of terahertz quantum cascade lasers," *Optics Letters*, vol. 29, no. 6, p. 575, Mar. 2004.

[34] K. Ohtani, M. Beck, and J. Faist, "Electrical laser frequency tuning by three terminal terahertz quantum cascade lasers," *Applied Physics Letters*, vol. 104, no. 1, p. 011107, Jan. 2014.

[35] I. Kundu, P. Dean, A. Valavanis, J. R. Freeman, M. C. Rosamond, L. Li, Y. Han, E. H. Linfield, and A. G. Davies, "Continuous Frequency Tuning with near Constant Output Power in Coupled Y-Branched Terahertz Quantum Cascade Lasers with Photonic Lattice," *ACS Photonics*, vol. 5, no. 7, pp. 2912–2920, Jul. 2018.

[36] I. Kundu, J. R. Freeman, P. Dean, L. Li, E. H. Linfield, and A. G. Davies, "Wideband Electrically Controlled Vernier Frequency Tunable Terahertz Quantum Cascade Laser," *ACS Photonics*, vol. 7, no. 3, pp. 765–773, Mar. 2020.

[37] A. W. M. Lee, B. S. Williams, S. Kumar, Q. Hu, and J. L. Reno, "Tunable terahertz quantum cascade lasers with external gratings," *Optics Letters*, vol. 35, no. 7, pp. 910–912, Apr. 2010.

[38] J. Xu, J. M. Hensley, D. B. Fenner, R. P. Green, L. Mahler, A. Tredicucci, M. G. Allen, F. Beltram, H. E. Beere, and D. A. Ritchie, "Tunable terahertz quantum cascade lasers with an external cavity," *Applied Physics Letters*, vol. 91, no. 12, p. 121104, Sep. 2007.

[39] L. Mahler, A. Tredicucci, F. Beltram, H. E. Beere, and D. A. Ritchie, "Tuning a distributed feedback laser with a coupled microcavity," *Optics Express*, vol. 18, no. 18, pp. 19 185–19 191, Aug. 2010.

[40] Q. Qin, J. L. Reno, and Q. Hu, "MEMS-based tunable terahertz wire-laser over 330 GHz," *Optics Letters*, vol. 36, no. 5, pp. 692–694, Mar. 2011.

[41] A. Hugi, R. Terazzi, Y. Bonetti, A. Wittmann, M. Fischer, M. Beck, J. Faist, and E. Gini, "External cavity quantum cascade laser tunable from 7.6 to 11.4 μm," *Applied Physics Letters*, vol. 95, no. 6, p. 061103, Aug. 2009.

[42] T. Alam, M. Wienold, X. Lü, K. Biermann, L. Schrottke, H. T. Grahn, and H.-W. Hübers, "Wideband, high-resolution terahertz spectroscopy by light-induced frequency tuning of quantum-cascade lasers," *Optics Express*, vol. 27, no. 4, pp. 5420–5432, Feb. 2019.

[43] Q. Qin, B. S. Williams, S. Kumar, J. L. Reno, and Q. Hu, "Tuning a terahertz wire laser," *Nature Photonics*, vol. 3, no. 12, pp. 732–737, Dec. 2009.

[44] M. Harwit, G. Helou, L. Armus, C. M. Bradford, P. F. Goldsmith, M. Hauser, D. Leisawitz, D. F. Lester, G. Rieke, and S. A. Rinehart, "Far-Infrared/Submillimeter Astronomy from Space: Tracking on Evolving Universe and the Emergence of Life: A White Paper and Set of Recommendations for the Astronomy & Astrophysics Decadal Survey of 2010," *Infrared Processing and Analysis Center (IPAC) at Caltech*, May 2008.

[45] D. T. Leisawitz, E. G. Amatucci, L. N. Allen, J. W. Arenberg, L. Armus, C. Battersby, J. M. Bauer, B. G. Beaman, R. M. B. Jr, P. Beltran, D. J. Benford, E. Bergin, J. A. Bolognese, C. M. Bradford, D. C. Bradley, D. Burgarella, S. J. Carey,

R. C. Carter, D. Chi, A. Cooray *et al.*, "Origins Space Telescope: baseline mission concept," *Journal of Astronomical Telescopes, Instruments, and Systems*, vol. 7, no. 1, p. 011002, Jan. 2021.

[46] M. C. Wiedner, S. Aalto, L. Armus, E. Bergin, J. Birkby, C. M. Bradford, D. Burgarella, P. Caselli, V. Charmandaris, A. Cooray, E. De Beck, J. M. Desert, M. Gerin, J. Goicoechea, M. Griffin, P. Hartogh, F. Helmich, M. Hogerheijde, L. Hunt, A. Karska *et al.*, "Origins space telescope: from first light to life," *Experimental Astronomy*, vol. 51, no. 3, pp. 595–624, Jun. 2021.

[47] M. C. Wiedner, S. Aalto, E. G. Amatucci, A. M. Baryshev, C. Battersby, V. Y. Belitsky, E. Bergin, B. Borgo, R. C. Carter, E. Caux, A. Cooray, J. A. Corsetti, E. D. Beck, Y. Delorme, V. P. Desmaris, M. J. DiPirro, B. N. Ellison, A. M. D. Giorgio, M. J. Eggens, J. D. Gallego-Puyol *et al.*, "Heterodyne Receiver for Origins," *Journal of Astronomical Telescopes, Instruments, and Systems*, vol. 7, no. 1, p. 011007, Jan. 2021.

[48] C. Kulesa, "Terahertz Spectroscopy for Astronomy: From Comets to Cosmology," *IEEE Transactions on Terahertz Science and Technology*, vol. 1, no. 1, pp. 232–240, Sep. 2011.

[49] A. Qaiyum, "Millimeter and Submillimeter Emissions from Galactic and Extragalactic Photodissociation Regions," *Astrophysics and Space Science*, vol. 305, no. 1, pp. 1–10, Sep. 2006.

[50] K. I. Öberg, R. Murray-Clay, and E. A. Bergin, "The Effects of Snowlines on C/O in Planetary Atmospheres," *The Astrophysical Journal*, vol. 743, p. L16, Dec. 2011.

[51] R. T. Boreiko and A. L. Betz, "Heterodyne Spectroscopy of the 63 μm O I Line in M42," *The Astrophysical Journal*, vol. 464, no. 1, p. L83, Jun. 1996.

[52] A. Songaila, E. J. Wampler, and L. L. Cowie, "A high deuterium abundance in the early Universe," *Nature*, vol. 385, no. 6612, pp. 137–139, Jan. 1997.

[53] F. Matteucci, "The cosmic origin of deuterium," *Nature*, vol. 405, no. 6790, pp. 1009–1010, Jun. 2000.

[54] E. Peeters, N. L. Martín-Hernández, F. Damour, P. Cox, P. R. Roelfsema, J.-P. Baluteau, A. G. G. M. Tielens, E. Churchwell, M. F. Kessler, J. S. Mathis, C. Morisset, and D. Schaerer, "ISO spectroscopy of compact HII regions in the Galaxy - I. The catalogue," *Astronomy & Astrophysics*, vol. 381, no. 2, pp. 571–605, Jan. 2002.

[55] C. Walker, C. Kulesa, J. Kloosterman, D. Lesser, T. Cottam, C. Groppi, J. Zmuidzinas, M. Edgar, S. Radford, P. Goldsmith, W. Langer, H. Yorke, J. Kawamura, I. Mehdi, D. Hollenbach, J. Stutzki, H. Huebers, J. R. Gao, and C. Martin, "Large format heterodyne arrays for observing far-infrared lines with SOFIA," in *Millimeter,*

Submillimeter, and Far-Infrared Detectors and Instrumentation for Astronomy V, vol. 7741. SPIE, Jul. 2010, pp. 293–298.

[56] W. D. Langer, T. Velusamy, J. L. Pineda, P. F. Goldsmith, D. Li, and H. W. Yorke, "C+ detection of warm dark gas in diffuse clouds," *Astronomy & Astrophysics*, vol. 521, p. L17, Oct. 2010.

[57] M. Wienold, A. Semenov, E. Dietz, S. Frohmann, P. Dern, X. Lü, L. Schrottke, K. Biermann, B. Klein, and H. W. Hübers, "OSAS-B: A balloon-borne terahertz spectrometer for atomic oxygen in the upper atmosphere," *IEEE Transactions on Terahertz Science and Technology*, pp. 1–9, 2024.

[58] H. Richter, C. Buchbender, R. Güsten, R. Higgins, B. Klein, J. Stutzki, H. Wiesemeyer, and H.-W. Hübers, "Direct measurements of atomic oxygen in the mesosphere and lower thermosphere using terahertz heterodyne spectroscopy," *Communications Earth & Environment*, vol. 2, no. 1, pp. 1–9, Jan. 2021.

[59] T. d. Graauw, F. P. Helmich, T. G. Phillips, J. Stutzki, E. Caux, N. D. Whyborn, P. Dieleman, P. R. Roelfsema, H. Aarts, R. Assendorp, R. Bachiller, W. Baechtold, A. Barcia, D. A. Beintema, V. Belitsky, A. O. Benz, R. Bieber, A. Boogert, C. Borys, B. Bumble *et al.*, "The Herschel-Heterodyne Instrument for the Far-Infrared (HIFI)," *Astronomy & Astrophysics*, vol. 518, p. L6, Jul. 2010.

[60] J. L. Kloosterman, D. J. Hayton, Y. Ren, T. Y. Kao, J. N. Hovenier, J. R. Gao, T. M. Klapwijk, Q. Hu, C. K. Walker, and J. L. Reno, "Hot electron bolometer heterodyne receiver with a 4.7-THz quantum cascade laser as a local oscillator," *Applied Physics Letters*, vol. 102, no. 1, p. 011123, Jan. 2013.

[61] A. Shurakov, Y. Lobanov, and G. Goltsman, "Superconducting hot-electron bolometer: from the discovery of hot-electron phenomena to practical applications," *Superconductor Science and Technology*, vol. 29, no. 2, p. 023001, Dec. 2015.

[62] Y.-J. Lin and M. Jarrahi, "Heterodyne terahertz detection through electronic and optoelectronic mixers," *Reports on Progress in Physics*, vol. 83, no. 6, p. 066101, Jun. 2020.

[63] D. Hayton, J. Treuttel, J.-V. Siles, C. P. Chen, R. Lin, C. Lee, E. Schlecht, and I. Mehdi, "A Compact Schottky Heterodyne Receiver for 2.06 THz Neutral Oxygen [OI]," in *2018 43rd International Conference on Infrared, Millimeter, and Terahertz Waves (IRMMW-THz)*, Sep. 2018, pp. 1–2.

[64] A. Maestrini, B. Thomas, H. Wang, C. Jung, J. Treuttel, Y. Jin, G. Chattopadhyay, I. Mehdi, and G. Beaudin, "Schottky diode-based terahertz frequency multipliers and mixers," *Comptes Rendus Physique*, vol. 11, no. 7, pp. 480–495, Aug. 2010.

[65] I. Mehdi, J. V. Siles, C. Lee, and E. Schlecht, "THz Diode Technology: Status, Prospects, and Applications," *Proceedings of the IEEE*, vol. 105, no. 6, pp. 990–1007, Jun. 2017.

[66] J. S. Ward, G. Chattopadhyay, J. Gill, H. Javadi, C. Lee, R. Lin, A. Maestrini, F. Maiwald, I. Mehdi, E. Schlecht, and P. Siegel, "Tunable broadband frequency-multiplied terahertz sources," in *2008 33rd International Conference on Infrared, Millimeter and Terahertz Waves*, Sep. 2008, pp. 1–3.

[67] J. V. Siles and J. Grajal, "Physics-Based Design and Optimization of Schottky Diode Frequency Multipliers for Terahertz Applications," *IEEE Transactions on Microwave Theory and Techniques*, vol. 58, no. 7, pp. 1933–1942, Jul. 2010.

[68] M. v. Ehrenfried, *Stratospheric Balloons: Science and Commerce at the Edge of Space*, 1st ed. Springer, Mar. 2021.

[69] M. Cui, J. N. Hovenier, Y. Ren, N. Vercruyssen, J. R. Gao, T. Y. Kao, Q. Hu, and J. L. Reno, "Beam and phase distributions of a terahertz quantum cascade wire laser," *Applied Physics Letters*, vol. 102, no. 11, p. 111113, Mar. 2013.

[70] A. Khalatpour, J. L. Reno, N. P. Kherani, and Q. Hu, "Unidirectional photonic wire laser," *Nature Photonics*, vol. 11, no. 9, pp. 555–559, Sep. 2017.

[71] A. Khalatpour, A. Paulsen, S. J. Addamane, C. Deimert, J. L. Reno, Z. R. Wasilewski, and Q. Hu, "A Tunable Unidirectional Source for GUSTO's Local Oscillator at 4.74 THz," *IEEE Transactions on Terahertz Science and Technology*, pp. 1–1, 2021.

[72] C. Walker, C. Kulesa, A. Young, W. Verts, J.-R. Gao, Q. Hu, J. Silva, B. Mirzaei, W. Laauwen, J. Hesler, C. Groppi, and A. Emrich, "Gal/Xgal U/LDB Spectroscopic/Stratospheric THz Observatory: GUSTO," in *Millimeter, Submillimeter, and Far-Infrared Detectors and Instrumentation for Astronomy XI*, vol. 12190. SPIE, Aug. 2022, pp. 225–235.

[73] C. K. Walker, C. A. Kulesa, C. E. Groppi, E. Young, T. McMahon, P. Bernasconi, C. Lisse, D. Neufeld, J. Kawamura, P. Goldsmith, W. Langer, H. Yorke, J. Sterne, A. Skalare, I. Mehdi, S. Weinreb, J. Kooi, J. Stutzki, U. Graf, C. Honingh *et al.*, "The Stratospheric Terahertz Observatory (STO)," in *19th International Symposium on Space Terahertz Technology*, Apr. 2008.

[74] M. I. Amanti, M. Fischer, G. Scalari, M. Beck, and J. Faist, "Low-divergence single-mode terahertz quantum cascade laser," *Nature Photonics*, vol. 3, no. 10, pp. 586–590, Oct. 2009.

[75] M. I. Amanti, G. Scalari, F. Castellano, M. Beck, and J. Faist, "Low divergence Terahertz photonic-wire laser," *Optics Express*, vol. 18, no. 6, pp. 6390–6395, Mar. 2010.

[76] D. J. Hayton, J. L. Kloosterman, J.-r. Gao, N. Vercruyssen, C. K. Walker, Q. Hu, and T.-Y. Kao, "A 4.7 THz HEB/QCL heterodyne receiver for STO-2," in *2014 39th International Conference on Infrared, Millimeter, and Terahertz waves (IRMMW-THz)*, Sep. 2014, pp. 1–2.

[77] T.-Y. Kao, Q. Hu, and J. L. Reno, "Perfectly phase-matched third-order distributed feedback terahertz quantum-cascade lasers," *Optics Letters*, vol. 37, no. 11, pp. 2070–2072, Jun. 2012.

[78] D. J. Hayton, A. Khudchencko, D. G. Pavelyev, J. N. Hovenier, A. Baryshev, J. R. Gao, T. Y. Kao, Q. Hu, J. L. Reno, and V. Vaks, "Phase locking of a 3.4 THz third-order distributed feedback quantum cascade laser using a room-temperature superlattice harmonic mixer," *Applied Physics Letters*, vol. 103, no. 5, Jul. 2013.

[79] O. F. Littleton, "GUSTO Breaks NASA Scientific Balloon Record for Days in Flight - NASA," Feb. 2024.

[80] J. R. G. Silva, B. Mirzaei, W. Laauwen, N. More, A. Young, C. Kulesa, C. Walker, A. Khalatpour, Q. Hu, C. Groppi, and J. R. Gao, "4×2 HEB receiver at 4.7 THz for GUSTO," in *Millimeter, Submillimeter, and Far-Infrared Detectors and Instrumentation for Astronomy IX*, vol. 10708. SPIE, Jul. 2018, pp. 200–209.

[81] A. V. Khudchenko, D. J. Hayton, D. G. Pavelyev, A. M. Baryshev, J. R. Gao, T.-Y. Kao, Q. Hu, J. L. Reno, and V. L. Vaks, "Phase locking a 4.7 THz quantum cascade laser using a super-lattice diode as harmonic mixer," in *2014 39th International Conference on Infrared, Millimeter, and Terahertz waves (IRMMW-THz)*, Sep. 2014, pp. 1–2.

[82] S. Heyminck, U. U. Graf, R. Güsten, J. Stutzki, H. W. Hübers, and P. Hartogh, "GREAT: the SOFIA high-frequency heterodyne instrument," *Astronomy & Astrophysics*, vol. 542, p. L1, Jun. 2012.

[83] M. Wienold, A. Tahraoui, L. Schrottke, R. Sharma, X. Lü, K. Biermann, R. Hey, and H. T. Grahn, "Lateral distributed-feedback gratings for single-mode, high-power terahertz quantum-cascade lasers," *Optics Express*, vol. 20, no. 10, pp. 11 207–11 217, May 2012.

[84] H. Richter, M. Wienold, L. Schrottke, K. Biermann, H. T. Grahn, and H.-W. Hübers, "4.7-THz Local Oscillator for the GREAT Heterodyne Spectrometer on SOFIA," *IEEE Transactions on Terahertz Science and Technology*, vol. 5, no. 4, pp. 539–545, Jul. 2015.

[85] M. Justen, C. Bonzon, K. Ohtani, M. Beck, U. Graf, and J. Faist, "2D patch antenna array on a double metal quantum cascade laser with >90% coupling to a Gaussian beam and selectable facet transparency at 1.9 THz," *Optics Letters*, vol. 41, no. 19, pp. 4590–4592, Oct. 2016.

[86] L. Bosco, C. Bonzon, K. Ohtani, M. Justen, M. Beck, and J. Faist, "A patch-array antenna single-mode low electrical dissipation continuous wave terahertz quantum cascade laser," *Applied Physics Letters*, vol. 109, no. 20, p. 201103, Nov. 2016.

[87] E. T. Young, E. E. Becklin, P. M. Marcum, T. L. Roellig, J. M. D. Buizer, T. L. Herter, R. Güsten, E. W. Dunham, P. Temi, B.-G. Andersson, D. Backman,

M. Burgdorf, L. J. Caroff, S. C. Casey, J. A. Davidson, E. F. Erickson, R. D. Gehrz, D. A. Harper, P. M. Harvey, L. A. Helton *et al.*, "EARLY SCIENCE WITH SOFIA, THE STRATOSPHERIC OBSERVATORY FOR INFRARED ASTRONOMY," *The Astrophysical Journal Letters*, vol. 749, no. 2, p. L17, Mar. 2012.

[88] D. Büchel, P. Pütz, K. Jacobs, M. Schultz, U. U. Graf, C. Risacher, H. Richter, O. Ricken, H.-W. Hübers, R. Güsten, C. E. Honingh, and J. Stutzki, "4.7-THz Superconducting Hot Electron Bolometer Waveguide Mixer," *IEEE Transactions on Terahertz Science and Technology*, vol. 5, no. 2, pp. 207–214, Mar. 2015.

[89] C. Risacher, R. Güsten, J. Stutzki, H.-W. Hübers, D. Büchel, U. U. Graf, S. Heyminck, C. E. Honingh, K. Jacobs, B. Klein, T. Klein, C. Leinz, P. Pütz, N. Reyes, O. Ricken, H.-J. Wunsch, P. Fusco, and S. Rosner, "First Supra-THz Heterodyne Array Receivers for Astronomy With the SOFIA Observatory," *IEEE Transactions on Terahertz Science and Technology*, vol. 6, no. 2, pp. 199–211, Mar. 2016.

[90] C. Risacher, R. Güsten, J. Stutzki, H.-W. Hübers, P. Pütz, A. Bell, D. Büchel, I. Camara, R. Castenholz, M. Choi, U. Graf, S. Heyminck, C. Honingh, K. Jacobs, M. Justen, B. Klein, T. Klein, C. Leinz, N. Reyes, H. Richter *et al.*, "The upGREAT heterodyne array receivers for far Infrared astronomy," in *2014 39th International Conference on Infrared, Millimeter, and Terahertz waves (IRMMW-THz)*, Sep. 2014, pp. 1–2.

[91] C. Risacher, R. Güsten, J. Stutzki, H.-W. Hübers, R. Aladro, A. Bell, C. Buchbender, D. Büchel, T. Csengeri, C. Duran, U. U. Graf, R. D. Higgins, C. E. Honingh, K. Jacobs, M. Justen, B. Klein, M. Mertens, Y. Okada, A. Parikka, P. Pütz *et al.*, "The upGREAT Dual Frequency Heterodyne Arrays for SOFIA," *Journal of Astronomical Instrumentation*, vol. 07, no. 04, p. 1840014, Dec. 2018.

[92] A. D. Semenov, M. Wienold, M. Sidorova, and H.-W. Hübers, "Analytical correction for direct detection in the retrieval of gas spectral lines measured with superconducting hot-electron bolometer mixer," *Journal of Applied Physics*, vol. 135, no. 13, p. 134502, Apr. 2024.

[93] H. Wiesemeyer, R. Güsten, R. Aladro, B. Klein, H.-W. Hübers, H. Richter, U. U. Graf, M. Justen, Y. Okada, and J. Stutzki, "First detection of the atomic ^{18}O isotope in the mesosphere and lower thermosphere of Earth," *Physical Review Research*, vol. 5, no. 1, p. 013072, Feb. 2023.

[94] B. T. Pham and S. G. Neff, "Cosmic Origins Program Annual Technology Report," Oct. 2016.

[95] L. Xu, C. A. Curwen, P. W. C. Hon, Q.-S. Chen, T. Itoh, and B. S. Williams, "Metasurface external cavity laser," *Applied Physics Letters*, vol. 107, no. 22, p. 221105, Nov. 2015.

[96] A. W. M. Lee, T.-Y. Kao, D. Burghoff, Q. Hu, and J. L. Reno, "Terahertz tomography using quantum-cascade lasers," *Optics Letters*, vol. 37, no. 2, pp. 217–219, Jan. 2012.

[97] W. L. Chan, J. Deibel, and D. M. Mittleman, "Imaging with terahertz radiation," *Reports on Progress in Physics*, vol. 70, no. 8, p. 1325, Jul. 2007.

[98] P. Siegel, "Terahertz technology in biology and medicine," *IEEE Transactions on Microwave Theory and Techniques*, vol. 52, no. 10, pp. 2438–2447, Oct. 2004.

[99] Y. Peng, C. Shi, X. Wu, Y. Zhu, and S. Zhuang, "Terahertz Imaging and Spectroscopy in Cancer Diagnostics: A Technical Review," *BME Frontiers*, vol. 2020, p. 2547609, Sep. 2020.

[100] D. M. Mittleman, "Twenty years of terahertz imaging [Invited]," *Optics Express*, vol. 26, no. 8, pp. 9417–9431, Apr. 2018.

[101] P. W. C. Hon, A. A. Tavallaee, Q.-S. Chen, B. S. Williams, and T. Itoh, "Radiation Model for Terahertz Transmission-Line Metamaterial Quantum-Cascade Lasers," *IEEE Transactions on Terahertz Science and Technology*, vol. 2, no. 3, pp. 323–332, May 2012.

[102] S. V. Hum and J. Perruisseau-Carrier, "Reconfigurable Reflectarrays and Array Lenses for Dynamic Antenna Beam Control: A Review," *IEEE Transactions on Antennas and Propagation*, vol. 62, no. 1, pp. 183–198, Jan. 2014.

[103] P. Genevet and F. Capasso, "Holographic optical metasurfaces: a review of current progress," *Reports on Progress in Physics*, vol. 78, no. 2, p. 024401, Jan. 2015.

[104] S. S. Bukhari, J. Y. Vardaxoglou, and W. Whittow, "A Metasurfaces Review: Definitions and Applications," *Applied Sciences*, vol. 9, no. 13, p. 2727, Jan. 2019.

[105] S. Zahra, L. Ma, W. Wang, J. Li, D. Chen, Y. Liu, Y. Zhou, N. Li, Y. Huang, and G. Wen, "Electromagnetic Metasurfaces and Reconfigurable Metasurfaces: A Review," *Frontiers in Physics*, vol. 8, Jan. 2021.

[106] L. Xu, D. Chen, T. Itoh, J. L. Reno, and B. S. Williams, "Focusing metasurface quantum-cascade laser with a near diffraction-limited beam," *Optics Express*, vol. 24, no. 21, pp. 24 117–24 128, Oct. 2016.

[107] L. Xu, D. Chen, C. A. Curwen, M. Memarian, J. L. Reno, T. Itoh, and B. S. Williams, "Metasurface quantum-cascade laser with electrically switchable polarization," *Optica*, vol. 4, no. 4, pp. 468–475, Apr. 2017.

[108] L. Xu, C. A. Curwen, J. L. Reno, and B. S. Williams, "High performance terahertz metasurface quantum-cascade VECSEL with an intra-cryostat cavity," *Applied Physics Letters*, vol. 111, no. 10, p. 101101, Sep. 2017.

[109] C. A. Curwen, J. L. Reno, and B. S. Williams, "Terahertz quantum-cascade patch-antenna VECSEL with low power dissipation," *Applied Physics Letters*, vol. 116, no. 24, p. 241103, Jun. 2020.

[110] C. Curwen, J. Reno, and B. Williams, "Broadband metasurface design for terahertz quantum-cascade VECSEL," *Electronics Letters*, vol. 56, no. 23, pp. 1264–1267, 2020.

[111] Y. Wu, C. A. Curwen, D. J. Hayton, J. L. Reno, and B. S. Williams, "Continuous wave operation of terahertz metasurface quantum-cascade VECSEL with a long intra-cryostat cavity," *Applied Physics Letters*, vol. 121, no. 19, p. 191106, Nov. 2022.

[112] E. Morag, S. Li, A. Kim, S. J. Addamane, and B. S. Williams, "THz quantum-cascade VECSELs based upon disordered metasurfaces," in *Vertical External Cavity Surface Emitting Lasers (VECSELs) XII*, vol. 12404. SPIE, Mar. 2023, p. 124040E.

[113] Y. Shen, A. D. Kim, M. Shahili, C. A. Curwen, S. Addamane, J. L. Reno, and B. S. Williams, "THz time-domain characterization of amplifying quantum-cascade metasurface," *Applied Physics Letters*, vol. 119, no. 18, p. 181108, Nov. 2021.

[114] L. Xu, C. A. Curwen, D. Chen, J. L. Reno, T. Itoh, and B. S. Williams, "Terahertz Metasurface Quantum-Cascade VECSELs: Theory and Performance," *IEEE Journal of Selected Topics in Quantum Electronics*, vol. 23, no. 6, pp. 1–12, Nov. 2017.

[115] P. W. C. Hon, Z. Liu, T. Itoh, and B. S. Williams, "Leaky and bound modes in terahertz metasurfaces made of transmission-line metamaterials," *Journal of Applied Physics*, vol. 113, no. 3, p. 033105, Jan. 2013.

[116] N. Laman and D. Grischkowsky, "Terahertz conductivity of thin metal films," *Applied Physics Letters*, vol. 93, no. 5, p. 051105, Aug. 2008.

[117] Y. Wu, Y. Shen, S. Addamane, J. L. Reno, and B. S. Williams, "Tunable quantum-cascade VECSEL operating at 1.9 THz," *Optics Express*, vol. 29, no. 21, pp. 34 695–34 706, Oct. 2021.

[118] C. Walther, M. Fischer, G. Scalari, R. Terazzi, N. Hoyler, and J. Faist, "Quantum cascade lasers operating from 1.2to1.6THz," *Applied Physics Letters*, vol. 91, no. 13, p. 131122, Sep. 2007.

[119] S. Kumar, B. S. Williams, Q. Hu, and J. L. Reno, "1.9THz quantum-cascade lasers with one-well injector," *Applied Physics Letters*, vol. 88, no. 12, p. 121123, Mar. 2006.

[120] J. S. Blakemore, "Semiconducting and other major properties of gallium arsenide," *Journal of Applied Physics*, vol. 53, no. 10, pp. R123–R181, Oct. 1982.

[121] W. J. Moore and R. T. Holm, "Infrared dielectric constant of gallium arsenide," *Journal of Applied Physics*, vol. 80, no. 12, pp. 6939–6942, Dec. 1996.

[122] A. A. Tavallaee, P. W. C. Hon, K. Mehta, T. Itoh, and B. S. Williams, "Zero-Index Terahertz Quantum-Cascade Metamaterial Lasers," *IEEE Journal of Quantum Electronics*, vol. 46, no. 7, pp. 1091–1098, Jul. 2010.

[123] E. Strupiechonski, D. Grassani, D. Fowler, F. H. Julien, S. P. Khanna, L. Li, E. H. Linfield, A. G. Davies, A. B. Krysa, and R. Colombelli, "Vertical subwavelength mode confinement in terahertz and mid-infrared quantum cascade lasers," *Applied Physics Letters*, vol. 98, no. 10, p. 101101, Mar. 2011.

[124] S. Kumar and Q. Hu, "Investigation of possible microcavity effect on lasing threshold of nonradiative-scattering-dominated semiconductor lasers," *Applied Physics Letters*, vol. 100, no. 4, p. 041105, Jan. 2012.

[125] G. Scamarcio, M. S. Vitiello, V. Spagnolo, S. Kumar, B. Williams, and Q. Hu, "Nanoscale heat transfer in quantum cascade lasers," *Physica E: Low-dimensional Systems and Nanostructures*, vol. 40, no. 6, pp. 1780–1784, Apr. 2008.

[126] M. A. Kainz, M. Wenclawiak, S. Schönhuber, M. Jaidl, B. Limbacher, A. M. Andrews, H. Detz, G. Strasser, and K. Unterrainer, "Thermal-Dynamics Optimization of Terahertz Quantum Cascade Lasers with Different Barrier Compositions," *Physical Review Applied*, vol. 14, no. 5, p. 054012, Nov. 2020.

[127] C. A. Curwen, S. J. Addamane, J. L. Reno, M. Shahili, J. H. Kawamura, R. M. Briggs, B. S. Karasik, and B. S. Williams, "Thin THz QCL active regions for improved continuous-wave operating temperature," *AIP Advances*, vol. 11, no. 12, p. 125018, Dec. 2021.

[128] C. Walther, G. Scalari, J. Faist, H. Beere, and D. Ritchie, "Low frequency terahertz quantum cascade laser operating from 1.6to1.8THz," *Applied Physics Letters*, vol. 89, no. 23, p. 231121, Dec. 2006.

[129] M. E. Motamedi, W. H. Southwell, and W. J. Gunning, "Antireflection surfaces in silicon using binary optics technology," *Applied Optics*, vol. 31, no. 22, p. 4371, Aug. 1992.

[130] W. Li, Y. Ma, Y. Xu, J. Liu, L. Wang, N. Zhuo, Q. Lu, J. Zhang, S. Zhai, S. Liu, and F. Liu, "Continuous-wave single-mode quantum cascade laser at 5.1 THz based on graded sampled grating design," *Photonics Research*, vol. 10, no. 12, pp. 2686–2692, Dec. 2022.

[131] M. Shahili, S. J. Addamane, A. D. Kim, C. A. Curwen, J. H. Kawamura, and B. S. Williams, "Continuous-wave GaAs/AlGaAs quantum cascade laser at 5.7 THz," *Nanophotonics*, vol. 13, no. 10, pp. 1735–1743, Apr. 2024.

[132] P. Dean, Y. L. Lim, A. Valavanis, R. Kliese, M. Nikolić, S. P. Khanna, M. Lachab, D. Indjin, Z. Ikonić, P. Harrison, A. D. Rakić, E. H. Linfield, and A. G. Davies, "Terahertz imaging through self-mixing in a quantum cascade laser," *Optics Letters*, vol. 36, no. 13, pp. 2587–2589, Jul. 2011.

[133] M. Wienold, T. Hagelschuer, N. Rothbart, L. Schrottke, K. Biermann, H. T. Grahn, and H.-W. Hübers, "Real-time terahertz imaging through self-mixing in a quantum-cascade laser," *Applied Physics Letters*, vol. 109, no. 1, p. 011102, Jul. 2016.

[134] A. Valavanis, P. Dean, Y. L. Lim, R. Alhathlool, M. Nikolic, R. Kliese, S. P. Khanna, D. Indjin, S. J. Wilson, A. D. Rakic, E. H. Linfield, and G. Davies, "Self-Mixing Interferometry With Terahertz Quantum Cascade Lasers," *IEEE Sensors Journal*, vol. 13, no. 1, pp. 37–43, Jan. 2013.

[135] P. Dean, A. Valavanis, J. Keeley, K. Bertling, Y. Leng Lim, R. Alhathlool, S. Chowdhury, T. Taimre, L. H. Li, D. Indjin, S. J. Wilson, A. D. Rakić, E. H. Linfield, and A. Giles Davies, "Coherent three-dimensional terahertz imaging through self-mixing in a quantum cascade laser," *Applied Physics Letters*, vol. 103, no. 18, p. 181112, Oct. 2013.

[136] P. Dean, O. Mitrofanov, J. Keeley, I. Kundu, L. Li, E. H. Linfield, and A. Giles Davies, "Apertureless near-field terahertz imaging using the self-mixing effect in a quantum cascade laser," *Applied Physics Letters*, vol. 108, no. 9, p. 091113, Mar. 2016.

[137] Y. Ren, R. Wallis, D. S. Jessop, R. Degl'Innocenti, A. Klimont, H. E. Beere, and D. A. Ritchie, "Fast terahertz imaging using a quantum cascade amplifier," *Applied Physics Letters*, vol. 107, no. 1, p. 011107, Jul. 2015.

[138] N. Rothbart, H. Richter, M. Wienold, L. Schrottke, H. T. Grahn, and H.-W. Hubers, "Fast 2-D and 3-D Terahertz Imaging With a Quantum-Cascade Laser and a Scanning Mirror," *IEEE Transactions on Terahertz Science and Technology*, vol. 3, no. 5, pp. 617–624, Sep. 2013.

[139] Y. Xie, Y. Wang, L. Li, Y. Li, M. Salih, J.-L. Sun, E. H. Linfield, N. Yang, W. Chu, and Z. Zhao, "Realization of high depth resolution using two-beam self-mixing interferometry with a terahertz quantum cascade laser," *Optics Communications*, p. 129737, Jul. 2023.

[140] A. D. Rakić, T. Taimre, K. Bertling, Y. L. Lim, P. Dean, D. Indjin, Z. Ikonić, P. Harrison, A. Valavanis, S. P. Khanna, M. Lachab, S. J. Wilson, E. H. Linfield, and A. G. Davies, "Swept-frequency feedback interferometry using terahertz frequency QCLs: a method for imaging and materials analysis," *Optics Express*, vol. 21, no. 19, pp. 22 194–22 205, Sep. 2013.

[141] T. Hagelschuer, M. Wienold, H. Richter, L. Schrottke, K. Biermann, H. T. Grahn, and H.-W. Hübers, "Terahertz gas spectroscopy through self-mixing in a quantum-cascade laser," *Applied Physics Letters*, vol. 109, no. 19, p. 191101, Nov. 2016.

[142] M. C. Giordano, S. Mastel, C. Liewald, L. L. Columbo, M. Brambilla, L. Viti, A. Politano, K. Zhang, L. Li, A. G. Davies, E. H. Linfield, R. Hillenbrand, F. Keilmann, G. Scamarcio, and M. S. Vitiello, "Phase-resolved terahertz self-detection near-field microscopy," *Optics Express*, vol. 26, no. 14, pp. 18 423–18 435, Jul. 2018.

[143] F. P. Mezzapesa, L. L. Columbo, M. Brambilla, M. Dabbicco, M. S. Vitiello, and G. Scamarcio, "Imaging of free carriers in semiconductors via optical feedback in terahertz quantum cascade lasers," *Applied Physics Letters*, vol. 104, no. 4, p. 041112, Jan. 2014.

[144] Y. Leng Lim, P. Dean, M. Nikolić, R. Kliese, S. P. Khanna, M. Lachab, A. Valavanis, D. Indjin, Z. Ikonić, P. Harrison, E. H. Linfield, A. Giles Davies, S. J. Wilson, and A. D. Rakić, "Demonstration of a self-mixing displacement sensor based on terahertz quantum cascade lasers," *Applied Physics Letters*, vol. 99, no. 8, p. 081108, Aug. 2011.

[145] R. Degl'Innocenti, R. Wallis, B. Wei, L. Xiao, S. J. Kindness, O. Mitrofanov, P. Braeuninger-Weimer, S. Hofmann, H. E. Beere, and D. A. Ritchie, "Terahertz Nanoscopy of Plasmonic Resonances with a Quantum Cascade Laser," *ACS Photonics*, vol. 4, no. 9, pp. 2150–2157, Sep. 2017.

[146] R. Chhantyal-Pun, A. Valavanis, J. T. Keeley, P. Rubino, I. Kundu, Y. Han, P. Dean, L. Li, A. G. Davies, and E. H. Linfield, "Gas spectroscopy with integrated frequency monitoring through self-mixing in a terahertz quantum-cascade laser," *Optics Letters*, vol. 43, no. 10, p. 2225, May 2018.

[147] T. Hagelschuer, M. Wienold, H. Richter, L. Schrottke, H. T. Grahn, and H.-W. Hübers, "Real-time gas sensing based on optical feedback in a terahertz quantum-cascade laser," *Optics Express*, vol. 25, no. 24, p. 30203, Nov. 2017.

[148] Y. J. Han, J. Partington, R. Chhantyal-Pun, M. Henry, O. Auriacombe, T. Rawlings, L. H. Li, J. Keeley, M. Oldfield, N. Brewster, R. Dong, P. Dean, A. G. Davies, B. N. Ellison, E. H. Linfield, and A. Valavanis, "Gas spectroscopy through multimode self-mixing in a double-metal terahertz quantum cascade laser," *Optics Letters*, vol. 43, no. 24, p. 5933, Dec. 2018.

[149] A. D. Rakić, T. Taimre, K. Bertling, Y. L. Lim, P. Dean, A. Valavanis, and D. Indjin, "Sensing and imaging using laser feedback interferometry with quantum cascade lasers," *Applied Physics Reviews*, vol. 6, no. 2, p. 021320, Jun. 2019.

[150] K. S. Reichel, E. A. A. Pogna, S. Biasco, L. Viti, A. D. Gaspare, H. E. Beere, D. A. Ritchie, and M. S. Vitiello, "Self-mixing interferometry and near-field nanoscopy in quantum cascade random lasers at terahertz frequencies," *Nanophotonics*, vol. 10, no. 5, pp. 1495–1503, Mar. 2021.

[151] S. Han, K. Bertling, P. Dean, J. Keeley, A. D. Burnett, Y. L. Lim, S. P. Khanna, A. Valavanis, E. H. Linfield, A. G. Davies, D. Indjin, T. Taimre, and A. D. Rakić, "Laser Feedback Interferometry as a Tool for Analysis of Granular Materials at Terahertz Frequencies: Towards Imaging and Identification of Plastic Explosives," *Sensors*, vol. 16, no. 3, p. 352, Mar. 2016.

[152] Y. L. Lim, T. Taimre, K. Bertling, P. Dean, D. Indjin, A. Valavanis, S. P. Khanna, M. Lachab, H. Schaider, T. W. Prow, H. P. Soyer, S. J. Wilson, E. H. Linfield, A. G.

Davies, and A. D. Rakić, "High-contrast coherent terahertz imaging of porcine tissue via swept-frequency feedback interferometry," *Biomedical Optics Express*, vol. 5, no. 11, pp. 3981–3989, Nov. 2014.

[153] S. Donati, "Developing self-mixing interferometry for instrumentation and measurements," *Laser & Photonics Reviews*, vol. 6, no. 3, pp. 393–417, 2012.

[154] S. Donati, G. Giuliani, and S. Merlo, "Laser diode feedback interferometer for measurement of displacements without ambiguity," *IEEE Journal of Quantum Electronics*, vol. 31, no. 1, pp. 113–119, Jan. 1995.

[155] R. P. Green, J.-H. Xu, L. Mahler, A. Tredicucci, F. Beltram, G. Giuliani, H. E. Beere, and D. A. Ritchie, "Linewidth enhancement factor of terahertz quantum cascade lasers," *Applied Physics Letters*, vol. 92, no. 7, p. 071106, Feb. 2008.

[156] M. C. Cardilli, M. Dabbicco, F. P. Mezzapesa, and G. Scamarcio, "Linewidth measurement of mid infrared quantum cascade laser by optical feedback interferometry," *Applied Physics Letters*, vol. 108, no. 3, p. 031105, Jan. 2016.

[157] J. Keeley, J. Freeman, K. Bertling, Y. L. Lim, R. A. Mohandas, T. Taimre, L. H. Li, D. Indjin, A. D. Rakić, E. H. Linfield, A. G. Davies, and P. Dean, "Measurement of the emission spectrum of a semiconductor laser using laser-feedback interferometry," *Scientific Reports*, vol. 7, no. 1, p. 7236, Aug. 2017.

[158] J. v. Staden, T. Gensty, W. Elsäßer, G. Giuliani, and C. Mann, "Measurements of the α factor of a distributed-feedback quantum cascade laser by an optical feedback self-mixing technique," *Optics Letters*, vol. 31, no. 17, pp. 2574–2576, Sep. 2006.

[159] M. Piccardo and F. Capasso, "Laser Frequency Combs with Fast Gain Recovery: Physics and Applications," *Laser & Photonics Reviews*, vol. 16, no. 2, p. 2100403, Feb. 2022.

[160] M. Franckié, M. Bertrand, and J. Faist, "Sensitive dependence of the linewidth enhancement factor on electronic quantum effects in quantum cascade lasers," *Applied Physics Letters*, vol. 122, no. 2, p. 021107, Jan. 2023.

[161] M. Wienold, B. Röben, L. Schrottke, and H. T. Grahn, "Evidence for frequency comb emission from a Fabry-Pérot terahertz quantum-cascade laser," *Optics Express*, vol. 22, no. 25, pp. 30 410–30 424, Dec. 2014.

[162] R. Tkach and A. Chraplyvy, "Regimes of feedback effects in 1.5-μm distributed feedback lasers," *Journal of Lightwave Technology*, vol. 4, no. 11, pp. 1655–1661, 1986.

[163] G. Agrawal, "Line narrowing in a single-mode injection laser due to external optical feedback," *IEEE Journal of Quantum Electronics*, vol. 20, no. 5, pp. 468–471, May 1984.

[164] L. Goldberg, H. Taylor, A. Dandridge, J. Weller, and R. Miles, "Spectral characteristics of semiconductor lasers with optical feedback," *IEEE Journal of Quantum Electronics*, vol. 18, no. 4, pp. 555–564, Apr. 1982.

[165] L. Jumpertz, M. Carras, K. Schires, and F. Grillot, "Regimes of external optical feedback in 5.6 μm distributed feedback mid-infrared quantum cascade lasers," *Applied Physics Letters*, vol. 105, no. 13, p. 131112, Oct. 2014.

[166] X. Qi, K. Bertling, T. Taimre, G. Agnew, Y. L. Lim, T. Gillespie, A. Robinson, M. Brünig, A. Demić, P. Dean, L. H. Li, E. H. Linfield, A. G. Davies, D. Indjin, and A. D. Rakić, "Observation of optical feedback dynamics in single-mode terahertz quantum cascade lasers: Transient instabilities," *Physical Review A*, vol. 103, no. 3, p. 033504, Mar. 2021.

[167] H. Hübers, H. Richter, R. Eichholz, M. Wienold, K. Biermann, L. Schrottke, and H. T. Grahn, "Heterodyne Spectroscopy of Frequency Instabilities in Terahertz Quantum-Cascade Lasers Induced by Optical Feedback," *IEEE Journal of Selected Topics in Quantum Electronics*, vol. 23, no. 4, pp. 1–6, Jul. 2017.

[168] O. Spitz, J. Wu, M. Carras, C.-W. Wong, and F. Grillot, "Chaotic optical power dropouts driven by low frequency bias forcing in a mid-infrared quantum cascade laser," *Scientific Reports*, vol. 9, no. 1, p. 4451, Mar. 2019.

[169] O. Spitz, J. Wu, A. Herdt, G. Maisons, M. Carras, W. E. Elsäßer, C.-W. Wong, and F. Grillot, "Extreme events in quantum cascade lasers," *Advanced Photonics*, vol. 2, no. 6, p. 066001, Oct. 2020.

[170] X. Qi, G. Agnew, T. Taimre, S. Han, Y. L. Lim, K. Bertling, A. Demić, P. Dean, D. Indjin, and A. D. Rakić, "Laser feedback interferometry in multi-mode terahertz quantum cascade lasers," *Optics Express*, vol. 28, no. 10, pp. 14 246–14 262, May 2020.

[171] X. Qi, K. Bertling, T. Taimre, G. Agnew, Y. L. Lim, T. Gillespie, A. Demić, P. Dean, L. H. Li, E. H. Linfield, A. G. Davies, D. Indjin, and A. D. Rakić, "Terahertz quantum cascade laser under optical feedback: effects of laser self-pulsations on self-mixing signals," *Optics Express*, vol. 29, no. 24, pp. 39 885–39 894, Nov. 2021.

[172] L. Jumpertz, S. Ferré, K. Schires, M. Carras, and F. Grillot, "Nonlinear dynamics of quantum cascade lasers with optical feedback," in *Quantum Sensing and Nanophotonic Devices XII*, vol. 9370. SPIE, Feb. 2015, pp. 230–237.

[173] F. P. Mezzapesa, L. L. Columbo, M. Brambilla, M. Dabbicco, S. Borri, M. S. Vitiello, H. E. Beere, D. A. Ritchie, and G. Scamarcio, "Intrinsic stability of quantum cascade lasers against optical feedback," *Optics Express*, vol. 21, no. 11, pp. 13 748–13 757, Jun. 2013.

[174] Y. Wu, C. A. Curwen, M. Shahili, J. L. Reno, and B. S. Williams, "RF Injection Locking of THz Metasurface Quantum-Cascade VECSEL," *Laser & Photonics Reviews*, vol. 17, no. 8, p. 2300007, 2023.

[175] X.-G. Wang, B.-B. Zhao, Y. Deng, V. Kovanis, and C. Wang, "Nonlinear dynamics of a quantum cascade laser with tilted optical feedback," *Physical Review A*, vol. 103, no. 2, p. 023528, Feb. 2021.

[176] C. A. Curwen, A. D. Kim, B. S. Karasik, J. H. Kawamura, and B. S. Williams, "Optical injection locking of a THz quantum-cascade VECSEL with an electronic source," *Optics Letters*, vol. 48, no. 14, pp. 3809–3812, Jul. 2023.

[177] K. Petermann, "External optical feedback phenomena in semiconductor lasers," *IEEE Journal of Selected Topics in Quantum Electronics*, vol. 1, no. 2, pp. 480–489, Jun. 1995.

[178] ——, *Laser Diode Modulation and Noise*. Dordrecht: Springer Netherlands, 1988.

[179] T. Taimre, M. Nikolić, K. Bertling, Y. L. Lim, T. Bosch, and A. D. Rakić, "Laser feedback interferometry: a tutorial on the self-mixing effect for coherent sensing," *Advances in Optics and Photonics*, vol. 7, no. 3, p. 570, Sep. 2015.

[180] T. Taimre and A. D. Rakić, "On the nature of Acket's characteristic parameter C in semiconductor lasers," *Applied Optics*, vol. 53, no. 5, pp. 1001–1006, Feb. 2014.

[181] D. R. Bacon, J. R. Freeman, R. A. Mohandas, L. Li, E. H. Linfield, A. G. Davies, and P. Dean, "Gain recovery time in a terahertz quantum cascade laser," *Applied Physics Letters*, vol. 108, no. 8, p. 081104, Feb. 2016.

[182] H. Choi, L. Diehl, Z.-K. Wu, M. Giovannini, J. Faist, F. Capasso, and T. B. Norris, "Gain Recovery Dynamics and Photon-Driven Transport in Quantum Cascade Lasers," *Physical Review Letters*, vol. 100, no. 16, p. 167401, Apr. 2008.

[183] R. Paiella, R. Martini, F. Capasso, C. Gmachl, H. Y. Hwang, D. L. Sivco, J. N. Baillargeon, A. Y. Cho, E. A. Whittaker, and H. C. Liu, "High-frequency modulation without the relaxation oscillation resonance in quantum cascade lasers," *Applied Physics Letters*, vol. 79, no. 16, pp. 2526–2528, Oct. 2001.

[184] R. Martini, R. Paiella, F. Capasso, C. Gmachl, H. Y. Hwang, D. L. Sivco, A. Y. Cho, E. A. Whittaker, and H. C. Liu, "Absence of relaxation oscillation in quantum cascade lasers verified by high-frequency modulation," in *Conference on Lasers and Electro-Optics (2001), paper CPD17*. Optica Publishing Group, May 2001, p. CPD17.

[185] C. Henry, "Theory of the linewidth of semiconductor lasers," *IEEE Journal of Quantum Electronics*, vol. 18, no. 2, pp. 259–264, Feb. 1982.

[186] J. Faist, *Quantum Cascade Lasers*. Oxford University Press, Mar. 2013.

[187] T. Aellen, R. Maulini, R. Terazzi, N. Hoyler, M. Giovannini, J. Faist, S. Blaser, and L. Hvozdara, "Direct measurement of the linewidth enhancement factor by optical heterodyning of an amplitude-modulated quantum cascade laser," *Applied Physics Letters*, vol. 89, no. 9, p. 091121, Aug. 2006.

[188] J. Faist, F. Capasso, C. Sirtori, D. L. Sivco, A. L. Hutchinson, and A. Y. Cho, "Continuous wave operation of a vertical transition quantum cascade laser above T=80 K," *Applied Physics Letters*, vol. 67, no. 21, pp. 3057–3059, Nov. 1995.

[189] M. Lerttamrab, S. L. Chuang, C. Gmachl, D. L. Sivco, F. Capasso, and A. Y. Cho, "Linewidth enhancement factor of a type-I quantum-cascade laser," *Journal of Applied Physics*, vol. 94, no. 8, pp. 5426–5428, Oct. 2003.

[190] J. Kim, M. Lerttamrab, S. L. Chuang, C. Gmachl, D. Sivco, F. Capasso, and A. Cho, "Theoretical and experimental study of optical gain and linewidth enhancement factor of type-I quantum-cascade lasers," *IEEE Journal of Quantum Electronics*, vol. 40, no. 12, pp. 1663–1674, Dec. 2004.

[191] Y. Yu, J. Xi, E. Li, and J. F. Chicharo, "Measuring the linewidth enhancement factor of semiconductor lasers based on weak optical feedback effect," in *Semiconductor Lasers and Applications II*, vol. 5628. SPIE, Jan. 2005, pp. 34–39.

[192] Y. Yu, G. Giuliani, and S. Donati, "Measurement of the linewidth enhancement factor of semiconductor lasers based on the optical feedback self-mixing effect," *IEEE Photonics Technology Letters*, vol. 16, no. 4, pp. 990–992, Apr. 2004.

[193] G. Liu, X. Jin, and S. Chuang, "Measurement of linewidth enhancement factor of semiconductor lasers using an injection-locking technique," *IEEE Photonics Technology Letters*, vol. 13, no. 5, pp. 430–432, May 2001.

[194] C. Harder, K. Vahala, and A. Yariv, "Measurement of the linewidth enhancement factor α of semiconductor lasers," *Applied Physics Letters*, vol. 42, no. 4, pp. 328–330, Feb. 1983.

[195] L. Jumpertz, F. Michel, R. Pawlus, W. Elsässer, K. Schires, M. Carras, and F. Grillot, "Measurements of the linewidth enhancement factor of mid-infrared quantum cascade lasers by different optical feedback techniques," *AIP Advances*, vol. 6, no. 1, p. 015212, Jan. 2016.

[196] L. L. Columbo and M. Brambilla, "Multimode regimes in quantum cascade lasers with optical feedback," *Optics Express*, vol. 22, no. 9, pp. 10 105–10 118, May 2014.

[197] L. Weicker, D. Wolfersberger, and M. Sciamanna, "Stability analysis of a quantum cascade laser subject to phase-conjugate feedback," *Physical Review E*, vol. 98, no. 1, p. 012214, Jul. 2018.

[198] N. Vukovic, J. Radovanovic, V. Milanovic, and D. L. Boiko, "Numerical study of Risken–Nummedal–Graham–Haken instability in mid-infrared Fabry–Pérot quantum cascade lasers," *Optical and Quantum Electronics*, vol. 52, no. 2, p. 91, Jan. 2020.

[199] X.-G. Wang, B.-B. Zhao, F. Grillot, and C. Wang, "Spectral linewidth reduction of quantum cascade lasers by strong optical feedback," *Journal of Applied Physics*, vol. 127, no. 7, p. 073104, Feb. 2020.

[200] A. D. Kim, D. J. McGovern, and B. S. Williams, "Multi-bounce self-mixing in terahertz metasurface external-cavity lasers," *Optics Express*, vol. 32, no. 11, pp. 18 880–18 895, May 2024.

[201] R. Lang and K. Kobayashi, "External optical feedback effects on semiconductor injection laser properties," *IEEE Journal of Quantum Electronics*, vol. 16, no. 3, pp. 347–355, Mar. 1980.

[202] K. Vahala, L. C. Chiu, S. Margalit, and A. Yariv, "On the linewidth enhancement factor α in semiconductor injection lasers," *Applied Physics Letters*, vol. 42, no. 8, pp. 631–633, Apr. 1983.

[203] N. Kumazaki, Y. Takagi, M. Ishihara, K. Kasahara, A. Sugiyama, N. Akikusa, and T. Edamura, "Detuning characteristics of the linewidth enhancement factor of a midinfrared quantum cascade laser," *Applied Physics Letters*, vol. 92, no. 12, p. 121104, Mar. 2008.

[204] G. Acket, D. Lenstra, A. Den Boef, and B. Verbeek, "The influence of feedback intensity on longitudinal mode properties and optical noise in index-guided semiconductor lasers," *IEEE Journal of Quantum Electronics*, vol. 20, no. 10, pp. 1163–1169, Oct. 1984.

[205] D. M. Kane and K. A. Shore, *Unlocking Dynamical Diversity: Optical Feedback Effects on Semiconductor Lasers*. John Wiley & Sons, Nov. 2005.

[206] Y. Yu, J. Xi, J. F. Chicharo, and T. M. Bosch, "Optical Feedback Self-Mixing Interferometry With a Large Feedback Factor C : Behavior Studies," *IEEE Journal of Quantum Electronics*, vol. 45, no. 7, pp. 840–848, Jul. 2009.

[207] C.-M. Ri, C.-H. Kim, Y.-N. Oh, and S.-C. Kim, "Immediate estimation of feedback factor and linewidth enhancement factor from measured self-mixing signals under moderate or strong regime," *Measurement Science and Technology*, vol. 31, no. 6, p. 065204, Mar. 2020.

[208] J. Keeley, K. Bertling, P. L. Rubino, Y. L. Lim, T. Taimre, X. Qi, I. Kundu, L. H. Li, D. Indjin, A. D. Rakić, E. H. Linfield, A. G. Davies, J. Cunningham, and P. Dean, "Detection sensitivity of laser feedback interferometry using a terahertz quantum cascade laser," *Optics Letters*, vol. 44, no. 13, pp. 3314–3317, Jul. 2019.

[209] S. Kohen, B. S. Williams, and Q. Hu, "Electromagnetic modeling of terahertz quantum cascade laser waveguides and resonators," *Journal of Applied Physics*, vol. 97, no. 5, p. 053106, Feb. 2005.

[210] D.-S. Seo, J.-D. Park, J. McInerney, and M. Osinski, "Multiple feedback effects in asymmetric external cavity semiconductor lasers," *IEEE Journal of Quantum Electronics*, vol. 25, no. 11, pp. 2229–2238, Nov. 1989.

[211] X. Cheng and S. Zhang, "Multiple selfmixing effect in VCSELs with asymmetric external cavity," *Optics Communications*, vol. 260, no. 1, pp. 50–56, Apr. 2006.

[212] C. A. Curwen, J. H. Kawamura, D. J. Hayton, S. J. Addamane, J. L. Reno, B. S. Williams, and B. S. Karasik, "Phase Locking of a THz QC-VECSEL to a Microwave Reference," *IEEE Transactions on Terahertz Science and Technology*, vol. 13, no. 5, pp. 448–453, Sep. 2023.

[213] H.-W. Hübers, S. G. Pavlov, H. Richter, A. D. Semenov, L. Mahler, A. Tredicucci, H. E. Beere, and D. A. Ritchie, "Molecular Spectroscopy with TeraHertz Quantum Cascade Lasers," *Journal of Nanoelectronics and Optoelectronics*, vol. 2, no. 1, pp. 101–107, Apr. 2007.

[214] J. M. Hensley, J. Montoya, M. G. Allen, J. Xu, L. Mahler, A. Tredicucci, H. E. Beere, and D. A. Ritchie, "Spectral behavior of a terahertz quantum-cascade laser," *Optics Express*, vol. 17, no. 22, pp. 20 476–20 483, Oct. 2009.

[215] R. Kliese, T. Taimre, A. A. A. Bakar, Y. L. Lim, K. Bertling, M. Nikolić, J. Perchoux, T. Bosch, and A. D. Rakić, "Solving self-mixing equations for arbitrary feedback levels: a concise algorithm," *Applied Optics*, vol. 53, no. 17, pp. 3723–3736, Jun. 2014.

[216] Y. Gao, Y. Yu, J. Xi, Q. Guo, J. Tong, and S. Tong, "Improved method for estimation of multiple parameters in self-mixing interferometry," *Applied Optics*, vol. 54, no. 10, pp. 2703–2709, Apr. 2015.

[217] Y. Fan, Y. Yu, J. Xi, and J. F. Chicharo, "Improving the measurement performance for a self-mixing interferometry-based displacement sensing system," *Applied Optics*, vol. 50, no. 26, pp. 5064–5072, Sep. 2011.

[218] V. Jayaraman, G. D. Cole, M. Robertson, A. Uddin, and A. Cable, "High-sweep-rate 1310 nm MEMS-VCSEL with 150 nm continuous tuning range," *Electronics Letters*, vol. 48, no. 14, pp. 867–869, Jul. 2012.

[219] P. Qiao, K. T. Cook, K. Li, and C. J. Chang-Hasnain, "Wavelength-Swept VCSELs," *IEEE Journal of Selected Topics in Quantum Electronics*, vol. 23, no. 6, pp. 1–16, Nov. 2017.

[220] N. W. Almond, X. Qi, R. Degl'Innocenti, S. J. Kindness, W. Michailow, B. Wei, P. Braeuninger-Weimer, S. Hofmann, P. Dean, D. Indjin, E. H. Linfield, A. G. Davies, A. D. Rakić, H. E. Beere, and D. A. Ritchie, "External cavity terahertz quantum cascade laser with a metamaterial/graphene optoelectronic mirror," *Applied Physics Letters*, vol. 117, no. 4, p. 041105, Jul. 2020.

[221] S. J. Kindness, D. S. Jessop, B. Wei, R. Wallis, V. S. Kamboj, L. Xiao, Y. Ren, P. Braeuninger-Weimer, A. I. Aria, S. Hofmann, H. E. Beere, D. A. Ritchie, and R. Degl'Innocenti, "External amplitude and frequency modulation of a terahertz quantum cascade laser using metamaterial/graphene devices," *Scientific Reports*, vol. 7, no. 1, p. 7657, Aug. 2017.

[222] F. Lacy, "Developing a theoretical relationship between electrical resistivity, temperature, and film thickness for conductors," *Nanoscale Research Letters*, vol. 6, no. 1, p. 636, Dec. 2011.

[223] R. A. Matula, "Electrical resistivity of copper, gold, palladium, and silver," *Journal of Physical and Chemical Reference Data*, vol. 8, no. 4, pp. 1147–1298, Oct. 1979.

[224] N.-P. Chen, H. J. Ueng, D. B. Janes, J. M. Woodall, and M. R. Melloch, "A quantitative conduction model for a low-resistance nonalloyed ohmic contact structure utilizing low-temperature-grown GaAs," *Journal of Applied Physics*, vol. 88, no. 1, pp. 309–315, Jul. 2000.

[225] S. M. Sze, "Physics of Semiconductor Devices," in *Physics of Semiconductor Devices*. John Wiley & Sons, Ltd, 2006, pp. 77–133.

[226] J. Dai, J. Zhang, W. Zhang, and D. Grischkowsky, "Terahertz time-domain spectroscopy characterization of the far-infrared absorption and index of refraction of high-resistivity, float-zone silicon," *JOSA B*, vol. 21, no. 7, pp. 1379–1386, Jul. 2004.

[227] C. J. Chang-Hasnain, Y. Zhou, M. C. Y. Huang, and C. Chase, "High-Contrast Grating VCSELs," *IEEE Journal of Selected Topics in Quantum Electronics*, vol. 15, no. 3, pp. 869–878, May 2009.